UNIVERSIDAD NACIONAL AUTÓNOMA DE MÉXICO
POSGRADO EN CIENCIAS DE LA TIERRA
INSTITUTO DE GEOFÍSICA
SISMOLOGÍA

Active crustal faulting along Guerrero-Oaxaca forearc, Mexico, and its interaction with 2017/19 SSEs: seismo-geodetic study.

TESIS
QUE PARA OPTAR POR EL GRADO DE:
DOCTOR EN CIENCIAS

PRESENTA:
EKATERINA KAZACHKINA

TUTOR PRINCIPAL
DR VLADIMIR KOSTOGLODOV
(Instituto de Geofísica, UNAM, México)

MIEMBROS DEL COMITÉ TUTOR
DR ALLEN HUSKER (Caltech, EEUU)
DRA NATHALIE COTTE (Isterre, Francia)

Ciudad Universitaria, CD. MX., Enero de 2023

Active crustal faulting along Guerrero-Oaxaca forearc, Mexico, and its interaction with 2017/19 SSEs: seismo-geodetic study

por

Ekaterina Kazachkina

M.Sc., University Grenoble Alpes (2015)

Tesis presentada para obtener el grado de

Doctor en Ciencias

en el

Instituto de Geofisica

Universidad Nacional Autónoma de México

Mexico, Ciudad de Mexico. Enero, 2023

Agradecimientos

First of all, I would like to greatly thank my PhD advisor Dr Vladimir Kostoglodov for guiding me through this research work and always providing support for the benefit of this study.

I thank Dr Nathalie Cotte, my co-advisor, who generously passed to me her knowledge and experience in GPS processing. I am grateful for your patience, positive attitude and help both in scientific and organizational matters.

I thank Dr Andrea Walpersdorf for her very useful and timely help on different GAMIT/GLOBK issues.

I thank a lot Dr Mathilde Radiguet for her persistent support and detailed explanations on the ICA inversion strategy.

I thank Dr Allen Husker, also my co-advisor, for sharing his new approaches to analyse familiar data and general support for pursuing my PhD abroad, far from home.

And I also thank my colleagues Jorge Real and Jose Santiago for sharing their expertise in the field and long talks on the road.

Finally, I thank all the members of the Department of Seismology of the Institute of Geophysics for their diverse support, with special thanks to Paty Medina and also Araceli Chaman for their help, patience with all the paper work and for a simple kind word.

I thank señora Eva for her unconditional motherly support.

I thank my mother for pushing me to study, work and be independent.

A special thank you is to PG for having faith in me and for always having the right word to support and cheer me up.

Contents

Active crustal faulting along Guerrero-Oaxaca forearc, Mexico, and its interaction with 2017/19 SSEs: seismo-geodetic study

by

Ekaterina Kazachkina

Abstract

The Mexican oblique subduction zone encompasses a number of distinctive features and phenomena that draw the attention of many Earth scientists (e.g. H. Kanamori, K. Larson, M. Campillo, Y. Fialko, E, Fielding, N. Shapiro, etc.). According to the existing historical records, Mexico has suffered from at least four great earthquakes of $M_w \geq 8.0$. By analyzing seismic activity recorded by temporary and permanent stations Suárez *et al.* [1990] determined that a section of the Mexican subduction zone was flat. Later Perez Campos *et al.* [2008] estimated the dimensions of the flat segment to be ∼140 km long. In 1998 the first transient aseismic deformation classified as a slow slip event (SSE) was observed in the time series from the continuous GPS station in Cayaco, Guerrero [Lowry *et al.*, 2001]. The focus of present work is: first, to find reliable evidence that a system of active faults (or active shear zone) exists in the forearc area of Guerrero-Oaxaca, Southern Mexico; and second, to analyze the occurrence of slow slip events on the system of trench-parallel strike-slip faults bordering the Xolapa forearc sliver and their interaction with SSEs on the subduction interface in Guerrero and Oaxaca.

The objective of this work is to study the activity of the La Venta Chacalapa (LVC) system of crustal strike slip faults using seismic and geodetic data. Within the framework of this research the motion of the Xolapa sliver is analyzed and quantified using long term GPS time series, focal mechanisms and CMT solutions. This work also covers the anomalous sequence of subduction slow slip events of 2017-2019 in Guerrero and Oaxaca occurred after the 2017 M_w8.2 Tehuantepec earthquake. Apart from that, one of the main purposes of this study is to characterize the spatial and temporal interaction between subduction and strike-slip SSEs in Guerrero and Oaxaca. The last subduction SSE sequence of 2017-2019 helps to complement the analysis and reveal any changes in the slow slip events on the LVC after the Chiapas earthquake. Lastly, the SSEs analyzed in this study are supported by the non-volcanic tremor (NVT) observations from the nearby seismic stations.

According to the analysis of slip partitioning in the forearc of the Mexican subduction zone using the method of McCaffrey [1992], the Xolapa sliver velocity with respect to the fixed NA plate is 10±1 mm/year for local catalog and 5.6±0.8 mm/year for Global CMT compilation. The difference between the results for two catalogs is explained by the inconsistency in local and teleseismic estimations of earthquake source parameters such as strike, dip and rake for the same events. The result from the Global CMT catalog is taken as the reference since it is in good agreement with the geologic and geodetic observations (5-6 mm/year in Guerrero). Based on this observation, a compressive deformation of the Xolapa sliver is assumed likely caused by the presence of a buttressing structure, such as subducting seamount chains in Oaxaca, at its leading edge. Detailed analysis of GPS time series and a refined fault trace mapping, especially

in Oaxaca, will allow retrieving more information on the activity of forearc faults and associated seismic risk. [Kazachkina *et al.*, 2019]

Long-lasting GPS observations and geomorphology studies in the Guerrero-Oaxaca area of the Mexican subduction zone show that this mainly left-lateral shear zone is a complex and active system of numerous distributed strike-slip faults that accommodates strain partitioning produced by oblique subduction of the Cocos plate. As the result of the present study, it is important to admit that the La Venta-Chacalapa fault system is the principal active tectonic feature in Southern Mexico, which must be considered as a source of potential seismic hazard. It is still not known how long the LVC fault zone has been active, and what the cumulative offset is across the LVC fault zone in time. Existing GPS records only are not enough to constitute a previously unrecognized hazard in Southern Mexico related to the active LVC fault system. We need to obtain quantitative constraints on the age of the LVC faulting at least for the last few thousand years. Accurate trace and structure of the LVC was not yet explored except perhaps its western Guerrero segment [Gaidzik *et al.*, 2016]. The motion of the Xolapa sliver in Oaxaca remains rather hypothetical until more data is available on new GPS stations installed inland from the LVC zone.

Chapter 1

Introduction

1.1 Background

The Mexican oblique subduction zone encompasses a number of distinctive features and phenomena that draw the attention of many Earth scientists (e.g. H. Kanamori, K. Larson, M. Campillo, Y. Fialko, E, Fielding, N. Shapiro, etc.). According to the existing historical records, Mexico has suffered from at least four great earthquakes of $M_w \geq 8.0$. By analyzing seismic activity recorded by temporary and permanent stations Suárez *et al.* [1990] determined that a section of the Mexican subduction zone was flat. Later Perez Campos *et al.* [2008] estimated the dimensions of the flat segment to be ∼140 km long. In 1998 the first transient aseismic deformation classified as a slow slip event (SSE) was observed in the time series from the continuous GPS station in Cayaco, Guerrero [Lowry *et al.*, 2001]. The focus of present work is: first, to find reliable evidence that a system of active faults (or active shear zone) exists in the forearc area of Guerrero-Oaxaca, Southern Mexico; and second, to analyze the occurrence of slow slip events on the system of trench-parallel strike-slip faults bordering the Xolapa forearc sliver and their interaction with SSEs on the subduction interface in Guerrero and Oaxaca.

Slow slip events have been identified in subduction zones, where pairs of tectonic plates converge (e.g., Vidale and Houston [2012]). However, several continental strike-slip faults, such as the San Andreas Fault, exhibit segments that release strain fairly continuously or creep

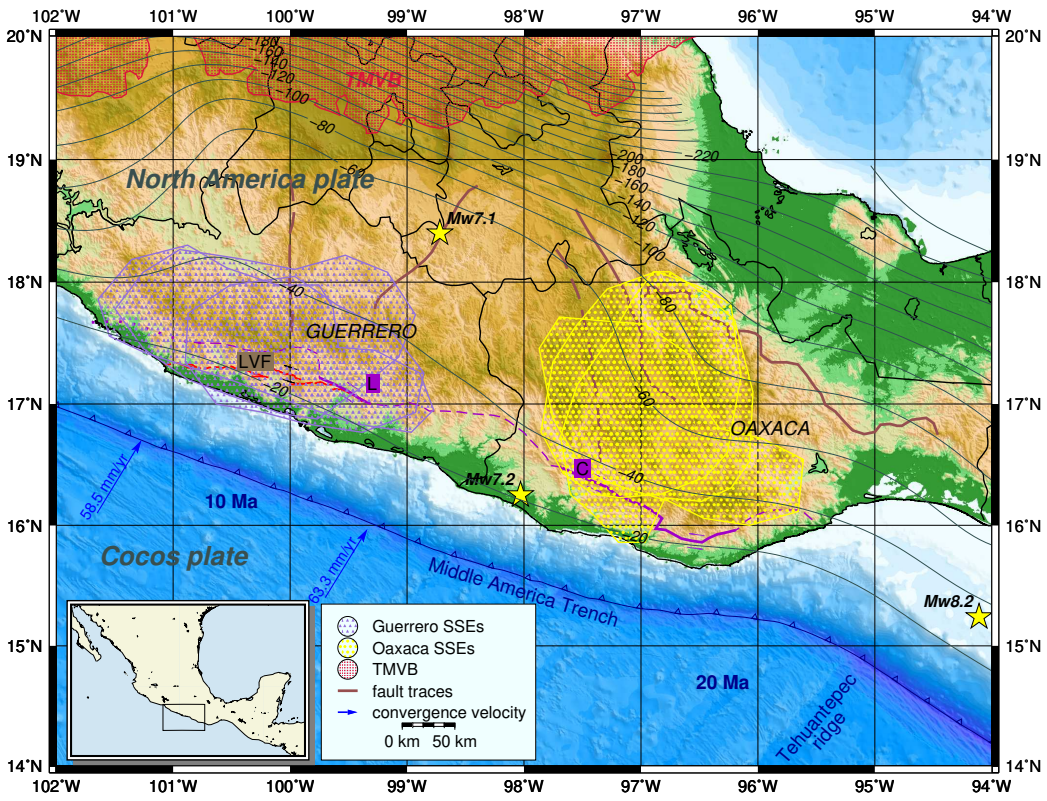

Figure 1-1: Map of Central and Southern mexico showing the Guerrero and Oaxaca SSE patches, fault traces, L - La Venta fault system from Solari *et al.* [2007] and Tolson [2005] LVF - Agua de Perro section of the La Venta fault system, C - Chacalapa fault system from Cerca *et al.* [2007] and Tolson [2005], TMVB - Trans-Mexican Volcanic Belt, thin gray lines mark the subduction slab depth profile [Hayes *et al.*, 2018], yellow stars are earthquake epicenters.

both at the surface [Galehouse, 2002] and at seismogenic depths [Wesson, 1988]. Mid-oceanic transform faults have also been shown to accommodate much of their plate motion (up to 85%) aseismically [Boettcher and Jordan, 2004].

The main difference of the slow slip event and the earthquake is that no seismic energy radiated from SSEs can be recorded by traditional seismometers. In this definition, observed pre-seismic or post-seismic slip, or creep emergent events may all be categorized as the silent earthquake or SSE [Kato, 2011]. Numerous observations revealed that SSE accompanied by non-volcanic tremors (NVT), more generally referred to as episodic tremor and slip (ETS), spans time periods from days to years and that the events can be periodic or not (e.g., Vidale

and Houston [2012]).

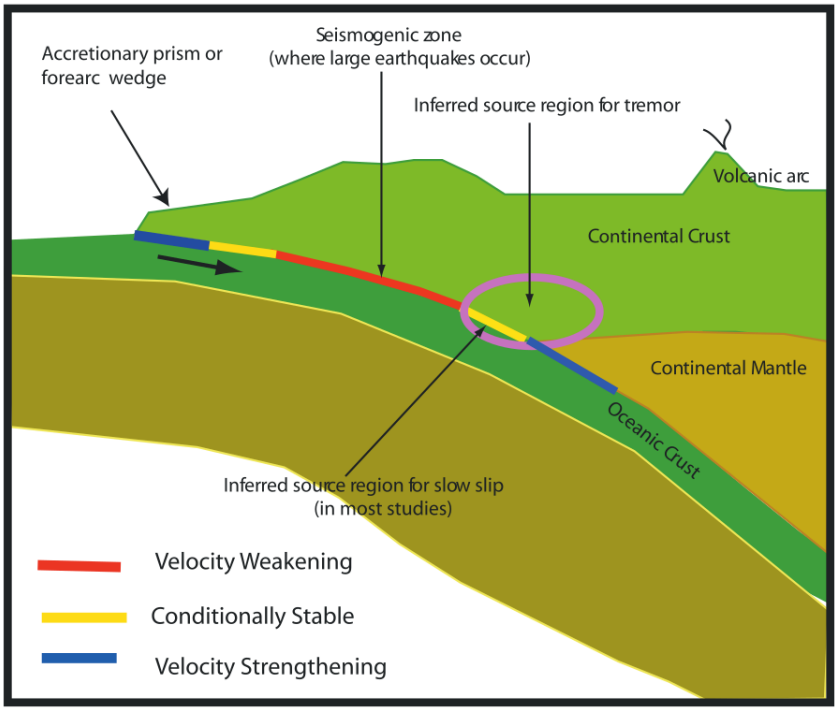

Figure 1-2: Schematic representation of the seismogenic zone at convergent plate boundaries with frictional properties labeled. Earthquakes nucleate in velocity weakening rheology and are capable of propagating into conditionally stable but not velocity strengthening regions [Schwartz and Rokosky, 2007].

The existence of slow events having source durations of days to years was first postulated for a segment of the San Andreas Fault on the basis of borehole strainmeter observations [Linde *et al.*, 1996]. This slow event duration is more likely associated with the time for slip on the fault to reach its final value (slip rise-time) rather than a rupture propagation time. Such slip episodes initiating in or near the seismogenic zone but radiating no seismic energy are referred to as "slow slip events" [Schwartz and Rokosky, 2007].

A comparison of long-term moment release rate at subduction zones could be made to detect slow events. If all strain accumulated along plate boundaries is released by seismic energy, then the released moment at the time of earthquake should be equal to the accumulated moment. Kawasaki *et al.* [2001] examined this hypothesis and found that the total moment released by earthquakes along the plate boundary is far smaller than the totally accumulated moment in

the interseismic stage. Bird and Kagan [2004] analyzed extensive global earthquake database and obtained coupling coefficients for different fault types. Subduction zones exhibit one of the highest coupling levels of 0.69 (Table 5 in Bird and Kagan [2004]). This studies prove that there are other unknown tectonic processes that release remaining moment at the plate boundaries [Kato, 2011] through a different mode of deformation. Those could be SSEs or postseismic slips.

More direct and convincing findings about slow slip events were brought in 1990s by the advent of the Global Positioning System (GPS). Rapid developments of GPS arrays all over the world, in particular along the Pacific Rim areas including the western coast of Mexico, enabled the discovery and analysis of silent earthquakes or slow slip events [Kato, 2011].

Global observations of the location, spatial extent, magnitude, duration, slip rate, and periodicity of these aseismic slip transients indicate significant variation that may be exploited to better understand their generation. Most of slow slip events occur just down-dip of the seismogenic zone, consistent with rate- and state-dependent frictional model (e.g. Hirose *et al.* [1999]; Dragert *et al.* [2001]) that requires unstable to stable transitional properties for slow slip generation (Fig. 1-2). At a few convergent margins the occurrence of slow slip events within the seismogenic zone (e.g., Sagiya [2004]; Kostoglodov *et al.* [2003]; Larson *et al.* [2004]) makes it highly likely that transitions in frictional properties exist there and are the loci of slow slip nucleation. Trends in global observations of slow slip events suggest that (1) slow slip is a common phenomenon observed at almost all subduction zones with instrumentation capable of recording it, (2) different frictional properties likely control fast versus slow slip, (3) the depth range of slow slip may be related to the thermal properties of the plate interface, and (4) the equivalent seismic moment of slow slip events was considered proportional to their duration ($M_0 \propto \tau$) [Schwartz and Rokosky, 2007; Audet and Kim, 2016], while more recent studies found no difference from the $M_0 \propto \tau^3$ scaling observed for usual earthquakes (e.g., Michel *et al.* [2019]).

Seismic moment at most plate boundaries accounts for only a fraction of plate tectonic motions, so the addition of SSEs can provide a better quantification of the moment release

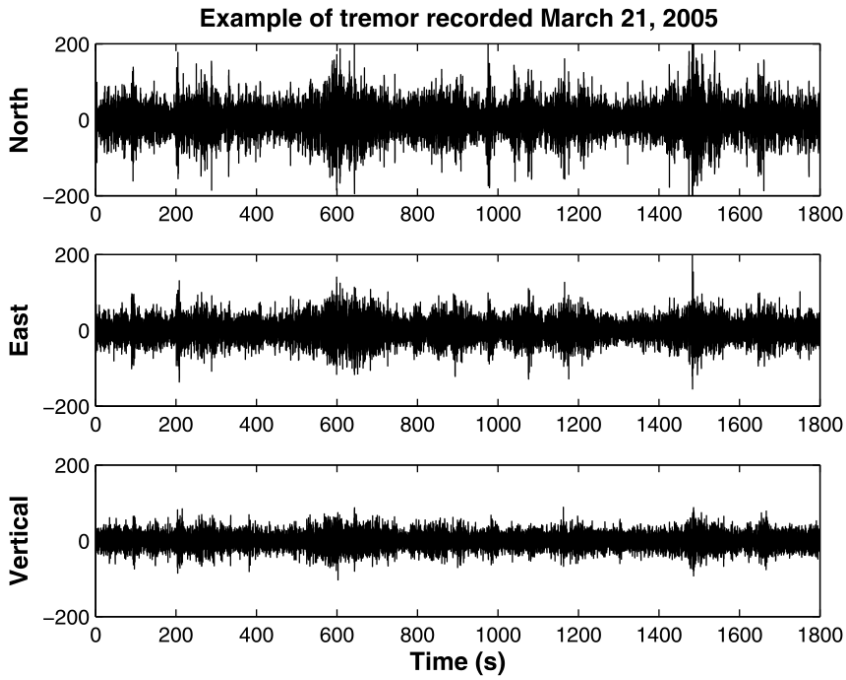

Figure 1-3: Example tremor seismogram [Husker *et al.*, 2012]. This is from an NVT episode recorded at the station TONA approximately 200 km from the trench [Perez Campos *et al.*, 2008].

budget. Slow fault slip as well as earthquake induced slip perturbs the surrounding stress field and may either increase or relieve stress on an adjacent fault segment, bringing it closer to or farther from earthquake failure, respectively [León-Loya *et al.*, 2022]. Therefore, a better understanding of slow slip events and their ability to trigger earthquakes is important for seismic hazard assessment [Schwartz and Rokosky, 2007].

Although extremely slow motion on faults generates no detectable seismic signal, it has been discovered that SSEs in various locations, including Southwestern Japan, northern Cascadia, Mexican subduction zone, south central Alaska, sections of San Andreas fault, correlate with episodes of non-volcanic tremor (NVT, Fig. 1-3) (e.g. Kostoglodov *et al.* [2009]; Peterson and Christensen [2009]; Obara [2011]). Tremor represents long duration (minutes to hours) of low-amplitude seismic signal, without clear body wave arrivals. Tremor duration varies between regions and episodes, and it is sometimes quite pulsed in nature (Fig. 1-3). Tremor is generally identified by the correlation of maxima of amplitude envelopes on several nearby stations (e.g.

Obara [2002]; McCausland *et al.* [2005]).

Subduction zone tremor is characterized by its relatively low frequency band ($\sim$ 1-10 Hz) that is lower than the local earthquakes have. Most tremor shows a rapid drop-off in frequency content above 6 Hz. Initial reports of tremor activity at subduction zones emphasized a comparison with the volcanic tremor. Although similarities between the two phenomena certainly require a special study, it is important to note that subduction tremor does not appear to be harmonic, a common feature in the volcanic tremor [Schwartz and Rokosky, 2007].

1.2 Previous studies

A variety of slow slip events whose time durations are months to years, have been discovered along the subducting plate boundaries [Kato, 2011]. Continuous Global Positioning System (GPS) networks have enabled recording of this important class of geophysical phenomena. Slow slip (Fig. 1-5) has been detected with continuous GPS networks in Japan [Heki *et al.*, 1997; Hirose *et al.*, 1999; Ozawa *et al.*, 2001], Cascadia [Dragert *et al.*, 2001], Mexico [Lowry *et al.*, 2001], Kamchatka [Bürgmann *et al.*, 2001], Alaska [Freymueller *et al.*, 2002], New Zealand [Douglas *et al.*, 2005], Hawaii [Cervelli *et al.*, 2002], northern Peru [Villegas-Lanza *et al.*, 2015] and Chile [Klein *et al.*, 2018].

Northern Cascadia hosts slow slip events located downdip of the seismogenic zone near the seismic/aseismic transition, they repeat at 13 to 16 month intervals, and are accompanied by seismic tremor [Miller *et al.*, 2002; Rogers and Dragert, 2003]. Ozawa *et al.* [2002] described the slow slip event on the subduction interface in the Tokai region of Japan that continued for over 4 years [Ohta *et al.*, 2004]. Similar events have been reported in southern Mexico [Lowry *et al.*, 2001], Alaska [Freymueller *et al.*, 2002], New Zealand [Douglas *et al.*, 2005], and Costa Rica [Protti *et al.*, 2004].

Between 1997, when the first continuous GPS receiver was installed in the Mexican subduction zone (MSZ), and 2020, at least 6 long-term SSEs were recorded on the subduction interface below the state of Guerrero and at least 16 SSEs below Oaxaca (e.g., Kostoglodov *et al.* [2003];

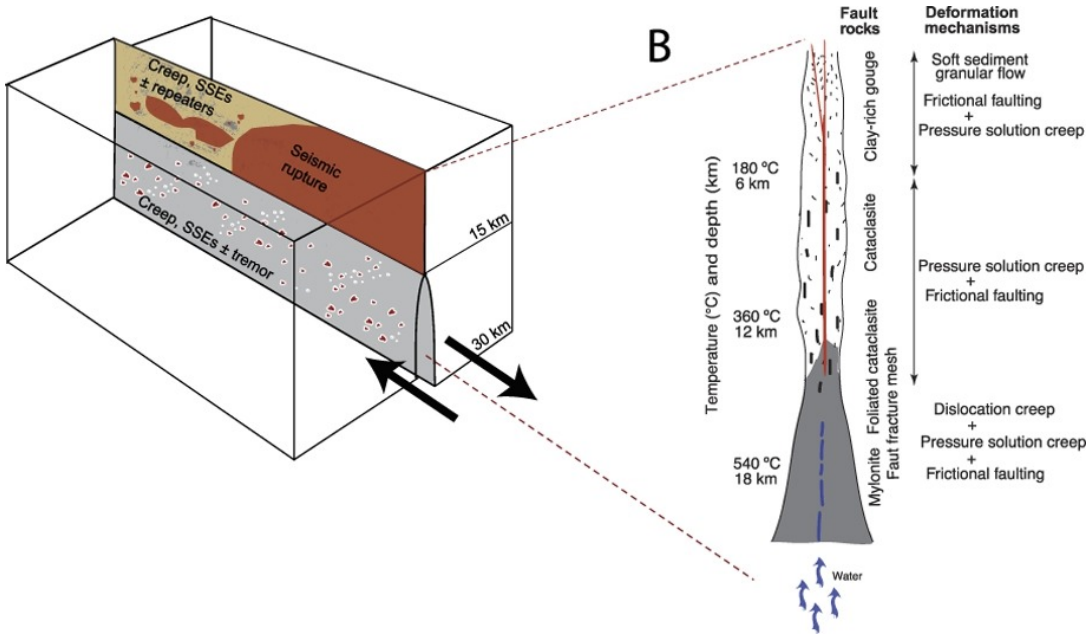

Figure 1-4: Schematic representation of shallow transients on strike-slip faults. *(on the left)* Distribution of seismic and aseismic slip and tremor on the partially coupled San Andreas Fault near Parkfield. Fluids at high pressures in the lower crust may be derived from underlying paleo-subduction rocks. *(on the right)* Conceptual strike-slip fault cross-section illustrating depth distribution of fault zone rocks and deformation mechanism accommodating slow slip. [Bürgmann, 2018]

Brudzinski *et al.* [2007]; Correa-Mora *et al.* [2008, 2009]; Radiguet *et al.* [2012]; Graham *et al.* [2015]. In addition, smaller SSEs, may have occurred, presently below the threshold of GPS detection [Vergnolle *et al.*, 2010].

GPS receivers continuously operating in Guerrero have detected SSEs every 3-4 years within a region that extends ∼250 km along the Pacific coast and up-dip into the seismogenic zone of the Guerrero seismic gap [Radiguet *et al.*, 2012], part of the Mexican subduction zone that has not ruptured in a large earthquake since 1911. The maximum observed slip on the interface has been ∼200 mm that is equivalent of a Mw∼7.5 earthquake (e.g., Lowry *et al.* [2001]; Kostoglodov *et al.* [2003]; Iglesias *et al.* [2004]; Yoshioka *et al.* [2004]; Larson *et al.* [2007]; Radiguet *et al.* [2012]; Cavalié *et al.* [2013]). Along the Oaxaca segment of the MSZ, slow slip has occurred every 1-2 years with smaller maximum slip amplitudes of ∼100 mm and smaller than in Guerrero moment releases equivalent to M_w=6.6-6.9 [Correa-Mora *et al.*, 2008, 2009;

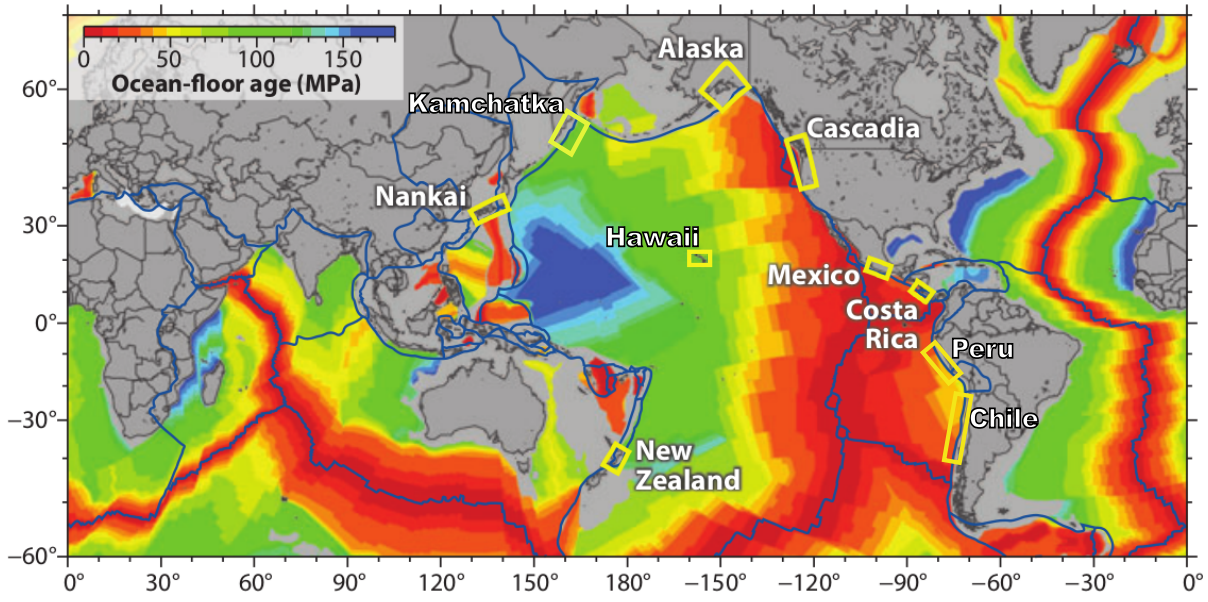

Figure 1-5: SSEs around the world (modified from Beroza and Ide [2011]).

Graham *et al.*, 2014a]. After the great M_w=8.2 intraplate earthquake in Chiapas, on September 8, 2017, the interplate coupling at the MSZ probably changed which affected the periodicity of SSEs. For instance, recent GPS observations in Guerrero show that now the smaller M_w SSEs are occurring every year (2017, 2018, 2019).

However, not only subduction zones host slow slip phenomena. On some continental strike-slip faults (e.g. San Andreas fault, North Anatolian fault) shallow transient creep events (Fig. 1-4) have been observed using strainmeters, creepmeters, geodetic and InSAR (interferometric synthetic aperture radar) measurements (e.g.,Aytun [1982]; Linde *et al.* [1996]; Rousset *et al.* [2016, 2019]; Bürgmann [2018]). For the case of Mexico it has recently been proposed by [Kazachkina *et al.*, 2020] that SSEs also occur on the trench-parallel system of strike-slip sinistral faults La Venta-Chacalapa. The characteristics of this fault and of the observed recurrent strike-slip SSEs are discussed further.

NVTs in the Mexican subduction zone are found to occur persistently at a distance of ∼215km from the trench, the region known as the "Sweet Spot" due to the proper conditions (i.e., temperature, pressure, and pore fluid content) for the NVT to occur with minimum shear slip. The sweet spot is a 75km long zone above the 140 km horizontal section of the slab, far

from the mantle wedge [Payero *et al.*, 2008]. NVT episodes are also observed every few months, extending ∼190km to ∼220km from the trench with durations of a few weeks [Husker *et al.*, 2012].

So far slow slip events have been located mainly on subduction faults but also on strike-slip faults. Satellite observation tools, such as GNSS and InSAR, have been of great importance in the task of SSE detection. Temporal and spatial connection between SSEs and NVTs has been observed and analyzed in different tectonic regions of the world. Nevertheless, there are still many details to be discovered and understood about slow transients. The triggering relationship between seismic and aseismic slip has not been fully explained yet. The main physical parameters responsible for SSE occurence are still being debated. New theories, data and methods would help gather a more complete picture on SSEs.

1.3 Geological framework

According to Mammerickx and Klitgord [1982], the tectonic history of southern MSZ, west of the intersection of the Tehuantepec ridge with the Middle America Trench (MAT), for the last 25 Ma has suffered at least three major plate reorganizations. The old Farallon plate evolved first to the Guadalupe plate, which was later segmented into the actual Rivera and Cocos plates. The position of the spreading centers moved east, from about 12.5 to 11 Ma, to the Mathematician seamounts. Later, between 6.3 to 3.5 Ma, it shifted to its actual position of the East Pacific Rise (EPR) Pardo and Suárez [1995] (Fig. 1-6).

The Cocos plate subducts at a rate that increases to the southeast from 48 mm/yr at 104.5°W to 75 mm/yr at 94°W [DeMets *et al.*, 1990]. The age of the young Cocos plate varies along the MAT, generally increasing southeastwards with two upsurges associated with fracture zones and the Tehuantepec ridge, which intersects the MAT near ∼95°W. The Tehuantepec ridge is interpreted as a bathymetric feature which is the morphological expression of a paleo-fracture zone that separates the oceanic lithosphere of significantly different ages. A younger and shallower crust to the northwest differs in age from the one southeast of the Tehuantepec

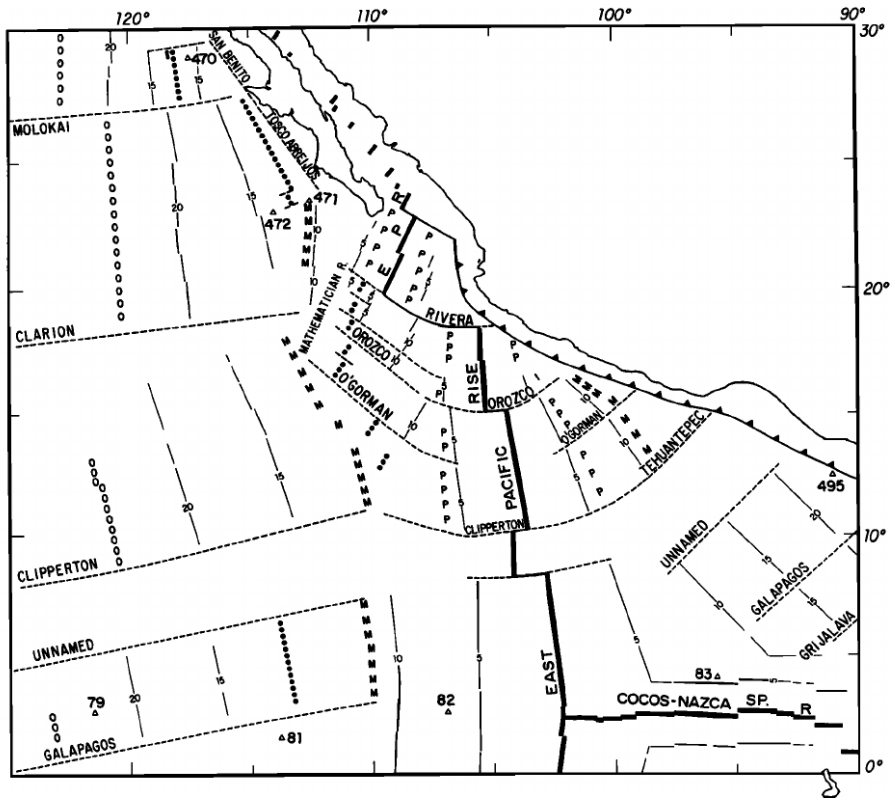

Figure 1-6: Tectonic map of the northeast Pacific. Traces in magnetics or bathymetry of spreading reorganization are OOO: 25 Ma B.P., MMM: 12.5 to 11 Ma B.P., and PPP for 6.5 to 3.5 Ma B.P. Isochrons in fine lines are drawn for crust 5, 10, 15 and 20 Ma old [Mammerickx and Klitgord, 1982]

ridge by approximately 7 to 12 Ma [Couch and Woodcock, 1981; Manea *et al.*, 2005a,b].

Suárez *et al.* [1990] defined that the subducting plate initially dips at ∼15° and then it becomes almost horizontal and underplates the North America upper lithosphere. This particular configuration of the young subducting Cocos plate (average of ∼14 Ma) apparently creates some distinct geodynamic consequences, such as thin continental lithosphere, relatively shallow intraslab seismicity, remote position of the volcanic front [Manea *et al.*, 2017]. In comparison to the subduction zones of Peru, Chile and central Argentina with similar sections of flat slab, Mexican continental crust is only half as thick as those of South America. A possible oceanic origin of the allochtonous terranes comprising southern Mexico may explain the presence of the anomalously thin lithosphere in this region [Suárez *et al.*, 1990].

Husker *et al.* [2017], found that long-lasting past magmatic activity most likely produced an

impermeable gabbroic layer in the lower continental crust within the Guerrero gap. This layer has acted as a seal to trap fluids and over-pressurize the plate interface, thereby generating a transient slip region allowing for SSEs to invade the seismogenic zone.

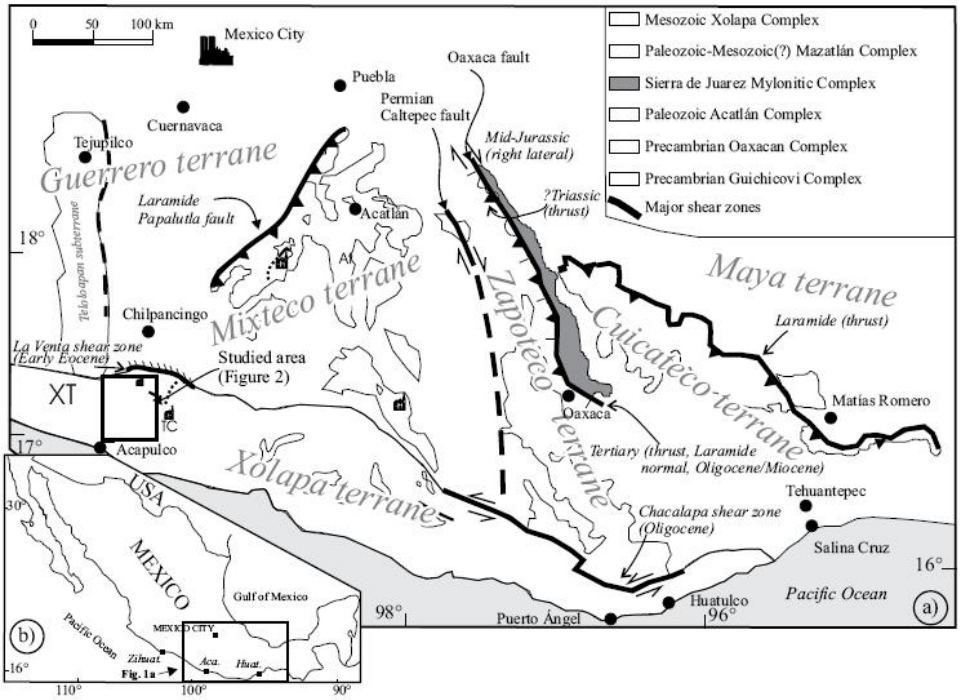

Figure 1-7: LVC –left-lateral transtensional and normal ductile shear zone that extends over a distance of around 200km. It separates the Xolapa terrain, a crustal block which is located along the Pacific coast of Mexico ∼600km long and ∼50-80km wide (Pérez-Gutiérrez et al., 2009).

Oblique convergence leads to a development of forearc slivers in different subduction zones. Geological studies indicate the sinistral transpression during Late Cretaceous to Early Tertiary in the coastal area of the present-day southern Mexico [Cerca *et al.*, 2007]. Significant left-lateral strike-slip motion characterized by the mylonitization of the Xolapa metamorphic complex [Campa and Coney, 1983] was dated as early Eocene in the La Venta [Solari *et al.*, 2007] and as Oligocene in the Chacalapa shear zones [Tolson, 2005]. Mylonites are ductilely deformed rocks formed by the accumulation of large shear strain, in ductile fault zones. Nonetheless there was not any evidence of the ongoing tectonic activity on the La Venta-Chacalapa fault system or on other trench-parallel faults in the central Mexico, except the Central Trans-Mexican Volcanic

Belt [Suter *et al.*, 1992]. The existence of a forearc sliver with contemporary sinistral motion with respect to the stable North America plate (wrt NA) should be expected as a result of the strain partitioning produced by oblique subduction of the Cocos plate (CO) [Kazachkina *et al.*, 2020].

The contact of the Xolapa terrane (Fig. 1-7) with the neighboring terranes is complex. It accommodates both brittle and ductile faults, and parts of the boundary are interrupted by Cenozoic plutons [Ortega-Gutiérrez *et al.*, 2014]. The most prominent boundary structure is the La Venta-Chacalapa (LVC), left-lateral transtensional and normal ductile shear zone.

1.4 Objectives

The objective of this work is to study the activity of the La Venta Chacalapa system of crustal strike slip faults using seismic and geodetic data. Within the framework of this research the motion of the Xolapa sliver is analyzed and quantified using long term GPS time series, focal mechanisms and CMT solutions. This work also covers the anomalous sequence of subduction slow slip events of 2017-2019 in Guerrero and Oaxaca occurred after the 2017 M_w8.2 Tehuantepec earthquake. Apart from that, one of the main purposes of this study is to characterize the spatial and temporal interaction between subduction and strike-slip SSEs in Guerrero and Oaxaca. The last subduction SSE sequence of 2017-2019 helps to complement the analysis and reveal any changes in the slow slip events on the LVC after the Chiapas earthquake.

Chapter 2

Data and Methods

2.1 Seismicity analysis using Global Centroid Moment Tensor (CMT) and local seismicity catalogs

One of the methods applied in this research work is based on the analisys of seismicity located in the coastal area of the Xolapa sliver. Both local and global CMT catalogs were used to build two independent datasets. Then the same geometric approximation of McCaffrey [1992] was applied to both compilations of seismicity data in order to quantify motion accommodated along the LVC fault system. The details of this method together with the analysis of the results are described in the article by Kazachkina *et al.* [2019] provided below.

Kazachkina *et al. Earth, Planets and Space* (2019) 71:104
https://doi.org/10.1186/s40623-019-1084-9

Earth, Planets and Space

FULL PAPER Open Access

Activity of crustal faults and the Xolapa sliver motion in Guerrero–Oaxaca forearc of Mexico, from seismic data

Ekaterina Kazachkina[1*], Vladimir Kostoglodov[1], Allen Husker[1] and Nathalie Cotte[2]

Abstract

Oblique convergent margins often host forearc slivers separated by the subduction interface and a trench parallel strike-slip fault system in the overriding plate. Mexican oblique subduction setting led to the formation of a forearc sliver and accomodation of part of the slip at the bounding system of strike-slip faults. The Xolapa sliver is, on average, a ~ 105-km-wide crustal block located along the coast of Guerrero and Oaxaca states of Mexico, and is limited by a ~ 650-km-long La Venta-Chacalapa fault zone. Two types of datasets, local catalog and Global CMT compilation, are used to estimate the motion of the Xolapa sliver using the rigid block model that describes the phenomenon of slip partitioning. According to the results obtained from local and Global CMT catalogs for selected subduction thrust earthquakes, the forearc sliver moves southeastwards with respect to the fixed North America plate at the rate of 10 ± 1 mm/year and 5.6 ± 0.8 mm/year, respectively. These velocities in general agree with the values obtained from long-term GPS observations (5–6 mm/year). The origin of the inconsistency between local and teleseismic estimates is attributed to a difference in the double couple focal mechanism parameters for two types of datasets. Convergence obliquity changes from 10.42° and the rate of 58 mm/year to 13.29° at the rate of 68 mm/year along the Guerrero and Oaxaca coast increasing from northwest to southeast; therefore, the Xolapa sliver is supposed to be stretched. However, the slip vector azimuths of thrust subduction earthquakes tend to approach plate convergence vectors southeastwards along the coast; so, we assume that this may produce the forearc block compression.

Keywords: Slip partitioning, Forearc sliver, Oblique subduction zone

Introduction

The phenomenon of forearc sliver motion has been observed in different subduction zones. In Sumatra, for example, around 60% of subduction obliquity is accommodated at the subduction interface, with about one-third transferred to the great strike-slip fault called the Great Sumatran Fault (GSF); the area between the GSF and the trench is referred to as the Sumatran Sliver (Diament et al. 1992). We observe a similar partitioning pattern in Ecuador and Colombia along the Dolores-Guayaquil Fault zone (Ego et al. 1996) and in South Chile along the Liquiñe-Ofqui Fault that forms part of the 7000-km-long South American subduction zone (e.g., Cembrano et al. 1996; Wang et al. 2007; Villegas-Lanza et al. 2016). The study of Villegas-Lanza et al. (2016) defines a Peruvian Sliver as a block extending N–S between the Gulf of Guayaquil and the Altiplano of Peru and between the trench and the boundary between the Eastern Cordillera and the Western Cordillera in E–W direction. Ryan and Scholl (1989) observe that oblique subduction in the Aleutian arc created a major right-lateral shear zone, the Hawley Ridge shear zone, that has geomorphical and geophysical characteristics similar to the San Andreas fault in California. The southwest Kuril arc is characterized by strike-slip movement between the volcanic and frontal arcs, a graben at the northeastern end of the forearc, and collision at the southwestern margin of the forearc. These tectonic features suggest the southwestward migration of the Kuril forearc sliver

*Correspondence: kazachkina@igeofisica.unam.mx
[1] Institute of Geophysics, National Autonomous University of Mexico, Mexico City, Mexico
Full list of author information is available at the end of the article

(Kimura 1986). A previous attempt to identify a sliver on the Pacific forearc of Mexico and to estimate its velocity was presented in the paper of Ego and Ansan (2002).

The coast of the Southern Mexican states, Guerrero and Oaxaca, between − 102.0°E to − 95.5°E and 15.5°N –18.0°N hosts a prominent geologic structure referred to as the Xolapa sliver. This crustal block (Fig. 1) is located along the Pacific coast of Mexico ∼ 650-km long and ∼ 50–80-km wide (Pérez-Gutiérrez et al. 2009) from the coast inland. The Xolapa sliver also includes ∼ 70 km from the trench to the coast. The contact of the Xolapa terrane with the neighboring terranes is complex. It accommodates both brittle and ductile faults, and parts of the boundary are interrupted by Cenozoic plutons (Ortega-Gutiérrez et al. 2014). The most prominent boundary structure is the La Venta-Chacalapa (LVC), left-lateral transtensional and normal ductile shear zone, which was active during the Eocene on the west (e.g., Riller et al. 1992; Solari et al. 2007) and the Oligocene in the east (Tolson 2005).

The convergence rate of Cocos (CO) plate with respect to the North America (NA) plate increases southeastwards from 58 to 68 mm/year [PVEL model, DeMets et al. (2010)] in the studied section of the Mexican subduction zone. Cocos–North America plate interface has large lateral variations in its dip, with a shallow subhorizontal segment bounded in Guerrero–Oaxaca area by segments that dip more steeply: ∼ 50° near the Rivera-Cocos plate boundary and ∼ 30° near the Isthmus of Tehuantepec (Pardo and Suarez 1995). The age of the oceanic Cocos plate subducting at the Middle America Trench (MAT) increases from about 10 Ma in the west to about 23 Ma (Manea et al. 2005) in the east (Pardo and Suarez 1995). The Cocos plate seafloor is irregularly covered with small- and medium-sized seamounts subducting under the coast of Guerrero and Oaxaca and delimited by Tehuantepec fracture zone in the south. While the Guerrero segment of the subduction zone is characterized by a relatively small number of seamounts with heights of ∼ 1 km, the Oaxaca segment is covered with a large number of seamounts arranged in chains almost parallel to the convergence direction. These seamount chains significantly affect the morphology of the trench and the forearc (Kanjorski 2003). There are several

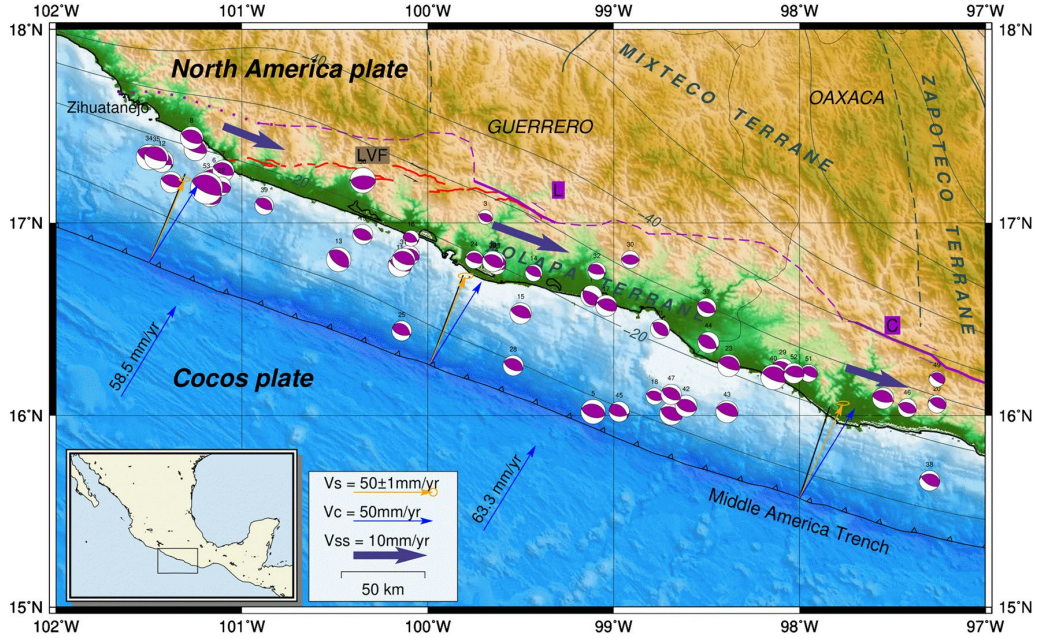

Fig. 1 Earthquakes from the local catalog. Subduction thrust events from Pacheco and Singh (2010) and Yamamoto et al. (2013). Three groups of vectors represent three regions. Black lines indicate normal to the trench, blue arrows—convergence velocity, orange arrows—average coseismic slip vectors projected to the surface for each region with 95% error ellipses. Violet lines are the trace of LVC fault: dashed [from Cerca et al. (2007) and Tolson (2005)], solid ["L"—from Solari et al. (2007) and "C"—from Tolson (2005)]. Red lines are the location of the La Venta fault system from the geomorphology study of Gaidzik et al. (2016). Terrane subdivision according to Campa and Coney (1983), Sedlock et al. (1993), and Keppie (2004). Darkblue arrows show the Xolapa sliver motion. Solid and dashed gray lines indicate regional faults [from Solari et al. (2007)]. Thin gray lines are the plate interface isodepth contours (Hayes 2018)

clusters of intense seismic activity, particularly in front of Oaxaca that correlate well with the location of seamounts on the incoming Cocos plate (Manea et al. 2017). This observation indicates a relationship between crustal seismicity and the subducting bathymetric structures.

The phenomenon of slip partitioning is observed along the coast of the Central and Southern Mexico. The forearc sliver is, on average, a ~ 105-km-wide crustal block bounded at northeast by a ~ 650-km-long LVC fault zone striking parallel to the MAT. This fault system accommodates most of the oblique component of convergence between the CO and NA plates. Long-term GPS observations show trench parallel motion of the sliver southeastwards at the rate of 6–8 mm/year with respect to the NA plate (Kostoglodov et al. 2016). This sliver geologically corresponds to the Xolapa complex and is composed by a sequence of high-grade metasedimentary and metaigneous rocks that are frequently intruded by both deformed and undeformed plutonic rocks. It is suggested that the Xolapa terrane is allochthonous, and was accreted to the continental margin of southern Mexico during Mesozoic–Tertiary (e.g., Corona-Chávez et al. 2006; Pérez-Gutiérrez et al. 2009). Present work analyses the slip partitioning phenomenon observed in oblique subduction zones applying the model of McCaffrey (1992) to the dataset of shallow thrust events on the subduction interface with $M_w > 3.6$ for the case of Mexico using regional and teleseismic data.

Sliver motion is explained by the slip partitioning at oblique convergent margins. Slip vectors of relatively shallow (< 60 km) thrust earthquakes at oblique subduction zones often lay between the normal to the trench axis and the vector of relative plate convergence (McCaffrey 1992), suggesting that oblique convergence is partially decoupled. This means that at the trench, a percentage of arc-parallel motion of the leading edge of the upper plate shows less oblique thrusting. Partial decoupling is represented by separating slip vectors from thrust earthquakes into slip on strike-slip faults parallel to the trench and slip on the thrust interface (McCaffrey 1992).

The Mexican subduction zone stands out among other subduction zones with a unique subducting slab geometry that plays a role in shear stress distribution. The seismogenic zone extends up to 81 km from the trench and is followed by a wide shallow subhorizontal plate interface at the distance between 115 and 270 km from the trench beneath the Guerrero state (e.g., Kostoglodov et al. 1996; Pérez-Campos et al. 2008) at depth of ~ 45 km. This part of the subduction interface hosts the transition zone that is characterized by slow slip events (SSE) and non-volcanic tremors (NVT). The remotest NE inland section of the subduction interface is in a stable sliding. This particular configuration of the young subducting Cocos plate (~ 14–16 Ma) apparently creates some distinct geodynamic consequences, such as thin continental lithosphere, relatively shallow intraslab seismicity and an unusual outlying position of the volcanic front (Manea et al. 2004). It can also have an effect on the stress and strain distribution in the forearc and as a consequence on the activity of the LVC fault system. At small angles of convergence obliquity such geometrical setting of the subduction interface, with an increased contact area between oceanic and continental crust, creates favorable conditions for the sliver motion.

The results obtained in this work confirm that the Xolapa sliver is active and its sinistral (with respect to the NA fixed plate) motion agrees well with the GPS estimates of velocities on the left-lateral strike-slip fault system bounding the Xolapa terrane. Nevertheless, our analysis of local and global CMT catalogs with carefully selected subduction thrust events shows that calculated average rates of the sliver motion are fairly different. Therefore, the principal objective of this paper is to assess sliver rates applying McCaffrey (1992) model and apprise the sources of this difference.

Data and methods

The data (focal mechanisms) obtained by local seismic networks and analyzed in several previous studies of Pacheco and Singh (2010), Yamamoto et al. (2013) and events localized and analyzed by National Seismologic Service (Mexican SSN http://www.ssn.unam.mx/) are used in this work. The study area includes 53 thrust earthquakes from local catalog (see Additional file 1). Selected events should be the subduction thrust earthquakes on the plate interface presumably satisfying the following criteria similar to those of Ego and Ansan (2002): plunge of the tension axis > 45°, angle between the event strike and local trench azimuth < 30°, depth < 60 km and direction of the rake is downdip along the subduction interface.

Three regions (− 102.0°E to −101.0°E, −101.0°E to − 99.0°E and − 99.0°E to − 97.0°E) are analyzed separately. Weighted mean coseismic slip vector for the events from the local catalog is computed for each region. The weights are assigned based on the seismic moment released (M_0) assuming that parameters of the events with bigger M_0 are defined more precisely (DeMets 1992). Figure 1 shows mean coseismic slip $\overline{V}_s$ with respect to the trench normal T_n and convergence rate V_c between the CO and NA plates. Convergence direction and rate are computed using the PVEL model (DeMets et al. 2010). Trench normal is the direction measured perpendicular to the local strike of the trench (DeMets 1992). The trench is approximated with the small circle with the pole at − 80.11°E, 51.01°N and radius of

4256.734 km. Trench normal lays in the direction to the pole of the small circle (Fig. 2).

Selected data from the Global CMT catalog for thrust events in 1976–2016 are analyzed for the same area (Fig. 3) and compared to the results from the local catalogs. 83 events with $M_w \geq 4.7$ have been selected. Selection criteria are the same as for the local catalog. Additionally only the events with percentage of double couple DC $\geq$ 80% are considered (see Additional file 2). The area is divided into three regions (Fig. 3).

The rigid block model developed by McCaffrey (1992) is used in this work to quantify the Xolapa sliver motion and corresponding strike-slip displacement on the LVC fault. Transcurrent motion at the LVC fault can be estimated from slip vectors of subduction thrust earthquakes occurring on the plate interface. Following the model of McCaffrey (1992), the Xolapa sliver and NA and CO plates are assumed to be a system of rigid blocks (no change of shape or size in time and no change of mass) on a spherical earth. The velocity vector of the subducting plate relative to the fixed upper plate has a magnitude V_c and forms an angle γ (obliquity) in the horizontal plane relative to the trench normal, T_n. The relative motion is partially accommodated by slip on the subduction interface and slip on the trench-parallel crustal strike-slip faults. Thus, the inland system of echelon faults isolates a third block of lithosphere, called *sliver* (Fig. 4). The model assumes that (1) the motions of the blocks are resisted only on the two bounding faults (i.e., the three plates are rigid) and the faults will slip when stress on them reaches a maximum yield stress; (2) the problem is two-dimensional so that there is no variation in stress in the x direction (parallel to strike of the trench); (3) forces are in equilibrium (excluding a short time during earthquakes

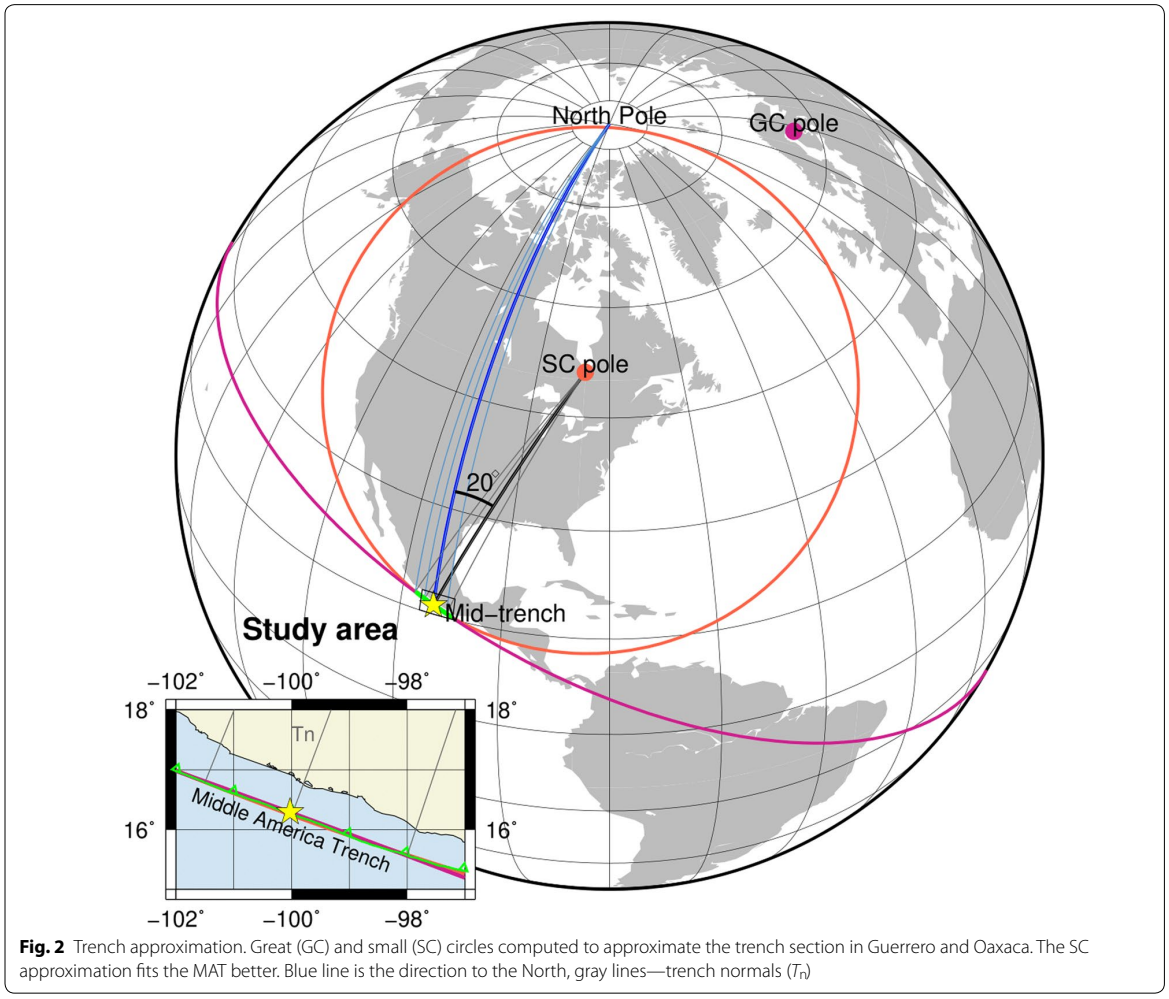

Fig. 2 Trench approximation. Great (GC) and small (SC) circles computed to approximate the trench section in Guerrero and Oaxaca. The SC approximation fits the MAT better. Blue line is the direction to the North, gray lines—trench normals (T_n)

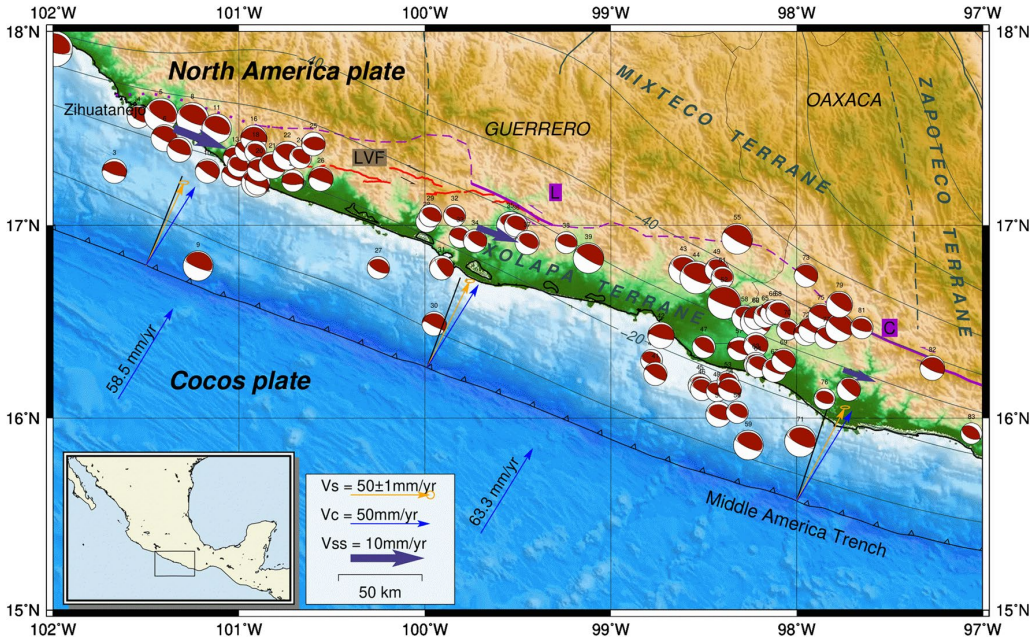

Fig. 3 Earthquakes from the Global CMT catalog. Selected subduction thrust events from the Global CMT catalog for 1976–2016. Other annotations are the same as in Fig. 1

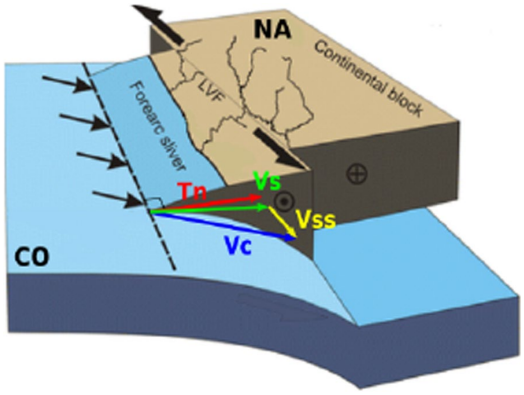

Fig. 4 Forearc sliver. Relative motion of the NA and CO tectonic plates is partially accommodated by slip on the subduction interface and slip on the La Venta-Chacalapa (LVF) system of trench-parallel crustal strike-slip faults. V_c—velocity vector of the subducting plate relative to the fixed upper plate; T_n—trench normal; V_s—surface projection of the coseismic slip vector for subduction thrust earthquakes; V_{ss}—forearc sliver velocity. Black arrows indicate direction of convergence; black half-arrows show sinistral motion at the LVF [Modified from Gaidzik et al. (2016)]

when accelerations occur); (4) no body forces act in the x direction; and (5) the stresses are considered vertically integrated. The vertical extents of the thrust and strike-slip faults are allowed to differ (McCaffrey 1992).

Coseismic slip vectors V_s of the thrust earthquakes lay between the trench normal T_n and the vector of convergence, V_c, and forms an angle ψ with the trench normal (Fig. 5). Therefore,

$$V_s = \frac{V_c \cos\gamma}{\cos\psi}, \tag{1}$$

where V_c is the rate of oblique convergence. The strike-slip vector is then obtained as (McCaffrey 1992)

$$V_{ss} = V_c \sin\gamma - V_c \cos\gamma \tan\psi. \tag{2}$$

The values of V_{ss} are compared for the teleseismic and regional seismicity catalogs. Both catalogs provide information on the earthquake parameters (epicenter location, strike, dip and rake). The earthquake focal mechanism parameters are used to calculate γ and ψ by applying axes rotations.

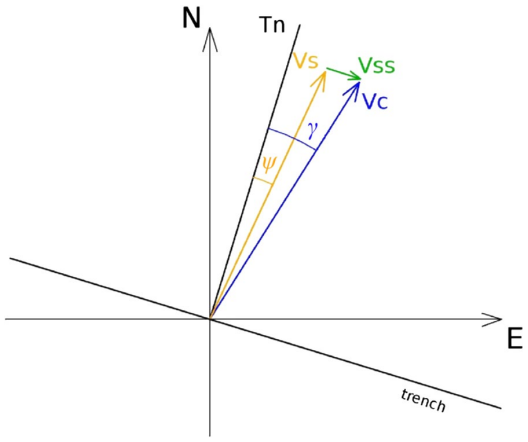

Fig. 5 Schematic representation of oblique subduction system kinematics. Black line (T_n)—normal to the trench, blue arrow (V_c)—convergence velocity vector, orange arrow (V_s)—coseismic slip vector, green arrow (V_{ss})—strike-slip component, γ—convergence obliquity, ψ—subduction obliquity

The rigid-body model allows for an approximation of the forearc strike-slip motion through simple geometrical calculations, furthermore, tan ψ characterizes average friction coefficient on the sliver bounding fault (Haq and Davis 2010).

Results

Figure 5 shows the model of sliver motion along oblique convergence margin (McCaffrey 1992). Based on the difference between azimuths of the coseismic slip vector (V_s) and convergence vector (V_c), we can infer information about slip partitioning. By doing so we determine the presence of forearc sliver motion with respect to the continental plate (Eq. 2). Model parameters that describe this motion are further analyzed.

Average angles of coseismic slip ($\overline{\psi}$) with respect to the trench normal and average plate convergence obliquity ($\overline{\gamma}$) for each zone along the coast are presented in Table 1. According to Fig. 6 ψ-angles mainly vary in the range $-20°$ to $20°$ increasing to the southeast along the coast. Convergence obliquity γ also grows from northwest to southeast. There are average differences of $\pm$ 10° in ψ-angle values for the local catalog and the selected Global CMT thrust events.

The mean slip rate ($\overline{V}_{ss}$) of the forearc sliver relative to the fixed NA plate is 10 ± 1 mm/year for the local catalog in the area $-102.0°$E to $-97.0°$E. The average trench-parallel slip rate ($\overline{V}_{ss}$) estimated for the Global CMT catalog is 5.6 ± 0.8 mm/year for the same area. These results might have been influenced by the method of average coseismic slip estimation with weights assigned to events of higher seismic moment. The local catalog includes smaller earthquakes of $M_w = 2.9–4.7$, while the Global CMT catalog has a significant number of big events and lacks seismicity below $M_w = 4.7$

Two datasets used in this study have certain differences. The local catalog has fewer earthquakes (53 events) than the Global CMT compilation (83 events). Besides, the local catalog includes events with $M_w < 4$ and has only one major event, $M_w = 7.2$ (see Additional file 1). For this catalog, the earthquakes of smaller magnitude contribute to relatively higher V_{ss} (Fig. 7). The slip vector of major and great events is more oblique; therefore, V_{ss} is smaller. For example, V_{ss} estimated for the Petatlan earthquake $M_w = 7.2$ on 18 April 2014 is relatively small in both catalogs (7.7 mm/year for Global CMT and 6.7 mm/year for the local catalog).

Comparison of focal mechanism parameters (strike, dip and rake) for the same events in teleseismic and local data reveals systematic differences (Fig. 8). These inconsistencies can be attributed to the methods of determining focal mechanisms using different datasets. In case of the Global CMT catalog, the double couple model is only part of the full tensor solution, while the focal mechanisms in the local catalog were obtained assuming perfect double couple model. Therefore, the surface

Table 1 Average plate convergence obliquity ($\overline{\gamma}$), subduction obliquity ($\overline{\psi}$) and $\overline{V}_{ss}$—sinistral motion of the Xolapa sliver with restect to the fixed NA plate

Zones	Longitude, °E	Latitude, °N	$\overline{\gamma}$, °	$\overline{\psi}$, °	$\overline{V}_{ss}$, mm/year	Number of events
Local catalogs						
1	− 101.49	16.79	10.42	1.3 ± 1.5	9 ± 2	11
2	− 100.04	16.26	11.62	1.7 ± 1.9	11 ± 2	22
3	− 97.98	15.57	13.29	6.1 ± 1.4	9 ± 2	20
Global CMT						
1	− 101.49	16.79	10.42	2.8 ± 1.3	7.70 ± 1.25	13
2	− 100.04	16.26	11.62	6.0 ± 1.2	6.03 ± 1.26	26
3	− 97.98	15.57	13.29	9.1 ± 1.0	4.75 ± 1.19	44

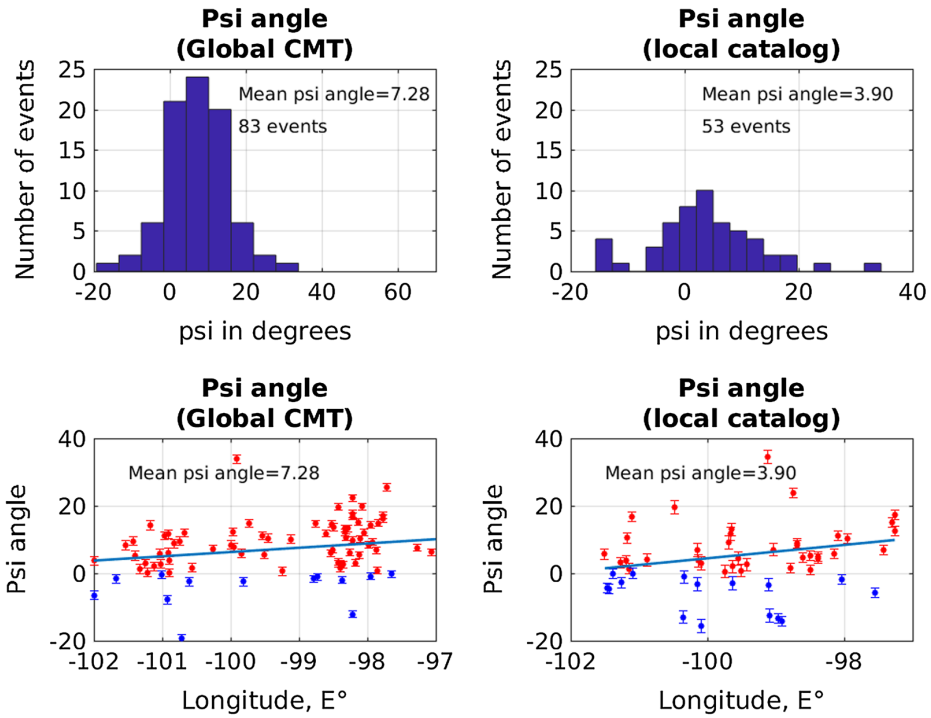

Fig. 6 ψ-angles. Histogram of ψ-angles and ψ-angles with respect to longitude, based on data from publications of Pacheco and Singh (2010), Yamamoto et al. (2013), Pacheco et al. (2005) and the catalog of the SSN (referred as local catalog), and from selected Global CMT solutions. Red circles are positive ψ-angles, blue circles—negative ψ-angles

projection of earthquake slip vectors V_s does not show identical results for the same events. This explains partly the difference in estimations of V_{ss} for these two catalogs. According to Hjörleifsdóttir et al. (2016), local and global catalogs for earthquakes in the Mexican subduction zone also present differences in epicentral locations. This phenomenon is attributed to systematic patterns in the velocity structure of the mantle, with consistently fast paths to the northeast and relatively slow paths towards the southwest. The errors are found to be larger for shallowly dipping thrust events close to the trench (Hjörleifsdóttir et al. 2016), that significantly contribute to our selected datasets.

Depending on the depth of the subduction thrust earthquakes different V_{ss} may be expected. It can also be assumed that the larger V_{ss} results from major magnitude earthquakes. However, the observations show that the extreme values of V_{ss} (33.33 mm/year—10 May 2014, $M_w = 5.0$, Tecpan, Global CMT catalog; − 28.23 mm/year—12 July 1998, $M_w = 5.5$, Acapulco, Global CMT catalog) were obtained for moderate earthquakes with epicenters at 72 and 56 km from the trench. Major and great earthquakes produce $V_{ss} < 17$ mm/year while the biggest contribution to the strike-slip trench parallel motion corresponds to moderate events (Fig. 7). Nonuniformity in the dataset of strike-slip vectors shows that the Xolapa sliver may present significant internal deformation. Some of its zones possibly undergo extension and others compression due to the difference in interplate coupling and geometry of the subduction zone.

The entire Xolapa sliver $\overline{V}_{ss}$ tends to decrease with increasing distance from the trench (Table 2). Therefore, maximum sinistral motion of the subducting slab with respect to the overriding plate is at shallow depths. With depth, the mean vector of coseismic slip approaches the convergence direction. Noticeable changes of strike-slip motion are observed at approximately 50- and 100-km distance from the trench where the latter corresponds to the location of the LVC fault system.

The value of $\overline{V}_{ss}$ varies along the coast (Table 3). This suggests that the Xolapa sliver may deform nonuniformly with a system of microblocks undergoing compression and extension. We expected to observe extension of the sliver in the zones bounding the areas of higher convergence obliquity γ. However, the results of this study show lower values of V_{ss} in the areas of

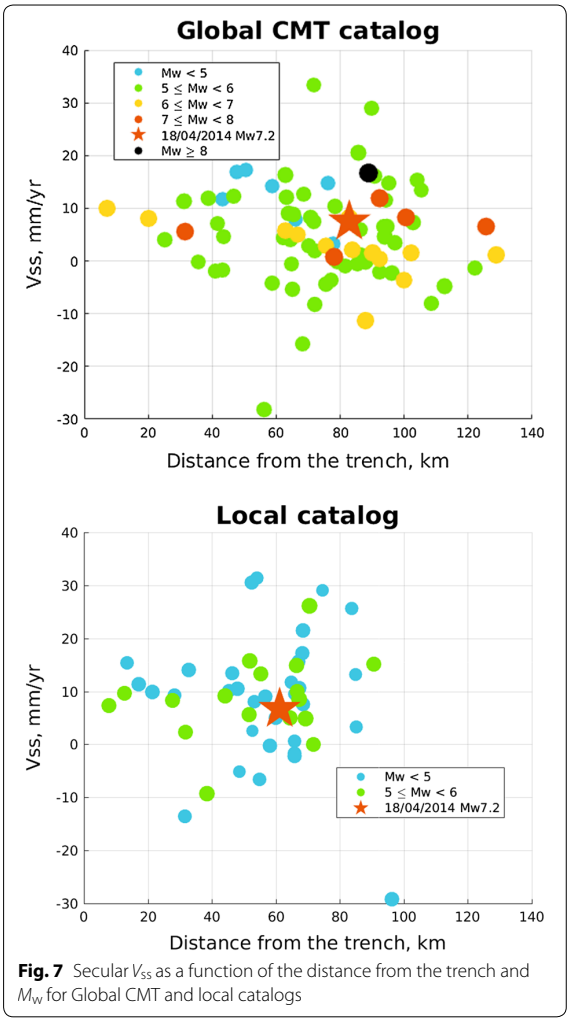

Fig. 7 Secular V_{ss} as a function of the distance from the trench and M_w for Global CMT and local catalogs

increasing γ in the southeastern part of the Xolapa sliver due to the growing angle of subduction obliquity ψ.

Forces acting on the sliver should be understood to explain its' motion. The Mexican subduction complex along the Guerrero–Oaxaca coast is formed by two rapidly (~ 60 mm/year) converging tectonic plates: NA and CO. The Xolapa sliver is a part of the forearc of the NA plate separated from the continent by the LVC fault system. Large thrust earthquakes, thrust and strike-slip slow slip events (Graham et al. 2015; Radiguet et al. 2016; Kostoglodov et al. 2016) are physical processes that take place in the study area and may affect the behavior of the sliver. Located under the northwestern part of the Xolapa sliver, the Guerrero Gap area has low long-term coupling at the seismogenic zone (Radiguet et al. 2012) that also may have an impact on the corresponding block motion.

Discussion

Estimates of the Xolapa sliver velocity (V_{ss}) with respect to the fixed NA plate obtained in this work using the CMT and local catalogs slip vectors in general agree with the V_{ss} values obtained from long-term GPS observations (5–6 mm/year). The average V_{ss} estimate from local catalog (10 ± 1 mm/year) is higher than those from the Global CMT catalog (5.6 ± 0.8 mm/year). The nature of this inconsistency is attributed mostly to a difference in the double couple focal mechanism parameters for local and teleseismic estimates. Comparison of earthquake source parameters such as strike, dip and rake for the same events shows inconsistency between local and teleseismic estimations (Fig. 8). Thus, we conclude that the resulting speed of the Xolapa sliver or the motion on the strike-slip fault calculated using the model of McCaffrey (1992) is sensitive to the type of dataset used. V_{ss} vary between 1 and 20 mm/year with the greater speed corresponding to events of smaller magnitudes ($M_w < 5.2$). A few events in the catalogs may be misinterpreted as the subduction thrust type earthquakes on the plate interface because of not so perfect selection criteria or the error in the hypocenter depth estimates. This would result in somewhat biased values of V_{ss}. Since values of V_{ss} obtained from Global CMT catalog are closer to the GPS estimates, it is generally more reasonable to use those data for earthquakes' slip appraisals (at least in case of Mexico). The geological estimates of the slip on the LVC fault system (4–5 mm/year of sinistral motion (Gaidzik et al. 2016)) also supports the results from the Global CMT catalog.

It is critical to make accurate calculations of the trench normal (T_n) and convergence obliquity (γ) to obtain reliable estimates of the sliver motion (V_{ss}). In this study, T_n is calculated through the approximation of the Mexican trench by a small circle. Convergence obliquity (γ) is estimated using the PVEL model which is more appropriate for the NA–CO plates convergence (DeMets et al. 2010). Convergence obliquity is observed to increase southeastward along the coast. Subduction obliquity ψ shows the same tendency. As a result of the combination of these two parameters, the Xolapa sliver motion V_{ss} decreases from northwest to southeast. Therefore, instead of the extension regime in the area of high convergence obliquity, we would rather predict compression of the southeastern part of the sliver.

According to the rigid sliver model of McCaffrey (1992), shear forces on the subduction interface and on the crustal faults depend on the slab dip, fault depths and convergence obliquity. Notably, the convergence rate of ~ 65 mm/year in Mexico is lower than in many oblique subduction zones: ~ 91 mm/year in Philippines (Barrier et al. 1991), 125 mm/year in Western New Guinea

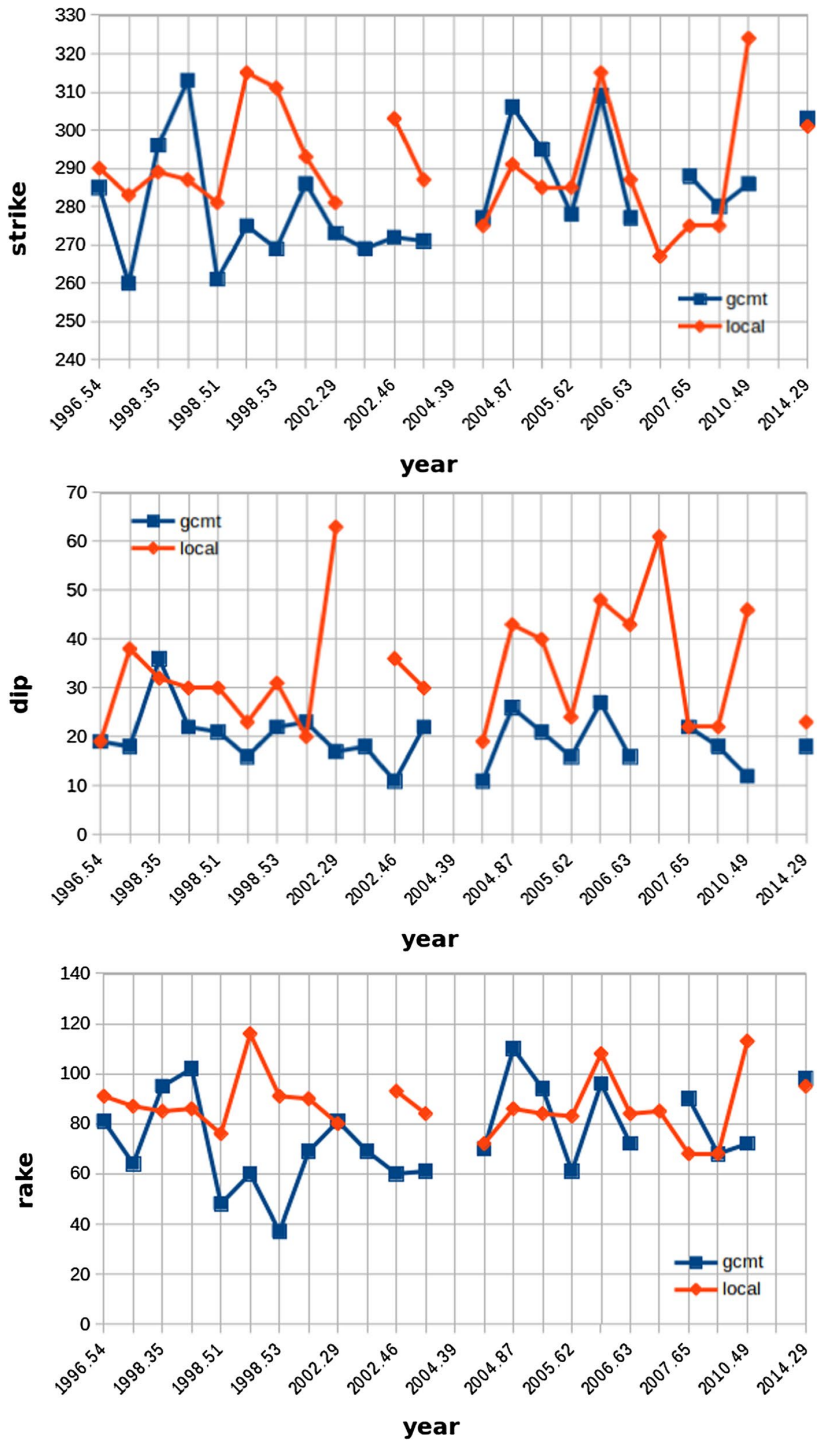

Fig. 8 Comparison of earthquake focal mechanism parameters (strike, dip, rake) for local data and Global CMT compilation

Table 2 Mean strike-slip components of the Xolapa sliver motion ($\overline{V}_{ss}$) for different distances from the trench calculated using data from the Global CMT

Distance (km)	$\overline{V}_{ss}$ (mm/year)
0–50	10.2 ± 1.6
50–75	5.4 ± 1.8
75–100	5.4 ± 1.5
> 100	2.4 ± 2.2

Table 3 Mean strike-slip components of the Xolapa sliver motion ($\overline{V}_{ss}$) for the earthquakes grouped in longitude ranges, calculated using data from Global CMT compilation

Longitude (°E)	$\overline{V}_{ss}$ (mm/year)
− 102 to − 100	10 ± 2
− 100 to − 99	− 1 ± 3
− 99 to − 98	6 ± 1
− 98 to − 97	4 ± 2

(Ekström and Engdahl 1989), 76 mm/year in Aleutians (McCaffrey 1992). The results of this study showed the Xolapa sliver has a speed of 5–10 mm/year. In comparison, there are examples of faster rates obtained with the same method: 45–60 mm/year in Sumatra, ∼ 27 mm/year at the Philippine trench, up to 50 mm/year in Aleutians (McCaffrey 1992). These subduction zones are characterized by faster convergence rates and greater obliquity.

The Xolapa sliver velocity or the slip rate at the LVC fault system obtained in this work is a product of the mean value of the oblique component of subduction thrust seismicity along the coast of Guerrero and Oaxaca. However, due to a varying degree of coupling, the sliver motion changes magnitude and direction along the trench. Apart from that, the Xolapa sliver may experience buttressing (Beck 1991) and significant along-strike variations in structure due to the presence of irregularities in its margin (Haq and Davis 2010). Several fracture zones (Orozco, O'Gorman, Tehuantepec) and seamount chains (mainly in Oaxaca) subducting below the Xolapa sliver may serve as a buttress and affect its deformation. The final displacement of the sliver needs a special tectonic analysis of its deformation. The sliver moving southeastwards at the rate of ∼ 5 mm/year is expected to produce some noticeable extension at its' northern edge close to Zihuatanejo and propagation of the sliver to the Gulf of Tehuantepec in the South. The translational motion of the sliver can as well be accompanied by the rotation of microblocks that makes it more complicated to evaluate its deformation. Apart from that, a prior knowledge of the sliver motion initiation is required to quantify the final sliver displacement. Thus, further modeling of the forearc deformation using GPS data and a refined fault trace mapping will lead to better understanding of the motion at the LVC fault system and associated seismic risk.

Conclusions

According to the analysis of slip partitioning in the forearc of the Mexican subduction zone using the method of McCaffrey (1992), the Xolapa sliver velocity with respect to the fixed NA plate is 10 ± 1 mm/year for local catalog and 5.6 ± 0.8 mm/year for Global CMT compilation. The difference between the results for two catalogs is explained by the inconsistency in local and teleseismic estimations of earthquake source parameters such as strike, dip and rake for the same events. The result from the Global CMT catalog is taken as the reference since it is in good agreement with the geologic and geodetic observations. Despite the increase of convergence velocity and obliquity to the southeast, the slip rate on the LVC fault is decreasing contrary to what would be expected. Based on this observation, we assume a compressive deformation of the Xolapa sliver likely caused by the presence of a buttressing structure, such as subducting seamount chains in Oaxaca, at its leading edge (Fig. 3). Detailed analysis of GPS time series and a refined fault trace mapping, especially in Oaxaca, will allow retrieving more information on the activity of forearc faults and associated seismic risk.

Supplementary information

Supplementary information accompanies this paper at https://doi.org/10.1186/s40623-019-1084-9.

Additional file 1. Local catalog. Thrust events compiled from publications of Pacheco and Singh (2010) (1), Yamamoto et al. (2013) (2), Pacheco et al. (2005) (3) and from the catalog of the SSN (4).

Additional file 2. Global CMT compilation. Selected thrust events from the Global CMT catalog for 1976–2016 for the events with double couple percentage DC ≥ 80%.

Abbreviations

LVC: La Venta-Chacalapa; NA: North America; CO: Cocos; MAT: Middle American Trench; GSF: Great Sumatran Fault.

Acknowledgements

Data from the seismic catalog of National Seismologic Service of Mexico (SSN) and Global CMT Catalog (Ekström et al. 2012) were used in this study. The figures are made with Generic Mapping Tools (Wessel and Smith 1998).

Authors' contributions

EK analyzed the data and wrote the text; VK managed the study and analyzed the data; AH corrected the results and text; NC analyzed the data. All authors read and approved the final manuscript.

Funding
The authors acknowledge financial support from the PAPIIT IG100617 and CONACYT 284212 projects.

Availability of data and materials
All data generated or analysed during this study are included in this published article and its additional information files.

Competing interests
The authors declare that they have no competing interests.

Author details
[1] Institute of Geophysics, National Autonomous University of Mexico, Mexico City, Mexico. [2] University Grenoble Alpes, Grenoble, France.

Received: 22 May 2019 Accepted: 28 September 2019
Published online: 15 October 2019

References

Barrier E, Huchon P, Aurelio M (1991) Philippine fault: a key for Philippine kinematics. Geology 19(1):32–35
Beck ME (1991) Coastwise transport reconsidered: lateral displacements in oblique subduction zones, and tectonic consequences. Phys Earth Planet Inter 68(1–2):1–8
Campa MF, Coney PJ (1983) Tectono-stratigraphic terranes and mineral resource distributions in Mexico. Can J Earth Sci 20:1040–1051
Cembrano J, Hervé F, Lavenu A (1996) The Liquiñe Ofqui fault zone: a long-lived intra-arc fault system in southern Chile. Tectonophysics 259(1—-3):55–66
Cerca M, Ferrari L, López-Martínez M, Martiny B, Iriondo A (2007) Late cretaceous shortening and early tertiary shearing in the central Sierra Madre del Sur, southern Mexico: insights into the evolution of the Caribbean–North American plate interaction. Tectonics 26:1–34
Corona-Chávez P, Poli S, Bigioggero B (2006) Syn-deformational migmatites and magmatic-arc metamorphism in the Xolapa Complex, southern Mexico. J Metamorph Geol 24:169–191. https://doi.org/10.1111/j.1525-1314.2006.00632.x
DeMets C (1992) Oblique convergence and deformation along the Kuril and Japan trenches. J Geophys Res 97(B12):17615–17625
DeMets C, Gordon RG, Argus DF (2010) Geologically current plate motions. Geophys J Int 181:1–80
Diament M, Harjono H, Karta K, Deplus D, Dahrin D, Zen M, Gérard M, Lassal O, Martin A, Malod A (1992) Mentawai fault zone off Sumatra: a new key to the geodynamics of western Indonesia. Geology 20:259–262
Ego F, Ansan V (2002) Why is the Central Trans-Mexican Volcanic Belt (102o–99oW) in transtensive defomation? Tectonophysics 359(1–2):189–208
Ego F, Sébrier M, Lavenu A, Yepes H, Egues A (1996) Quaternary state of stress in the northern Andes and the restraining bend model for the Ecuadorian Andes. Tectonophysics 259(1–3):101–116
Ekström G, Engdahl E (1989) Earthquake source parameters and stress distribution in the Adak Island Region of the Central Aleutian Islands, Alaska. J Geophys Res 94:15499–15519
Ekström G, Nettles M, Dziewonski AM (2012) The global CMT project 2004–2010: centroid-moment tensors for 13,017 earthquakes. Phys Earth Planet Inter 200–201:1–9. https://doi.org/10.1016/j.pepi.2012.04.002
Gaidzik K, Ramirez-Herrera MT, Kostoglodov V (2016) Active crustal faults in the Forearc region. Guerrero sector of the Mexican subduction zone. Pure Appl Geophys 173:3419–3443
Graham S, DeMets C, Cabral-Cano E, Kostoglodov V, Rousset B, Walpersdorf A, Cotte N, Lasserre C, McCaffrey R, Salazar-Tlaczani L (2015) Slow slip history for the Mexico subduction zone: 2005 through 2011. Pure Appl Geophys. https://doi.org/10.1007/s00024-015-1211-x
Haq SSB, Davis DM (2010) Mechanics of fore-arc slivers: insights from simple analog models. Tectonics 29:TC5015. https://doi.org/10.1029/2009TC002583
Hayes G (2018) Slab2—a comprehensive subduction zone geometry model: U.S. Geological Survey data release. https://doi.org/10.5066/F7PV6JNV
Hjörleifsdóttir V, Krishna Singh S, Husker A (2016) Differences in epicentral location of Mexican earthquakes between local and global catalogs: an update. Geofísica Internacional 55(1):79–93
Kanjorski NM (2003) Cocos plate structure along the middle America subduction zone off Oaxaca and Guerrero, Mexico. Influence of subducting plate morphology on tectonics and seismicity, University of California, San Diego
Keppie JD (2004) Terranes of Mexico revisited: a 1.3 billion year odyssey. Int Geol Rev 46:765–794
Kimura G (1986) Oblique subduction and forearc tectonics of the collision: Kuril arc. Geology 14:404–407
Kostoglodov V, Bandy W, Cominguez J, Mena M (1996) Gravity and seismicity over the Guerrero seismic gap, Mexico. Geophys Res Lett 23:3385–3388
Kostoglodov V, Husker AL, Santiago JA, Cotte N, Walpersdorf A (2016) Slow slip events on the strike slip fault in Guerrero, Mexico. In: Paper presented at the AGU Chapman Conference, Ixtapa, Guerrero, Mexico, 21–25 February 2016
Manea VC, Manea M, Kostoglodov V, Currie CA, Sewell G (2004) Thermal structure, coupling and metamorphism in the Mexican subduction zone beneath Guerrero. Geophys J Int 158:775–784
Manea M, Manea VC, Ferrari L, Kostoglodov V, Bandy W (2005) Tectonic evolution of the Tehuantepec ridge. Earth Planet Sci Lett 238:64–77
Manea M, Yoshioka S, Manea VC (2017) Subduction of oceanic plate irregularities in South-Central Mexico and the influence on subduction seismicity. Technical report, Research Center for Urban Safety and Security, Kobe University
McCaffrey R (1992) Oblique plate convergence, slip vectors, and forearc deformation. J Geophys Res 97(B6):8905–8915
Ortega-Gutiérrez F, Elías-Herrera M, Morán-Zenteno DJ, Solari L, Luna-González L, Schaaf P (2014) A review of batholiths and other plutonic intrusions of Mexico. Gondwana Res 26(3):834–868. https://doi.org/10.1016/j.gr.2014.05.002
Pacheco JF, Singh SK (2010) Seismicity and state of stress in Guerrero segment of the Mexican subduction zone. J Geophys Res 115:B01303. https://doi.org/10.1029/2009JB006453
Pacheco J, Jiménez C, Pérez Santana J, Estrada J, Cruz J, Cárdenas A, Li Yi T, Gutiérrez M, Rubí B, Santiago J (2005) Sismicidad del centro y sur de México. (Periodo enero a junio, 2004). Geos 24(3):457–461
Pardo M (1995) Shape of the subducted Rivera and Cocos plates in southern Mexico: Seismic and tectonic implications. J Geophys Res 100(B7):12357–12373
Pérez-Campos X, Kim Y, Husker A, Davis PM, Clayton RW, Iglesias A, Pacheco JF, Singh SK, Manea VC, Gurnis M (2008) Horizontal subduction and truncation of the Cocos Plate beneath Central Mexico. Geophys Res Lett 35:L18303. https://doi.org/10.1029/2008GL035127
Pérez-Gutiérrez R, Solari L, Gómez-Tuena A, Martens U (2009) Mesozoic geologic evolution of the Xolapa migmatic complex north of Acapulco, southern Mexico: implications for paleogeographic reconstructions. Revista Mexicana de Ciencias Geológicas 26(1):201–221
Radiguet M, Cotton F, Vergnolle M, Campillo M, Walpersdorf A, Cotte N, Kostoglodov V (2012) Slow slip events and strain accumulation in the Guerrero gap, Mexico. J Geophys Res 117(4):1–13
Radiguet M, Perfettini H, Cotte N, Gualandi A, Valette B, Kostoglodov V, Lhomme T, Walpersdorf A, Cabral Cano E, Campillo M (2016) Triggering of the 2014 Mw7.3 Papanoa earthquake by a slow slip event in Guerrero, Mexico. Nat Geosci 9:829–833
Riller U, Ratschbacher L, Frisch W (1992) Left-lateral transtension along the Tierra Colorada deformation zone, northern margin of the Xolapa magmatic arc of southern Mexico. J S Am Earth Sci 5:237–249
Ryan FD, Scholl WD (1989) The evolution of forearc structures along an oblique convergent margin, central Aleutian Arc. Tectonics 8(3):497–516
Sedlock RL, Ortega-Gutiérrez F, Speed RC (1993) Tectonostratigraphic terranes and tectonic evolution of Mexico. Geological Society of America Special Paper 278
Solari LA, Torres de Leon R, Hernandez Pineda G, Sole J, Solis-Pichardo G, Hernandez-Trevino T (2007) Tectonic significance of Cretaceous-Tertiary magmatic and structural evolution of the northern margin of the Xolapa Complex, Tierra Colorada area, southern Mexico. GSA Bull 119(9/10):1265–1279
Tolson G (2005) La falla Chacalapa en el sur de Oaxaca. Bol Soc Geol Mex 57:111–122

Villegas-Lanza JC, Chlieh M, Cavalié O, Tavera H, Baby P, Chire-Chira J, Nocquet J-M (2016) Active tectonics of Peru: Heterogeneous interseismic coupling along the Nazca megathrust, rigid motion of the Peruvian Sliver, and Subandean shortening accommodation. J Geophys Res Solid Earth. https://doi.org/10.1002/2016JB013080

Wang K, Hu Y, Bevis M, Kendrick E, Smalley R, Vargas RB, Lauría E (2007) Crustal motion in the zone of the 1960 Chile earthquake: detangling earthquake-cycle deformation and forearc-sliver translation. Geochem Geophys Geosyst 8:Q10010. https://doi.org/10.1029/2007GC001721

Wessel P, Smith WHF (1998) New, improved version of Generic Mapping Tools released. EOS Trans Am Geophys Union 79(47):579

Yamamoto J, Gonzalez-Moran T, Quintanar L, Zavaleta AB, Zamora A, Espindola VH (2013) Seismic patterns of the Guerrero–Oaxaca, Mexico region, and its relationship to the continental margin structure. Geophys J Int 192:375–389

Publisher's Note

2.2 GPS Data Processing with GAMIT/GLOBK Software

The GAMIT / GLOBK software package for processing geodetic data uses the double difference method that calculates the differences between stations and also between satellites (unlike the Gipsy program that occupies the precise point positioning (PPP) algorythm). IGS (International GNSS Service) final combination solutions for orbits (with accuracies of 1-2 cm) and Earth Orientation Parameters (EOP) are used as the input parameters of GAMIT. In the processing, ionospheric and atmospheric corrections are applied. Hydrostatic and water vapor delays are corrected using Vienna Mapping Functions (VMF). The Solid Earth tidal model (IERS03), the oceanic tidal load (FES2004), the tables for the Earth's rotation parameters (IAU2000 nutation, polar motion, universal time) and the IAU76 precession constant are applied. The resulting GPS time series are calculated in the ITRF14 reference frame and then rotated relative to the North American fixed plate using the rotation pole of Altamimi *et al.* [2017]. Post-processing of daily position time series includes offset fixes and outlier removal which was done with the help of the python package pyacs.

Unlike the PPP-based processing in the Gipsy package, the GAMIT / GLOBK double-difference method makes it possible to better reduce satellite clock and orbit errors, localized atmospheric errors, and also completely cancel out the effects of variations in the receiver clock. The GAMIT / GLOBK strategy gives better results in the estimation of daily positions (with errors 1-2mm less than those of Gipsy) for the wide networks of geodetic stations (of the regional or global size) that is the case of the Mexican GPS network. Thus, the results of the GAMIT / GLOBK processing provide better information for the analysis of regional phenomena such as slow events in the Mexican subduction zone, post-seismic deformation of large earthquakes and other large-scale surface deformations.

2.2.1 Global Navigation Satellite Systems (GNSS)

Global Navigation Satellite System (GNSS) refers to a constellation of satellites providing signals from space that transmit their positioning and timing data to GNSS receivers. The receivers

	GLONASS	GPS
Number of nominal satellites	24	24
Number of orbital planes	3	6
Orbital inclination	64°8’	55°
Orbital altitude	19 140km	20 180km
Period of revolution	11h 15m	11h 58m
Launch site	Baikonur/Plesetsk	Cape Canaveral
Date of first launch	02/10/82	22/02/78
Satellites for launch	1/3	1
Datum	PZ-90.11	WGS-84

Table 2-1: Differences between GNSS constellations.

then use this data to determine the site location. By definition, GNSS provides global coverage. Examples of GNSS include Europe’s Galileo, the USA’s NAVSTAR Global Positioning System (GPS), Russia’s Global Navigation Satellite System (GLONASS) and China’s BeiDou Navigation Satellite System, etc.

GPS satellites fly in medium Earth orbit (MEO) at the altitude of approximately 20,200 km (Table 2-1). Each satellite circles the Earth twice a day (every 11 h 58 min). The satellites in the GPS constellation are arranged into six equally-spaced orbital planes surrounding the Earth (Fig. 2-1a). Inclination of GPS satellite orbits is 55°. Each plane contains four ”slots” occupied by baseline satellites. The minimum number of satellites for the full constellation is 24 operational 95% of the time. This 24-slot arrangement ensures users can view at least four satellites from virtually any point on the planet. However, at the poles GPS observations encounter certain limitations. The Arctic circle begins at about 66.5°N. At these high latitudes satellites never pass directly overhead. The highest elevation GPS satellite is 45° above the horizon. This situation leads to better horizontal satellite geometry, but worse vertical satellite geometry compared to the situation at mid and low latitudes. Another limitation is high ionospheric activity that fluctuates in intensity based on the solar cycle. GPS satellites are not impervious to ionospheric activity, which can cause signal scintillation, creating changes in the amplitude or phase of signals. This can cause errors in timing, which then translates to errors with positioning calculations. As of April 18, 2017, there were 31 operational satellites in the GPS constellation.

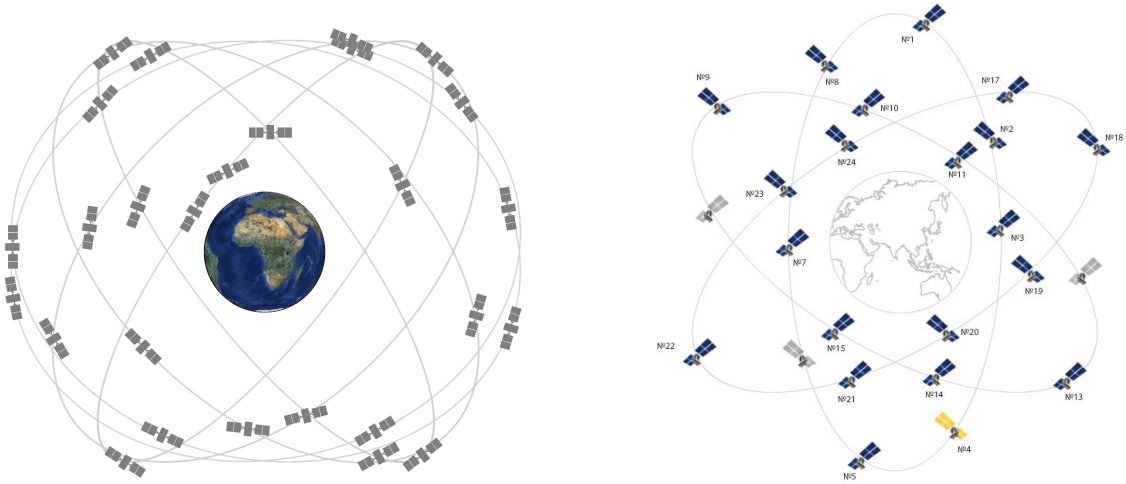

(a) GPS constellation.

(b) GLONASS constellation.

Figure 2-1: Constellation of satellites.

The GLONASS space segment consists nominally of 24 operational satellites (Table 2-1), distributed over three orbital planes (Fig. 2-1b). The longitude of ascending node differs by 120° from plane to plane. There are eight satellites per plane, separated 45° in argument of latitude. The difference in the argument of latitude of satellites in equivalent slots in two different orbital planes is 15°. Each satellite is identified by its slot number, which defines the orbital plane and its location within the plane. GLONASS satellites operate in circular orbits at an altitude of 19,100 km, an inclination of 64.8° and each satellite completes the orbit in approximately 11h 15min. This means that for a stationary observer the same satellite is visible at the same point in the sky every eight sidereal days. Since there are eight satellites in each orbital plane, satellite positions in the sky get repeated each (although by different satellites).

2.2.2 GPS Satellite Signals (Modified from Shmaliy [2006]

Officially, the Global Positioning System has two levels of service: the Precise Positioning Service (PPS) which is afforded to the United States military, allied military forces and some other U.S. government agencies, and the Standard Positioning Service (SPS), available to all users worldwide. Currently, the SPS is provided by way of the Coarse/Acquisition (C/A) 1.023 megachip per second pseudorandom noise (PRN) code on the GPS L1-frequency at 1575.42

MHz. The vast majority of GPS receivers now in existence, including virtually all civil-use handheld receivers, are SPS receivers which determine their positions by tracking the L1 C/A-code. SPS policy initially dictated a predictable positioning accuracy of 100 meters, at the 95% confidence level, horizontally and 156 meters (95%) vertically. SPS positioning accuracy was purposely degraded to this level through the use of Selective Availability (SA). When SA was removed on May 2, 2000, SPS accuracy improved greatly, approaching that of the PPS. The L2-frequency (1227.60 MHz) is used to measure the ionospheric delay by PPS (precise positioning service) equipped receivers. PPS Predictable Accuracy: 22m horizontal accuracy; 27.7m vertical accuracy; 200 nanosecond time (UTC) accuracy.

Three binary codes shift the L1 and/or L2 carrier phase.

1. The C/A Code (Coarse/Acquisition) modulates the L1 carrier phase. The C/A code is a repeating 1 MHz Pseudo Random Noise (PRN) Code. This noise-like code modulates the L1 carrier signal, "spreading" the spectrum over a 1 MHz bandwidth. The C/A code repeats every 1023 bits (one millisecond). There is a different C/A code PRN for each SV (space vehicle). GPS satellites are often identified by their PRN number, the unique identifier for each pseudo-random-noise code. The C/A code that modulates the L1 carrier is the basis for the civil SPS.

2. The P-Code (Precise) modulates both the L1 and L2 carrier phases. The P-Code is a very long (seven days) 10 MHz PRN code. In the Anti-Spoofing (AS) mode of operation, the P-Code is encrypted into the Y-Code. The encrypted Y-Code requires a classified AS Module for each receiver channel and is for use only by authorized users with cryptographic keys. The P (Y)-Code is the basis for the PPS.

3. The Navigation Message also modulates the L1-C/A code signal. The Navigation Message is a 50 Hz signal consisting of data bits that describe the GPS satellite orbits, clock corrections, and other system parameters.

A GPS receiver determines the travel time of a signal from a satellite by comparing the "pseudo random code" it's generating, with an identical code in the signal from the satellite.

The receiver slides its code later and later in time until it syncs up with the satellite's code. The amount it has to slide the code is equal to the signal's travel time. http://www.trimble.com/gpstutorial/subphases.aspx

2.2.3 Sources of Position Error (Modified from Introduction to GNSS [2015])

1. Site selection.

   Site selected for a GPS receiver installation should allow to minimize unwanted antenna motion and permit undisturbed record of the satellite signal. Receiver installed on the bedrock is provided maximum stability. However, if at the selected site is affected by the changes of the underground water level it can introduce noise into the signal. As the GPS signal arrives at the earth's surface, it may be reflected by local obstructions before it gets to the receiver's antenna (Fig. 2-2). This is called multi-path error.

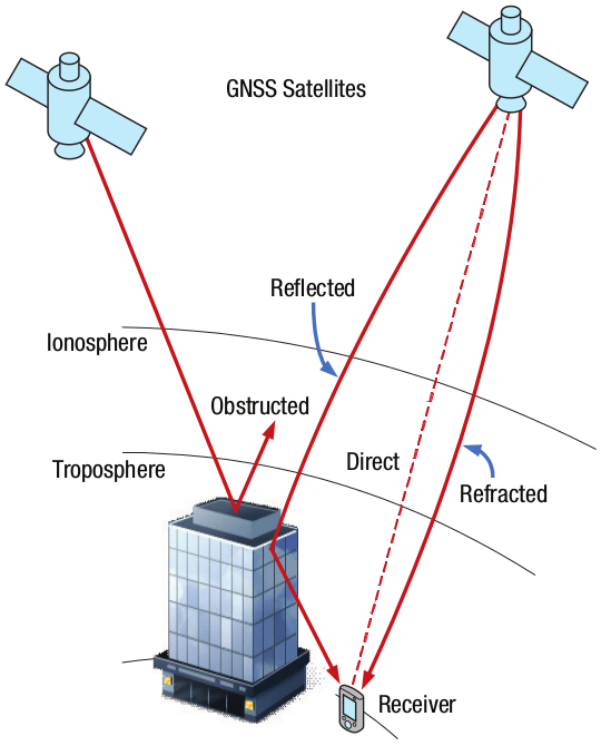

Figure 2-2: Multi-path effect. [Introduction to GNSS, 2015]

The multi-path effect is caused by reflection of satellite signals (radio waves) on flat

objects. For GPS signals this effect mainly appears in the neighborhood of large buildings or other elevations. The reflected signal takes more time to reach the receiver than the direct signal. The resulting error typically lies in the range of a few meters. These multi-path errors can often cause both position and velocity "spikes" on a GPS receiver. One technique for minimizing multi-path errors is to track only those satellites that are at least 15° above the horizon, a threshold called the "mask angle." Longer observation can help "average out" multi-path error. Under the same environment, the presence of multi-path errors can be verified using a day-to-day correlation of the estimated residuals. This is because the satellite-reflector-antenna geometry repeats every sidereal day. However, multi-path errors in the undifferenced pseudorange measurements can be identified if dual-frequency observations are available. A good general multi-path model is still not available, mainly because of the variant satellite-reflector-antenna geometry. There are, however, several options to reduce the effect of multi-path. The straightforward option is to select an observation site with no reflecting objects in the vicinity of the receiver antenna. Another option is to reduce the effect of multi-path is to use a chock ring antenna (a chock ring device is a ground plane that has several concentric metal hoops, which attenuate the reflected signals). As the GPS signal is right-handed circularly polarized while the reflected signal is left-handed, reducing the effect of multi-path may also be achieved by using an antenna with a matching polarization to the GPS signal (i.e., right-handed). The disadvantage of this option, however, is that the polarization of the multi-path signal becomes right-handed again if it is reflected twice.

2. Quality of receiver phase center.

   The point at which the GPS signal is received is called the antenna phase center. Generally, the antenna phase center does not coincide with the physical (geometrical) center of the antenna. It varies depending on the elevation and the azimuth of the GPS satellite as well as the intensity of the observed signal. As a result, additional range error can be expected. The size of the error caused by the antenna-phase-center variation depends

on the antenna type, and is typically in the order of a few centimeters. It is, however, difficult to model the antenna-phase-center variation and, therefore, care has to be taken when selecting the antenna type. For short baselines with the same types of antennas at each end, the phase-center error can be canceled if the antennas are oriented in the same direction. Mixing different types of antennas or using different orientations will not cancel the error. Due to its rather small size, this error is neglected in most of the practical GPS applications. It should be pointed out that phase-center errors could be different on L1 and L2 carrier-phase observations. This can affect the accuracy of the ionosphere free linear combination, particularly when observing short baselines. As mentioned before, for short baselines, the errors are highly correlated over distance and cancel sufficiently through differencing. Therefore, using a single frequency might be more appropriate for short baselines in the static mode.

3. Satellite orbits.

   GPS receivers calculate coordinates relative to the known locations of satellites in space, a complex task that involves knowing the shapes of satellite orbits as well as their velocities, neither of which is constant. The GPS Control Segment monitors satellite locations at all times, calculates orbit eccentricities, and compiles these deviations in documents called ephemerides. An ephemeris is compiled for each satellite and broadcast with the satellite signal. GPS receivers that are able to process ephemerides can compensate for some orbital errors. Nominally, an ephemeris error is usually in the order of 2m to 5m, and can reach up to 50m under selective availability (not in operation since September 2007). Some applications, such as studies of the crustal dynamics of the earth, require more precise ephemeris data than the broadcast ephemeris. To support these applications, several institutions (e.g., the International GPS Service for Geodynamics (IGS), the U.S. National Geodetic Survey (NGS), and Geomatics Canada) have developed postmission precise orbital service. Precise ephemeris data is based on GPS data collected at a global GPS network coordinated by the IGS. At the present time, precise ephemeris data is

available to users with some delay, which varies from 12 hours for the IGS ultra rapid orbit to about 12 days for the most precise IGS precise orbit. The corresponding accuracies for the two precise orbits are in the order of a few decimeters to 1 decimeter, respectively.

4. Tropospheric delay.

   Tropospheric delays give an error of 1m. The troposphere is the lower part (from 8 to 13 km) of the atmosphere that experiences the changes in temperature, pressure, and humidity associated with weather changes. The satellite signal deflects in this media. Complex models of tropospheric delay require estimates or measurements of these parameters. Humidity is the parameter the most difficult to estimate due to its' heterogeneity.

5. Ionospheric delay.

   The ionosphere is the layer of atmosphere between 80 km and 600 km above the earth. This layer contains electrically charged particles called ions. These ions delay the satellite signals and can cause a significant amount of satellite position error (typically ±5 meters, but can be more during periods of high ionospheric activity (Fig. 2-3)). Ionospheric delay varies with solar activity, time of year, season, time of day and location. This makes it very difficult to predict how much ionospheric delay is impacting the calculated position.

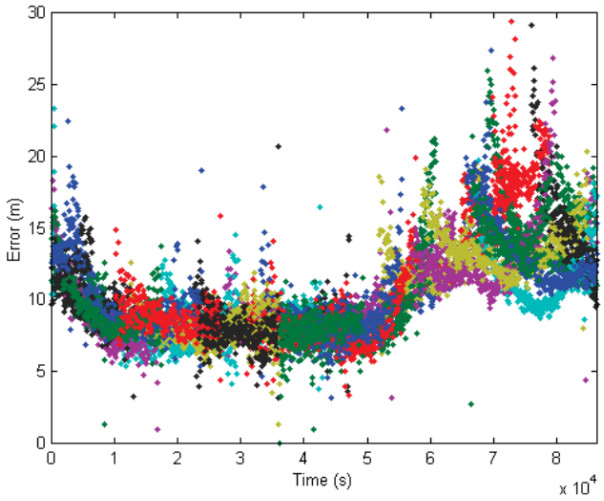

Figure 2-3: An example of ionospheric delay error for single-frequency GNSS observations for multiple satellites during 24 hours.

Ionospheric delay also varies based on the radio frequency of the signal passing through the ionosphere (Fig. 2-4). GNSS receivers that can receive more than one GNSS signal, L1 and L2 for example, can use this to their advantage. By comparing the measurements for L1 to the measurements for L2, the receiver can determine the amount of ionospheric delay and remove this error from the calculated position.

For receivers that can only track a single GNSS frequency, ionospheric models are used to reduce ionospheric delay errors. Due to the varying nature of ionospheric delay, models are not as effective as using multiple frequencies at removing ionospheric delay. Ionospheric conditions are very similar within a local area (tens of km), so the base station and rover receivers experience very similar delay. This allows Differential GNSS systems to compensate for ionospheric delay.

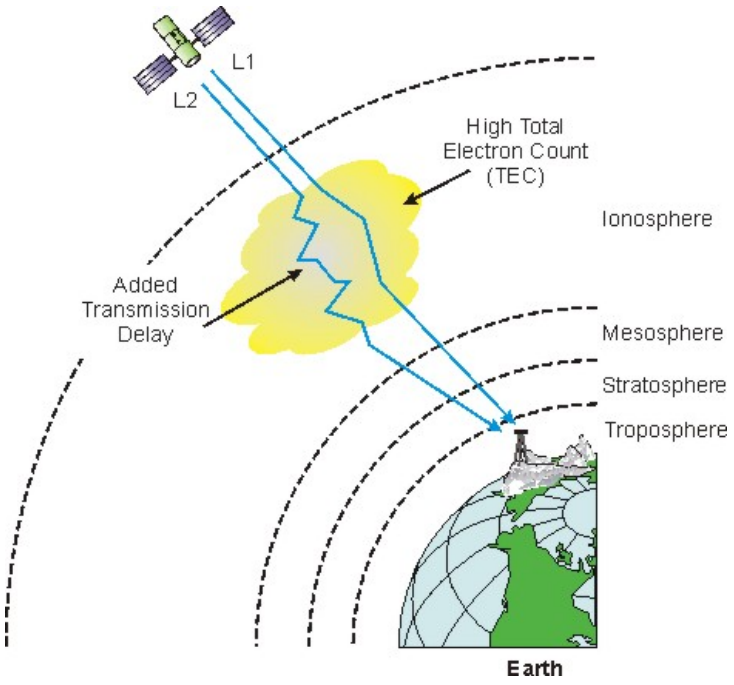

Figure 2-4: This example shows that the amount of ionospheric delay varies based on the electron density and that the electron density can vary based on geographic location and sunspot activity. This diagram also shows that the amount of delay is different for the different GPS frequencies. [Abba *et al.*, 2015]

6. Satellite clock.

Contributing source	Error range
Satellite clock	±2m
Ionospheric delay	±5m
Tropospheric delay	±0.5m
Orbit errors	±2.5m
Multipath	±1m

Table 2-2: GNSS system errors.

The atomic clocks in the GNSS satellites are very accurate, but they do drift a small amount. Unfortunately, a small inaccuracy in the satellite clock results in a significant error in the position calculated by the receiver (Table 2-2). For example, 10 nanoseconds of clock error results in 3m of position error. The clock on the satellite is monitored by the GNSS ground control system and compared to the even more accurate clock used in the ground control system. In the downlink data, the satellite provides the user with an estimate of its clock offset. Typically, the estimate has an accuracy of about ±2 meters, although the accuracy can vary between different GNSS systems. To obtain a more accurate position, the GNSS receiver needs to compensate for the clock error.

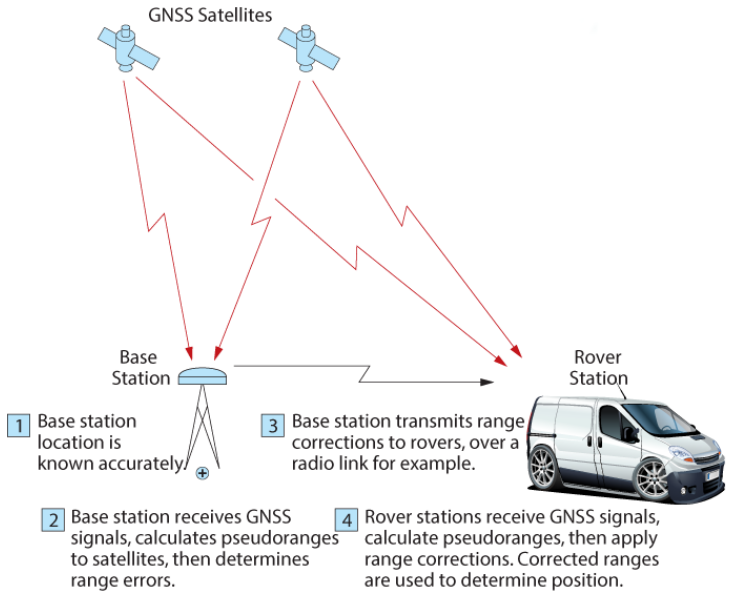

Figure 2-5: Differential GNSS. [Introduction to GNSS, 2015]

One way of compensating for clock error is to download precise satellite clock information from the Spaced Based Augmentation System (SBAS) or the Precise Point Positioning (PPP) service provider. The precise satellite clock information contains corrections for the clock errors that were calculated by the SBAS or PPP system.

Another way of compensating for clock error is to use a Differential GNSS or Real Time Kinematic (RTK) receiver configuration. In differential GNSS (Fig. 2-5), the position of a fixed GNSS receiver, referred to as a base station, is determined to a high degree of accuracy using conventional surveying techniques. Then, the base station determines ranges to the GNSS satellites in view using:

(a) The code-based positioning technique.

(b) The location of the satellites determined from the precisely known orbit ephemerides and satellite time.

The base station compares the surveyed position to the position calculated from the satellite ranges. Differences between the positions can be attributed to satellite ephemeris and clock errors, but mostly to errors associated with atmospheric delay. The base station sends these errors to other receivers (rovers), which incorporate the corrections into their position calculations.

Differential positioning requires a data link between the base station and rovers, if corrections need to be applied in real-time, and at least four GNSS satellites in view at both the base station and the rovers. The absolute accuracy of the rover's computed position will depend on the absolute accuracy of the base station's position. This method is quite useful for campaign occupation measurements.

Since GNSS satellites orbit high above the earth, the propagation paths from the satellites to the base stations and rovers pass through similar atmospheric conditions, as long as the base station and rovers are not too far apart. Differential GNSS works very well with base station-to-rover separations of up to tens of kilometers.

7. Solar and lunar tides.

   Tides are created mostly by the gravitational attraction of the Moon and Sun. Fig. 2-6 shows deformation caused by the solid Earth tide. In this example Moon lags the Sun by approximately 5 hours on this day.

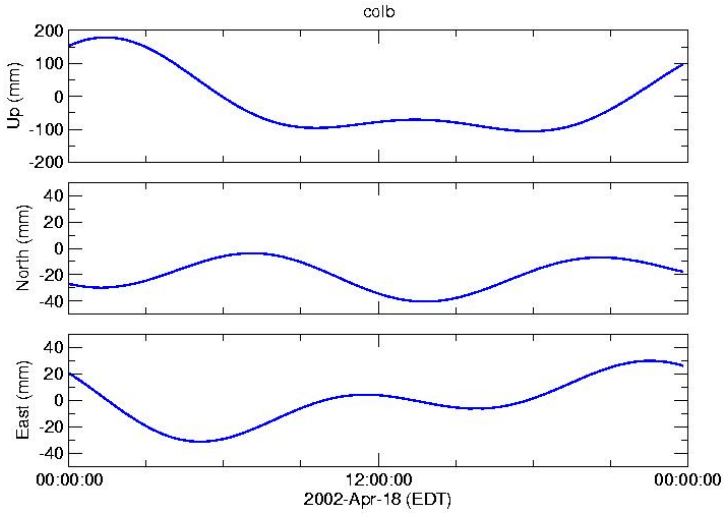

Figure 2-6: Deformation caused by the solid Earth tide at COLB station in Ohio.

8. Ocean and atmospheric loading.

   The effect of ocean tide loading (OTL) can be as large as several centimeters. Usually, OTL values derived from global ocean tide models are used. An on-line service providing OTL parameters is hosted by the Onsala Space Observatory `http://holt.oso.chalmers.se/loading/`. Much like OTL, the weight of the air above a site will deform the supporting crust of the Earth. Atmospheric loading (AL) is a more subtle effect than OTL which, in turn, is more subtle than the solid Earth tide. Nonetheless, it can be measurable in the very highest accuracy surveys. Efforts are under way to better understand and model AL deformations and it is rarely implemented in common GNSS processing software.

   Models used in the GAMIT software processing to correct for different sources of error are summarized in Table 2-3.

Atmospheric Propagation Delay	Vienna Mapping Function (VMF1)
Non-Tidal Atmospheric Pressure Loading	atmdisp_cm.2019_344
Reference Frame	North America ITRF14/IGS14
Inertial Frame	J2000
Moon ephemeris	luntab.2019.J2000
Earth (Solar) ephemeris	soltab.2019.J2000
Nutation table	nutabl.2019
Nutation model	IAU 2000
Earth Gravitational Model	EGM08
Precession Constant	IAU76
Model for Direct Solar Radiation Accelerations	BERNE
Solid Earth Tide Model	IERS03
Ocean Tide Model	FES2004
Euler pole (long, lat, ω) [Altamimi *et al.*, 2017]	-88.0194, -5.184, 0.1937
Euler pole (ω_x, ω_y, ω_z in mas/yr) [Altamimi *et al.*, 2017]	0.024, -0.694, -0.063
Orbits	IGS (sopac, cddis, unavco)
Elevation cutoff angle	10°

Table 2-3: Models and other parameters used in GAMIT processing.

2.2.4 Processing GNSS data with GAMIT/ GLOBK software

GAMIT/GLOBK is a comprehensive GPS analysis package developed at MIT, the Harvard-Smithsonian Center for Astrophysics (CfA), Scripps Institution of Oceanography (SIO), and Australian National University for estimating station coordinates and velocities, stochastic or functional representations of post-seismic deformation, atmospheric delays, satellite orbits, and Earth orientation parameters.

GAMIT uses double difference method that calculates the between-station differences and also between satellites. It reduces satellite clock and orbit errors, localized atmospheric errors and also allows to cancel completely the effects of variations in the receiver clocks. In this case the observations are just as accurate with low-cost crystal oscillators as with an atomic frequency standard.

GLOBK is a Kalman filter whose primary purpose is to combine various geodetic solutions such as GPS, Very Long Baseline Interferometry (VLBI), and Satellite Laser Ranging (SLR) experiments. It accepts as data, or "quasi-observations", the estimates and covariance matrices for station coordinates, earth-orientation parameters, orbital parameters, and source positions

generated from the analysis of the primary observations. The input solutions are generally performed with loose a priori uncertainties assigned to all global parameters, so that constraints can be uniformly applied in the combined solution.

To control processing the software uses C-shell scripts (stored in */com* and mostly named to begin with sh : *sh_get_nav*, *sh_gamit*, etc) which invoke the Fortran or C programs compiled in the */libraries*, */gamit*, and */kf* directories. The parameter logic allows a maximum of 99 sites but the standard distribution is dimensioned for 60 sites since greater efficiency is obtained for large networks by parallel processing using connected subnets.

GAMIT incorporates difference operator algorithms that map the carrier beat phases into singly and doubly differenced phases. These algorithms extract the maximum relative positioning information from the phase data regardless of the number of data outages, and take into account the correlations that are introduced in the differencing process. An alternative, (nearly) mathematically equivalent approach to processing GPS phase data is to use formally the (one-way) carrier beat phases but estimate at each epoch the phase offset due to the station and satellite. This approach is used by the autcln program in GAMIT to compute one-way phase residuals for editing, display, and estimating atmospheric and ionospheric slant delays.

In order to provide the maximum sensitivity to geometric parameters, the carrier phase must be tracked continuously throughout an observing session. If there is an interruption of the signal, causing a loss of lock in the receiver, the phase will exhibit a discontinuity of an integer number of cycles ("cycle-slip"). This discontinuity may be only a few cycles due to a low signal-to-noise ratio, or it may be thousands of cycles, as can occur when the satellite is obstructed at the receiver site. Initial processing of phase data is often performed using time differences of doubly differenced phase ("triple differences", or "Doppler" observations) in order to obtain a preliminary estimate of station or orbital parameters in the presence of cycle slips. The GAMIT software uses triple differences in editing but not in parameter estimation. Rather, it allows estimation of extra bias parameters whenever the automatic editor has flagged an epoch as a cycle slip that cannot be repaired.

A major source of error in single-frequency GPS measurement is the variable delay intro-

duced by the ionosphere. For day-time observations near solar maximum this effect can exceed several parts per million of the baseline length. Fortunately, the ionospheric delay is dispersive and can usually be reduced to a millimeter or less by forming a particular linear combination (LC, sometimes called L3) of the L1 and L2 phase measurements:

$$LC = 2.546L1 - 1.984L2 \tag{2-1}$$

Forming LC, however, magnifies the effect of other error sources. For baselines less than a few kilometers the ionospheric errors largely cancel, and it is preferable to treat L1 and L2 as two independent observables rather than form the linear combination. The station separation at which the ionospheric errors exceed the phase noise depends on many factors (receiver, antenna, multi-path environment, latitude, time of day, sunspot activity) and must be determined empirically by analyzing the data with both observable types.

2.2.5 Automatic Processing with GAMIT and GLOBK (adapted from GAMIT/ GLOBK Reference Manual, 2015)

GAMIT is composed of distinct programs which perform the functions of preparing the data for processing (makexp and makex), generating reference orbit and rotation values for the satellites (*arc*, *yawtab*), interpolating time- and location-specific values of atmospheric and loading models (*grdtab*), computing residual observations (O-C's) and partial derivatives from a geometrical model (*model*), detecting outliers or breaks in the data (*autcln*), and performing a least squares analysis (*solve*). Solve incorporates a weighted least squares algorithm to estimate the relative positions of a set of stations, orbital and Earth-rotation parameters, zenith delays, and phase ambiguities by fitting to doubly differenced phase observations. Since the functional (mathematical) model relating the observations and parameters is non-linear, GAMIT produces two solutions, the first to obtain coordinates within a few decimeters, and the second to obtain the final estimates. Although the modules can be run individually, they are tied together through the data flow, particularly file-naming conventions, in such a way that most processing

is best done with shell scripts and a sequence of batch files set up by a driver module (*fixdrv*) for modeling, editing, and estimation. Though the data editing is almost always performed automatically, the solution residuals can be displayed or plotted so that problematic data can be identified (*cview*). A summary of GAMIT processing tools, inputs and outputs is provided in Table 2-4.

Likewise, GLOBK operates through distinct programs, which can be invoked with a single command or run separately. The primary functions are to combine quasi-observations –either GAMIT/GLOBK "h-files" or the internationally accepted SINEX format –from multiple networks and/or epochs (*glred* or *globk*), and to impose on this solution a reference frame appropriate to the scientific objective (*glorg*). Note that *globk* and *glred* are the same program, just called in different modes: *glred* to read data from one day at a time for generating time series, *globk* for stacking multiple epochs to obtain a mean position and/or velocity.

The full sequence of steps to go from phase data to time series is accomplished with two shell scripts: *sh_gamit* looks for raw or Receiver Independent Exchange Format (RINEX) data over a range of days and invokes the GAMIT programs to produce constrained and loose estimates of coordinates together with sky plots of phase data as a record of the processing; *sh_glred* uses the GAMIT results to produce time series of day-to-day repeatability or a combined h-file that may be further combined with those from other epochs to estimate station velocities. The only preparation required is assembling the meta-data from station logs; setting up the control files, most of which are common to all analyses of a particular era; and assembling the non-IGS phase data in one or more directories on your system.

2.2.6 GAMIT Processing Setup

The first step in running the scripts is to create a project directory (e.g. */2016*) with two subdirectories : */rinex* and */tables*. Copy into the */rinex* directory all of the local RINEX files to use in the processing. RINEX files for IGS reference stations can be downloaded automatically during the processing using command ftprnx in 'sites.defaults' file or manually running the following command:

Table 2-4: Automatic processing with GAMIT

sh_gamit			
SUBROUTINE	**FUNCTION**	**INPUT**	**OUTPUT**
makexp	determines the stations to be included in a session from the RINEX or X-files present or linked in the day directory and creates the input control files for makex, makej, and fixdrv	- RINEX (or X-) files - station.info - session.info	- D-file (driver file of sessions and receivers) - session.info (optional) - input batch files for makex, makej, bctot
makej	creates a (J-) file of satellite clock values from the navigation message	- RINEX navigation file (brdc0010.yyn) - C-file (observed - computed partial derivatives)	- J-file (satellite clock polynomial coefficients)
makex	creates GAMIT observation (X-) files from the RINEX files	- raw observations (RINEX) - station.info (rcvr, ant, firware, HI) - session.info (scenario file) - RINEX nav file - J-file - L-file (coordinates of stations)	- K-file (receiver clock offsets) - X-file (input observations)
arc	creates a T-file of tabulated ephemerides of the satellite coordinates and the partial derivatives of these coordinates with respect to initial conditions and the other adjustable parameters	- arc.bat (batch input file) - G-file (orbital initial conditions and non-gravitational parameter values)	- arcout.ddd (output print file) - T-file (tabular ephemeris for all sat. ses.)
fixdrv	reads the analysis control files and creates a batch file for GAMIT processing	- D-file (list of X-, J-, L-, T-files) - sestbl. (session control) - sittbl. (site control) - T, J, L, X (or C) input	- B-file (bexpy.bat: primary batch file) - B-file (bexpy.nnn: secondary batch files) - I-file (receiver clock polynomials)
model	creates a C-file containing the observation residuals and partial derivatives to be used in *solve* to estimate adjustments to parameters	- L-file (site coordinates) - station.info (antenna heights) - X-file - I, J, T, Y-files - antmod.dat (PCV models) - RINEX met file - otl.list/grid, atml.list/grid	- C-file (residuals and partials) - P-file (record of a *model* run)
autcln	uses the residuals written to the C-file by *model*, performs automatic editing, and writes an output C-file with outliers removed, cycle-slips repaired, and extra bias flags inserted for slips that cannot be reliably repaired	- C-file	- C-file (cleaned) - N-file (data-weight overrides for solve created from autcln.sum.postfit)
cfmrg	creates an M-file to control the combination of C-files and selection of adjustable parameters to be input to the estimation module *solve*	- C-file	- M-file (controls merging of data (C-) files for *solve* and editing programs)
solve	rewrites the M-file, adding adjustments to the parameters	- C-file - M-file - N-file	- Q-file - G-file - H-file - L-file

sh_get_rinex -archive sopac unavco -yr 2016 -doy 100 -ndays 1 -sites ineg

Then run *sh_setup* or the below mentioned set of commands to link or copy into the [project]/tables directory the appropriate control and data files:

sh_links.tables -frame J2000 -year 2016

cp ~/gg/tables/igs14_comb.apr .

cp ~/gg/tables/sittbl. .

cp ~/gg/tables/sestbl. .

cp ~/gg/tables/process.defaults .

cp ~/gg/tables/autcln.cmd .

All of the required templates and tables reside in ~/gg/tables, where ~/gg is a required alias pointing to the highest level of the GAMIT/GLOBK installation. Executing *sh_setup* will invoke *sh_links.tables* to link the standard data tables and will copy the eight control and data files.

process.defaults: Edit this file to specify the computation environment, sources for internal and external data and orbit files, start time and sampling interval, and instructions for archiving the results.

sites.defaults: Edit this file to specify which local and IGS stations are to be used and how station meta-data are to be handled.

station.info: This file contains the receiver and antenna type and height of instrument (HI) values as a function of time for all occupations of the stations used in the project. Although it can be generated during processing by *sh_gamit*, the best approach is usually to manually construct the file prior to processing.

coordinate files (.apr): *sh_gamit* maintains in the experiment */tables* directory two files of a priori coordinates. The file ending in .apr (set as aprf in 'process.defaults', 'itrf14_noam_all.apr' in our example for the latest ITRF2014) contains the Cartesian coordinates of stations you wish to have unchanged throughout the processing. Initial velocities of local stations are set to zero. For convenience two .apr files are prepared: 'itrf14_noam_all.apr' – for all the IGS reference sites; 'itrf14_mex.apr' – for local stations. The L-file (lfile.), which can contain either Cartesian

position and velocity (default, same as .apr file) or spherical position, is updated after each day is processed if the adjustments exceed a specified value (0.3m by default). If good coordinates for stations are available but are not in the .apr file, they should be manually appended to the apr-file if you want them to be unchanged. For any station that does not have coordinates in lfile. , *sh_gamit* will attempt to calculate coordinates via a pseudorange solution, or (if use_rxc Y in process.defaults) use the coordinates in the RINEX header. When GAMIT runs, these coordinates will be updated from the phase solution so that for successive days on which the same station is observed, the accurate coordinates will be used.

sestbl. and *sittbl.*: Edit these files to set the appropriate options for the current analysis. Make sure that any station for which you specify tight constraints in sittbl. has accurate coordinates in the .apr file.

autcln.cmd: Controls for cleaning the data in program autcln. This file will usually not require editing unless you encounter unusual data during the processing.

2.2.7 Launching the processing

To process time series for the current study I use a reference network of 36 IGS stations. This network was selected to create the most uniform distribution in all the directions with respect to the local stations. Total number of local sites is 104 (the number varies from year to year depending on the data availability and equipment functioning). For computational reasons all the stations were divided in four subnetworks corresponding to their geographical locations: Mexico City and nearby areas (25 stations), Guerrero (40), Oaxaca (20) and Southern Mexican states (19).

Once the template files are edited appropriately, you can start the processing from within the experiment directory by giving *sh_gamit* simply the 4-character code for the experiment and a range of days to process:

sh_gamit -s 2016 1 100 -expt test -orbit IGSF ¿ sh_gamit.out.

For processing only final orbits (IGSF), which are the most precise, have been used. When the script runs, it will write to the screen a record of each step, which you may choose to

redirect to a file (e.g., > sh_gamit.out). Examining the screen log together with the comments and source code in ∼/gg/com/sh_gamit and the 'GAMIT.fatal' file, will allow you to identify the point and reason for failure should that occur. sh_gamit generates h-files for every day included in the processing. These files contain covariance matrix and parameter adjustments for solution generated with loose constraints, used as input to GLOBK.

To use sh_glred to obtain time series of position estimates, you need to edit the command file 'glorg_comb.cmd' to specify which sites will be used to define your reference frame (>20 stations). If you want to omit some sites or indicate where steps should be applied in the time series to account for earthquakes or changes in instrumentation, you may need to edit also 'globk_comb.cmd' and an earthquake/rename file. Then run, e.g., (from */gsoln*)

*ls ../glbf/h17011*glx > list_hfiles.gdl* - creates global directory list with all the h-files that will be used to calculate a combined solution.

glred 0 2017.prt 2017.log list_hfiles.gdl globk_comb.cmd - builds position time series

sh_plotcrd -f 2017.org -expt test -cols 1 - plots time series

To build a velocity field you need to create and modify two files: 'globk_vel.cmd' and 'glorg_vel.cmd' and execute the following commands:

globk 6 vel.prt vel.log vel.gdl globk_vel.cmd sh_plotvel -f vel.org -R

However, another approach to obtain a combined solution and produce position time series is used in this work due to its' advantage in computational speed. Once h-files are obtained for each day they are combined into global .GLX files from all the subnetworks using globk. Then I use pyacs, a python-based geodetic analysis package developed by J.-M. Nocquet, to produce time series for each station for the entire observation time. It takes 30-40 minutes to produce a solution for 14 years of data on an Intel(R) Core(TM) i7-8550U CPU @ 1.80GHz machine with four cores. The same pyacs package is used afterwards to rotate time series with respect to the fixed North American plate, to remove occasional steps in time series and to remove outliers. Euler pole is calculated using the model for absolute plate rotation in ITRF2014 reference frame from Altamimi *et al.* [2017] [long, lat, ang_vel] = [-88.0194, -5.184, 0.1937].

Resulting position time series are provided in Appendix A (Fig. A-1).

For further manipulation of the data, that includes decomposition and inversion, I apply detrending strategy. I use a single station approach where I calculate the average of interSSE velocities for each site (Table C-1) and then remove this trend from the GPS time series.

2.3 Slow Slip Inversion Strategy Using Independent Component Analysis Inversion Method (ICAIM)

2.3.1 Independent Component Analysis Inversion Method

The slip on the subduction interface during SSEs in Guerrero and Oaxaca in 2017-2019 is analyzed using the Independent Component Analysis-based Inversion Method (ICAIM). This approach allows to decompose the dataset into independent components (IC) before the inversion. The ICA is a standard approach to solve Blind Source Separation (BSS) problems, and it assumes that the sources are statistically temporally independent, not moving in space, and that their signals are linearly mixed when recorded by the stations. This multivariate technique still remains in the field of linear decompositions. However, the data are projected onto a system of coordinates where each component is no longer constrained to be orthogonal to another one. In other words, the independent components (ICs) constitute a non-orthogonal basis for this reference system [Gualandi *et al.*, 2016]. In this work, the modified variational Bayesian ICA (vbICA) is used. Choudrey [2002] has shown that vbICA is a more flexible method to perform an optimal decomposition if transient signals have non-unimodal probability density functions (pdfs). Gualandi *et al.* [2016] modified vbICA to account for the missing data in time series.

The dataset is represented by a matrix $\mathbf{X}(\mathbf{M}, \mathbf{T})$ where $\mathbf{M}$ is the number of time series and $\mathbf{T}$ is the total number of recorded epochs. $\mathbf{M}$ is obtained as the total number of stations multiplied by three components of observations (North, East, Vertical). The linear combination of the sources to reconstruct the observed data considering that some Gaussian noise is perturbing the measurements can be summarized as follows:

$$\mathbf{X_{M\times T}} = \mathbf{A_{M\times L}S_{L\times T}} + \mathbf{N_{M\times T}}, \tag{2-2}$$

where **A** is called the mixing matrix, **S** source matrix, and **N** noise matrix. Each row of **S** contains the temporal evolution associated to a given source **L**, and the sources are statistically independent one from the other.

ICAIM code used in this work to invert for the slip on the subduction interface is written in Matlab by Adriano Gualandi. The code is based on the PCAIM (Principal Component Analysis) driver developed by [Kositsky and Avouac, 2010]. The inversion part of the ICAIM code is based on the least-squares formulation of Tarantola [2005] for linear problems modified by Radiguet *et al.* [2011].

In the time series use of the code, the data matrix is decomposed using the Singular Value Decomposition (SVD) approach:

$$\mathbf{X} = \mathbf{USV^t} \tag{2-3}$$

where **U** are spatial vectors, **S** is a diagonal matrix weighting matrix with eigenvalues, **V** are vectors of temporal evolution. **U** has the length of the number of time series traces. Each eigenvalue of **S** represents the amplitude of the independent components. **V** has the length equal to the number of time steps. After ICA decomposition the sizes of these matrices are defined by the number of independent components (ICs) selected in the analysis.

The displacement at each GPS station (Fig. 2-7) is the linear sum of all subfaults contributions: $\mathbf{d} = \mathbf{Gm}$, where **d** are the observed displacements (3 components for each station), **G** is the matrix of transfer functions and **m** is the unknown vector of model parameters (slip on each subfault). The cost (misfit) function $S(m)$ is:

$$S(m) = \frac{1}{2}[\underbrace{(\mathbf{Gm}-\mathbf{d})^\mathbf{t}\mathbf{C_d^{-1}}(\mathbf{Gm}-\mathbf{d})}_{\sum_i\left(\frac{d^i_{mod}-d^i_{obs}}{\sigma^i_d}\right)^2 \text{ fit between model and data}} + \underbrace{(\mathbf{m}-\mathbf{m_0})^\mathbf{t}\mathbf{C_m^{-1}}(\mathbf{m}-\mathbf{m_0})}_{\sum_i\left(\frac{m^i-m^i_0}{\sigma^i_m}\right)^2 \text{ proximity to initial model}}] \tag{2-4}$$

and the model expectation $\mathbf{m}$ is:

$$\mathbf{m} = \mathbf{m_0} + \mathbf{C_m G^t}(\mathbf{G C_m G^t} + \mathbf{C_d})^{-1}(\mathbf{d} - \mathbf{G m}) \tag{2-5}$$

where $\mathbf{m_0}$ is the starting model, $\mathbf{C_d}$ and $\mathbf{C_m}$ are, respectively, the covariance matrix for data and model parameters. $\mathbf{C_d}$ is the diagonal matrix of the variances ($\sigma_\mathbf{d}^\mathbf{2}$) associated with the data errors. The standard deviations ($\sigma_\mathbf{d}$) associated with North, East and Vertical component are two times the average standard deviations (95% confidence level) for this component for all stations (2.1, 2.5 and 5.1 mm, respectively). Thus, all stations have the same weighting in the inversion, but a different weight depending on the component [Radiguet *et al.*, 2011]. Green's functions $\mathbf{G}$ are computed using Okada [1985] formulation.

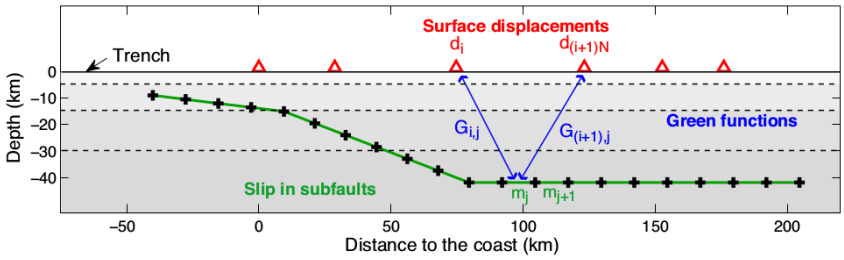

Figure 2-7: Geometry of the subduction interface with illustrated inversion parameters. $\mathbf{d}$ - are observations (GPS time series); $\mathbf{m}$ - model parameters (slip on the fault plane discretized in patches; $\mathbf{G}$ - Green's function (response to unit slip on a given fault patch).

The model covariance matrix $\mathbf{C_m}$ is used to introduce correlation between nearby parameters, that is, spatial smoothing. The element (i, j) of $\mathbf{C_m}$ is given by the relation:

$$\mathbf{C_m(j, j + n)} = \left(\sigma_\mathbf{m}\frac{\lambda_0}{\lambda}\right)^2 exp\left(\frac{-\mathbf{d(j, j + n)}}{\lambda}\right) \tag{2-6}$$

where $\mathbf{d}(j, j + n)$ is the distance between subfaults j and $j + n$.

To introduce the correlation between nearby parameters a decreasing exponential function $exp\left(\frac{-\mathbf{d}(j,j+n)}{\lambda}\right)$ is used (Fig. 2-8). Compared to the usually applied Gaussian function (Fig. 2-8), the decreasing exponential stabilizes the solution at large distance, while allowing important variations in the slip amplitude for nearby subfaults. The model covariance matrix is weighted

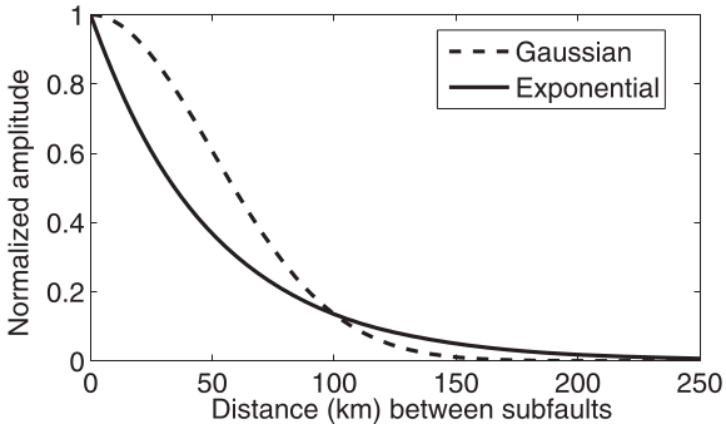

Figure 2-8: Comparison of the Gaussian and decreasing exponential correlation functions.

by a factor $\left(\sigma_{\mathbf{m}}\frac{\lambda_0}{\lambda}\right)^2$: $\sigma_{\mathbf{m}}$ is the a priori standard deviation of model parameters, $\lambda 0$ is a scaling factor fixed to 10km (about the size of a subfault) and λ is the correlation length, fixing the distance over which parameters are correlated. As λ increases, more coefficients of the matrix $\mathbf{C_m}$ become non-null (more parameters are correlated). At the same time, the weighting factor $\left(\sigma_{\mathbf{m}}\frac{\lambda_0}{\lambda}\right)^2$ decreases as λ increases. The total weight of the matrix $\mathbf{C_m}$ thus remains constant for different values of λ [Radiguet *et al.*, 2011].

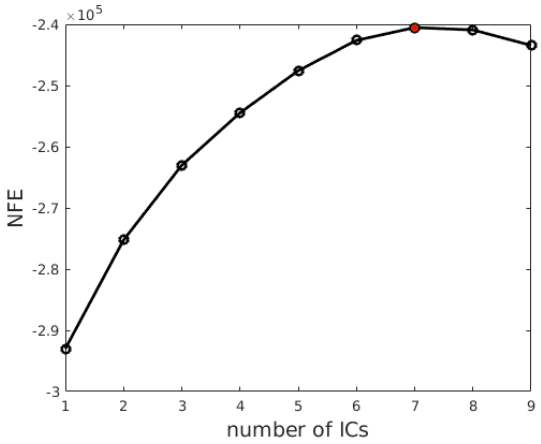

Figure 2-9: Free negative energy (NFE) as a function of the number of independent components.

To select the optimal solution, I apply the negative free energy (NFE) criterion. Choudrey [2002] proposed a variational approximation, which allows for the use of the NFE as a contrast function to be maximized to find an approximating posterior *pdf* for the weights $p'(W \mid \mathcal{M})$

such that the divergence between the true $p(W \mid X, \mathcal{M})$ and the approximate posteriors is minimized. The posterior *pdf* of the weights, given a model $\mathcal{M}$, is indicated as $p'(W \mid \mathcal{M})$. Weights given a model $\mathcal{M}$ and the observed data X are indicated as $p(W \mid X, \mathcal{M})$ [Gualandi *et al.*, 2016]. The higher the negative free energy, the higher the likelihood of the data under that model, and, therefore, the better that model is at explaining the data [Choudrey, 2002].

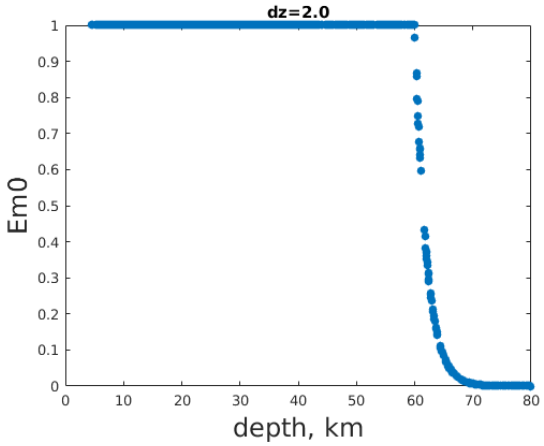

Figure 2-10: σ_m as a function of depth.

NFE decreases starting after 7 independent components. Therefore, I select 7 ICs to optimize the reconstruction of the dataset (Fig. 2-9). "Positivity" constraint is imposed on the 1st IC so that the inversion solves only for slip values with the rake between 0° and 180°. Smoothing parameters introduced in the model covariance matrix $\mathbf{C_m}$ (Eq. 2-6) are selected iteratively. Standard deviation of model parameters is set to vary from $\sigma_m = 0.063$ up till 60km depth to almost zero at maximum fault plane depth of 80km (Fig. 2-10). Optimal correlation length λ that controls the distance of the exponential decay is set to 80km. For selected smoothing parameters λ and σ_m minimum χ^2 is reached for tectonic angle (optimal inversion azimuth) of 243° counterclockwise from the East. The selection of above mentioned parameters is described in Supplemetary Material (Fig. D-1).

Fault geometry is defined by Slab2.0 [Hayes *et al.*, 2018] model for the Mexican subduction zone that includes the flat section of the slab approximating it in the Guerrero Gap. [Kazachkina *et al.*, in process].

2.3.2 Treatment of co- and post-seismic signals

One of the challenges of inverting time series for certain time intervals is to resolve the complex nature of the simultaneous physical phenomena recorded in the signal. Significant portion of the SSE signal is overlapped in time, and mixed together with the postseismic deformation generated by the three large earthquakes: 08/09/2017 M_w8.2 (Chiapas-Tehuantepec), 19/09/2017 M_w7.1 (Puebla-Morelos), and 16/02/2018 M_w7.2 in the Pinotepa area. Coseismic offsets from these three events are removed by averaging position estimates before and after the event over 3 days. These results are then compared with the predicted surface displacements due to a finite rectangular source in an elastic half space using Okada [1985] formulation in F. Beauducel's Okada85 Matlab code Appendix B (Fig. B-1). The parameters (epicenter location, depth and magnitude) that gave the best fit between observed (removed from GPS time series) and modeled displacements were taken from SSN report for Puebla-Morelos earthquake, from Guo *et al.* [2019] for Tehuantepec earthquake, from Geoscope catalog `http://geoscope.ipgp.fr/index.php/en/catalog/236-catalog-of-earthquakes-in-2018` for Pinotepa earthquake.

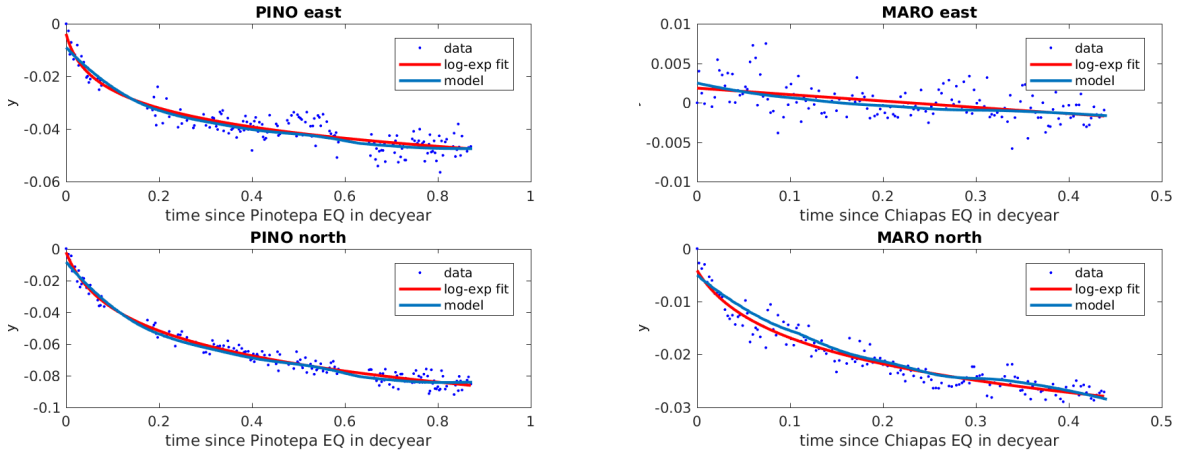

(a) (b)

Figure 2-11: Postseismic signals obtained with the ICAIM for Chiapas and Oaxaca EQs at PINO and MARO GPS stations. Blue dots are data; red curve –postseismic deformation approximated with logarithmic and exponential functions; blue curve –modeled postseismic deformation extracted with ICA decomposition.

The postseismic deformation is removed using the ICA decomposition similar to [Gualandi

et al., 2016] for one independent component with initial time corresponding to each of the seismic events. Postseismic signal was removed for subnetworks of GPS stations affected by (1) Tehuantepec and (2) Pinotepa earthquakes. Puebla-Morelos event didn't produce observable postseismic change in the GPS time series. The acquired postseismic signal is well approximated by a combination of logarithmic and exponential functions (Fig. 2-11) using the formulation of Altamimi *et al.* [2016]. This approximation serves as proof that the signal extracted from the original time series indeed corresponds to postseismic deformation that normally follows logarithmic or log-exponential decay.

Chapter 3

Results

3.1 Results of the Independent Component Analysis Inversion Method

3.1.1 ICA decomposition of the dataset

A network of 57 stations with time series detrended and corrected for co- and post-seismic deformation is used in the decomposition analysis. As described in the Subsection 2.3.1 the optimal number of independent components that satisfies the negative free energy (NFE) criterion is seven. The spatial and temporal vectors corresponding to each IC are plotted in Fig. 3-1. The first 3 components have the biggest amplitude that is shown by the eigenvalues (S_i). The combination of these three ICs characterizes the dominant signal of the dataset that is the slow slip events in Guerrero and Oaxaca. IC6 shows a notable unidirectionality of horizontal and vertical components of its spatial vectors. Therefore, this independent component likely stands for the common mode error and can be removed from the analysis. However, the respective amplitude of the IC6 is quite low compared to other components and its impact on the final results is insignificant.

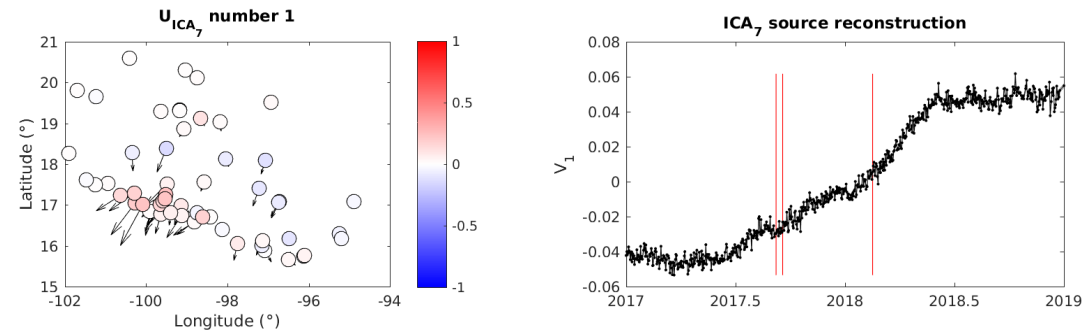

(a) S1 = 2359.37861

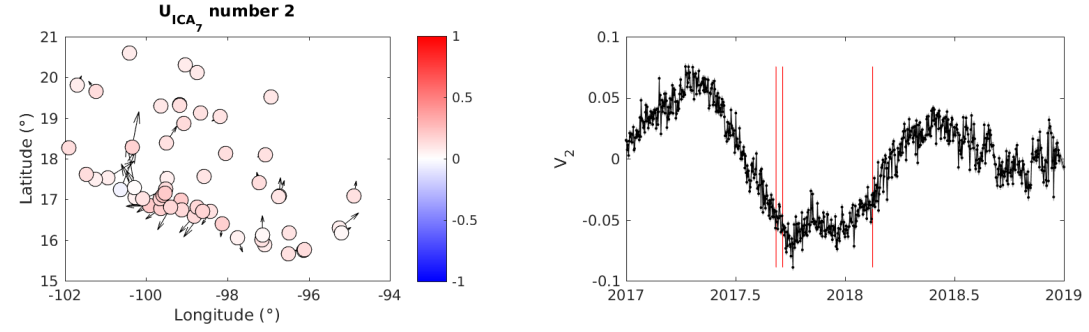

(b) S2 = 1162.816438

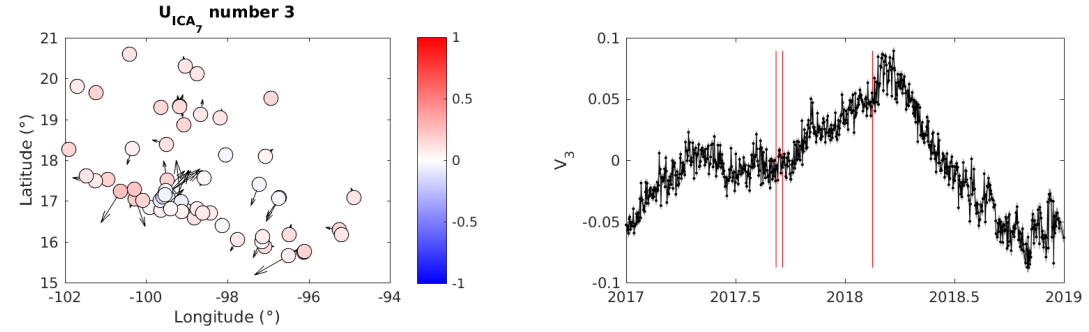

(c) S3 = 759.918499

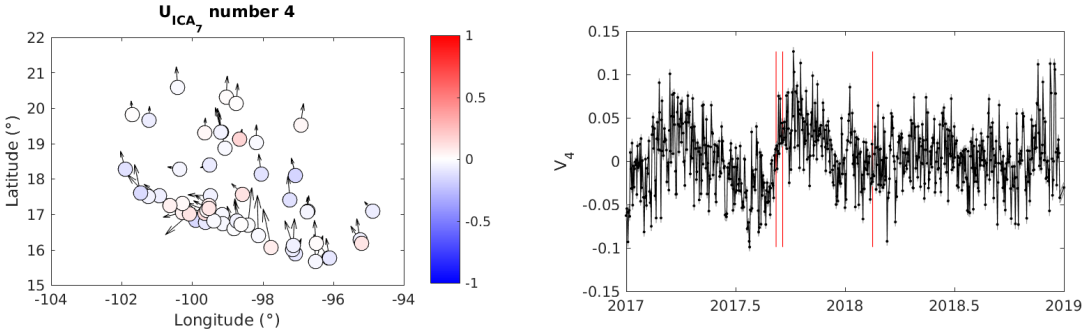

(d) S4 = 273.1533176

Figure 3-1: Seven ICs extracted from the dataset with ICA decomposition. Left: the spatial vectors corresponding to each IC, black arrows indicate horizontal motion, colorbar shows normalized vertical motion at each station (blue - downwards, red - upwards). Right: corresponding temporal evolution, vertical red lines mark Tehuantepec, Puebla and Pinotepa earthquakes. S-values correspond to IC amplitudes.

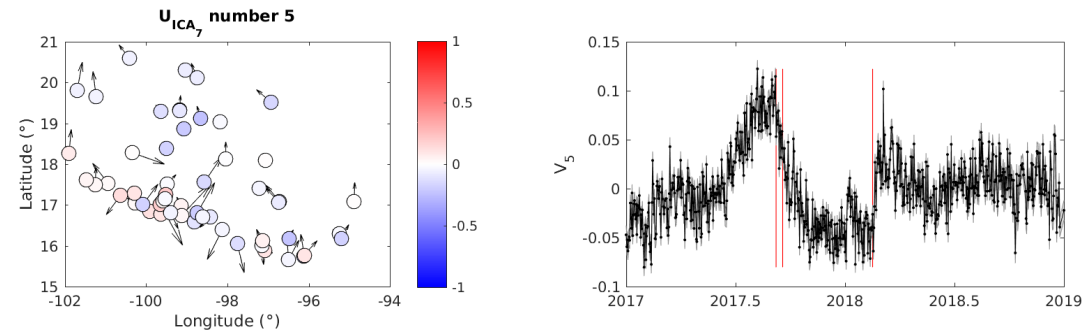

(e) S5 = 237.5478936

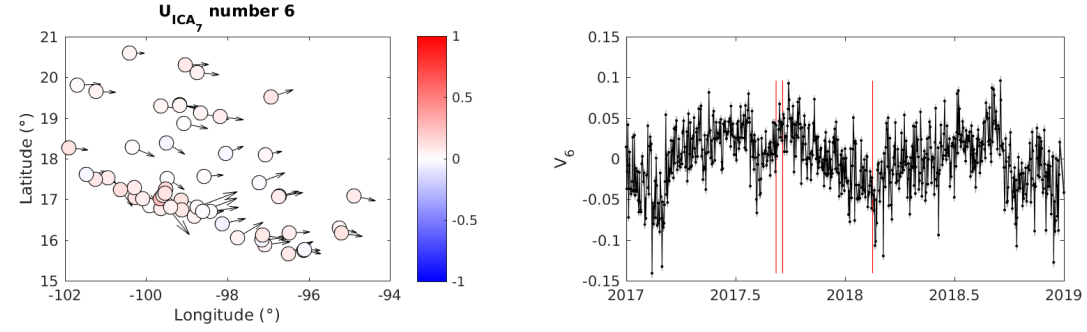

(f) S6 = 307.120713932

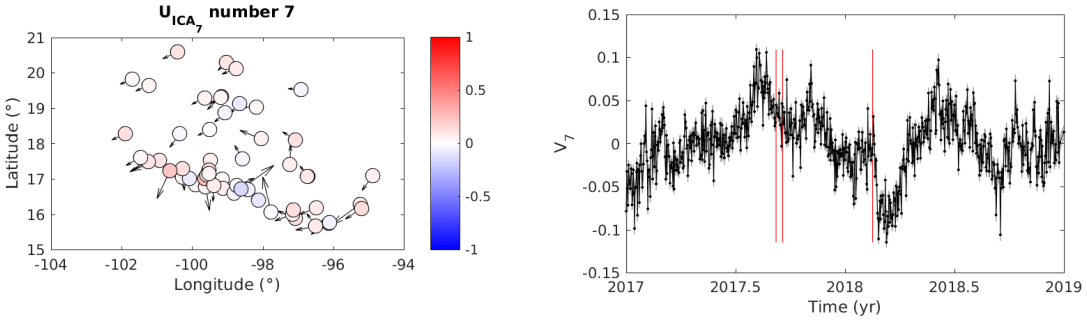

(g) S7 = 263.9661146

Figure 3-1: Seven ICs extracted from the dataset with ICA decomposition. Left: the spatial vectors corresponding to each IC, black arrows indicate horizontal motion, colorbar shows normalized vertical motion at each station (blue - downwards, red - upwards). Right: corresponding temporal evolution, vertical red lines mark Tehuantepec, Puebla and Pinotepa earthquakes. S-values correspond to IC amplitudes.

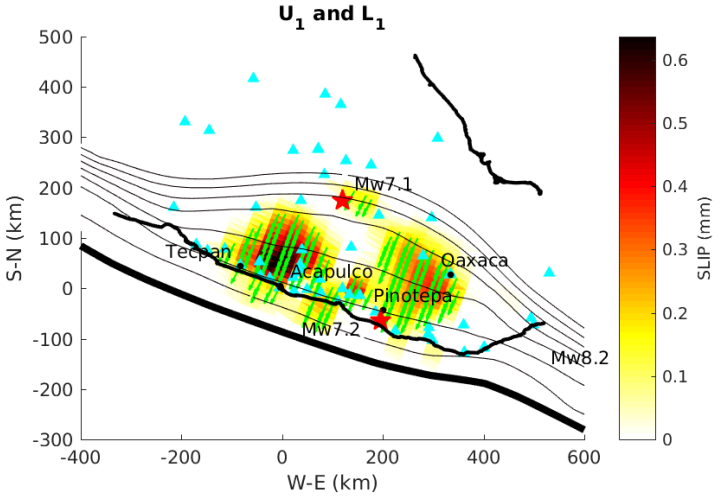

(a)

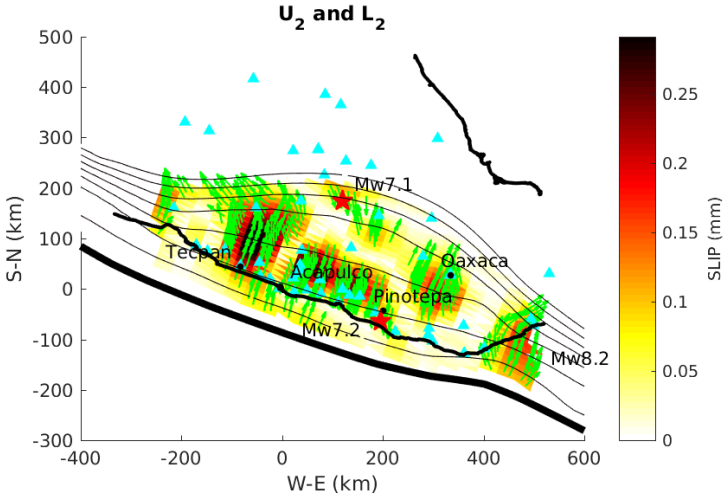

(b)

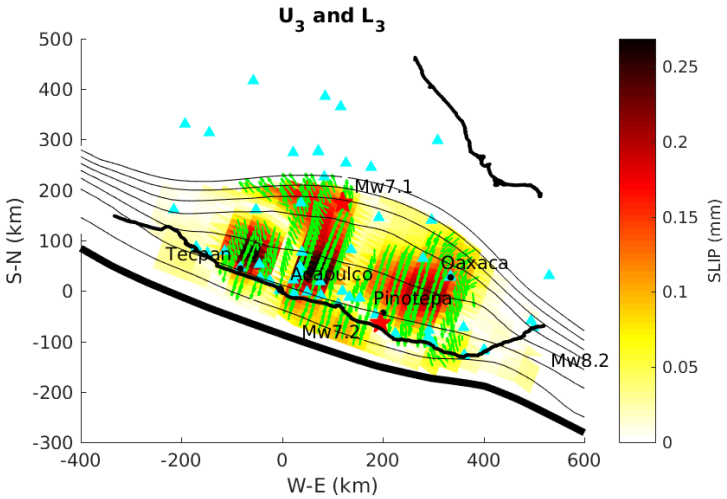

(c)

Figure 3-2

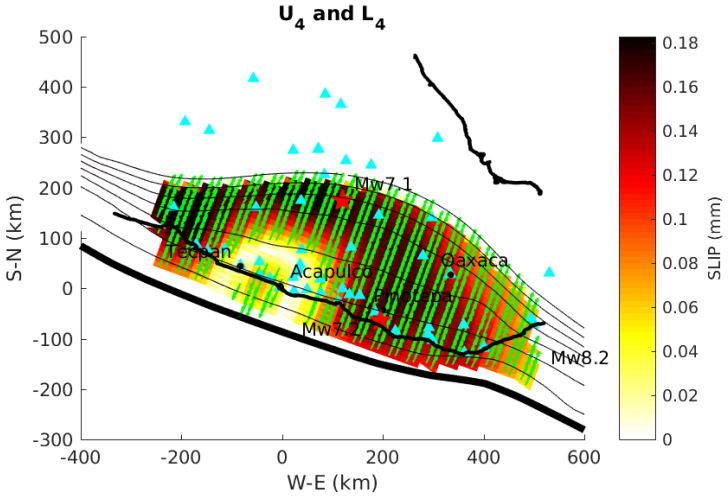

(d)

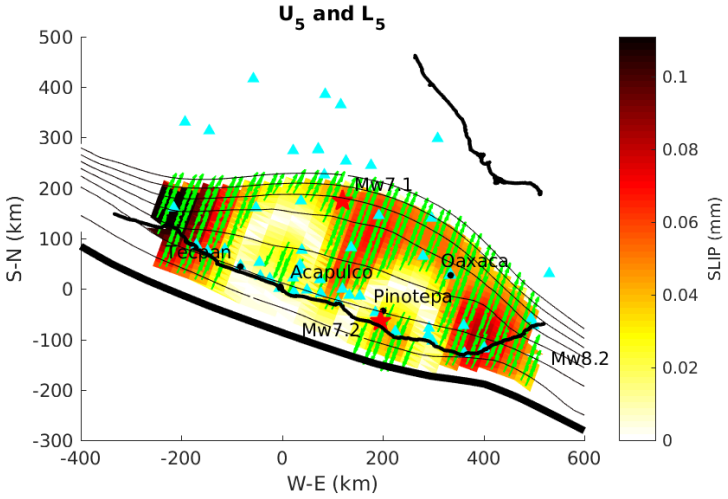

(e)

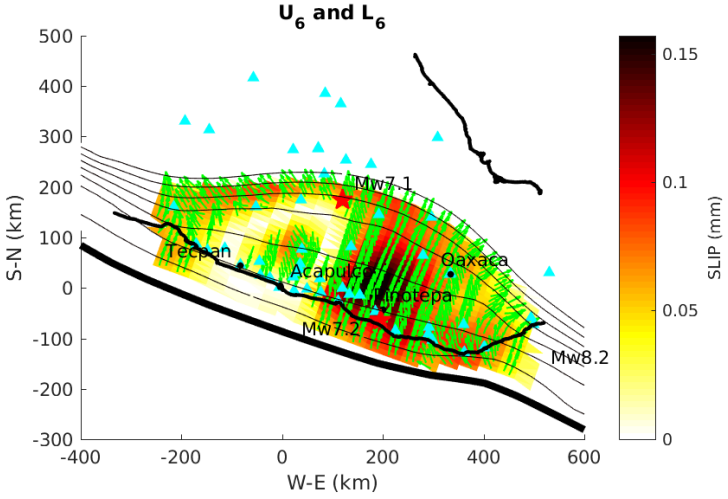

(f)

Figure 3-2

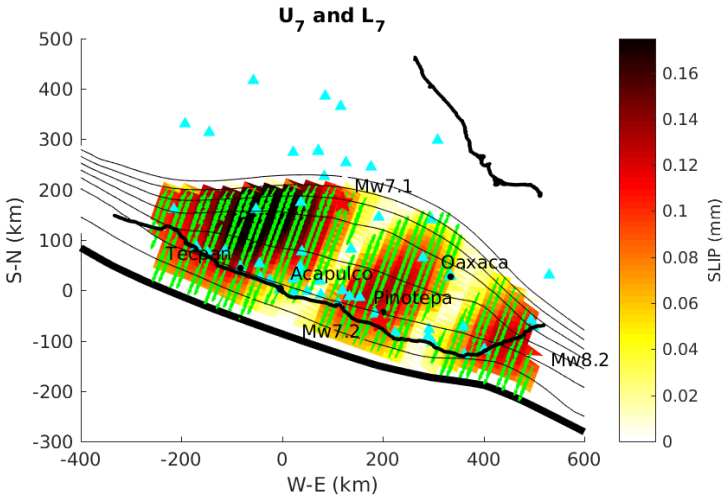

(g)

Figure 3-2: Slip distribution at the plate interface produced by each independent component. Blue triangles are GPS stations used in the ICA analysis. Green vectors are slip directions at each triangular patch at the fault interface. Thin black lines are isodepth contours. Red stars are earthquake epicenters. IC1 (3-2a) describes the major portion of slip due to SSEs.

Each independent component is then inverted for the slip on the fault (Fig. 3-2). It is clear that the IC1 has the highest slip amplitude and it accounts for the dominant SSE deformation observed in the GPS time series. The rest of the independent components contribute significantly smaller portions of slip to the Guerrero and Oaxaca SSE patches.

3.1.2 Pinotepa earthquake postseismic slip distributon

The slip produced by the Pinotepa earthquake is modeled using ICAIM (Fig. 3-3). M_w7.2 Pinotepa earthquake near Pinotepa Nacional in Oaxaca was a thrust event on the subduction interface [Fielding *et al.*, 2018]. The epicenter of this event is located at -98.03°E, 16.25°N at the border of the SSE patch.

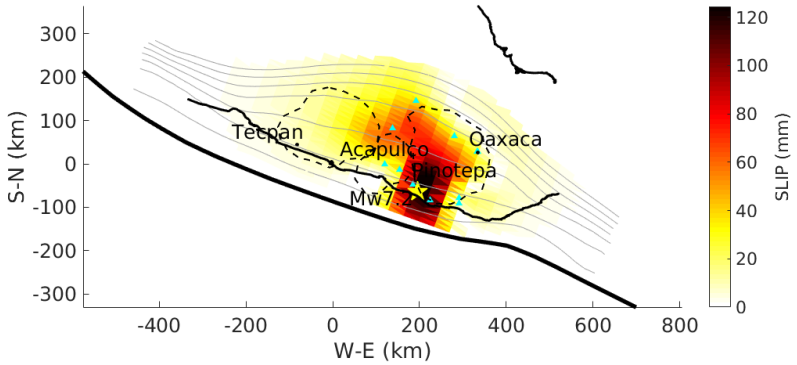

Figure 3-3: Postseismic slip distribution due to Pinotepa earthquake. Star denotes the earthquake epicenter. Blue triangles are GPS stations used in the inversion for postseismic deformation. Black dashed lines mark 2017-2019 SSE patches in Guerrero, Oaxaca and intermediate zone.

For the purposes of further analysis the dataset should be free from other dominant signals except for the SSE. In this work I assume that after the earthquake the postseismic signal dominates the time series at the nearest stations. Therefore, to extract the postseismic signal from the dataset I choose a subnetwork of 11 stations located close to the epicenter with observable afterslip trend. The part of time series after the 2018 February, 16 Pinotepa earthquake was selected and used in the ICA decomposition for one independent component representing the most prominent deformation. The removed afterslip signal is described in the Subsection 2.3.2 (Fig. 2-11). Resulting IC obtained after the decomposition is subtracted from the dataset. Postseismic signal produced by the Pinotepa earthquake is then separately inverted for the slip distribution on the subduction interface (Fig. 3-3).

3.1.3 Chiapas earthquake postseismic slip distribution

Chiapas earthquake occurred on September 8, 2017 and had a magnitude of M_w8.2. This normal faulting earthquake ruptured within the subducting Cocos Plate ~70km landward from the Middle American Trench beneath the Tehuantepec gap [Ye *et al.*, 2017]. The epicenter of this event is located by USGS at -93.94°E, 14.94°N. The rupture likely broke through the entire lithosphere of the young subducted slab in response to downdip slab pull [Ye *et al.*, 2017].

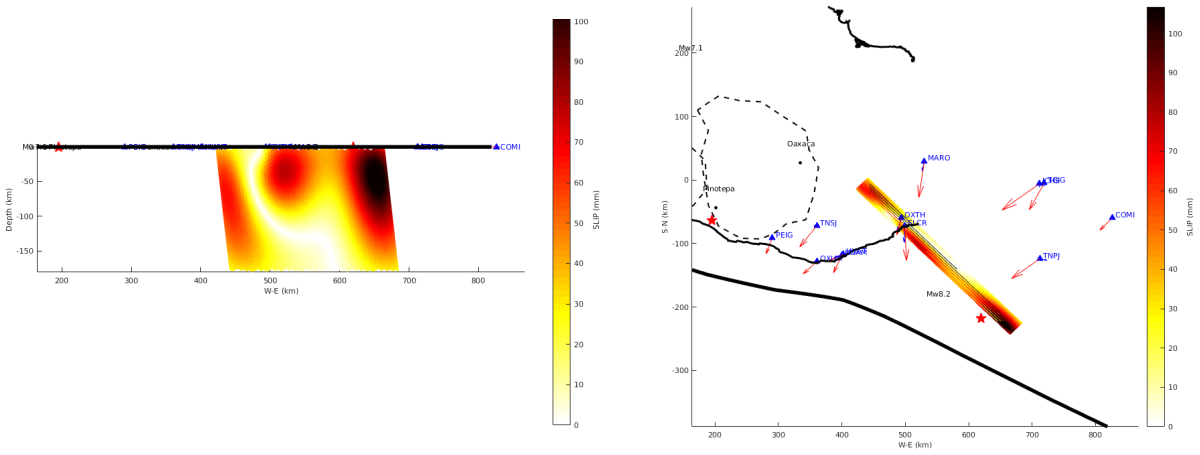

(a) (b)

Figure 3-4: Postseismic slip distribution for Chiapas earthquake. Blue vectors indicate model, red vectors –data; blue triangles are GPS stations used in the inversion; thick black line shows the location of the Middle America Trench.

Postseismic deformation produced by the Chiapas earthquake affected the geodetic time series of a number of stations used in the analysis of the Guerrero and Oaxaca SSEs. Therefore, it was decided to extract the afterslip signal as a strategy to obtain time series that only contain the information about the slow slip events of 2017-2019. Similar to the Pinotepa event a subnetwork of 13 sites affected by the Chiapas postseismic slip was selected. ICA for one independent component was applied to decompose the dataset. The obtained IC was compared to the log-exponential function and after removed from the time series [Altamimi *et al.*, 2016].

In order to check whether the removed signal can explain the afterslip around the mainshock the extracted part of the time series was inverted. The fault is approximated by a rectangular plane extended from the Guo *et al.* [2019] solution. Fault parameters are: strike = 311°, dip = 77°, rake = -103.8°, depth = 97.4km. The resulting postseismic slip distribution is shown in Fig. 3-4.

Finally, all three modeled signals - SSE in Guerrero and Oaxaca, postseismic deformation due to Chiapas and Pinotepa earthquakes - were combined and inverted in order to see how well the selected model fits the data. The figure of slip distribution obtained with reconstructed dataset is attached in Appendix G (Fig. G-1).

3.1.4 Slow Slip Events in Guerrero and Oaxaca

Once the postseismic signals produced by the Chiapas and Pinotepa earthquakes were removed then the resulting time series were inverted for the slip distribution during the SSEs of 2017-2019 (Fig. 3-5).

Inversion results locate two main patches of slip on the subduction interface. The Guerrero patch shows maximum slip of 140mm (check the colorbar in the plot) to the north of Acapulco. Comparison to previous SSEs in Guerrero (Table 3-1) shows that the event of 2017-2019 is most similar to the one of 2009-2010. Both SSEs occurred in two stages (Fig. 3-6), SSE parameters (Table 3-1) such as the location of the slip on the subduction interface along strike and along dip add to similarities between the two events.

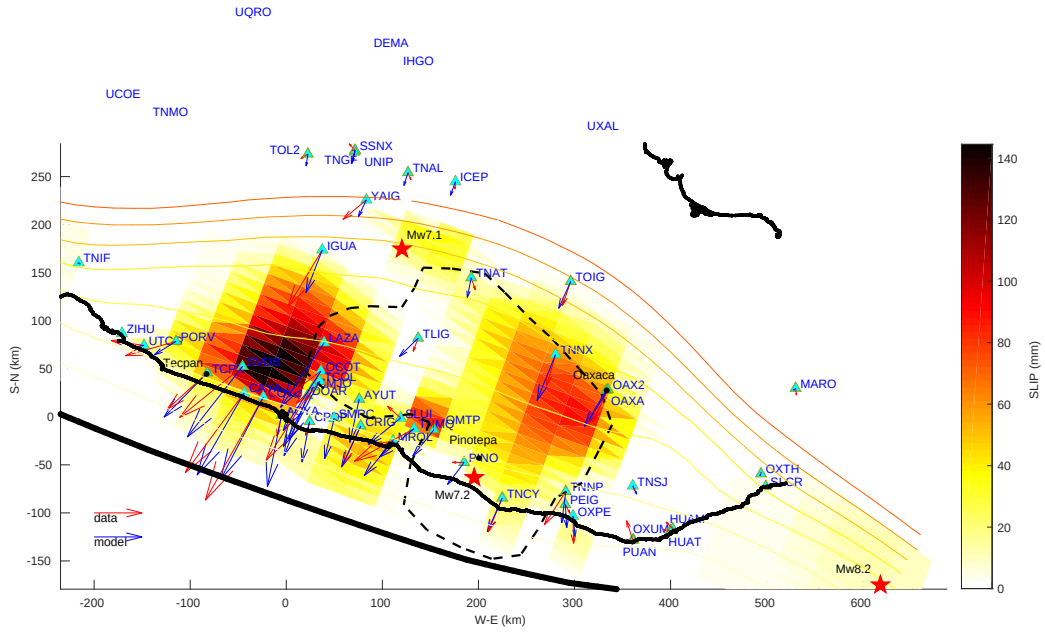

Figure 3-5: Slip distribution at the subduction interface produced by the 2017-2019 slow slip event sequence. Blue triangles are the GPS stations, red stars - earthquake epicenters, black dashed line denotes the contour of Pinotepa postseismic slip, thin yellow to orange lines are isodepth contours of the subducting Cocos plate.

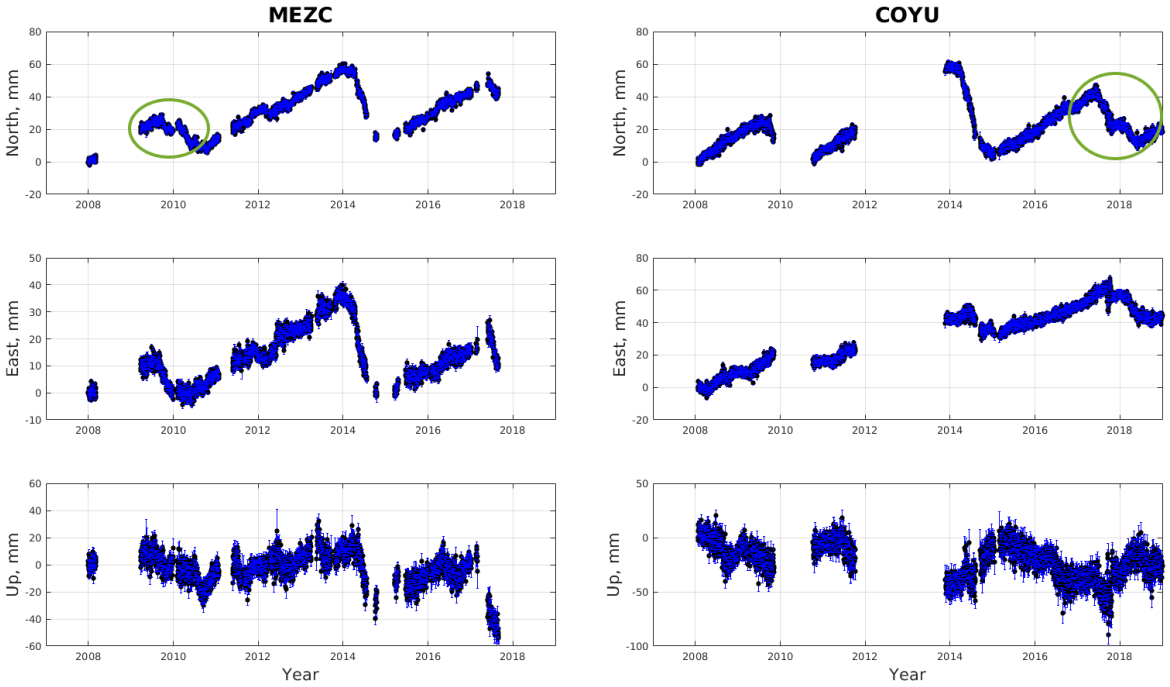

(a) (b)

Figure 3-6: Position time series for GPS stations in Guerrero (a) in Mezcala and (b) in Coyuca. Green ellipses mark the SSEs of 2009/10 and 2017/18 with similar 2-stage pattern.

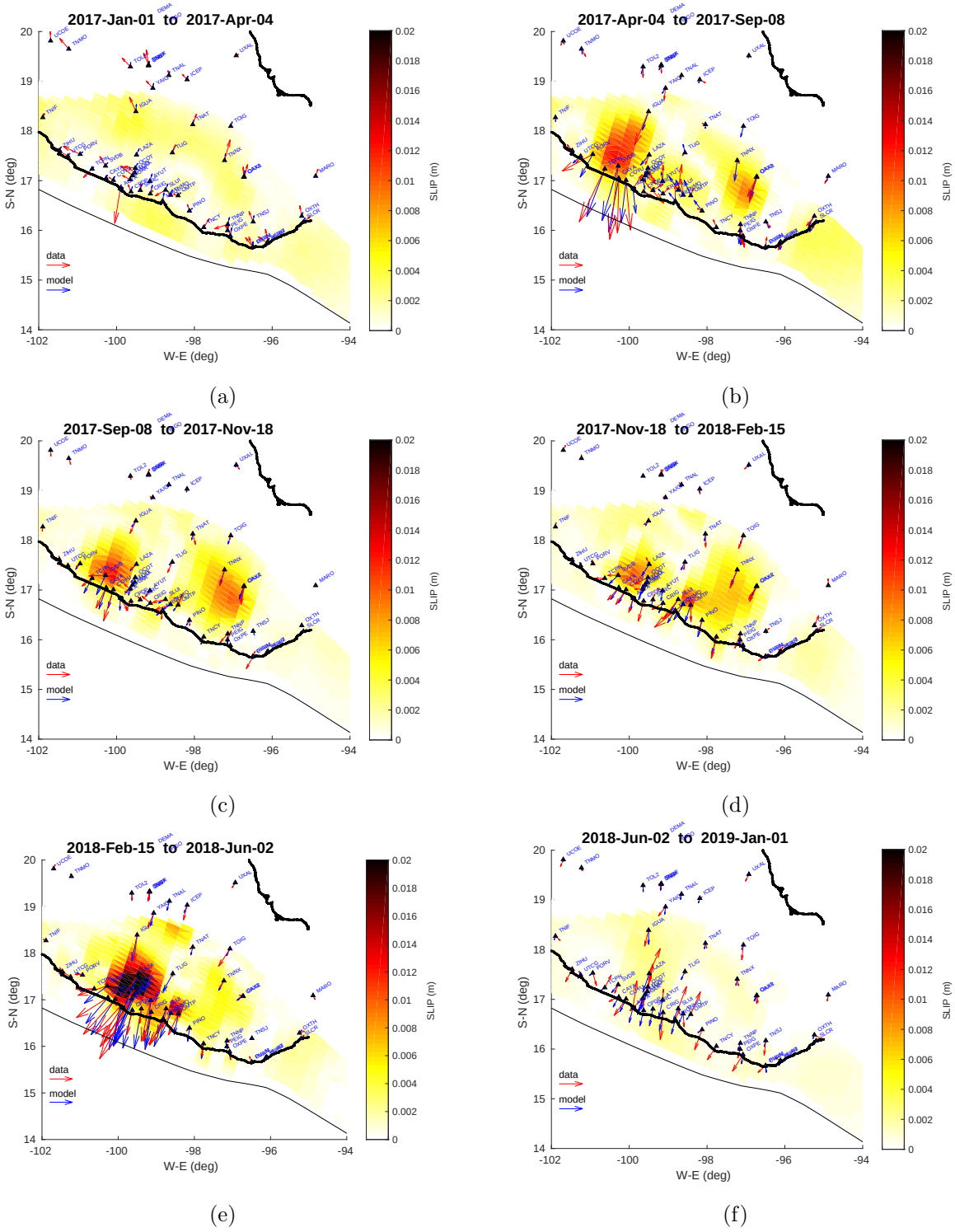

Figure 3-7: History of slip evolution at the subduction interface during 2017-2019 SSE sequence.

	SSE	Location along strike	Location downdip (km)	Duration in months	Max slip amplitude (mm)	Equivalent magnitude (M_w)	Migration direction	Source
GUERRERO	2001/02	∼99° to ∼101.5°W	20 to 50	9	200	7.65	N/A	Radiguet et al., 2012
	2006	∼98.5° to ∼102°W	20 to 45	∼8	270	7.3	N108E	Graham et al., 2015
	2009/10	∼99° to ∼102°W	20 to 45	∼12	280	7.4	N108E	Graham et al., 2015
	2014	∼99° to ∼101.7°W	20 to 65	∼11	250	7.6	N/A	Radiguet et al., 2016
	2017/19	∼99° to ∼101.5°W	20 to 45	∼13	200	7.6	N/A	current study
OAXACA	2004	∼97.5° to ∼101.5°W	∼30	4	115	7.3	N/A	Correa-Mora et al., 2008
	2005/06	∼96.5° to ∼98.5°W	∼18 to 45	∼6	120	7.1	N120E	Graham et al., 2015
	2007	∼96.5° to ∼97.5°W	centered at 30	∼5	80	6.5	N/A	Graham et al., 2015
	2008/09	∼97° to ∼98.5°W	∼30 to 45	∼6	120	7.2	N140E	Graham et al., 2015
	2010/11	∼97° to ∼98.5°W	centered at 40	∼6	120	7.2	N180E	Graham et al., 2015
	2011/12	∼95.5° to ∼98°W	20 to 40	5	105	6.9	N36W	Graham et al., 2014a
	2017/18	∼96.5° to ∼98°W	∼18 to 45	9	120	7.3	N/A	current study

Table 3-1: Comparison of Guerrero and Oaxaca SSE parameters through the observation period.

The Oaxaca SSE patch shows slip that propagates from the city of Oaxaca southwest towards Pinotepa with maximum amplitude of the cumulative slip of 80mm (check the colorbar in the plot). The SSE starts approximately in May 2017 and after four months it gets interrupted by two large earthquakes. The time series trend returns to its interseismic mode by February-March 2018. However, the observed deformation at the end of the SSE is mixed with the postseismic signal from the Pinotepa and Chiapas earthquakes making it difficult to determine the end of the slow slip event. The 2017/2018 Oaxaca SSE lasted for about 9 months and appears to be the longest among the previously observed slow transient events in that area (Table 3-1).

Fig. 3-7 shows the slip evolution in time windows selected with respect to the Chiapas and Pinotepa earthquakes and the slow slip episodes (two stages in Guerrero and one stage in Oaxaca). It is observed that Guerrero and Oaxaca slow slip events begin simultaneously. Guerrero SSE propagates from northwest near ARIG station towards Acapulco in the southeast.

3.2 La Venta Chacalapa fault system

3.2.1 Active 650-km Long Fault System and Xolapa Sliver in Southern Mexico

La Venta Chacalapa fault system still keeps many unknowns in terms of its trace, geometry, seismicity, recurrence periods. The article by [Kazachkina *et al.*, 2020] provided below is a compilation of available observations including geology, seismicity, bathymetry and geodesy that gives a rather complete description of this geological feature in the South of Mexico up to date.

frontiers in Earth Science

ORIGINAL RESEARCH
published: 16 June 2020
doi: 10.3389/feart.2020.00155

Active 650-km Long Fault System and Xolapa Sliver in Southern Mexico

Ekaterina Kazachkina[1], Vladimir Kostoglodov[1], Nathalie Cotte[2], Andrea Walpersdorf[2], Maria Teresa Ramirez-Herrera[3], Krzysztof Gaidzik[3,4], Allen Husker[1] and Jose Antonio Santiago[1]*

[1] Instituto de Geofisica, Departmento de Sismología, Universidad Nacional Autónoma de México, Ciudad Universitaria, Mexico City, Mexico, [2] Université Grenoble Alpes, Université Savoie Mont Blanc, Centre National de Recherche Scientifique, Institut de Recherche pour le Développement, Institut Français des Sciences et Technologies des Transports, de l'Aménagement et des Réseaux, Institut de Sciences de la Terre, Grenoble, France, [3] Laboratorio de Tsunami y Paleosismología, Instituto de Geografía, Universidad Nacional Autónoma de México, Ciudad Universitaria, Mexico City, Mexico, [4] Institute of Earth Sciences, University of Silesia, Sosnowiec, Poland

New estimates of long-term velocities of permanent GPS stations in Southern Mexico reveal that the geologically discernible ∼650-km long shear zone, which strikes parallel to the Middle America trench, is active. This left-lateral strike-slip, La Venta–Chacalapa (LVC) fault system, is apparently associated with a motion of the Xolapa terrain and at the present time is the northern boundary of a ∼110–160-km wide forearc sliver with a sinistral motion of 3–6 mm/year with respect to the North America plate. This sliver is the major tectonic feature in the Guerrero and Oaxaca regions, which accommodates most of the oblique component of the convergence between the Cocos and North America plates. Previous studies based purely on the moment tensor coseismic slips exceedingly overestimated the sliver inland extent and allocated its northern margin on or to the north of the Trans-Mexican Volcanic Belt. While the LVC fault system probably slips slowly over geologic scale time and there is not any historic evidence of large earthquakes on the fault so far, its seismic potential could be very high, assuming a feasible order of $\sim 10^3$ years recurrence cycle. A detailed analysis of long-term position time series of permanent GPS stations in the Guerrero and Oaxaca states, Southern Mexico discards previous models and provides clear evidence of an active LVC fault zone bounding the Xolapa forearc sliver. The southeastward motion of this sliver may have persisted for the last ∼8–10 Million year and played an important role in the tectonic evolution of the region.

Keywords: fault system, oblique subduction, sliver motion, tectonics, GPS, earthquake slip

OPEN ACCESS

Edited by:
Jeroen Van Hunen, Durham University, United Kingdom

Reviewed by:
Bernard Mercier De Lépinay, Centre National de la Recherche Scientifique (CNRS), France
Luis E. Lara, Servicio Nacional de Geología y Minería de Chile (SERNAGEOMIN), Chile

****Correspondence:***
Ekaterina Kazachkina
kazachkina@igeofisica.unam.mx

Specialty section:
This article was submitted to Structural Geology and Tectonics, a section of the journal Frontiers in Earth Science

Received: *01 February 2020*
Accepted: *27 April 2020*
Published: *16 June 2020*

Citation:
Kazachkina E, Kostoglodov V, Cotte N, Walpersdorf A, Ramirez-Herrera MT, Gaidzik K, Husker A and Santiago JA (2020) Active 650-km Long Fault System and Xolapa Sliver in Southern Mexico. Front. Earth Sci. 8:155. doi: 10.3389/feart.2020.00155

INTRODUCTION

The existence of a forearc sliver with contemporary sinistral motion with respect to the stable North America plate (wrt NA) should be expected as a result of the strain partitioning produced by oblique subduction of the Cocos plate (CO). Geological studies indicate the sinistral transpression during Late Cretaceous to Early Tertiary in the coastal area of the present-day southern Mexico (Cerca et al., 2007). Significant left-lateral strike-slip motion characterized by the mylonitization of the Xolapa metamorphic complex (Campa and Coney, 1983) was dated as Early Eocene in the La Venta

(Solari et al., 2007) and as Oligocene in the Chacalapa shear zones (Tolson, 2005). Nonetheless, there was not any evidence of the ongoing tectonic activity on the La Venta–Chacalapa (LVC) fault system (Ramírez-Herrera et al., 2018) or on other trench-parallel faults in the central Mexico, except the Central Trans-Mexican Volcanic Belt (TNVB; Suter et al., 1992).

Sliver models (e.g., McCaffrey, 1992) provide simple methods to appraise the forearc deformation and relative sliver velocity using slip vectors of shallow subduction thrust earthquakes. Nevertheless, these models are unable to restrict the geometry and location of strike-slip fault zones bordering slivers. One attempt to use this technique for the subduction zone in central Mexico was the study of Ego and Ansan (2002). Using focal mechanisms of thrust earthquakes corresponding to the seismogenic segment of the plate interface they considered the left-lateral slip rate of the forearc to be less than 8 mm/year. As the only known active E–W fault zone with left-lateral transtensive deformation was in the Central TNVB, the northern limit of the forearc sliver has been assigned to this fault zone, which is located as far as ∼350–380 km from the Middle America trench (MAT). A further study by Andreani et al. (2008), proposed that this sliver, the so-called "Southern Mexico Block," undergoes a counterclockwise rotation wrt NA and may be not related to oblique subduction.

To ascertain that the LVC fault system is tectonically active and represents the northern boundary of the forearc Xolapa sliver in Southern Mexico we analyzed continuous GPS data collected since 1997 at permanent GNSS networks in the Guerrero and Oaxaca areas. Long-term GPS velocities definitely indicate a left-lateral strike-slip motion across the fault zone with the rate of 3–6 mm/year. This result agrees with revised estimates of the sliver speed obtained from slip vectors of the subduction thrust earthquakes. An overall stretching of the forearc of ∼40 km between the Michoacan and Guerrero regions may be produced by a relative to the Michoacan sinistral retreat of the Xolapa sliver. Supposing that the Cocos–North America convergence conditions have not radically changed since the Late Miocene time, the reactivation of the LVC fault system could have occurred some ∼8–10 Ma ago.

DATA AND ANALYSIS

GPS Observations

The data used in this study (**Figure 1**) are 5–16 years of continuous measurements on the permanent GPS stations operated by the Instituto de Geofísica, UNAM, and one station, TOL2, of the Instituto Nacional de Estadística y Geografía, INEGI. To establish the reference frame ITRF2008 (Altamimi et al., 2011) we added also the data from several global IGS (International GNSS Service) GPS stations. The total GPS dataset was processed with the GAMIT-GLOBK software (version 10.60, Herring et al., 2015). Modeling of environmental effects on the GPS measurements (see Vergnolle et al., 2010) decreased notably the noise in the position time series. Years-lasting GPS observations are essential in the presence of periodic signals (e.g., Blewitt and Lavallée, 2002) to estimate secular tectonic deformations and velocities. This is of particular importance in the Guerrero and Oaxaca areas, where large subduction slow slip events (SSE) are happening regularly, about every 4 and 1 year, respectively (e.g., Cotte et al., 2009; Graham et al., 2016).

For several GPS stations in the Michoacan state we used already processed position time series from the Tlalocnet network, downloaded from the UNAVCO[1].

Secular GPS velocities, V_S, were calculated by weighted least-square linear fit to the time series at each station. To avoid the effect of recent large subduction thrust earthquakes, we subtracted beforehand corresponding coseismic displacements of the 2014 Papanoa, Mw 7.3 event (Unam_Seismology_Group, 2015) from the time series in Guerrero and truncated the Oaxaca time series by the date of the 2012 Ometepec, Mw 7.5 earthquake (Unam_Seismology_Group, 2013). **Figure 2** demonstrates an example of linear fits to the CAYA northern time series affected by several large quasiperiodic SSEs. Of course, in this extreme case the SSEs produce very large displacements and resulting V_{SN} value varies within some ∼10% depending on the end bound of the fitting window. For the Oaxaca time series, an effect of the SSE on the V_S is relatively smaller because of slow events smaller displacement and their shorter recurrence period.

The trench-parallel component of secular velocity, V_{SS}, rests on an assessment of the trench normal azimuth, *T*n, at each location of GPS station. The shape of the MAT is arc-curved and may be approximated by a few segments of small circles on a spherical Earth (Guzman-Speziale, 1995). Using this approach, we selected four successive sections of the MAT with approximately consistent curvatures and fitted each of those to a small circle (**Supplementary Figure A1**). Thus, the pole of best fitting small circle is the center of curvature of the trench section (**Supplementary Table A1**). The azimuth of big circle passing through this pole and a location point of GPS station corresponds to the *T*n. The trench normal at each station is calculated according its location in a sector of corresponding small circle (see **Table 1** and **Supplementary Figure A1**). By applying the same method, it is possible to define the obliquity angle variation along the MAT as the angle between plate convergence direction (we used PVEL Cocos-North America plates model, DeMets et al., 2010) and trench normal (**Figure 3**). The obliquity in Guerrero and Oaxaca segment of the MAT is relatively higher (10°–15°) than in Michoacan and Chiapas, where it is close to ∼0° in average.

All V_S and V_{SS} vectors are plotted in **Figure 1**, where an abrupt reduction of secular trench-parallel velocity, V_{SS}, is obvious from south-west to north-east, across the LVC fault zone, especially in Guerrero, with a broader coverage of the GPS network. To reveal a tectonic significance of the LVC fault zone, we projected V_{SS} amplitudes onto a general profile perpendicular to the MAT (**Figure 4**). As it is seen in **Figure 4**,

[1]https://www.unavco.org/instrumentation/networks/status/tlalocnet

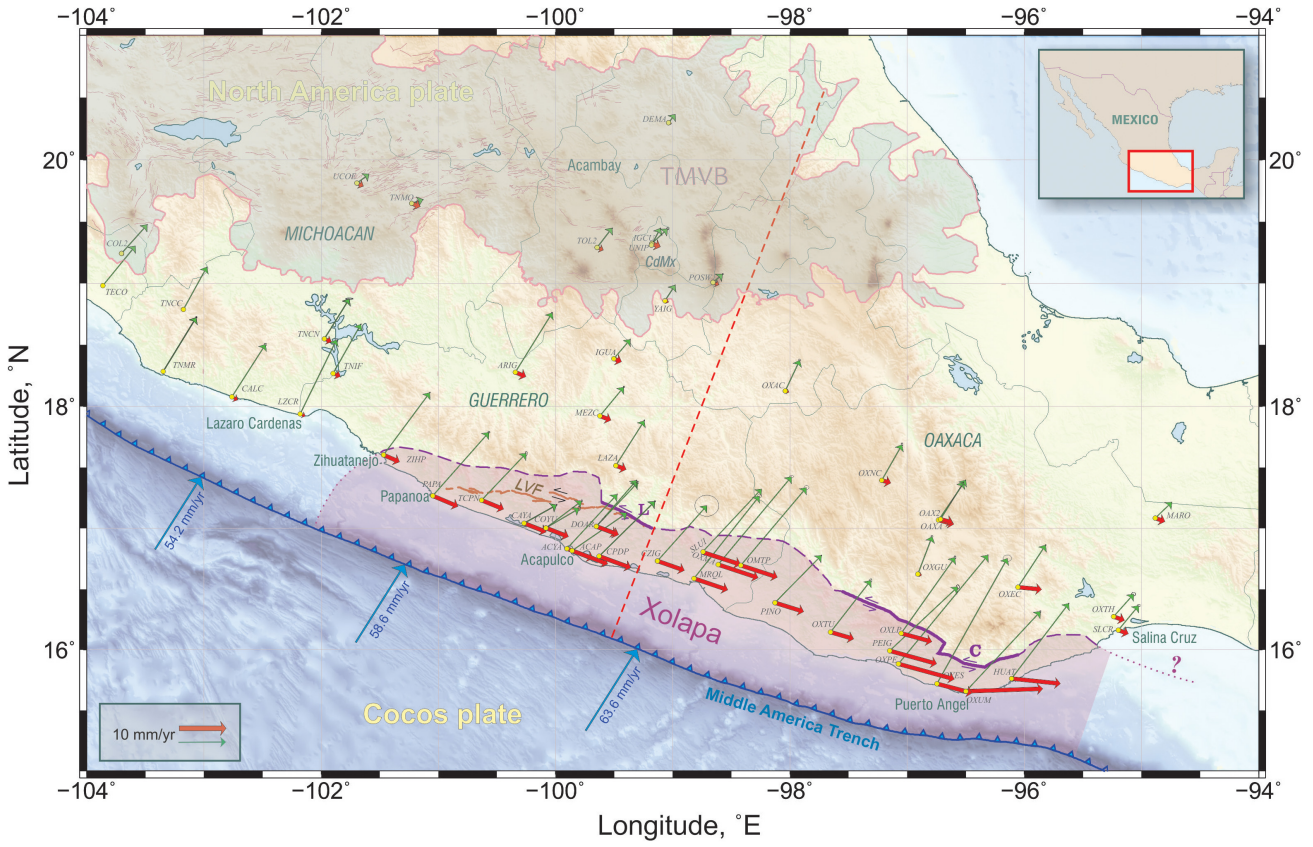

FIGURE 1 | The study area (Inset) and location of permanent GPS stations (small yellow circles). Secular GPS velocities (wrt North America plate, mm/year) are shown as green vectors, and red vectors are their oblique components (parallel to the MAT). The solid-dashed purple line delineates the La Venta–Chacalapa (LVC) fault zone according to Tolson (2005). *L*, La Venta segment (Solari et al., 2007). *C*, Chacalapa segment (Tolson, 2005). The segmented dark brown line is a trace of the LVF according to Gaidzik et al. (2016). An abrupt decrease of the secular oblique velocity is noticeable across the LVC fault zone (Ramírez-Herrera et al., 2018), which is roughly the northern border of the Xolapa allochthonous terraine (XOLAPA, shaded area located between the MAT and the LVC). Blue vectors are the Cocos–North America PVEL convergence velocities (DeMets et al., 2010) at the MAT. The red dashed line normal to the MAT specifies the horizontal axis of a cross-section shown in **Figures 2**, **3**. The gray shaded region to the north of 19°N shows the Trans Mexican Volcanic Belt (TMVB) with a dense E–W extended fault cluster [adapted from Ferrari et al. (2012)]. The fault sequence mapped close to the Acambay area is the northern margin of the sliver proposed by Ego and Ansan (2002).

the strain rate in Guerrero suddenly changes roughly from −93 to −4 nrad/year at approximately 100–120 km inland from the MAT, which is an average location of the LVC shear zone. At the same distance, the *V*ss diminishes by 2–5 mm/year in Guerrero and by more than 6 mm/year in Oaxaca. These velocity slumps may represent a partitioning of the oblique convergence between the Cocos and North America plates with a sinistral motion (wrt NA) of the forearc Xolapa sliver. Abrupt fault-parallel velocity change as a function of fault-perpendicular distance is a usual attribute of major active strike-slip faults (e.g., Smith and Sandwell, 2006; Alchalbi et al., 2010; Smith-Konter et al., 2011; Jolivet et al., 2015); thus, our observations suggest that the LVC fault area is tectonically active, at least during the GPS epoch.

There are not enough GPS stations to reliably model the LVC fault properties along all of its extent (**Figure 1**). The only fairly acceptable GPS covered area is in Guerrero, where the ∼450-km-long cross-section could be roughly appraised using a simple screw dislocation model (Savage and Burford, 1973; Cohen, 1999) for the infinite vertical strike-slip fault (**Figure 5**). The modeled fits to the observed *V*ss data show strike-slip displacement on the surface produced by the creeping fault at the depth more than 10 km while its shallower section is locked. Of course, these models cannot constrain the fault coupling depth, but they highlight the slower strike-slip motion (∼3 mm/year) on the LVC fault zone within the Guerrero seismic gap compared to the adjacent areas (∼5 mm/year). This inconsistency may be related to the influence of periodic SSEs, which effectively reduce the long-term subduction plate interface coupling in the gap area (e.g., Radiguet et al., 2012).

Based on the variation of GPS sinistral secular velocities along the coast (**Figure 1**), the active LVC fault zone strikes off the Zihuatanejo city area, some ∼650 km eastward along the Pacific coast, and gets somewhere close to the Salina Cruz city on the land. A continuation of the LVC into the Guatemala basin

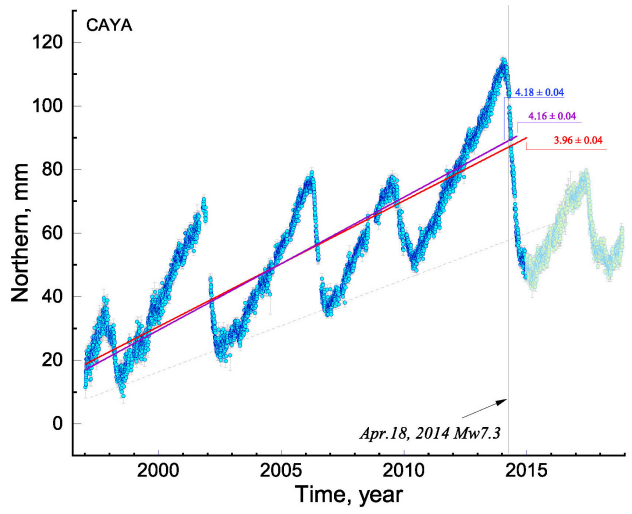

FIGURE 2 | Example of few linear fits to the CAYA northern time series. The resulting estimate of V_{SN} value depends on the selected time interval. To eliminate the impact of the Papanoa Mw 7.3 earthquake the fitting window closes just before the earthquakes starts.

remains problematic to trace as yet without detailed bathymetry and marine geophysics data.

Seismicity

Large historic strike-slip earthquakes are unknown in the continental crust along the entire length of the fault system. Only a few shallow and small magnitude earthquakes have probably occurred on it, according to the catalog of the National Seismological Service of Mexico (SSN). Just one well-documented normal type with a small strike-slip component, Mw 5.8, Coyuca earthquake, followed by numerous aftershocks, has been recorded on October 8, 2001 (Pacheco et al., 2002; Pacheco and Singh, 2010), on the reactivated sub-fault, south of the La Venta fault (LVF; **Figure 6**). This rare event occurred right after the large 2001 SSE that created a temporal extension of the forearc (Kostoglodov et al., 2003).

Seismic events hypocenters in the SSN catalog (1962–2015) do not have sufficient precision to make a definite conclusion on the LVC seismicity. **Supplementary Figure A2** shows only that the fault zone approximately coincides with the location where density of seismic events drops significantly to the north of the fault trace. The higher-precision catalog obtained from the local seismic network in the seismic gap of Guerrero [1.0 < Mc < 4.0, (Suárez et al., 1990)] may be used to examine the seismic activity of the LVC. Seismicity cross-sections perpendicular to the MAT show that this fault zone is mainly aseismic for the time span of the catalog (1987–1995; **Figure 6**). Very low seismicity on active faults needs to be explained. One of the plausible insights may be a the model of Lamb and Smith (2013), where the strike-slip fault is totally locked in the surface elastic layer during a long-lasting interseismic period and is thus behaving almost aseismically. This locked shallow patch of the fault produces a background secular linear surface strain trend of ∼4 nrad/year (see **Figure 4**). In the deeper part of the crust, beneath the locked fault zone, the fault is creeping on a narrow shear zone that produces an apparent near-fault geodetic signal, which depends on the maximum depth of the locked segment of the fault. This model may explain the total observed GPS surface displacements and a lack of seismicity on the LVC. Strain accumulation on the upper locked zone of the fault is relatively slow, ΔVss = 3–5 mm/year (**Figure 5**), which should lead to a long-lasting seismic cycle of the order of thousand years.

Recently reported local seismic swarms in the Oaxaca section of the LVC (Fasola et al., 2019) are apparently related to someway relocated fault. Still insufficient accuracy and precision of the local seismic catalog (Fasola et al., 2016) does not permit us to make a definitive conclusion on the seismic activity of the LVC.

LA VENTA–CHACALAPA FAULT TRACE MAPPING

The fault shape and its location are essential to analyze the stress pattern and appraise the elastic strain accumulation, which may finally be released seismically. The precise position of the LVC shear zone is unknown for most of its length. There are only two explored segments of this zone detected by geological studies, Chacalapa (Tolson, 2005) and La Venta (Solari et al., 2007)—C and L annotations accordingly in **Figure 1**. All published LVC fault configurations render a geologically depicted borderline of the Xolapa terrane (e.g., Cerca et al., 2007). Gaidzik et al. (2016), acquired and analyzed abundant structural field data in the western part of the Xolapa terrane (∼99°–101.3°W), and after a morphotectonic interpretation of 15-m resolution digital elevation model (DEM) and satellite images of the area, they could trace the superficial left-lateral strike-slip continuation of the La Venta fault zone (LVF in **Figure 1**). According to this study, the LVF is segmented with 4- to 8-km-wide compressional or extensional step-overs and its nearly E–W average trace crosses the coastline close to the town of Papanoa.

The westernmost segment of the fault is less well constrained. As the Zihuatanejo GPS (ZIHP in **Figure 1**) has a clear secular trench-parallel motion comparable to other GPS sites on the Xolapa sliver, we can assume that the active LVF extends up to that longitude of approximately −101.5°. An absence of GPS stations between LVF and LVC does not permit us to determine the northern limit of the Xolapa sliver, while the LVF trace is more reliable based on detailed study of Gaidzik et al. (2016). It is important to note that the Xolapa sliver is not identical to the geologically determined Xolapa complex (Ducea et al., 2004) or the same name terrain. The LVF location may be considered as a trace of active LVC fault system (Ramírez-Herrera et al., 2018) in western Guerrero mainly because the northern boundary of

TABLE 1 | Secular velocities of the GPS stations (V_{SE}, V_{SN}, east and north components accordingly, referenced to the fixed North America plate), and corresponding standard errors (σVs_E, σVs_N); trench parallel velocities (Vss) with standard errors (σVss) and azimuth of trench normal (ϑTn, clockwise from North); T1 and T2 are the start and end limits of the fitting time span, respectively.

Station (site)	Lon °E	Lat °N	V_{SE} mm/year	V_{SN} mm/year	σV_{SE} mm/year	σV_{SN} mm/year	V_{SS} mm/year	σV_{SS} mm/year	ϑTn °cw from N	T1 Year	T2 Year
ACAP	−99.857	16.822	11.64	7.99	0.02	0.05	8.10	0.04	−20.51	1999.92	2013.08
ACYA	−99.903	16.838	10.72	11.58	0.03	0.06	5.96	0.04	−20.59	2004.12	2014.28
ANIG	−104.521	21.054	0.94	1.67	0.03	0.02	−0.79	0.03	−53.97	2006.84	2014.93
ARIG	−100.344	18.281	7.86	12.63	0.05	0.06	2.43	0.05	−22.49	2009.88	2014.21
AYUT	−99.145	16.988	0.37	12.54	0.13	0.12	−3.91	0.13	−19.45	2010.34	2013.68
CALC	−102.762	18.079	7.19	11.20	0.08	0.11	1.40	0.09	−26.66	2007.94	2013.65
CAYA	−100.267	17.049	6.98	3.91	0.02	0.04	5.08	0.03	−21.35	1997.09	2014.28
CHAM	−105.045	19.498	5.11	10.07	0.03	0.03	−3.75	0.03	−46.26	2006.83	2014.72
COL2	−103.702	19.244	5.50	6.14	0.02	0.02	0.61	0.02	−37.66	2006.87	2014.97
COMI	−92.137	16.282	3.04	3.53	0.01	0.02	0.87	0.02	−30.01	2002.12	2014.91
COYB	−100.081	17.008	7.11	4.17	0.09	0.20	5.14	0.16	−21.01	2008.18	2012.62
COYU	−100.081	17.008	7.67	5.78	0.03	0.10	5.09	0.07	−21.01	2003.29	2014.23
CPDP	−99.628	16.776	11.92	11.71	0.03	0.05	7.17	0.04	−20.10	2003.42	2014.25
CZIG	−99.131	16.736	10.53	11.78	1.05	0.92	6.06	0.99	−19.25	2009.87	2010.30
DEMA	−99.035	20.300	1.41	1.76	0.01	0.01	0.65	0.01	−22.02	2003.87	2014.95
DOAP	−99.651	17.021	8.84	9.35	0.06	0.11	5.04	0.09	−20.32	2004.41	2011.92
DOAR	−99.651	17.021	8.56	9.78	0.03	0.06	4.64	0.05	−20.32	2003.23	2013.43
HUAT	−96.108	15.769	12.23	16.03	0.01	0.01	10.53	0.01	−5.88	2000.57	2014.32
IGCU	−99.176	19.327	3.36	3.13	0.11	0.08	1.99	0.09	−21.38	2011.40	2014.31
IGUA	−99.502	18.392	3.52	4.11	0.02	0.03	1.80	0.03	−21.15	2000.43	2014.28
INEG	−102.284	21.856	1.30	2.33	0.01	0.02	−0.79	0.01	−46.45	2006.83	2014.94
LAZA	−99.487	17.519	6.11	9.60	0.04	0.04	2.38	0.04	−20.42	2006.71	2014.26
LZCR	−102.178	17.939	7.76	15.83	0.12	0.11	1.17	0.12	−22.32	2008.94	2011.37
MARO	−94.884	17.091	3.58	3.41	0.01	0.02	2.22	0.02	−19.74	2005.03	2014.97
MEZC	−99.620	17.925	5.09	6.14	0.04	0.07	2.55	0.06	−20.97	2005.04	2014.28
MRQL	−98.817	16.594	13.97	17.58	0.17	0.14	7.63	0.15	−18.62	2010.23	2012.19
OAX2	−96.717	17.078	4.96	7.89	0.04	0.05	2.70	0.04	−15.29	2006.85	2012.20
OAXA	−96.733	17.073	5.82	8.53	0.02	0.02	3.36	0.02	−15.32	2001.20	2012.18
OMTP	−98.419	16.700	14.01	16.59	0.20	0.18	8.19	0.19	−18.02	2009.83	2012.18
OXAC	−98.041	18.130	3.08	6.52	0.08	0.09	0.86	0.09	−18.37	2009.23	2012.19
OXEC	−96.055	16.520	5.93	9.02	0.04	0.04	5.05	0.04	−5.48	2009.01	2013.85
OXES	−96.746	15.727	15.03	26.74	0.37	0.29	7.82	0.35	−14.58	2009.12	2010.86
OXGU	−96.910	16.630	3.06	8.02	0.08	0.08	0.83	0.08	−15.37	2009.00	2013.85
OXLP	−97.051	16.142	11.49	16.19	0.09	0.12	6.80	0.10	−15.33	2009.13	2013.99
OXMA	−98.611	16.709	15.65	18.74	0.13	0.13	8.96	0.13	−18.35	2009.16	2011.75
OXNC	−97.218	17.400	4.34	7.60	0.08	0.13	2.02	0.09	−16.39	2009.11	2012.18
OXPE	−97.075	15.889	19.11	23.17	0.03	0.05	12.36	0.04	−15.23	2008.02	2014.25
OXTH	−95.239	16.281	4.27	4.77	0.18	0.15	2.50	0.16	−18.87	2009.00	2010.62
OXTU	−97.654	16.151	8.61	11.03	0.10	0.14	5.52	0.11	−16.37	2009.01	2013.86
OXUM	−96.499	15.662	15.90	17.02	0.06	0.08	16.45	0.07	1.90	2009.14	2013.99
PAPA	−101.047	17.273	11.98	13.53	0.08	0.06	5.81	0.07	−22.78	2010.14	2014.00
PEIG	−97.148	15.998	14.51	13.61	0.14	0.18	10.37	0.16	−15.42	2012.87	2015.00
PENA	−104.101	19.391	4.02	7.01	0.02	0.02	−1.54	0.02	−40.78	2007.12	2019.93
PINO	−98.127	16.393	9.94	10.10	0.02	0.03	6.48	0.03	−17.33	2000.53	2012.18
POPO	−98.628	19.067	−0.72	7.91	0.56	0.55	−0.72	0.56	−20.17	2013.51	2014.29
POSW	−98.657	19.010	2.07	1.79	0.05	0.05	1.32	0.05	−20.17	1997.01	2003.44
SABY	−91.187	18.967	1.43	1.63	0.02	0.02	0.31	0.02	−33.28	2004.54	2014.10
SLCR	−95.197	16.168	4.34	5.24	0.13	0.09	2.28	0.11	−20.13	2009.00	2012.91
SLUI	−98.741	16.811	13.55	14.41	0.21	0.12	8.39	0.18	−18.13	2009.84	2011.92

(Continued)

TABLE 1 | Continued

Station (site)	Lon °E	Lat °N	V_{SE} mm/year	V_{SN} mm/year	σ V_{SE} mm/year	σ V_{SN} mm/year	V_{SS} mm/year	σ V_{SS} mm/year	ϑTn °cw from N	T1 Year	T2 Year
TAMP	−97.864	22.278	0.88	1.25	0.02	0.01	0.36	0.02	−21.70	2006.83	2014.27
TCPN	−100.631	17.234	9.53	10.01	0.10	0.16	5.07	0.13	−22.08	2009.32	2014.28
TECO	−103.861	18.985	6.94	8.47	0.01	0.01	0.39	0.01	−37.29	2007.17	2019.95
TNCC	−103.173	18.791	4.98	9.02	0.04	0.03	−0.59	0.04	−32.15	2015.82	2019.98
TNCN	−101.971	18.554	5.31	8.52	0.32	0.06	1.58	0.27	−22.87	2016.18	2019.95
TNIF	−101.896	18.272	5.91	10.46	0.04	0.03	1.68	0.04	−21.40	2015.80	2019.99
TNMO	−101.228	19.649	2.43	0.83	0.02	0.02	1.98	0.02	−25.26	2008.48	2019.96
TNMR	−103.346	18.289	7.06	11.51	0.05	0.05	0.10	0.05	−31.09	2014.71	2018.72
TNMZ	−104.402	19.124	7.94	10.56	0.07	0.07	−0.94	0.07	−41.00	2015.49	2018.24
TOL2	−99.644	19.293	3.20	4.14	0.02	0.02	1.40	0.02	−22.18	2006.86	2014.23
UCOE	−101.694	19.813	2.57	1.88	0.01	0.01	1.50	0.01	−26.21	2005.81	2019.94
UNIP	−99.181	19.313	1.90	3.57	0.02	0.02	0.47	0.02	−21.38	2005.95	2013.77
YAIG	−99.067	18.862	2.18	3.35	0.02	0.02	0.85	0.02	−20.78	1999.82	2014.19
ZIHP	−101.465	17.607	9.86	13.26	0.03	0.04	3.69	0.03	−23.73	2000.53	2014.22

Position time series for the sites in italic are from the TLALOCNET network (https://www.unavco.org/instrumentation/networks/status/tlalocnet).

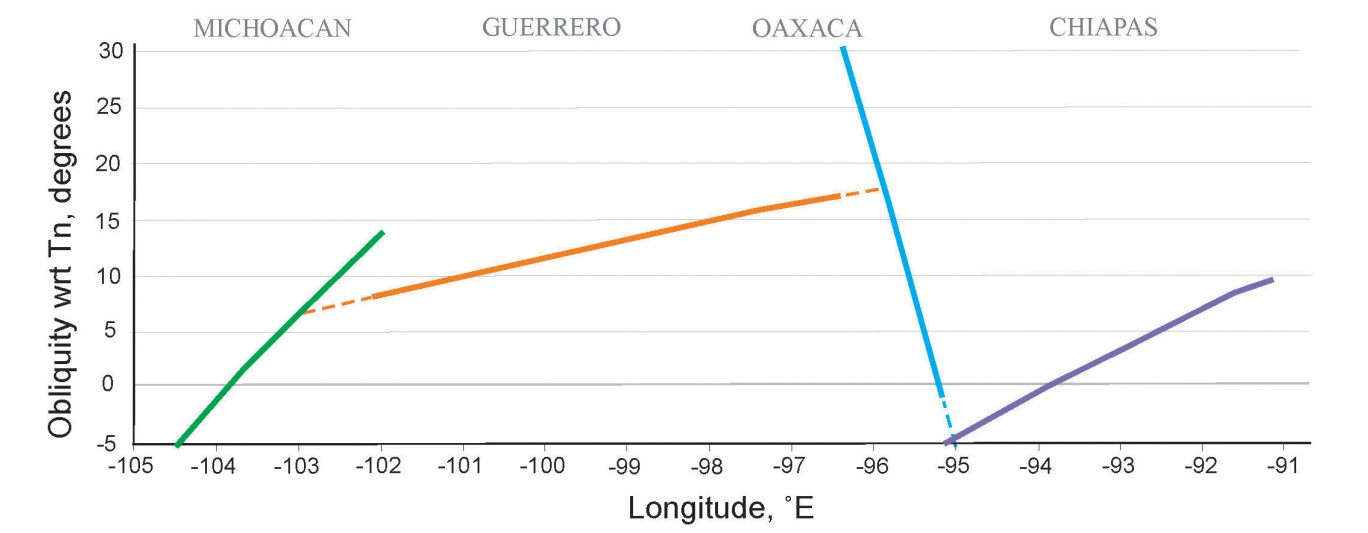

FIGURE 3 | Variation of obliquity angle along the Mexican fragment of the Middle America Trench. The obliquity is relatively higher in the Guerrero–Oaxaca segment of the MAT and low or negative in Michoacan and Chiapas.

the Xolapa complex has no clear expression on the landscape (Gaidzik et al., 2016). Part of the LVF (Gaidzik et al., 2016) appears to coincide with the geologically defined Eocene–Oligocene LVC shear zone (Riller et al., 1992; Tolson, 2005; Solari et al., 2007).

Nevertheless, GPS estimates show that the westernmost section of the LVC should extend up to the Zihuatanejo city area where the Xolapa sliver is stretching from the NA plate. Thus, some of the LVF segments possibly are subfaults of the LVC fault system (Ramírez-Herrera et al., 2018). Therefore, the principal conclusions of Gaidzik et al. (2016) study concerning the age of the LVF, its seismic activity, stress regime, and reactivation would be valid similarly for the LVC (Ramírez-Herrera et al., 2018).

The trace of the tectonically active eastern part of the LVC fault zone needs to be investigated using the same methodology as in Gaidzik et al. (2016) together with high resolution GPS and local seismological studies. Until now there is only geologically defined trace of the LVC shear zone (Ramírez-Herrera et al., 2018), which is poorly confirmed by any reliable observations, particularly in Oaxaca region (between −99.0 and −97°E; dashed line in **Figure 1**). Just a few GPS stations landward from and close to the LVC zone are not enough to estimate the active fault zone location. For that reason, the geological LVC trace is the only one that can tentatively be used as a reference for the active LVC in Oaxaca. Analyzing secular trench-parallel velocities, V_{SS}, of the easternmost GPS stations (OXUM, HUAT, SLCR, OZTH, and MARO; **Figure 1**) we conclude that the

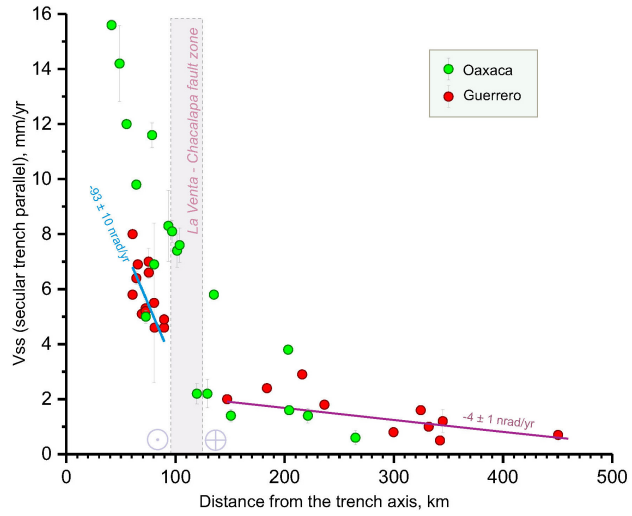

FIGURE 4 | Distribution of trench-parallel component of GPS secular velocity (V_{SS}) along the profile perpendicular to the MAT (**Figure 1**, red vectors amplitudes projected on the profile shown by the red dashed line). Red circles correspond to the GPS stations in the Guerrero state and green circles to those in the Oaxaca state. Blue line annotated with the strain rate estimate is a best fit to the V_{SS} measurements for the Xolapa sliver (south of the LVC fault zone) in Guerrero, while the magenta line is the best fit to the V_{SS} data north of the LVC. Sharp change in the strain rate across the LVC is evident as well as an abrupt drop of V_{SS} by 3–5 mm/year in Guerrero and by more than 6 mm/year in Oaxaca. Thus, the LVC fault zone is active at least during the epoch of GPS observations. Light gray band shows roughly the LVF zone.

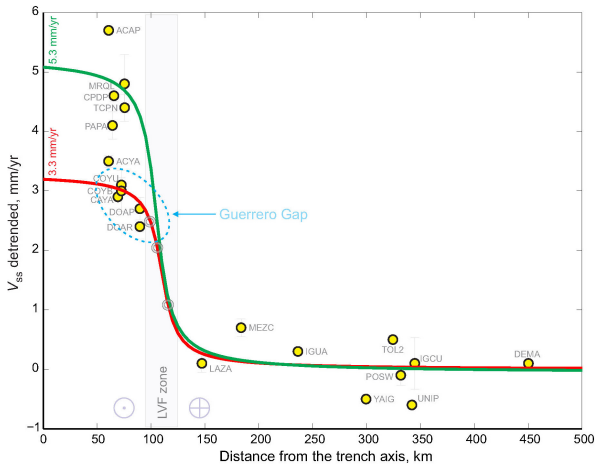

FIGURE 5 | Screw dislocation models in elastic half space for a vertical strike slip fault (Savage and Burford, 1973) in the LVC zone. The models show strike-slip displacement on the surface produced by the creeping fault at the depth more than 10 km. The fault is locked from 0 to 10 km. Yellow circles are detrended trench parallel rates (*V*ss, wrt NA fixed plate) at the permanent GPS stations (see **Figure 1**), ΔVss, (after the secular linear strain trend is subtracted from the *V*ss). The trend north from the LVF fault zone is produced by the simple shear in the upper 10 km of the locked fault segment. Red line is a feasible fit for the *V*ss in the area of the Guerrero seismic gap (G-GAP, ~100–101°W) for the Xolapa sliver velocity, ΔVss, of 3.3 mm/year. Green line is the fit for *V*ss values for the Guerrero GPS stations located off the G-GAP, and ΔVss = 5.3 mm/year. Light gray band indicates the LVF zone. Error bars are 3σ. Gray open circles show only locations of three GPS stations recently installed in the LVF zone to constrain better the fault model.

active LVC fault zone (Ramírez-Herrera et al., 2018) should cross the shoreline somewhere between Huatulco (HUAT) and Salina Cruz cities. Tectonic implication of this observation is considered later.

XOLAPA SLIVER

Azimuthal angle differences (slip partitioning) between slip vectors of subduction thrust earthquakes and the direction normal to the trench allow assessing the partial decoupling of the seismogenic plate interface and the rigid forearc sliver rate in oblique convergence margins (McCaffrey, 1992; Haq and Davis, 2010). Ego and Ansan (2002) thoroughly selected shallow thrust earthquakes on the subduction interface of Southern Mexico from the Harvard centroid moment tensor (CMT, 1977–2001, Mw ≥ 5.3) catalog. They analyzed 31 slip vector angles for the area between 96°W and 105°W, the subduction zone segment, which includes both partially the LVC fault zone (Ramírez-Herrera et al., 2018) and the area outside of it. For the Guerrero area, between 102°W and 96°W along the MAT, they observed a significant slip partitioning up to 10° and estimated an average sliver rate of V_{sl} = 8 ± 3 mm/year. This inference is slightly higher but roughly consistent with our direct GPS observations of V_{SS}.

Using similar selection criteria for the CMT events as of Ego and Ansan (2002), we have compiled a more ample catalog of the CMTs from 1976 up to 2018, which contains 89 shallow thrust events that corresponded only to the LVC longitudinal extent (-95.5 and −101.5°E, see **Supplementary Table A2** for other criteria). Analyzing this CMT data subset, the average estimate of $V_{sl} \approx$ 5.4–6.3 mm/year (see **Supplementary Figure A3**), which is closer to the V_{SS} values obtained with the GPS. The large dispersion of CMT slip vector angles is apparently related to uncertainties in the CMT catalog, complicated structures of the LVC fault system (Ramírez-Herrera et al., 2018) and the Xolapa sliver, inhomogeneous Co-NA plate interface, variation of the plate coupling (e.g., Kostoglodov and Ponce, 1994), and more complicated than just a simple friction rheology of the fault (Kazachkina et al., 2019). Furthermore, observed dispersion is partially related to the increase of the Co-NA convergence velocity southeastward along the MAT. Obviously, McCaffrey's model is too simple to allow for all these factors. Nevertheless, it provides some useful appraisals of sliver motion rate and average static friction coefficient on the fault (Haq and Davis, 2010), which in case of the LVC should be $\mu \leq 0.15$ (**Supplementary Figure A4**). For many crustal faults $\mu < 0.3$ (e.g., Behr and Platt, 2014; Middleton and Copley, 2014).

TECTONIC IMPLICATIONS

As the Xolapa sliver, in reality, is not a rigid block, it should undergo some internal deformation that depends on

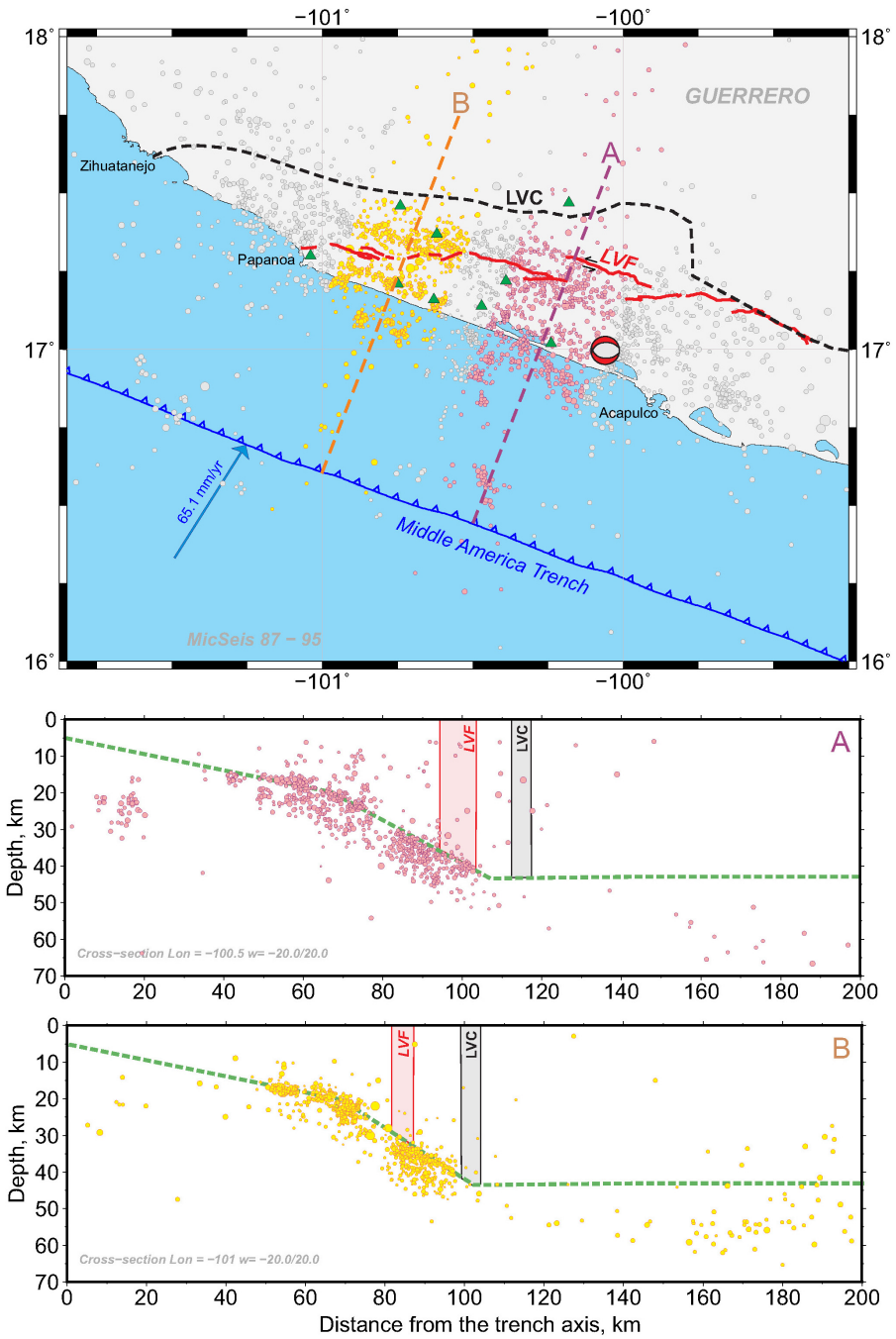

FIGURE 6 | Top map: seismicity in the Guerrero seismic gap area from the local network catalog [1987–1995, 1.0 < Mc < 4.0, (Suárez et al., 1990)]. Green triangles are locations of short period seismometers of the network. LVC, black dashed line shows location of the La Venta–Chacalapa fault zone from geological studies (Tolson, 2005; Solari et al., 2007). Red lines denote a trace of the La Venta fault, LVF, according to Gaidzik et al. (2016). Dashed lines A and B perpendicular to the trench mark two profiles on which the seismic events from the catalog were projected. The events in each cross-section, yellow and magenta on the map, are from the bands of 40-km-wide, centered along the profiles. Red-white focal mechanism shows a location of the October 8, 2001 Coyuca, Mw 5.8, Earthquake (Pacheco and Singh, 2010). A: seismicity cross-section along the profile A (magenta line and events on the map). Pink trapezoid shows roughly a projection of the LVF zone assuming that the fault is vertical. Gray rectangle is a projection of the LVC fault zone assuming that the fault is vertical. Green dashed line is an approximation of the plate interface. B: seismicity cross-section along the profile B (yellow line and seismic events on the map). Other notations are the same as for the cross-section A.

the convergence rate and the interplate coupling, which are changing along its extent. The systematic increase of the subduction velocity in the southeastern direction should result in general extension of the sliver. However, the plate coupling modulates the strain, and this results in some variation of the secular trench-parallel velocity, V_{SS}, for example in the

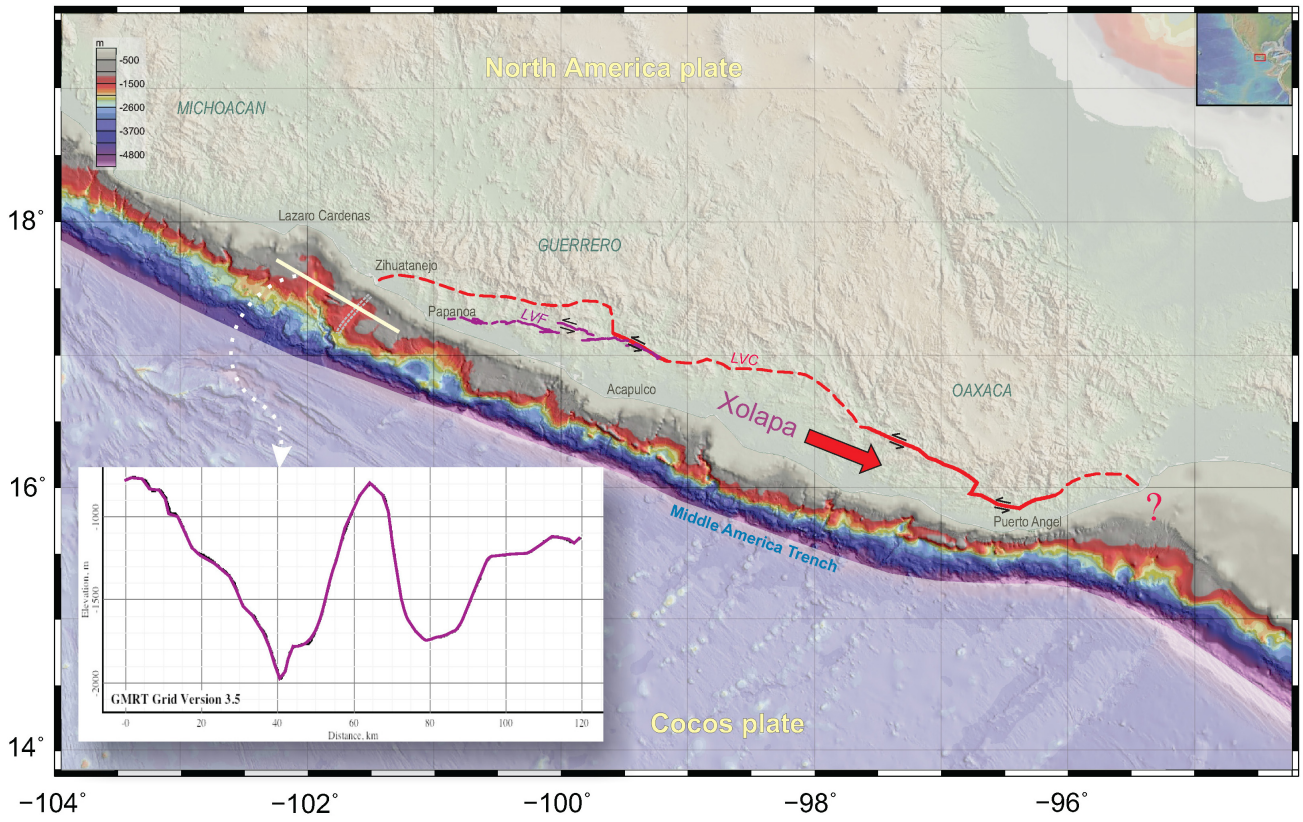

FIGURE 7 | Topographic and bathymetry map [The Global Multi-Resolution Topography synthesis, GMRT (Ryan et al., 2009)], exposing a continental margin in Southern Mexico. The 750–1,600 m depth range is in red. A bathymetric profile at ∼1,500 m from Lazaro Cardenas city to Papanoa is shown in the bottom inlet. Two prominent depressions have a total average width of ∼40 km (at 1,500 km depth). The red arrow indicates the Xolapa sliver southeast motion. Local concave shape of the continental margin is seen in the area of the Tehuantepec ridge. The red line is a trace of the LVC fault system (Tolson, 2005). Magenta lines in the coastal area show the LVF fault discovered by Gaidzik et al. (2016).

area of Guerrero seismic gap, between −101° and −100° of longitude (**Figure 1**).

Northwestern End of the Xolapa Sliver

In western Guerrero, an expected transtensional offshore continuation of the LVF on the continental slope is not so clear because of a lack of detailed bathymetric data. Low-resolution bathymetry offshore of Papanoa and Zihuatanejo [The Global Multi-Resolution Topography synthesis, GMRT (Ryan et al., 2009)] shows only two wide depressions on the continental slope that can be interpreted as an extension produced by the trailing edge of the Xolapa sliver moving southeastward (**Figure 7**). The total stretching of the continental margin estimated from the trench parallel bathymetric profile presented in **Figure 7** is of the order of 40 km (referenced to the depth of 1,500 m). Southeastern displacement of the Xolapa sliver leading edge is expected to be of a similar distance, assuming that the sliver was rigid. The Cocos–North America spreading rate was almost invariable since at least the Late Miocene (Cande and Kent, 1992; Conrad and Lithgow-Bertelloni, 2007) and if the average mobility of the sliver was unchanging (∼5 mm/year), the reactivation of the LVC fault system (Ramírez-Herrera et al., 2018) could have occurred some ∼8–10 million year ago after the reorganization of spreading from the failing Mathematician ridge to the new propagating East Pacific Rise (Klitgord and Mammerickx, 1982; Mammerickx et al., 1988).

Mexico–Guatemala Triple Junction and Eastern Extent of the Xolapa Sliver

While the geologic and tectonic history of the Xolapa terrain is still under discussion (e.g., Cerca et al., 2007; Moran-Zenteno et al., 2009; Talavera-Mendoza et al., 2013; Peña-Alonso et al., 2018), the earlier sinistral motion on the LVC fault system is recognized to occur in Early Eocene–Oligocene (50–25 Ma) (Tolson, 2005; Solari et al., 2007). Since then, it is unknown how long has been the LVC active and what the tectonic consequences are of the Xolapa sliver motion. The models of the Xolapa tectonic evolution are usually related to the translation of the Chortis block from its initial position, possibly bordering the Xolapa from the south (Schaaf et al., 1995), to its present location along the Polochic-Motagua fault system in Guatemala and Honduras (e.g., Ortega-Gutiérrez et al., 2007; Rogers et al., 2007). Regardless of the tectonic and geologic

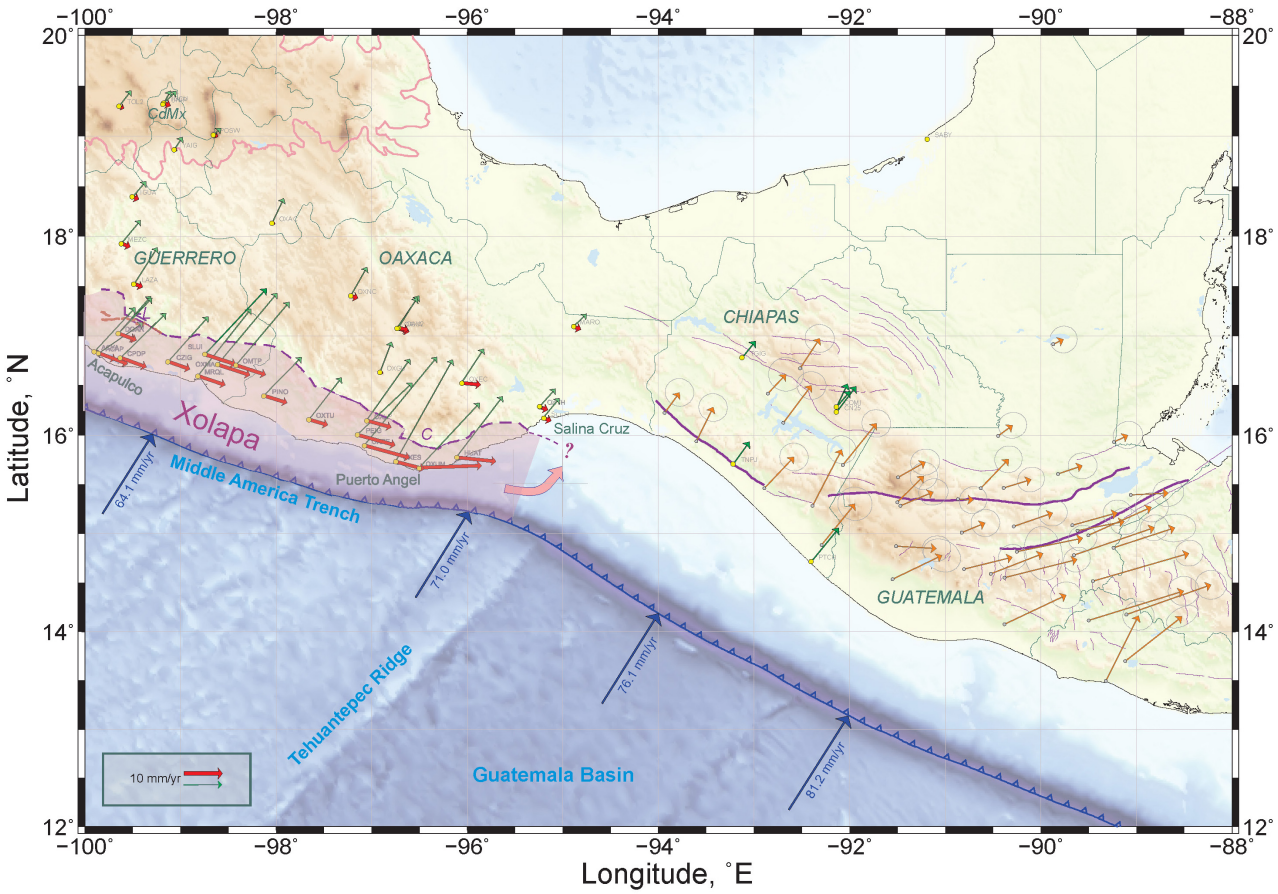

FIGURE 8 | A map of southern Mexico that illustrates models of LVC sliver progression in the Guatemala basin. There is no obliquity in the Cocos–North America convergence offshore of the Chiapas segment of the MAT (-95.0 to −92.0°E). That causes an absence of a driving force for the sliver at a distance of more than 300 km along the MAT. Pink curved arrow indicates probable northward bending of the Xolapa sliver. Orange GPS vectors in Chiapas and Guatemala are from Ellis et al. (2018). Other captions are the same as in **Figure 1**.

history of the Xolapa terrain, the present-day activity of the LVC fault system (Ramírez-Herrera et al., 2018) and the Xolapa sliver motion should be relevant to the seismotectonic situation in southern Mexico.

The next question, related to the challenging problem of the North America–Cocos–Caribbean tectonic plates triple junction, is how do the LVC (Ramírez-Herrera et al., 2018) and the Xolapa sliver continue to the continental margin of Chiapas. Lack of detailed bathymetry and marine geophysics data in this area leaves any hypothesis on the matter to be tentative. Thick accumulated sediments (e.g., Straume et al., 2019) entirely hide the tectonic structure on a wide continental margin. The Xolapa sliver movement into this area cannot stop abruptly. Still, it may lead to a deformation of the sliver body, or the sliver continues its trajectory along the trench. In the latter case, a left-lateral continuation of the LVC sub-parallel to the trench fault would exist on the continental margin of Chiapas (**Figure 8**). Further speculating, this fault may be lined up with the Polochic-Motagua fault system. Obviously, there are two main observations that would contradict this hypothesis: First, there is no obliquity in the Cocos-North America convergence offshore of the Chiapas segment of the MAT (-95.0 to −92.0°E). That causes an absence of a driving force for the sliver at a distance of more than 300 km along the trench. Second, the Central America forearc sliver (DeMets, 2001) southeastward motion in the NA reference frame starts only at −92°E, as it is seen at GPS stations (**Figure 8**; Franco et al., 2012; Ellis et al., 2018).

Bearing in mind the inconsistencies of the previous hypothesis, another model of the Xolapa sliver leading-edge progression may be that it is bending northeastward in the area of Tehuantepec ridge subduction. This bending may be accompanied by fracturing, which depends on the force moment loading rate (the function of coupling, etc.) and the mechanical properties of the sliver. This scenario is probably more reliable, but it requires the existence of a system of faults limiting the sliver on the continental margin of Chiapas. Scarce seismologic data (Roman-Reinoso, 2004) in this region indicate only that this concept may be valid. In **Figure 9**, we demonstrate several faults (the area location is on **Figure 9**) and just a few rare CMT solutions of the strike-slip type in the crust forearc of Chiapas, which may be interpreted as consequences of the Xolapa sliver northeastern bending and fracturing. Unfortunately, the last

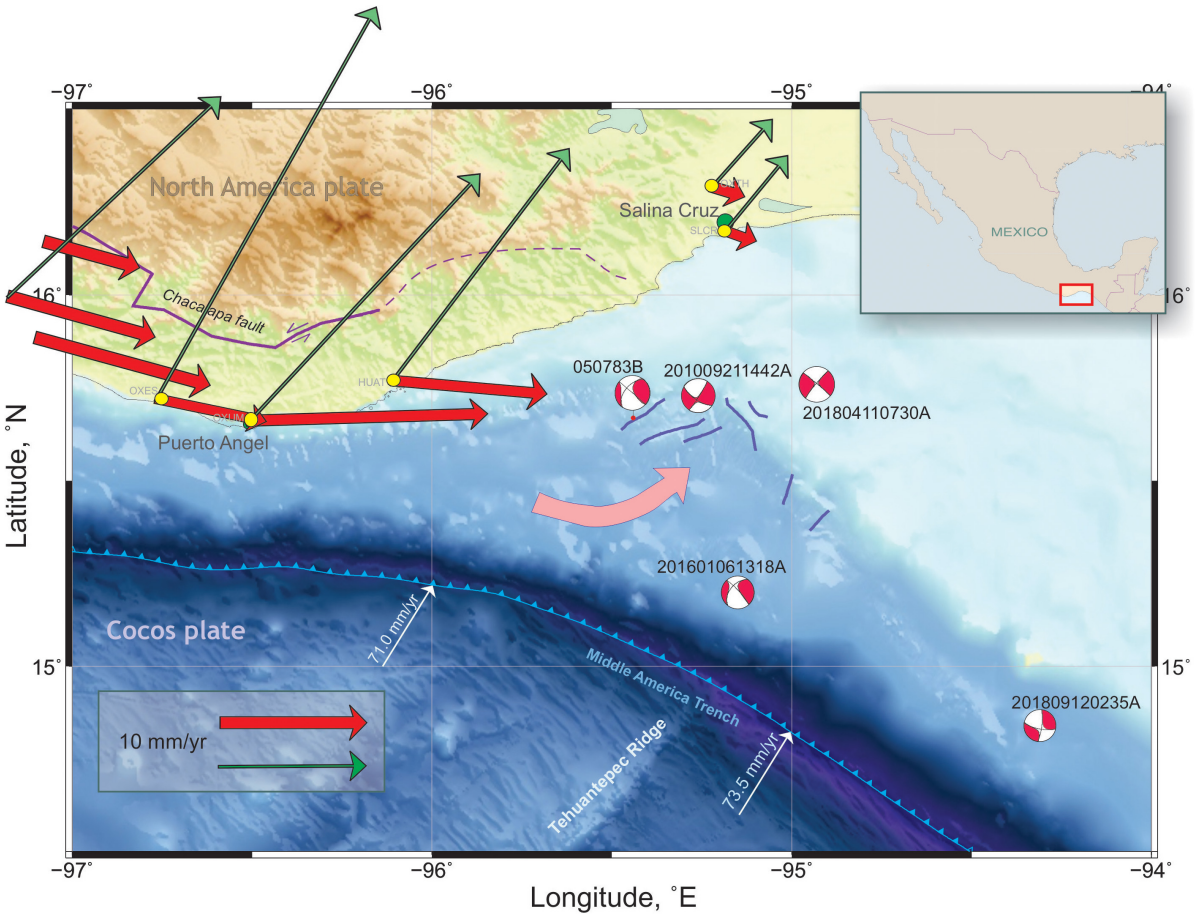

FIGURE 9 | Detailed map of the subduction zone in the region of the Tehuantepec ridge. The inset shows a location of this area. Red vectors are secular sinistral GPS velocities (the same as in **Figure 8**). The only crustal strike-slip events in the Global CMT catalog are shown as red beach balls with their catalog codes. Blue lines offshore, south of Salina Cruz city are conceivably active faults (Roman-Reinoso, 2004).

hypothesis leaves the triple junction problem still unresolved until more marine geophysics data would be available.

CONCLUSION

Long-lasting GPS observations and geomorphology studies in the Guerrero–Oaxaca area of the Mexican subduction zone show that, despite the almost complete absence of historic and instrumentally recorded seismicity in the western LVC fault zone, this mainly left-lateral shear zone is a complex and active system of numerous distributed strike-slip faults that accommodates strain partitioning produced by oblique subduction of the CO. The average velocity of the sinistral motion of the Xolapa sliver predicted from the slip vectors of subduction thrust earthquakes (∼5.4–6.3 mm/year) is consistent with the direct GPS observed trench parallel velocity component across the LVC fault (5–6 mm/year in Guerrero). As the result of the present study, we should admit that the LVC fault system is the principal active tectonic feature in Southern Mexico, which must be considered as a source of potential seismic hazard.

It is not known so far for how long time was the LVC fault zone active and what is a cumulative offset across the LVC fault zone in time. Existing GPS records only are not enough to constitute a previously unrecognized hazard in Southern Mexico related to the active LVC fault system. We need to obtain quantitative constraints on the age of the LVC faulting at least for the last few thousand years. Accurate trace and structure of the LVC was not yet explored except perhaps its western Guerrero segment (Gaidzik et al., 2016). The motion of the Xolapa sliver in Oaxaca remains rather hypothetic until more data would be available on new GPS stations installed inland from the LVC zone. Apart of the more precise location of the LVC fault and its coupling structure modeling, future investigations will also focus on a possible relationship between large subduction thrust SSE and displacements on the LVC fault zone.

The Xolapa sliver is not a rigid block and should undergo different internal deformations, which depend on subduction rate, coupling, and changes in the friction along the 650-km length of the LVC. The leading edge of the LVC in the Guatemala basin is still undefined. It is apparently not related to the triple junction, but a contortion of the Xolapa sliver in the area of the Tehuantepec ridge is probably a key to make this problem clearer.

DATA AVAILABILITY STATEMENT

All datasets generated for this study are included in the article/**Supplementary Material**.

AUTHOR CONTRIBUTIONS

EK carried out the main part of the study and wrote the manuscript. VK developed the main idea and wrote the manuscript. NC and AW participated in GPS data processing and analysis. MR-H and KG contributed to geomorphological interpretations. AH participated in project discussion and manuscript writing. JS managed the GPS network and provided the most of raw data used in this study.

FUNDING

This research was supported by the UNAM PAPIIT IN109117, IN110514, and IN110519, CONACYT 178058, 284212, and 284365 grants.

ACKNOWLEDGMENTS

Some of the GPS and seismological data are from the National Seismological Service of Mexico (SSN, http://www.ssn.unam.mx/). The GPS data for the Oaxaca region were partly provided by Enrique Cabral Cano. Several GPS position time series for the Michoacan and Colima states of Mexico are in free access from the UNAVCO web site (https://www.unavco.org/instrumentation/networks/status/tlalocnet). We thank Victor Cruz Atienza and Michel Campillo for helpful discussions. Several figures were generated with the Generic Mapping Tools (GMT) software (Wessel and Smith, 1998). We thank Jorge Real Perez and Juan Payero for their efforts in collecting the data and maintenance of the Guerrero GPS network in very complicated field conditions of Southern Mexico.

SUPPLEMENTARY MATERIAL

The Supplementary Material for this article can be found online at: https://www.frontiersin.org/articles/10.3389/feart.2020.00155/full#supplementary-material

REFERENCES

Alchalbi, A., Daoud, M., Gomez, F., Mcclusky, S., Reilinger, R., Romeyeh, M. A., et al. (2010). Crustal deformation in northwestern Arabia from GPS measurements in Syria: slow slip rate along the northern Dead Sea Fault. *Geophys. J. Int.* 180, 125–135. doi: 10.1111/j.1365-246X.2009.04431.x

Altamimi, Z., Collilieux, X., and Métivier, L. (2011). ITRF2008: an improved solution of the international terrestrial reference frame. *J. Geodesy* 85, 457–473. doi: 10.1007/s00190-011-0444-4

Andreani, L., Le Pichon, X., Rangin, C., and Martinez-Reyes, J. (2008). The southern Mexico block: main boundaries and new estimation for its Quaternary motion. *Bull. Soc. Geol. France* 179, 209–223. doi: 10.2113/gssgfbull.179.2.209

Behr, W. M., and Platt, J. P. (2014). Brittle faults are weak, yet the ductile middle crust is strong: implications for lithospheric mechanics. *Geophys. Res. Lett.* 41, 8067–8075. doi: 10.1002/2014GL061349

Blewitt, G., and Lavallée, D. (2002). Effect of annual signals on geodetic velocity. *J. Geophys. Res. Solid Earth* 107, 9–11. doi: 10.1029/2001JB000570

Campa, M. F., and Coney, P. J. (1983). Tectono-stratigraphic terranes and mineral resource distributions in Mexico. *Can. J. Earth Sci.* 20, 1040–1051. doi: 10.1139/e83-094

Cande, S. C., and Kent, D. V. (1992). A new geomagnetic polarity time scale for the Late Cretaceous and Cenozoic. *J. Geophys. Res. Solid Earth* 97, 13917–13951. doi: 10.1029/92JB01202

Cerca, M., Ferrari, L., Lopez-Martinez, M., Martiny, B., and Iriondo, A. (2007). Late Cretaceous shortening and early Tertiary shearing in the central Sierra Madre del Sur, southern Mexico: insights into the evolution of the Caribbean-North American plate interaction. *Tectonics* 26:TC3007. doi: 10.1029/2006tc001981

Cohen, S. C. (1999). "Numerical models of crustal deformation in seismic zones," in *Advances in Geophysics*, eds D. Renata and S. Barry (Elsevier), 133–231. doi: 10.1016/s0065-2687(08)60027-8

Conrad, C. P., and Lithgow-Bertelloni, C. (2007). Faster seafloor spreading and lithosphere production during the mid-Cenozoic. *Geology* 35, 29–32. doi: 10.1130/g22759a.1

Cotte, N., Walpersdorf, A., Kostoglodov, V., Vergnolle, M., Santiago, J.-A., Manighetti, I., et al. (2009). Anticipating the next large silent earthquake in Mexico. *Eos Trans. AGU* 90, 181–182. doi: 10.1029/2009EO210002

DeMets, C. (2001). A new estimate for present-day cocos-caribbean plate motion: implications for slip along the Central American Volcanic Arc. *Geophys. Res. Lett.* 28, 4043–4046. doi: 10.1029/2001gl013518

DeMets, C., Gordon, R. G., and Argus, D. F. (2010). Geologically current plate motions. *Geophys. J. Int.* 181, 1–80. doi: 10.1111/j.1365-246X.2009.04491.x

Ducea, M. N., Gehrels, G. E., Shoemaker, S., Ruiz, J., and Valencia, V. A. (2004). Geologic evolution of the Xolapa complex, southern Mexico: evidence from U-Pb zircon geochronology. *GSA Bull.* 116, 1016–1025. doi: 10.1130/B25467.1

Ego, F., and Ansan, V. (2002). Why is the central trans-mexican volcanic belt (102o-ì99oW) in transtensive deformation? *Tectonophysics* 359, 189–208. doi: 10.1016/s0040-1951(02)00511-5

Ellis, A., Demets, C., Briole, P., Cosenza, B., Flores, O., Graham, S. E., et al. (2018). GPS constraints on deformation in northern Central America from 1999 to 2017, Part 1 – Time-dependent modelling of large regional earthquakes and their post-seismic effects. *Geophys. J. Int.* 214, 2177–2194. doi: 10.1093/gji/ggy249

Fasola, S., Brudzinski, M. R., Ghouse, N., Solada, K., Sit, S., Cabral-Cano, E., et al. (2016). New perspective on the transition from flat to steeper subduction in Oaxaca, Mexico, based on seismicity, nonvolcanic tremor, and slow slip. *J. Geophys. Res. Solid Earth* 121, 1835–1848. doi: 10.1002/2015JB012709

Fasola, S. L., Brudzinski, M. R., Holtkamp, S. G., Graham, S. E., and Cabral-Cano, E. (2019). Earthquake swarms and slow slip on a sliver fault in the Mexican subduction zone. *Proc. Natl. Acad. Sci.* 116, 7198–7206. doi: 10.1073/pnas.1814205116

Ferrari, L., Orozco-Esquivel, T., Manea, V., and Manea, M. (2012). The dynamic history of the Trans-Mexican Volcanic Belt and the Mexico subduction zone. *Tectonophysics* 522-523, 122–149. doi: 10.1016/j.tecto.2011.09.018

Franco, A., Lasserre, C., Lyon-Caen, H., Kostoglodov, V., Molina, E., Guzman-Speziale, M., et al. (2012). Fault kinematics in northern Central America and coupling along the subduction interface of the Cocos Plate, from GPS data in Chiapas (Mexico), Guatemala and El salvador. *Geophys. J. Int.* 189, 1223–1236. doi: 10.1111/j.1365-246X.2012.05390.x

Gaidzik, K., Ramírez-Herrera, M. T., and Kostoglodov, V. (2016). Active crustal faults in the forearc region, Guerrero Sector of the Mexican Subduction Zone. *Pure Appl. Geophys.* 173, 3419–3443. doi: 10.1007/s00024-015-1213-8

Graham, S., Demets, C., Cabral-Cano, E., Kostoglodov, V., Rousset, B., Walpersdorf, A., et al. (2016). Slow Slip History for the MEXICO Subduction Zone: 2005 Through 2011. *Pure Appl. Geophys.* 173, 3445–3465. doi: 10.1007/s00024-015-1211-x

Guzman-Speziale, M. (1995). Hypocentral cross-sections and arc-trench curvature. *Geofisica Int.* 34, 131–141.

Haq, S. S. B., and Davis, D. M. (2010). Mechanics of fore-arc slivers: insights from simple analog models. *Tectonics* 29:TC5015. doi: 10.1029/2009tc002583

Herring, T. A., King, R. W., and Mcclusky, S. C. (2015). *Introduction to GAMIT/GLOBK*. Cambridge, MA: Mass. Inst. of Technol.

Jolivet, R., Simons, M., Agram, P. S., Duputel, Z., and Shen, Z. K. (2015). Aseismic slip and seismogenic coupling along the central San Andreas Fault. *Geophys. Res. Lett.* 42, 297–306. doi: 10.1002/2014GL062222

Kazachkina, E., Kostoglodov, V., Husker, A., and Cotte, N. (2019). Activity of crustal faults and the Xolapa sliver motion in Guerrero–Oaxaca forearc of Mexico, from seismic data. *Earth Planet. Space* 71:104. doi: 10.1186/s40623-019-1084-9

Klitgord, K. D., and Mammerickx, J. (1982). Northern East Pacific Rise: magnetic anomaly and bathymetric framework. *J. Geophys. Res. Solid Earth* 87, 6725–6750. doi: 10.1029/JB087iB08p06725

Kostoglodov, V., and Ponce, L. (1994). Relationship between subduction and seismicity in the Mexican Part of the Middle America Trench. *J. Geophys. Res. Solid Earth* 99, 729–742. doi: 10.1029/93jb01556

Kostoglodov, V., Singh, S. K., Santiago, J. A., Franco, S. I., Larson, K. M., Lowry, A. R., et al. (2003). A large silent earthquake in the Guerrero seismic gap, Mexico. *Geophys. Res. Lett.* 30:GL017219. doi: 10.1029/2003gl017219

Lamb, S., and Smith, E. (2013). The nature of the plate interface and driving force of interseismic deformation in the New Zealand plate-boundary zone, revealed by the continuous GPS velocity field. *J. Geophys. Res. Solid Earth* 118, 3160–3189. doi: 10.1002/jgrb.50221

Mammerickx, J., Naar, D. F., and Tyce, R. L. (1988). The mathematician paleoplate. *J. Geophys. Res. Solid Earth* 93, 3025–3040. doi: 10.1029/JB093iB04p03025

McCaffrey, R. (1992). Oblique plate convergence, slip vectors, and forearc deformation. *J. Geophys. Res. Solid Earth* 97, 8905–8915. doi: 10.1029/92jb00483

Middleton, T. A., and Copley, A. (2014). Constraining fault friction by re-examining earthquake nodal plane dips. *Geophys. J. Int.* 196, 671–680. doi: 10.1093/gji/ggt427

Moran-Zenteno, D. J. K., Duncan, J., Martiny, B., and Gonzales-Torres, E. (2009). Reassessment of the Paleogene position of the Chortis block relative to southern Mexico: hierarchical ranking of data and features. *Rev. Mexicana Ciencias Geol.* 26, 177–188.

Ortega-Gutiérrez, F., Solari, L. A., Ortega-Obregón, C., Elías-Herrera, M., Martens, U., Morán-Icál, S., et al. (2007). The maya-chortís boundary: a tectonostratigraphic approach. *Int. Geol. Rev.* 49, 996–1024. doi: 10.2747/0020-6814.49.11.996

Pacheco, J. F., Iglesias, A., Singh, S. K., Gutierrez, C., Espitia, G., and Alcantara, L. (2002). The 8 October 2001 Coyuca, Guerrero, Mexico earthquake (Mw 5.9): a normal fault in an expected compressional environment. *Seismol. Res. Lett.* 73, 263–264.

Pacheco, J. F., and Singh, S. K. (2010). Seismicity and state of stress in Guerrero segment of the Mexican subduction zone. *J. Geophys. Res.* 115:B01303. doi: 10.1029/2009jb006453

Peña-Alonso, T. A., Molina-Garza, R. S., Villalobos-Escobar, G., Estrada-Carmona, J., Levresse, G., and Solari, L. (2018). The opening and closure of the Jurassic-Cretaceous Xolapa basin, southern Mexico. *J. South Am. Earth Sci.* 88, 599–620. doi: 10.1016/j.jsames.2018.10.003

Radiguet, M., Cotton, F., Vergnolle, M., Campillo, M., Walpersdorf, A., Cotte, N., et al. (2012). Slow slip events and strain accumulation in the Guerrero gap, Mexico. *J. Geophys. Res.* 117:B04305. doi: 10.1029/2011jb008801

Ramírez-Herrera, M. T., Gaidzik, K., Forman, S., Bürgmann, R., and Johnson, C. W. (2018). Relating long-term and short-term vertical deformation across of the foreac in the Central mexican subduction zone. *Geosphere* 14, 419–439. doi: 10.1130/GES01446.1

Riller, U., Ratschbacher, L., and Frisch, W. (1992). Left-lateral transtension along the Tierra Colorada deformation zone, northern margin of the Xolapa magmatic arc of southern Mexico. *J. S. Am. Earth Sci.* 5, 237–249. doi: 10.1016/0895-9811(92)90023-R

Rogers, R. D., Mann, P., and Emmet, P. A. (2007). "Tectonic terranes of the Chortis block based on integration of regional aeromagnetic and geologic data," in *Geologic and Tectonic Development of the Caribbean Plate Boundary in Northern Central America*, ed. P. Mann (Boulder: Geological Society of America).

Roman-Reinoso, S. J. (2004). *Procesamiento y Análisis Estratigrátigrafico de Perfiles de Reflexión Sísmica en el Talud Continental del Golfo de Tehuantepec*. BSc thesis, Universidad Nacional Atónoma de México, México.

Ryan, W. B. F., Carbotte, S. M., Coplan, J. O., O'hara, S., Melkonian, A., Arko, R., et al. (2009). Global Multi-Resolution Topography synthesis. *Geochem. Geophys. Geosyst.* 10:GC002332. doi: 10.1029/2008gc002332

Savage, J. C., and Burford, R. O. (1973). Geodetic determination of relative plate motion in central California. *J. Geophys. Res.* 78, 832–845. doi: 10.1029/JB078i005p00832

Schaaf, P., Morán-Zenteno, D., Hernández-Bernal, M. D. S., Solís-Pichardo, G., Tolson, G., and Köhler, H. (1995). Paleogene continental margin truncation in southwestern Mexico: Geochronological evidence. *Tectonics* 14, 1339–1350. doi: 10.1029/95TC01928

Smith, B. R., and Sandwell, D. T. (2006). A model of the earthquake cycle along the San Andreas Fault System for the past 1000 years. *J. Geophys. Res. Solid Earth* 111:B01405. doi: 10.1029/2005JB003703

Smith-Konter, B. R., Sandwell, D. T., and Shearer, P. (2011). Locking depths estimated from geodesy and seismology along the San Andreas Fault System: implications for seismic moment release. *J. Geophys. Res. Solid Earth* 116:B06401. doi: 10.1029/2010JB008117

Solari, L. A., De León, R. T., Hernández Pineda, G., Solé, J., Solís-Pichardo, G., and Hernández-Treviño, T. (2007). Tectonic significance of Cretaceous, Tertiary magmatic and structural evolution of the northern margin of the Xolapa Complex, Tierra Colorada area, southern Mexico. *Geol. Soc. Am. Bull.* 119, 1265–1279. doi: 10.1130/b26023.1

Straume, E. O., Gaina, C., Medvedev, S., Hochmuth, K., Gohl, K., Whittaker, J. M., et al. (2019). GlobSed: updated total sediment thickness in the World's Oceans. *Geochem. Geophys. Geosyst.* 20, 1756–1772. doi: 10.1029/2018gc008115

Suárez, G., Monfret, T., Wittlinger, G., and David, C. (1990). Geometry of subduction and depth of the seismogenic zone in the Guerrero gap, Mexico. *Nature* 345:336. doi: 10.1038/345336a0

Suter, M., Quintero, O., and Johnson, C. A. (1992). Active faults and state of stress in the central part of the Trans-Mexican Volcanic Belt, Mexico 1. The Venta de Bravo Fault. *J. Geophys. Res. Solid Earth* 97, 11983–11993. doi: 10.1029/91JB00428

Talavera-Mendoza, O., Ruiz, J., Corona-Chavez, P., Gehrels, G. E., Sarmiento-Villagrana, A., García-Díaz, J. L., et al. (2013). Origin and provenance of basement metasedimentary rocks from the Xolapa Complex: new constraints on the Chortis–southern Mexico connection. *Earth Planet. Sci. Lett.* 36, 188–199. doi: 10.1016/j.epsl.2013.03.021

Tolson, G. (2005). La falla Chacalapa en el sur de Oaxaca. *Boletín Soc. Geol. Mexic.* 57, 111–122. doi: 10.18268/bsgm2005v57n1a6

Unam_Seismology_Group (2013). Ometepec-Pinotepa Nacional, Mexico Earthquake of 20 March 2012 (Mw 7.5): a preliminary report. *Geofísica Int.* 52, 173–196. doi: 10.1016/S0016-7169(13)71471-5

Unam_Seismology_Group (2015). Papanoa, Mexico earthquake of 18 April 2014 (M w 7.3). *Geofísica Int.* 54, 363–386.

Vergnolle, M., Walpersdorf, A., Kostoglodov, V., Tregoning, P., Santiago, J. A., Cotte, N., et al. (2010). Slow slip events in Mexico revised from the processing of 11 year GPS observations. *J. Geophys. Res.* 115:B08403. doi: 10.1029/2009jb006852

Wessel, P., and Smith, W. H. F. (1998). New, improved version of generic mapping tools released. *EOS Trans. Am. Geophys. Union* 79, 579–579. doi: 10.1029/98EO00426 doi: 10.1029/98eo00426

Conflict of Interest: The authors declare that the research was conducted in the absence of any commercial or financial relationships that could be construed as a potential conflict of interest.

3.2.2 Geodetic Observations of Slow Slip Events on the La Venta Chacalapa fault

Slow slip or creep events on strike-slip faults have been previously observed on the creeping section of the San Andreas fault in central California with creepmeter measurements [Abaimov *et al.*, 2007]. Khoshmanesh and Shirzaei [2018] used radar interferometry to study semi-periodic slow slip events at the central San Andreas fault during 2003-2010. Ambient stress perturbations due to nearby earthquakes [Tymofyeyeva *et al.*, 2019] and inflow of mantle-driven fluid are among the major suggested causes of these creep events. However, Khoshmanesh and Shirzaei [2018] proposed that, compaction-driven elevated pore fluid pressure in hydraulically isolated fault zone and subsequent frictional dilation cause the observed slow slip episodes. Rousset *et al.* [2019] detected and quantified transient aseismic slip at 16-km depth in the roots of the Parkfield segment of the San Andreas fault using tremor activity and the dense Parkfield-area global positioning system network.

Sinistral motion along the LVC fault system in the study area has been observed with GPS measurements. There is a hypothesis that the system of crustal faults La Venta Chacalapa are active and probably (1) are characterized by long, non-instrumental recurrence period or, 2) they experience slow events or associated fault creep. The La Venta Fault may be capable of producing earthquakes of maximum moment magnitude M_w7.7 [Gaidzik *et al.*, 2016]. GPS observations reveal an abrupt decrease of trench-parallel component of GPS secular velocity V_{ss} associated with the LVC fault (Fig. 4 from Kazachkina *et al.* [2020]). The anomalous surface deformation observed at the trench parallel component of GPS time series from Guerrero and Oaxaca could indicate strike-slip slow slip events at the LVC fault (Fig. 3-8).

The observed lack of registered seismicity at the LVC fault has made it complicated to evaluate its activity. However, it became possible to observe motion along this fault system with the help of available GPS stations. More than 20 years of continuous geodetic record allows to detect a recurrent transient phenomenon at the LVC.

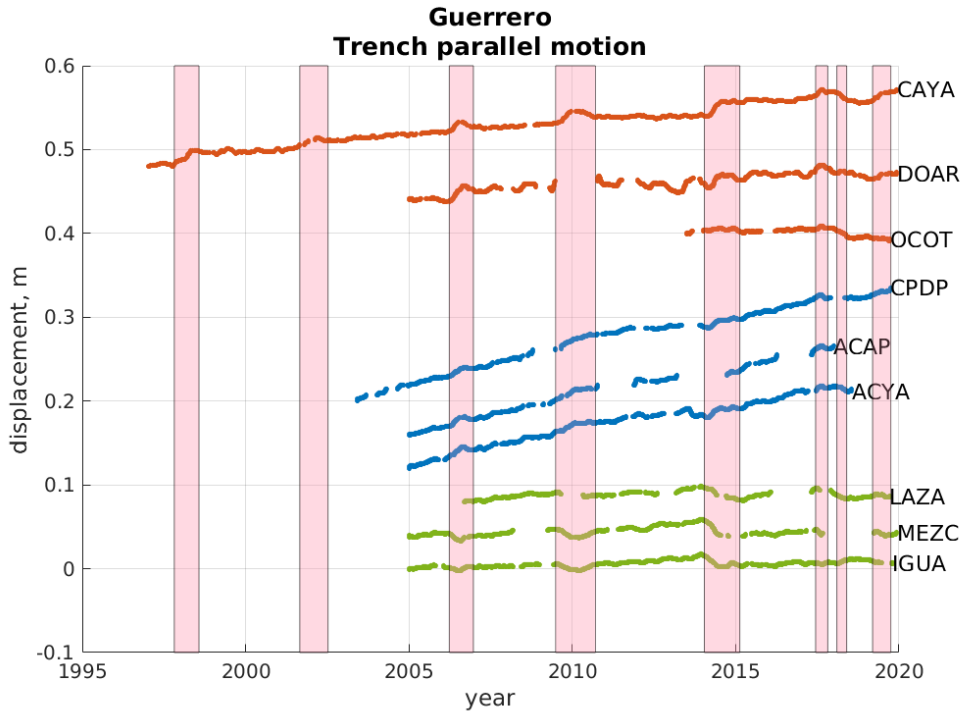

(a)

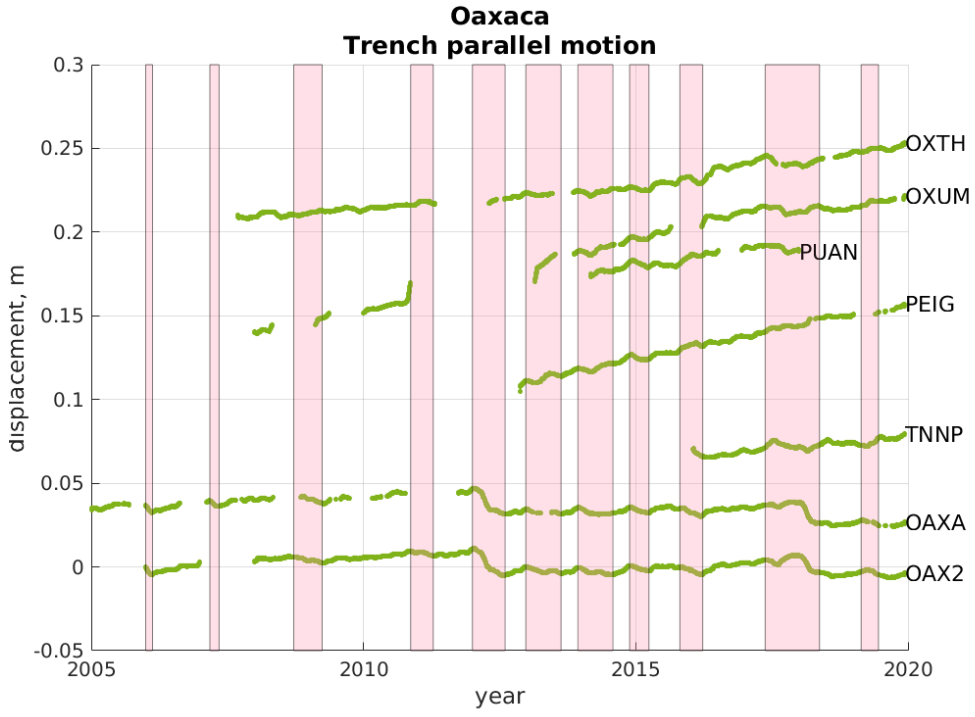

(b)

Figure 3-8: Trench parallel displacements observed in GPS time series at the stations in Guerrero and Oaxaca.

3.2.3 Non-Volcanic Tremor Activity Correlated with Seismic and Aseismic Slip on the Subduction Interface and on the Strike-Slip Faults

It has been shown by Husker *et al.* [2019] that non-volcanic tremor bursts occur during subduction SSEs. Therefore, NVT activity can be used to detect slow slip events especially when SSEs are below the geodetic detection threshold. A correlation between tremor activity and slow transients has also been observed along strike-slip faults. Deep slow slip events below locked seismogenic zone were detected at the Parkfield section of the San Andreas fault [Guilhem and Nadeau, 2012]. In the following article by Husker *et al.* [2019] we describe a method to detect NVTs using single seismic station. It allows to identify both long- and short-term SSEs which is particularly important when GPS time series don't have enough resolution for short events. This method can potentially be used to analyse tectonic activity at the LVC fault zone using seismic stations located in the vicinity.

JGR Solid Earth

RESEARCH ARTICLE
10.1029/2018JB016517

Special Section:
Slow Slip Phenomena and Plate Boundary Processes

Characteristic Tectonic Tremor Activity Observed Over Multiple Slow Slip Cycles in the Mexican Subduction Zone

Allen Husker[1], William B. Frank[2], Guillermo Gonzalez[1], Leticia Avila[1], Vladimir Kostoglodov[1], and Ekaterina Kazachkina[1]

[1]Instituto de Geofísica, Universidad Nacional Autónoma de México, México City, Mexico, [2]Department of Earth Sciences, University of Southern California, Los Angeles, CA, USA

Key Points:
- A single-station tectonic tremor detection using spectral temples algorithm is applied to Mexican permanent seismic stations
- Tectonic tremor activity correlates well with geodetic observations and the combined observations improve analysis of slow slip
- The analysis found discrete intervals of tremor rate in Guerrero and Oaxaca, suggesting characteristic moment release rates of slow slip

Supporting Information:
- Supporting Information S1
- Data Set S1
- Data Set S2
- Data Set S3

Correspondence to:
A. Husker,
allen@igeofisica.unam.mx

Citation:
Husker, A., Frank, W. B., Gonzalez, G., Avila, L., Kostoglodov, V., & Kazachkina, E. (2019). Characteristic tectonic tremor activity observed over multiple slow slip cycles in the Mexican subduction zone. *Journal of Geophysical Research: Solid Earth*, *124*, 599–608. https://doi.org/10.1029/2018JB016517

Received 6 AUG 2018
Accepted 19 DEC 2018
Accepted article online 21 DEC 2018
Published online 12 JAN 2019

Abstract We develop a single-station tremor spectrum template detection method that we applied to continuous seismic data recorded by the Mexican National Seismological Service broadband stations. This allows for an unprecedented long-term analysis of tectonic tremor in Mexico over multiple slow slip events (SSEs). We only detect tremor that are within previously discovered tremor regions, thereby extending the catalog in time but not space. The resulting catalog demonstrates the strong correlation of bursts of tremor activity and aseismic slip over multiple slow slip cycles. The M ~ 7 long-term SSEs in the states of Guerrero and Oaxaca are associated with the longest sequences of tremor bursts. Each of these tremor bursts are made up of a series of smaller bursts. In between the large M7 SSEs, there are shorter-duration, isolated tremor bursts. In Guerrero, these shorter bursts were found to accompany M ~ 6 short-term SSEs. The occurrence of these short-duration tremor bursts in Oaxaca demonstrates that small short-term SSEs occur in both major slow slip regions in Mexico. The discrete range of tremor burst sizes and rates suggests that slow slip events in the Mexican subduction zone are organized into characteristic moment and moment rates. The catalog also reveals other aseismic transients, such as postseismic slip in Oaxaca after the 16 February 2018 M_w 7.2 Pinotepa Nacional earthquake. We highlight that such long-term catalogs are a useful tool together with geodetic observations to monitor slow slip activity that potentially plays a role in the subduction megathrust cycle.

1. Introduction

Tectonic tremor (e.g., Obara, 2002) and their constituent low-frequency earthquakes (LFEs; e.g., Shelly et al., 2007) are important geophysical proxies to track and better understand slow slip events (SSEs: e.g., Frank, Shapiro, Husker, Kostoglodov, & Campillo, 2016; Frank et al., 2018). These aseismic ruptures occur downdip of the seismogenic zone (e.g., Dragert et al., 2001) and are capable of releasing as much strain along plate boundaries as $M > 7$ earthquakes. Understanding the dynamics of slow slip is essential if we are to better estimate its potential impact on the adjacent seismic cycle (e.g., Obara & Kato, 2016; Radiguet et al., 2016).

The Mexican subduction zone hosts a number of slow slip cycles that have produced some of the largest reported SSEs in the world. In the Guerrero Gap, which is located on the subduction interface beneath the Mexican state of Guerrero, a 6-month-long M_w 7.5 SSE occurs about every 4 years (e.g., Kostoglodov et al., 2010). In between these major events, there are shorter and smaller M_w ~ 6 SSEs in Guerrero every few months (Frank et al., 2015). Directly east of Guerrero in the Oaxaca region, M_w ~ 6.75 SSEs happen about every 1.5 years (e.g., Graham et al., 2016). Recent work has leveraged the accompanying intense tremor and LFE activity to unravel the spatiotemporal evolution of slow slip (Brudzinski et al., 2010; Frank et al., 2014; Husker et al., 2012).

Tectonic tremor in the Mexican subduction zone has most often been observed using temporary seismic networks (Figure 1) due to denser station spacing compared to permanent networks (Brudzinski et al., 2016; Frank et al., 2013; Husker et al., 2012; Maury et al., 2018; Payero et al., 2008). They are however unable to capture a full cycle of the largest Mexican SSEs: none of the individual temporary networks have continuously recorded a full 4-year SSE cycle, let alone multiple cycles. The Mexican National Seismological Service (SSN = Servicio Sismológico Nacional) has maintained a network for more than 100 years, but only more recently has the continuous broadband data been archived (Pérez-Campos et al., 2018). Figure 1 shows the starting date from when those data were available. Those stations in dark blue

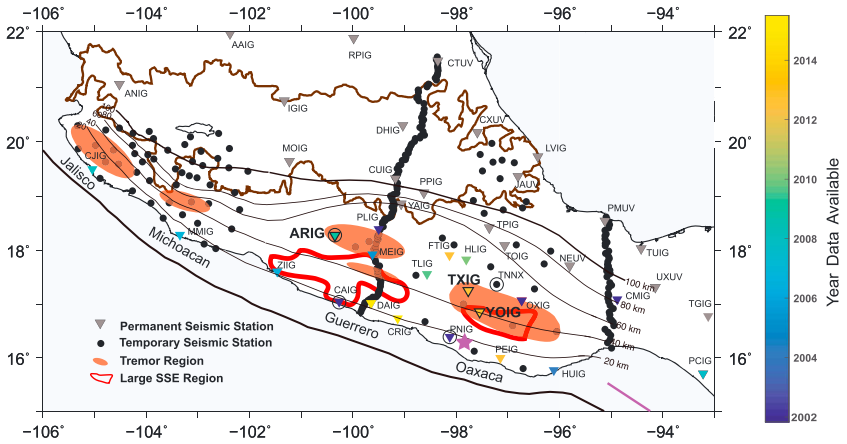

Figure 1. Map of broadband seismic station continuous data availability in Mexico since 2000. The black dots represent temporary seismic stations. The colored triangles are permanent Mexican National Seismological Service stations, although many have only been installed in the last few years. The highlighted stations represent the stations with tremor catalogs that we present here. Those in gray are far from the tectonic tremor region and were not used in this study. Those within the tremor region and on the coast are color coded by the year they were installed, as shown by the color bar. The open circles indicate the locations of GPS stations used in this study, which are all colocated with Mexican National Seismological Service stations or a previous temporary seismic station. The depth contours show the depth to the top of the subducted slab (Ferrari et al., 2012). The pink-shaded regions are where tremor has been found in previous studies (e.g., Brudzinski et al., 2010, 2016; Husker et al., 2012), although Maury et al. (2018) suggest that tremor is continuous across the entire zone. The red outlines represent the slow slip event regions (Graham et al., 2016). The name off the coast of each tremor region is the name of the state where that tremor is located. The purple star is the epicenter of the Pinotepa Nacional earthquake. The purple line is the fault line of the Tehuantepec earthquake.

were installed before 2002, but continuous data were not archived before then. The SSN network is much sparser than the temporary networks, but single station detection of tremor can generate multiyear catalogs to compliment the shorter, but higher-resolution, temporary catalogs (e.g., Brudzinski & Allen, 2007).

Multiple studies have shown that tremor is typically observed just above the background noise level (e.g., Beroza & Ide, 2011; Husker et al., 2010), making it challenging to automatically detect tremor. Previous detection methods have focused on leveraging information over a network in the time domain to identify tremor. Wech and Creager (2008) devised a network-based approach that employed a grid search over space to migrate continuous seismograms that were cross correlated in time to locate tremor with high correlations. Any locations with errors higher than 5 km were rejected as false detections. Husker et al. (2010) employed a 1- to 2-Hz notch filter and a median filter to eliminate local earthquakes and then summed all network stations within a short distance to identify tremor. Brudzinski and Allen (2007) developed a single-station detection method by analyzing seismic envelope amplitudes. They were however limited to the nighttime hours, because anthropogenic noise dominated the tremor bandwidth during the day.

Instead of analyzing tremor waveforms in the time domain, Walter et al. (2011) developed a detection method based in the frequency domain. Events were identified within sliding time windows when spectral amplitudes between 2 and 7 Hz rose above an empirical cutoff. However, single-station detection was not possible as they needed to stack the spectra over the entire network. Moreover, in order to eliminate local earthquakes with higher-frequency content than tremor, they had to remove detections that coincided with high energy at high frequencies.

Observations of tectonic tremor are consistently made in the 1- to 10-Hz frequency range, regardless of amplitude or source region (e.g., Beroza & Ide, 2011). This differs from earthquakes whose frequency content is strongly dependent on magnitude. We use this consistent spectral signature to develop a spectral detector that identifies tremor in the frequency domain. We searched for tremor in and around the general region where previous observations have been made in Mexico (Figure 1). Our method avoids the primary challenge that previous studies have encountered: avoiding false detections. The velocity spectra of local earthquakes (purple line in Figure 2) that are well above that of the tremor level (blue line in Figure 2) are eliminated because they are too high amplitude. However, smaller earthquakes (yellow line in

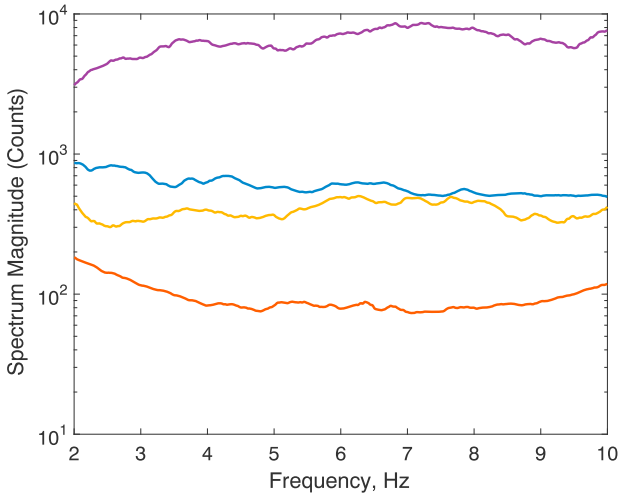

Figure 2. The velocity amplitude of a tremor spectral template at ARIG (blue) compared to a time window of background noise (red) and two earthquakes (purple and yellow). The purple line comes from a local earthquake seen on Figure 3 just before 14 hr. The yellow is an earthquake at 10.74 hr the same day with an amplitude similar to that of the tremor.

Figure 2) may be at the same level of the tremor. These events are eliminated by using a smoothing median filter. Signal stacking in time or over a network was not necessary with this method, and we did not need to limit our detection period to nighttime records. Here we present the methodology and an analysis of the new catalogs.

2. Methodology

We developed a spectral detection method to detect tectonic tremor within continuous seismic records. We created a tremor spectral template for each station by averaging the spectrum from at least five different visually identified tremors at each station. In order to generate a characteristic template for one station, tremors were randomly chosen over the entire recorded history at a station and no effort was made to use the same tremor between different stations. Each station was considered individually. The duration of the visually identified tremors varied, but they all lasted between 30 min and 2 hr for the catalogs presented in this study. This was because the only criteria for visually identifying the tremor was their spectrogram, and longer duration signals are more easily identifiable as tremor. No effort was made to locate any of the individual tremors. The averaging of many tremors was done in order to have an "average" template that represented a wide range of tremor sources detectable by the station. The template was compared with a running spectrum of the continuous data that was determined with a 60-s Fourier transform marched with 10% overlap between steps (54-s steps). Our average tremor template was generated in the same way to ensure the best match between tremor and the template during the detection process. We only used the horizontal components (average of the results of each individual component) as they always dominate the signal during tremor, due to the shearing mechanism responsible for tremor and their constituent LFEs (Cruz-Atienza et al., 2015; Frank et al., 2013). More often than not, it is difficult to observe tremor above the noise on the vertical component. This implies that the tremor we detect is within ~40 km of the station, which is the depth of the plate interface where they are located. We limited the spectral bandwidth of comparison to 2–10 Hz, because it has the greatest signal-to-noise ratio (SNR) in the SSN stations (Figure 2). The spectrums were smoothed with a 0.15-Hz-width running average to remove narrow-band spikes. The difference between the running spectrum and the template is normalized by the template to give a relative difference with respect to the template (equation (1)).

$$E_j = \frac{\left|\left(\sum_i (T_i - S_{ij})\right)\right|}{\sum_i (T_i)} \times 100, \tag{1}$$

where E is the difference percentage between the template, T, the spectrum, S, for frequency index i and time index j. This detection criteria allowed for eliminating earthquakes that were very different from the template (purple line Figure 2) and noise (red line Figure 2), but smaller local earthquakes still are relatively similar (yellow line Figure 2). These were eliminated by running a third-order median filter over E_j. Since the steps are 54 s long, as mentioned above, and the filter uses the median from the previous, current, and next step, earthquakes less than the step length are eliminated. This is effectively removes small earthquakes with similar amplitudes to tremor, because their durations are less than a minute. Finally, because the tremor signals can vary and be noisy themselves, a 12-min smoothing filter was applied as a last step to avoid "spiky" noise during a tremor episode. This last step also allowed for capturing any possible different tremor sources in the region and not just sources within the average template.

Figure 3 shows an example of tremor detection for one 24-hr period. The selection of the tremor in this spectrogram for averaging in the template would be the period from 20:30 to 21:30. The tremor extends slightly beyond this time period, but we select a window that contains the obvious tremor signal without any noise contamination. The low relative differences between the template and the spectrum is observed to coincide with the tremor seen on the spectrogram. The relative difference cutoff to detect tremor was set empirically to 67% using a visually determined catalog at ARIG, the SSN station closest to the Guerrero slow slip region

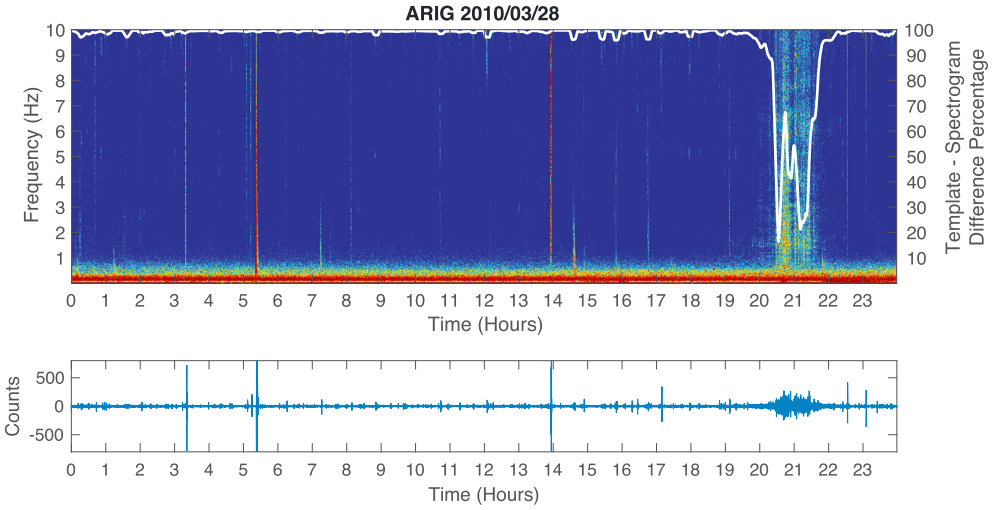

Figure 3. An example of tremor detection during 1 day. The top panel shows the spectrogram, while the bottom panel shows raw time series. (top) The white line indicates the difference percentage, E (equation (1)), between the template and the continuous seismic data. A detection is declared when the difference drops below 67%.

(Figure 4). We decided on this cutoff to reproduce as closely as possible the false detection rate of the visually determined catalog. We also tested cutoffs between 40% and 90% and found that the background rate does vary with the different thresholds. However, the relative rates between the different tremor burst types (discussed below) did not change with the threshold. We define the detected tremor as the time period below the chosen relative difference threshold. For example, the tremor shown in Figure 3 lasts from ~20:30 to ~21:40, making it just over 1 hr long. The detections with this method are well correlated with the visually identified tremor bursts (multiple detections of tremor over several days). The biggest difference was during the 2009 SSE: the automatic method detected more hours of tremor per day than the visual detection. We are confident in the results of our method, because it is well correlated with the GPS data (Figure 5). We speculate that the intense tremor activity during the 2009 SSE was difficult to visually capture in its entirety.

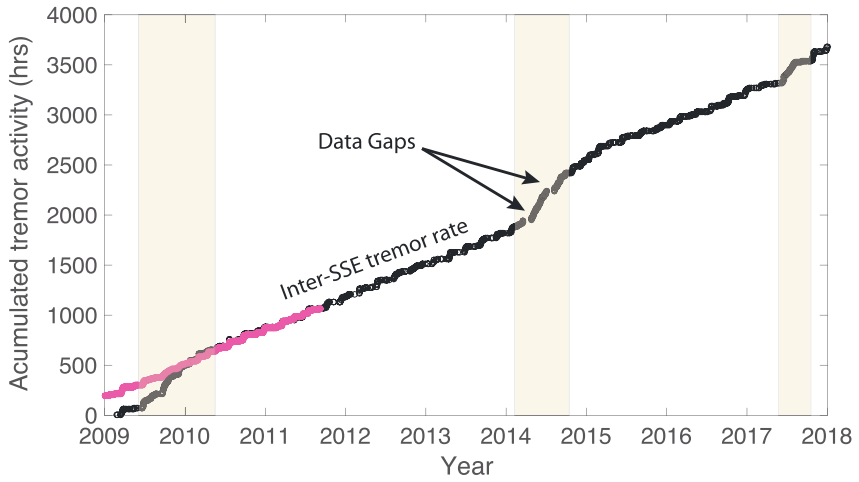

Figure 4. Automatic detection of tremor in the Guerrero region with the ARIG station (black circles) is compared to visual detection of tremors with many stations (purple circles). The visual detection was done with spectrograms from the permanent stations ARIG and MEIG and the temporary GGAP seismic array which included up to three more broadband seismometers. The visual catalog is vertically shifted (the y intercept is set to 200 instead of 0) so that it aligns with the automatically detected catalog. The khaki-colored regions show geodetically identified (GPS) SSEs. Note that there are two gaps in the data during the 2014 SSE. There are no other gaps in the data. SSE = slow slip event.

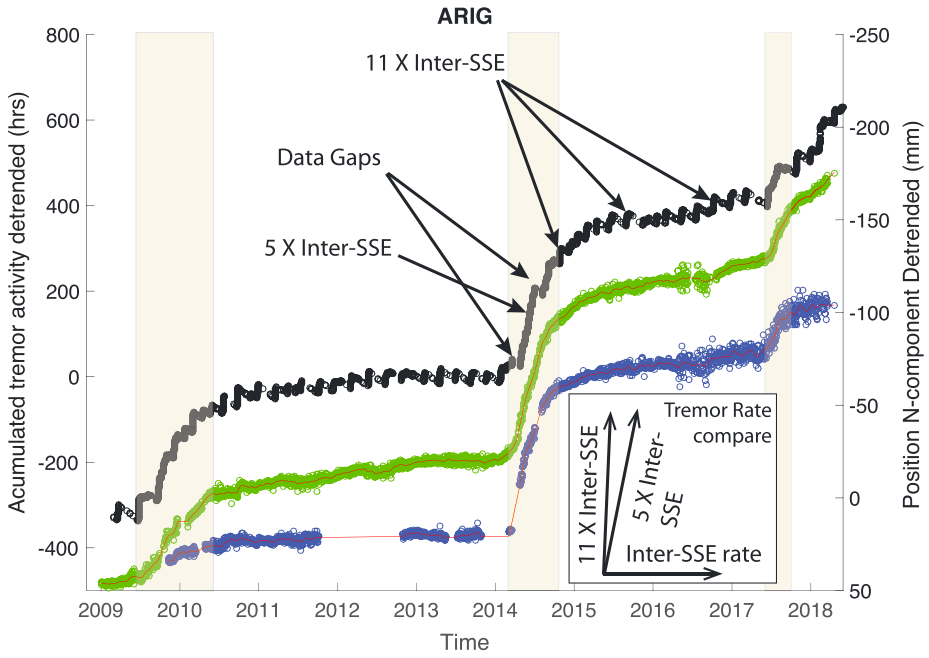

Figure 5. Automatic detection of Guerrero tremor from ARIG station. Cumulative tremor activity is detrended (black circles) and compared with the detrended N component of the GPS daily position time series at ARIG (blue circles) and CAIG (green circles). The removed trend for both the tremor catalogs and the GPS time series is estimated during the inter-SSE period. See Figure 1 for the locations of these stations. Note that the right axis is reversed (southward deformation is up) in order to align the GPS signal with the tremor. The khaki-colored regions show geodetically identified SSEs. The red lines represent the running average of each GPS time series. SSE = slow slip event.

Aside from ARIG, we also looked for tremor at the other permanent stations within the tremor zones and near the coast in Figure 1 (nongray inverted triangles). We were unable to find convincing tremor signals on any of the coastal stations, and no previous studies have found tremor near them either (Figure 1). CJIG was close to the tremor there; however, the data are only available after the temporary network was uninstalled and any catalog developed at CJIG cannot be verified with one generated by the temporary network. Developing a catalog at CJIG is a subject of future work. TLIG is so noisy that it has been discarded from previous tremor studies with the temporary network (González Molina, 2015). We were unable to visually detect tremor at OXIG to use as a template. This may be due to noise since it is in the middle of Oaxaca City, or it may be due to tremor sources actually being further from the station. Brudzinski et al. (2010) did not use OXIG in their study either. MEIG, although ideally situated to observe Guerrero tremor, has gone through various equipment changes over a number of years, and the data quality is unfortunately inconsistent. MEIG is also located near a mine which makes the data quite noisy (Frank, Shapiro, Husker, Kostoglodov, Gusev, et al., 2016). There were however times when it corroborated tremor detections at ARIG, but to keep the analysis simple we only used ARIG to detect tremor in Guerrero. The station PLIG, just to the north of the Guerrero tremor zone (Figure 1), detected tremor intermittently. Again, it went through equipment changes and the only time we were confident in its detections was when they corresponded with ARIG. We continue to work with the PLIG data and may be able to develop a catalog for later publication. The automatic method detected tremor at FTIG and HLIG at times, but also seemed to detect noise as they were located outside of the tremor region (Figure 1). We were not confident in the outputs of the method from these stations, so we do not analyze or report them here. In Oaxaca, tremor detection with our spectral template method at stations TXIG and YOIG worked well. We present their individual catalogs below.

3. Results

3.1. ARIG—Guerrero Tremor Zone

The ARIG station is the lowest noise SSN station within the Guerrero SSE region (Figure 1). To compare the ARIG tremor catalog with the GPS position time series, we detrend both data sets by their inter-SSE trends.

Table 1
Average Characteristics of Tremor Bursts in Guerrero and Oaxaca

	Inter-SSE tremor			Co-SSE tremor			
Region	Burst rate (*X* long-term rate)	Burst duration (days)	Burst interval (days)	Average rate (*X* long-term inter-SSE rate)	Burst rate (*X* long-term inter-SSE rate)	Burst duration (days)	Burst interval (days)
Guerrero	11.1 ± 2.6	5–7	60–90	5.2 ± 1.0	12.6 ± 2.3	1–2	4–5
Oaxaca	17.7 ± 3.0	2–4	35–85	2.6 ± 0.3	16.2 ± 1.2	1–3	7–12

We estimate the inter-SSE trend during 2013, because it was prior to the 2014 SSE and data were available on all three sensors. The inter-SSE tremor rate varies depending upon the cutoff as discussed above, but it is near 1 hr/day. The average rate of tremor during the large SSEs in Guerrero also varies with the cutoff, but maintains a rate ~5.2 times the inter-SSE rate (Figure 5, Table 1). Figure 5 shows that the detrended tremor activity correlates well with the detrended GPS signal. This is expected because tremor bursts are usually concurrent with SSEs, both large and small (Frank et al., 2015; Husker et al., 2012). The small SSEs associated with the frequent tremor bursts (every 60–90 days) are not directly apparent in the GPS signal, but recent work has shown that the stacking of the GPS time series during tremor bursts makes the geodetic signature of these small SSEs emerge (Frank et al., 2015). The small tremor bursts maintain rates of ~11.1 times the inter-SSE background rate (Figure 5, Table 1).

3.2. YOIG and TXIG—Oaxaca Tremor Zone

YOIG and TXIG were the only low noise stations within the Oaxaca slow slip region that produced reliable catalogs. The closest GPS station at PNIG was actually quite far (~ 80 km to YOIG and ~ 100 km to TXIG; Figure 1), but the GPS signal still mirrored the tremor catalog quite closely (Figure 6). In fact, unlike

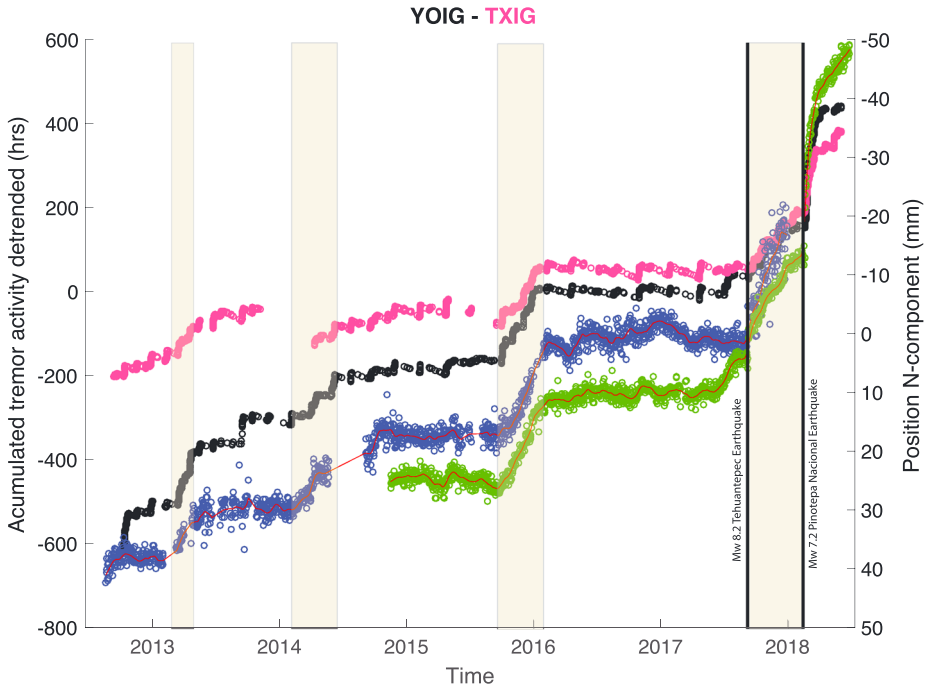

Figure 6. Automatic detection of tremor in Oaxaca from YOIG (black circles) and TXIG (pink circles) is detrended and compared with the detrended N component of the GPS daily record at PNIG (blue circles) and TNNX (green circles). Figure 1 shows the locations of those stations. Note that the right axis is reversed (southward deformation up) in order to align the GPS time series with the tremor. The red lines represent the running average of each GPS time series. The khaki-colored regions show geodetically identified slow slip events. Note that the gaps in the continuous seismic data at TXIG appear as reduced amounts of tremor after the data gaps. YOIG had no data gaps and should be used if there is doubt regarding gaps in TXIG data. The inset shows the GPS signal before removing the large postseismic signal of the 2012 Ometepec-Pinotepa Nacional earthquake with an exponentially decaying function.

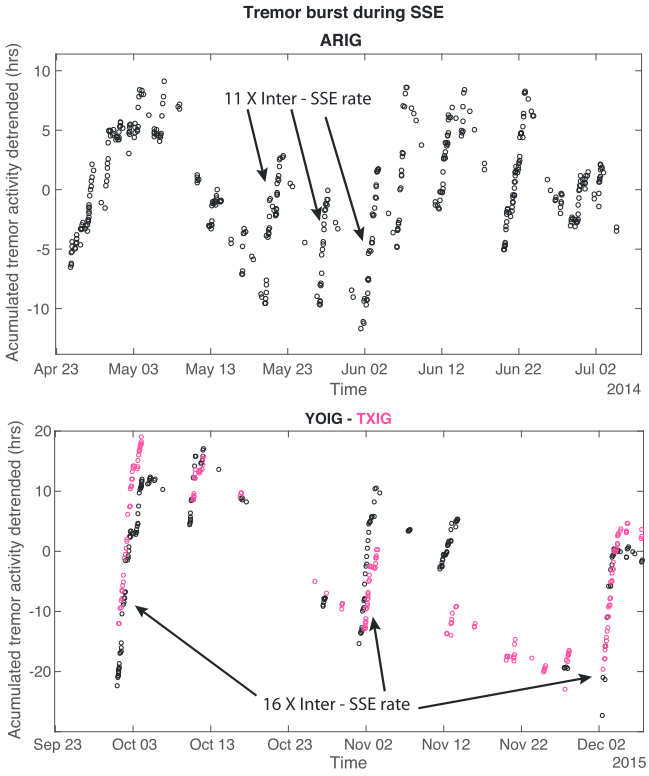

Figure 7. The cumulative tremor during the 2014 Guerrero SSE (top) and the 2015 Oaxaca SSE (bottom) are shown here detrended to be able to see the details. SSE = slow slip event.

ARIG, many of the smaller bursts here coincided with displacements in the GPS, particularly between the 2015–2016 SSE and the 2017–2018 SSE. The co-SSE rate is much larger than the inter-SSE rate similar to what we observed in Guerrero at ARIG (Table 1). The tremor rate between Oaxaca SSEs varied with the cutoff but was about 0.5 hr/day, similar to the Guerrero inter-SSE tremor rate. The larger tremor rate during Oaxaca SSEs was ~2.6 times the inter-SSE tremor rate.

Figure 7 shows the detected tremor activity during the 2014 Guerrero and 2015 Oaxaca SSEs. The intense tremor activity during slow slip is actually organized into a series of smaller bursts, similar to reports of clustered LFE and slow slip activity (Frank, Shapiro, Husker, Kostoglodov, & Campillo, 2016; Frank et al., 2018). This was also the case during the other large SSEs in both regions as well. The small bursts in Guerrero during slow slip were ~12.6 times the background inter-SSE rate (Figure 7). However, in Oaxaca the tremor rate in bursts (~16.2 times long-term inter-SSE rate) during the large SSEs were smaller on average than those between SSEs (~17.7 times long-term inter-SSE rate). Another difference between Guerrero and Oaxaca is that there is no clear sign of tapering from the SSE tremor rate to the inter-SSE rate in Oaxaca. This observation potentially suggests that the Oaxaca SSEs migrate over shorter distances than those in Guerrero.

The large tremor bursts associated with the large SSEs (which is actually made up of many smaller bursts) had a total duration of a few months in both regions. The smaller bursts in both regions had durations of several days, irrespective of whether they were inside or outside of the large SSE (Table 1). Focusing on a single burst, it is clear that there are even smaller bursts on the time scale of several hours. However, they were difficult to analyze in further detail, because our algorithm detects tremor on the time scale of tens of minutes, the same duration as the smallest scale bursts we observe. Observations of the clustering of LFE bursts down to timescales shorter than 20 min (Frank, Shapiro, Husker, Kostoglodov, & Campillo, 2016; Lengliné et al., 2017) corroborates our qualitative observation of tremor clustering on such timescales.

4. Discussion

The most common methods to identify tectonic tremor operate in the time domain, either detecting tremor through high SNR ratios over prolonged durations (Brudzinski & Allen, 2007; Nadeau & Dolenc, 2005) or by long-wavelength correlations of seismic envelopes (Ide, 2012; Obara, 2002; Wech & Creager, 2008). The detection method we present here operates instead in the frequency domain to take advantage of the characteristic spectral signature of tectonic tremor. A previously published method that operates in the frequency domain also searched for prolonged high SNR ratios over a network (Walter et al., 2011). By using spectral template comparison and a median filter, our method only requires one seismic station to make detections. This allows us to build tremor catalogs over time periods longer than the many temporary seismic deployments that drove previous work on tremor and LFEs in Mexico. The simplicity of our approach suggests that this method can be easily integrated into real-time analysis of continuous seismic data to provide rapid information on the status of imminent and ongoing SSEs.

Other authors have demonstrated that tremor and LFE activity is a precise indicator of slow fault slip from SSEs (e.g., Frank et al., 2015, 2018; Frank, Shapiro, Husker, Kostoglodov, & Campillo, 2016; Hawthorne & Rubin, 2013; Villafuerte & Cruz-Atienza, 2017). Here we observe this same relationship for tremor activity in Mexico during large SSEs, as summarized in Table 1. The SSEs in Guerrero were larger and produced faster tremor rates at ARIG than the large Oaxaca SSEs monitored by YOIG/TXIG. However, the smaller bursts within both regions had very similar tremor rates and similar recurrence intervals (Table 1). Previous work has shown that the smaller bursts in Guerrero are associated with small SSEs (Frank et al., 2015). We therefore suggest that the small tremor bursts in Oaxaca represent small SSEs that occur every ~50 days in

between the major SSEs. This implies that while Guerrero and Oaxaca have different characteristic recurrence times of SSEs, they both are organized into two main slow slip cycles: one long and one short. This method has no way of locating the tremors; therefore, the locations of the characteristic SSEs and their associated tremors must be assumed to be similar to previous studies.

We observe that the tremor rates and durations organize into discrete intervals forming tremor bursts during the inter-SSE period and a closely spaced series of tremor bursts during large-scale SSEs (Table 1). For example, in Guerrero continuous background tremor occurs on the order of ~1 hr/day (Figure 4) but is made up of week-long bursts with rates ~11 times the background rate every 60–90 days. During large SSEs, the tremor rate increases from ~1 hr/day to ~5 times that because the interval between bursts reduces significantly and the rate increases somewhat (Table 1). The bursts have very similar rates regardless of whether they occur during or in between major SSEs. This suggests that the dynamics of small short-term SSEs driving the tremor activity are the same, regardless of whether they occur individually or as part of a cascade of slow slip. This corroborates a recent study by Frank et al. (2018), which demonstrates that the large SSEs are made up of many small SSEs, just as a large tremor burst is a collection of many small bursts. Because the smaller tremor bursts/SSEs are similar both in rate and duration in both Guerrero and Oaxaca, we suggest that the smaller tremor bursts reflect a characteristic slow slip moment. This implies that the tremor rate is proportional to the rate of moment release and that the only way to achieve the higher tremor rates and moment release observed during large SSEs is to reduce the interevent times, or recurrence intervals, of the small SSEs driving tremor activity. An example of this is the 1-month period (June 2014, see top panel of Figure 7) during the 2014 Guerrero SSE when six small bursts occurred, or the 1-month period (November 2016, see bottom panel of Figure 7) during the 2015 Oaxaca SSE when two small bursts occurred. The small tremor bursts in Oaxaca are much higher relative to the background rate than those in Guerrero, but the total relative SSE burst rate in Guerrero (~5 times inter-SSE rate) is double that of Oaxaca (~2.6 times inter-SSE rate) due to the shorter time between the small bursts (Figure 7). This observation is both consistent with greater long-term moment release by slow slip in Guerrero than Oaxaca (Graham et al., 2016), and with reports of increased time clustering of slow earthquakes during large SSEs (Frank et al., 2018; Frank, Shapiro, Husker, Kostoglodov, & Campillo, 2016).

These tremor bursts are found to be made up of smaller individual tremor units that we have detected on the order of 20 min to a few hours. This corroborates physical models of tremor bursts within bursts (Daub et al., 2011) and suggests that this cascades down to LFEs (Frank, Shapiro, Husker, Kostoglodov, & Campillo, 2016; Lengliné et al., 2017). At each level the tremor organizes into specific discrete moment rates, which we identify here as a burst with a distinct tremor rate and duration, but there is no intermediate moment rate. We observe that long-term rates of tremor (~1 hr/day over several years) are composed of disparate tremor bursts (~10 hr/day over several days), which are themselves made up of individual tremors that last and recur on a timescale of minutes; we do not observe any intermediate rates or durations of tremor bursts. This is strong evidence of a mechanical or structural control on the moment rate of slow slip.

One of the useful aspects of these catalogs is that they help to distinguish when large slow slip is occurring. The geodetic signature of slow slip is emergent, and many months of GPS data must be seen in order to identify the start or stop of an SSE. Scientists at the Geophysics Institute, UNAM were monitoring the GPS time series in real time in anticipation of the 2018 Guerrero SSE but were unsure whether any deviation in the GPS signal in 2017 was an artifact or if the SSE had come early. The ARIG tremor catalog confirmed that the large SSE had indeed started earlier than expected. This SSE was very different than the previous SSEs. It appeared to have ended in August 2017 and caused a small surface displacement over a short duration relative to other large Guerrero SSEs. Continuing tremor observations suggest that there is more recent deformation, but precise GPS positions are not yet available to confirm. This example demonstrates that continuous catalogs are not only a useful tool for long-term research but are also essential for real-time monitoring.

Another analysis that is possible with the combination of the tremor catalog and the GPS observations is to observe SSE triggering. As mentioned above, it is difficult to identify the exact day an SSE starts from the emergent and scattered GPS records, but the tremor stops and starts with relatively clear phases seen in the cumulative records. This allows for the detailed mapping of when SSEs occur with respect to possible triggering events, such as a major regional or teleseismic earthquakes. Prolonged surface displacement at

both Oaxaca GPS stations and associated tremor on both Oaxaca seismic stations started 11 hr after the 8 September 2017 M_w 8.2 Tehuantepec earthquake (Figure 6). This may indicate that the earthquake triggered a large Oaxaca SSE, similar to observations of delayed triggering of slow slip on the San Andreas (Shelly et al., 2011). However, there was a moderate-sized SSE that appeared to end a month before and was only detected on the TNNX GPS station (Figure 6). We suggest that this was a separate event and that the M_w 8.2 earthquake triggered the large SSE, but this requires further study beyond the scope of this paper. Regardless of when the large SSE began, it continued until the 16 February 2018 M_w 7.2 Pinotepa Nacional earthquake. A tremor episode greater than any of the previous episodes detected and large deformation downdip at the TNNX GPS station coincided with the Pinotepa Nacional earthquake (Figure 6). A similar sequence occurred with the 2012 Mw 7.5 Ometepec earthquake, which was only 45 km from epicenter of this Pinotepa Nacional earthquake. It too was preceded by a large SSE; and after the earthquake occurred, there was large postseismic deformation downdip within the SSE region (Graham et al., 2014). Our observations suggest that the same sequence of an SSE, followed by a $M7+$ earthquake and large postseismic deformation downdip in the SSE region occurred in 2018, with the only difference being that perhaps the large SSE was triggered by the 2017 Tehuantepec M_w 8.2 earthquake. These observations for the most part are coincidental, using only the initiation times of the SSEs combined with the catalogs and comparing them with large earthquakes. The relationship between the 2017 Oaxaca SSE and the 2017 Tehuantepec earthquake in particular needs more analysis. However, it is clear that the Pinotepa Nacional earthquake occurred during a large SSE. This means that all three $M_w > 7$ thrust earthquakes on the subduction zone interface in Mexico, which have occurred since geodetic networks have been able to record slow slip, have occurred during an SSE (Graham et al., 2014; Radiguet et al., 2016). Although this is a small data set, it merits continued observation, which this method provides.

None of the dates of initiation or termination of tremor/SSE in Guerrero (ARIG) coincides with any of the recent large Mexican earthquakes. The 2014 M_w 7.3 Papanoa, Guerrero earthquake occurred during the first data gap in 2014, so our catalog provides no new information about the relation between it and tremor. Our catalog observed a week-long tremor burst starting about 30 min after the 2010 Maule, Chile earthquake coinciding with previous evidence of triggered tremor in Mexico by that earthquake (Zigone et al., 2012).

5. Conclusions

We present catalogs of tremor from permanent stations within the Mexican National Seismological Service (SSN). The catalogs were generated using single-station detection by means of spectral template matching. The catalogs correlate well with geodetically observed SSEs. These continuous catalogs allow for the analysis of many cycles of large SSEs in Mexico, which was previously not possible with previous tremor detection techniques that required interstation spacing smaller than that of the permanent network. The analysis found discrete intervals of tremor rate/duration in Guerrero and Oaxaca, suggesting characteristic moment release rates of slow slip. We also report the first evidence of short-term SSEs in Oaxaca, just as is observed in Guerrero. We provide further evidence that bursts of tremor are made up of a scale-invariant cluster of slow earthquakes (e.g., Frank et al., 2018; Frank, Shapiro, Husker, Kostoglodov, & Campillo, 2016). Finally, this technique can be extended to other regions with a sparse permanent network (50+-km station spacing) to improve real-time monitoring of slow aseismic slip.

Acknowledgments
SSN data were obtained from the Servicio Sismológico Nacional (México). We thank its personnel for station maintenance, data acquisition, and distribution. Data can be accessed at www.ssn.unam.mx. This work was funded by a grant from UNAM, PAPIIT IN107116.

References

Beroza, G., & Ide, S. (2011). Slow earthquakes and nonvolcanic tremor. *Annual Review of Earth and Planetary Sciences*, *39*(1), 271–296. https://doi.org/10.1146/annurev-earth-040809-152531

Brudzinski, M., Schlanser, K., Kelly, N., DeMets, C., Grand, S., Márquez-Azúa, B., & Cabral-Cano, E. (2016). Tectonic tremor and slow slip along the northwestern section of the Mexico subduction zone. *Earth and Planetary Science Letters*, *454*, 259–271. https://doi.org/10.1016/j.epsl.2016.08.004

Brudzinski, M. R., & Allen, R. M. (2007). Segmentation in episodic tremor and slip all along Cascadia. *Geology*, *35*(10), 907–910. https://doi.org/10.1130/G23740A.1

Brudzinski, M. R., Hinojosa-Prieto, H. R., Schlanser, K. M., Cabral-Cano, E., Arciniega-Ceballos, A., Diaz-Molina, O., & DeMets, C. (2010). Nonvolcanic tremor along the Oaxaca segment of the middle America subduction zone. *Journal of Geophysical Research*, *115*, B00A23. https://doi.org/10.1029/2008JB006061

Cruz-Atienza, V., Husker, A., Legrand, D., Caballero, E., & Kostoglodov, V. (2015). Nonvolcanic tremor locations and mechanisms in Guerrero, Mexico, from energy-based and particle motion polarization analysis. *Journal of Geophysical Research: Solid Earth*, *120*, 275–289. https://doi.org/10.1002/2014jb011389

Daub, E., Shelly, D., Guyer, R., & Johnson, P. (2011). Brittle and ductile friction and the physics of tectonic tremor. *Geophysical Research Letters*, *38*, L10301. https://doi.org/10.1029/2011gl046866

Dragert, H., Wang, K., & James, T. S. (2001). A silent slip event on the deeper Cascadia subduction interface. *Science*, *292*(5521), 1525–1528. https://doi.org/10.1126/science.1060152

Ferrari, L., Orozco-Esquivel, T., Manea, T., & Manea, M. (2012). The dynamic history of the trans-Mexican volcanic belt and the Mexico subduction zone. *Tectonophysics*, *522-523*, 122–149. https://doi.org/10.1016/j.tecto.2011.09.018

Frank, W. B., Radiguet, M., Rousset, B., Shapiro, N. M., Husker, A. L., Kostoglodov, V., et al. (2015). Uncovering the geodetic signature of silent slip through repeating earthquakes. *Geophysical Research Letters*, *42*, 2774–2779. https://doi.org/10.1002/2015GL063685

Frank, W. B., Rousset, B., Lasserre, C., & Campillo, M. (2018). Revealing the cluster of slow transients behind a large slow slip event. *Science Advances*, *4*(5), eaat0661. https://doi.org/10.1126/sciadv.aat0661

Frank, W. B., Shapiro, N. M., Husker, A. L., Kostoglodov, V., & Campillo, M. (2016). Repeating seismicity in the shallow crust modulated by transient stress perturbations. *Tectonophysics*, *687*, 105–110. https://doi.org/10.1016/j.tecto.2016.09.003

Frank, W. B., Shapiro, N. M., Husker, A. L., Kostoglodov, V., Gusev, A. A., & Campillo, M. (2016). The evolving interaction of low-frequency earthquakes during transient slip. *Science Advances*, *2*(4). https://doi.org/10.1126/sciadv.1501616

Frank, W. B., Shapiro, N. M., Husker, A. L., Kostoglodov, V., Romanenko, A., & Campillo, M. (2014). Using systematically characterized low-frequency earthquakes as a fault probe in Guerrero, Mexico. *Journal of Geophysical Research: Solid Earth*, *119*, 7686–7700. https://doi.org/10.1002/2014JB011457

Frank, W. B., Shapiro, N. M., Kostoglodov, V., Husker, A. L., Campillo, M., Payero, J. S., & Prieto, G. A. (2013). Low-frequency earthquakes in the Mexican sweet spot. *Geophysical Research Letters*, *40*, 2661–2666. https://doi.org/10.1002/grl.50561

González Molina, G. (2015). Tremores no volcánicos (tnvs): detección y localización, (Bachelor's thesis). Retrieved from TESIUNAM. (http://oreon.dgbiblio.unam.mx/F/A5HBI3M31C99LSV36LYS6FHYJC714N2CY7AX6MJNK2QDL4UUAQ-62236?func=find-b&request=husker&find_code=WASE&adjacent=N&local_base=TES01&x=0&y=0&filter_code_2=WYR&filter_request_2=2015&filter_code_3=WYR&filter_request_3=2015). Mexico City, Mexico.

Graham, S., DeMets, C., Cabral-Cano, E., Kostoglodov, V., Rousset, B., Walpersdorf, A., et al. (2016). Slow slip history for the Mexico subduction zone: 2005 through 2011. *Pure and Applied Geophysics*, *173*(10–11), 3445–3465.

Graham, S., DeMets, C., Cabral-Cano, E., Kostoglodov, V., Walpersdorf, A., Cotte, N., et al. (2014). GPS constraints on the *Mw* = 7.5 Ometepec earthquake sequence, southern Mexico: Coseismic and post-seismic deformation. *Geophysical Journal International*, *199*(1), 200–218. https://doi.org/10.1093/gji/ggu167

Hawthorne, J. C., & Rubin, A. M. (2013). Short-time scale correlation between slow slip and tremor in Cascadia. *Journal of Geophysical Research: Solid Earth*, *118*, 1316–1329. https://doi.org/10.1002/jgrb.50103

Husker, A., Peyrat, S., Shapiro, N., & Kostoglodov, V. (2010). Automatic non-volcanic tremor detection in the Mexican subduction zone. *Geofisica Internacional.*, *49*(1), 17–25.

Husker, A. L., Kostoglodov, V., Cruz-Atienza, V. M., Legrand, D., Shapiro, N. M., Payero, J. S., et al. (2012). Temporal variations of non-volcanic tremor (NVT) locations in the Mexican subduction zone: Finding the NVT sweet spot. *Geochemistry, Geophysics, Geosystems*, *13*, Q03011. https://doi.org/10.1029/2011GC003916

Ide, S. (2012). Variety and spatial heterogeneity of tectonic tremor worldwide. *Journal of Geophysical Research*, *117*, B03302. https://doi.org/10.1029/2011JB008840

Kostoglodov, V., Husker, A., Shapiro, N. M., Payero, J. S., Campillo, M., Cotte, N., & Clayton, R. (2010). The 2006 slow slip event and nonvolcanic tremor in the Mexican subduction zone. *Geophysical Research Letters*, *37*, L24301. https://doi.org/10.1029/2010GL045424

Lengliné, O., Frank, W. B., Marsan, D., & Ampuero, J. P. (2017). Imbricated slip rate processes during slow slip transients imaged by low-frequency earthquakes. *Earth and Planetary Science Letters*, *476*, 122–131. https://doi.org/10.1016/j.epsl.2017.07.032

Maury, J., Ide, S., Cruz-Atienza, V. M., & Kostoglodov, V. (2018). Spatiotemporal variations in slow earthquakes along the Mexican subduction zone. *Journal of Geophysical Research: Solid Earth*, *123*, 1559–1575. https://doi.org/10.1002/2017jb014690

Nadeau, R. M., & Dolenc, D. (2005). Nonvolcanic tremors deep beneath the San Andreas fault. *Science*, *307*(5708), 389–389. https://doi.org/10.1126/science.1107142

Obara, K. (2002). Nonvolcanic deep tremor associated with subduction in Southwest Japan. *Science*, *296*(5573), 1679–1681. https://doi.org/10.1126/science.1070378

Obara, K., & Kato, A. (2016). Connecting slow earthquakes to huge earthquakes. *Science*, *353*(6296), 253–257. https://doi.org/10.1126/science.aaf1512

Payero, J. S., Kostoglodov, V., Shapiro, N., Mikumo, T., Iglesias, A., Pérez-Campos, X., & Clayton, R. W. (2008). Nonvolcanic tremor observed in the Mexican subduction zone. *Geophysical Research Letters*, *35*, L07305. https://doi.org/10.1029/2007GL032877

Pérez-Campos, X., Espíndola, V. H., Pérez, J., Estrada, J. A., Monroy, C. C., Bello, D., et al. (2018). The Mexican national seismological service: An overview. *Seismological Research Letters*, *89*(2A), 18–323.

Radiguet, M., Perfettini, H., Cotte, N., Gualandi, A., Valette, B., Kostoglodov, V., et al. (2016). Triggering of the 2014 *Mw* 7.3 Papanoa earthquake by a slow slip event in Guerrero, Mexico. *Nature Geoscience*, *9*(11), 829–833. https://doi.org/10.1038/ngeo2817

Shelly, D. R., Beroza, G. C., & Ide, S. (2007). Non-volcanic tremor and low-frequency earthquake swarms. *Nature*, *446*(7133), 305–307. https://doi.org/10.1038/nature05666

Shelly, D. R., Peng, Z., Hill, D. P., & Aiken, C. (2011). Triggered creep as a possible mechanism for delayed dynamic triggering of tremor and earthquakes. *Nature Geoscience*, *4*(6), 384–388. https://doi.org/10.1038/ngeo1141

Villafuerte, C., & Cruz-Atienza, V. (2017). Insights into the causal relationship between slow slip and tectonic tremor in Guerrero, Mexico. *Journal of Geophysical Research: Solid Earth*, *122*, 6642–6656. https://doi.org/10.1002/2017JB014037

Walter, J., Schwartz, S., Protti, M., & Gonzalez, V. (2011). Persistent tremor within the northern Costa Rica seismogenic zone. *Geophysical Research Letters*, *38*, L01307. https://doi.org/10.1029/2010gl045586

Wech, A. G., & Creager, K. C. (2008). Automated detection and location of Cascadia tremor. *Geophysical Research Letters*, *35*, L20302. https://doi.org/10.1029/2008GL035458

Zigone, D., Rivet, D., Radiguet, M., Campillo, M., Voisin, C., Cotte, N., et al. (2012). Triggering of tremors and slow slip event in Guerrero, Mexico, by the 2010 *Mw* 8.8 Maule, Chile, earthquake. *Journal of Geophysical Research*, *117*, B09304. https://doi.org/10.1029/2012jb009160

In Fig. 3-9 the cumulative NVT count in 2016-2019 is compared to geodetic time series from the nearby GPS sites, both sets of time series detrended accordingly. It is clearly seen that the occurence of the tremor burst at ARIG (Arcelia) and PLIG (Platanillo) stations coincides with the initiation of the slow slip event observed at IGUA site. Therefore, the cumulative NVT time series allow to select the SSE onset especially when it is challenging to distinguish the signal of slow deformation overlapped by postseismic afterslip.

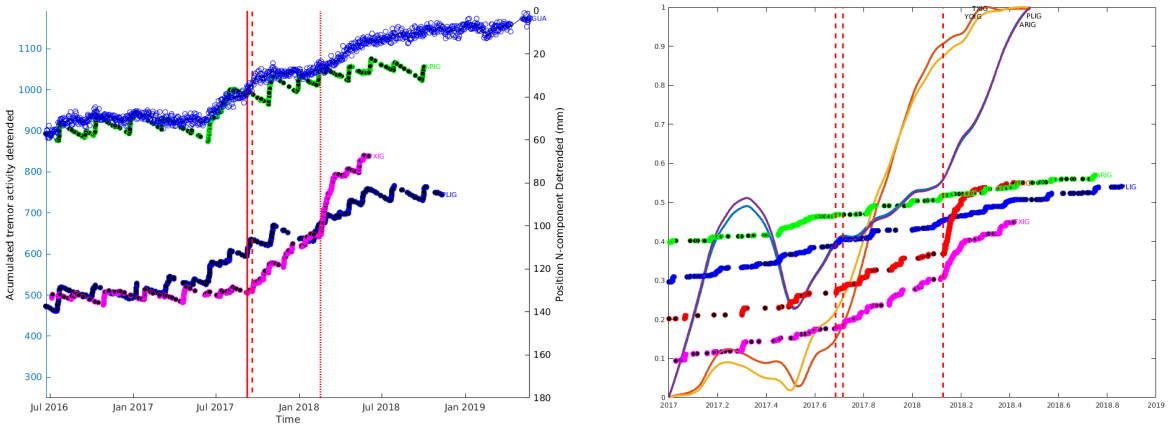

(a) (b)

Figure 3-9: (a) Cumulative NVT activity compared to detrended geodetic time series at IGUA station in Iguala, Guerrero. (b) Cumulative NVT activity compared to seismic moment rate at the stations in Oaxaca (TXIG and YOIG) and in Guerrero (PLIG and ARIG).

Chapter 4

Discussion

4.1 Interaction between Guerrero and Oaxaca SSEs in 2017-2019 with large earthquakes and its influence on the LVC fault system

An unusual sequence of tectonic phenomena observed in Mexico in 2017-2018 included several major events. Three large earthquakes occurred in different parts of the country and two SSEs took place in the states of Guerrero and Oaxaca (Fig. 4-1). All these events significantly alternated the state of stress in the region and produced causal effects on the subsequent tectonic deformation. First, the geodetic time series from the stations in Guerrero and Oaxaca showed the quasi-simultaneous initiation of the Oaxaca and the 1st stage Guerrero SSEs in April-June 2017. Next, on the September 8, 2017 the Chiapas earthquake M_w8.2 occurred on a normal fault offshore in the Tehuantepec Gap. It was the biggest event of the sequence. 11 days later, on September 19, 2017 Puebla-Morelos earthquake M_w7.1 produced significant shaking in the Mexican Valley. On February 16, 2018 Pinotepa earthquake M_w7.2 ruptured a shallow segment of Mexican subduction zone in Oaxaca. Nearly at the same time the Oaxaca SSE terminated. Eventually, the 2nd stage of Guerrero SSE started almost simultaneously with the Pinotepa event and continued till the beginning of June 2018.

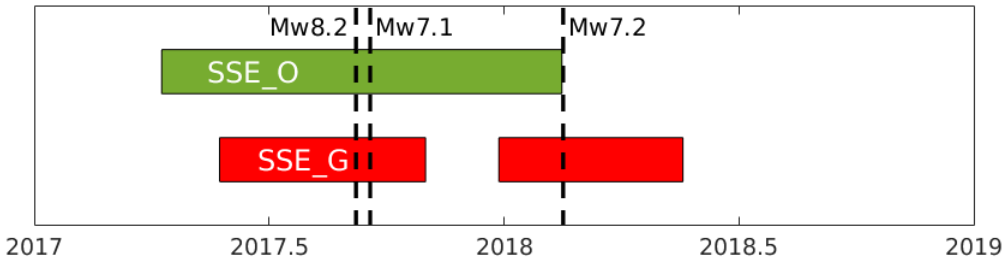

Figure 4-1: Timeline of the tectonic sequence of 2017-2018 in Guerrero and Oaxaca. *SSE_G* - two stages of Guerrero slow slip event, *SSE_O* - Oaxaca slow slip. Black dashed lines mark the three large earthquakes in Chiapas, Puebla-Morelos and Pinotepa consecutively.

The first stage of the Guerrero SSE initiates in the northwestern part of the Guerrero Gap and propagates southeastwards where the second stage takes place. Maximum slip (∼0.20m) of the 2 stages of Guerrero SSE is located inside the Guerrero Gap area (-101.2° —-99.2°E) at ∼ -100°E. The unusual 2-stage temporal evolution of the SSE in Guerrero is reminiscent of the event of 2009-2010 (Fig. 3-6).

In order to analyze the slow slip phenomena the initial dataset has been cleaned from the effects of postseismic deformation produced by Chiapas and Pinotepa earthquakes (described in Subsections 2.3.2, 3.1.2, 3.1.3). The maximum slip amplitude of the Pinotepa earthquake postseismic deformation is observed around the epicenter in the shallow part of the subduction zone extending several kilometers off-shore. Mainly the postseismic slip stays within the limits of the Oaxaca SSE patch. Some portion of the slip propagates towards northwest and reaches the area of the Guerrero SSE (Fig. 3-3). Thus I assume that the northwestern stations TLIG and TNAT are affected by three different tectonic signals (Oaxaca SSE, Guerrero SSE and Pinotepa afterslip) the most. The postseismic deformation from the Chiapas M_w8.2 earthquake didn't have any spatial interaction with the slow transients in Guerrero and Oaxaca since it occurred on a normal crustal fault and far away from the SSE patches.

The location of many slow slip events immediately down-dip from seismogenic zones suggests they could trigger large thrust earthquakes. For example, the 11 March 2011 M_w9.0 Tohoku-Oki earthquake in Japan [Ito *et al.*, 2013], 20 March 2012 M_w7.4 Ometepec earthquake on the Mexico subduction zone [Graham *et al.*, 2014a], and 2014 M_w8.1 Iquique earthquake

in Chile [Ruiz *et al.*, 2014] were all preceded by SSEs close to or overlapping the eventual earthquake rupture zones. Numerical simulations of slow slip suggest that repeated SSEs in the transition zone between stick-slip and creep areas concentrate stress at the down-dip limit of the seismogenic zone, which in turn increases the probability that a future SSE will evolve into a dynamic rupture [Segall and Bradley, 2012] [Graham *et al.*, 2015]. The snapshots of slip evolution (Fig. 3-7) show that Oaxaca SSE and the first stage of Guerrero SSE propagate towards and inside the seismogenic zone of the plate interface approaching the epicentral area of the Pinotepa earthquake. Therefore, it suggests that SSE induced stress changes at the subduction interface served as a trigger to onset the M_w7.2 seismic event in Pinotepa. According to the timing and a close proximity to the Pinotepa epicenter the second stage of Guerrero SSE seems to be triggered by the above-mentioned seismic event. Meanwhile, the Oaxaca SSE appears to be terminated before the M_w7.2 earthquake. However, it is important to consider that the method of separating postseismic deformation from the GPS time series could have affected the integrity of the SSE signal since both overlap in time. The Oaxaca SSE could still be ongoing for another couple of days or weeks after the Pinotepa earthquake struck.

Triggering relationships between seismic and aseismic events in Guerrero and Oaxaca in 2017-2019 can also be retrieved from the seismic moment rate. Moment rate is computed for the dataset without the postseismic contribution of Chiapas and Pinotepa earthquakes. The resulting curves are smoothed over a window of 70 days. The beginning of both Oaxaca and Guerrero SSEs is visible around June 2017 when the slope tangent of the moment rate increases (Fig. 4-2). The curves of the seismic moment rate show the change of slope following Chiapas and Oaxaca events for the region of Guerrero. It appears that after the Chiapas earthquake the seismic moment release in Guerrero slowed down. Meanwhile after the Pinotepa event the moment release slope for Guerrero area became more steep. For the Oaxaca region the trend is more linear. It is still noticeable that the Pinotepa earthquake decelerated seismic moment rate in Oaxaca area. That is also seen in the snapshots of slip evolution (Fig. 3-7). These observations support the hypothesis of the second stage of the Guerrero SSE triggered by the Pinotepa earthquake and the possibility that Pinotepa earthquake was brought to rupture by

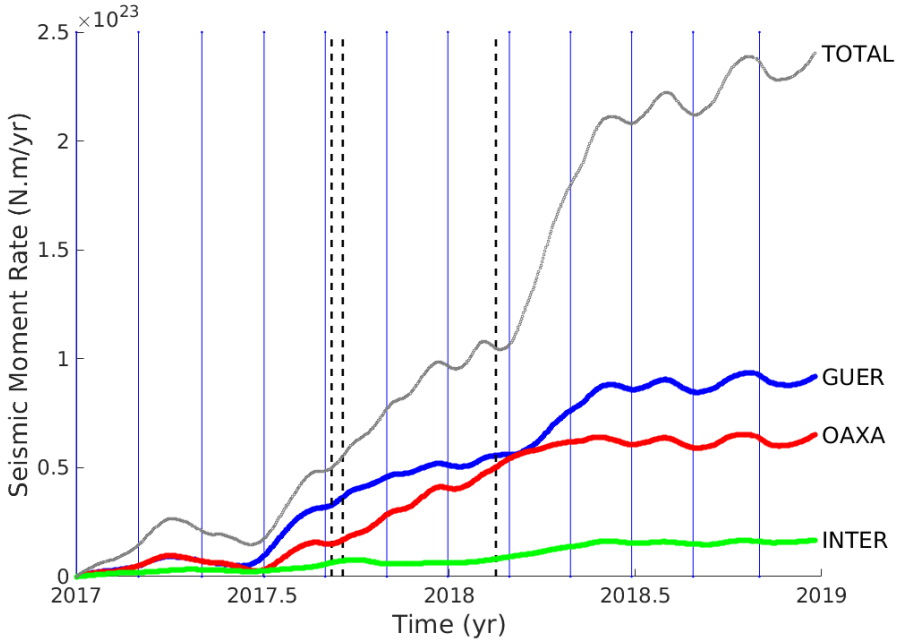

Figure 4-2: Comparison of seismic moment rates corresponding to SSEs only (blue, red and green curves) and to SSEs together with the contribution from the earthquakes (gray curve). The rates are calculated separately for Guerrero (blue), Oaxaca (red) and the intermediate zone (green). Blue horizontal lines mark every two months. Black dashed lines mark Chiapas, Puebla and Pinotepa earthquakes consecutively.

the propagation of Oaxaca and first stage Guerrero slow slip events. The Guerrero and Oaxaca sections of subduction zone apparently reached critical interseismic loading and were ready to release the accumulated stress. However, due to different mechanical rock properties [Radiguet *et al.*, 2012; Husker *et al.*, 2017] at the subduction interface the stress release resulted in different forms of deformation. Thus, in the shallow part of the subduction in the vicinity of Pinotepa the stress was released rapidly in a seismic event, while in conditionally stable fluid-rich downdip area of subduction in Guerrero Gap (Fig. 4-3) a slow slip transient was observed.

The impact of the subduction zone tectonic events on the LVC fault can be inferred from the Fig. 3-8. Trench-parallel components at 9 GPS stations in Guerrero state (Fig. 3-8a) show repeated episodes of velocity reversals attributed to motion at the La Venta Chacalapa fault zone. These anomalous transients have correlation in time with subduction slow slip events. Stations located along the coast (CAYA, DOAR, CPDP, ACAP, ACYA) have a common pattern

of accelerating-decelerating velocity reversals. On the contrary, stations located more inland (IGUA, MEZC, LAZA, OCOT) have an opposite decelerating-accelerating trend. Notably, these two groups of stations are located on different sides of the LVC trace. This observation implies that during the subduction SSE there is an accompanying strike-slip creeping motion along the segments of the LVC shear zone.

During interSSE periods while the interplate strain is accumulating the LVC fault system remains coupled and no anomalous motion is observed in the time series. The reversed motion in the trench parallel component occurs during subduction slow slip episodes. The stress that kept the LVC fault segments locked is reduced thus allowing left-lateral strike-slip motion along the forearc crustal faults. There are two distinguished stages of the observed strike-slip transient. During the first stage we observe eastward motion at the stations CAYA, DOAR, ACAP, ACYA, CPDP (less prominent) and westward motion at the sites LAZA, MEZC, IGUA, OCOT. During the second stage the above mentioned stations move in the opposite directions. In the SSE episodes of 1997, 2001/02, 2006, 2009/10 the deformation along the LVC fault system appears to be elastic since it fully recovers during the velocity reversals. Starting from the SSE of 2014, that triggered M_w7.3 Papanoa earthquake [Radiguet *et al.*, 2016], the reverse pattern seems to disappear. So the LVC faults begin accumulating sinistral deformation. However, at CAYA the reverse motion is observed again in the 2017-2018 SSE sequence. That change in the deformation behavior can be attributed to the complex nature of the slow slip and large earthquakes of 2017 interaction that caused stress redistribution along the fault zone.

Trench parallel motion along the coast of Oaxaca doesn't show a similar clear pattern of strike-slip SSEs along the LVC fault system (Fig. 3-8b). However, we still detect SSE-like deformation with shorter recurrence interval and of smaller magnitude than those in Guerrero that also corresponds to periods of subduction slow slip events. It is known that the SSEs in Oaxaca occur more frequently than in Guerrero and the slip magnitude of these events is smaller. This behavior apparently affects the type of creeping motion at the LVC in Oaxaca.

Evidence of mylonitization in the study area together with geodetic observations proves that the LVC fault system has been active till present day. So far only aseismic processes have

been detected at this tectonic structure. However, it is important to pay attention to the strain that accumulates after some subduction SSEs (similar to 2014 or 2017 events accompanied by major subduction earthquakes) at the Guerrero section of the LVC fault. This deformation pattern might occur again and then the accumulated stress could potentially be released either aseismically (as it happened before) or through a shallow crustal earthquake. The possibility to have a seismic event at the LVC fault strongly depends on the physical properties of rocks comprising it. Conductivity structure obtained from the magnetotelluric (MT) section [Arzate-Flores *et al.*, 2016] in Oaxaca crossing Xolapa terrain at the level of Puerto Escondido shows that LVC passes at the top of the subduction SSE where fluids rise into the upper crust (Fig. 4-4). These conditions are auspicious to aseismic deformations at the LVC fault system. Additional MT studies along LVC in Guerrero and other locations in Oaxaca with higher resolution at shallow depths would improve both the idea about the fault geometry as well as about its physical properties.

Further research and analysis of the LVC fault system is needed. Primarily, it is important to infer the geometry of the principal fault sections. The area where the fault passes is of challenging access along most part of its trace. Additional GPS stations, especially on the inland side of the LVC fault and along its Oaxaca section, would greatly complement present SSE observations. Seismic stations would as well contribute a significant portion of data on NVT episodes and low frequency earthquakes (LFE) in the study area. Parts of the fault that can safely be accessed would benefit from drone digital mapping. Since SSEs have been observed along this fault trace therefore we might expect the presence of fluids that can be revealed with electrical resistivity studies.

The LVC fault system poses a great potential risk to numerous highly vulnerable towns and villages as well as infrastructure located in the vicinity. Once the geometry of this fault system is known it'll become possible to perform inversions and locate the areas of higher strain accumulation and therefore identify the most risk-prone spots.

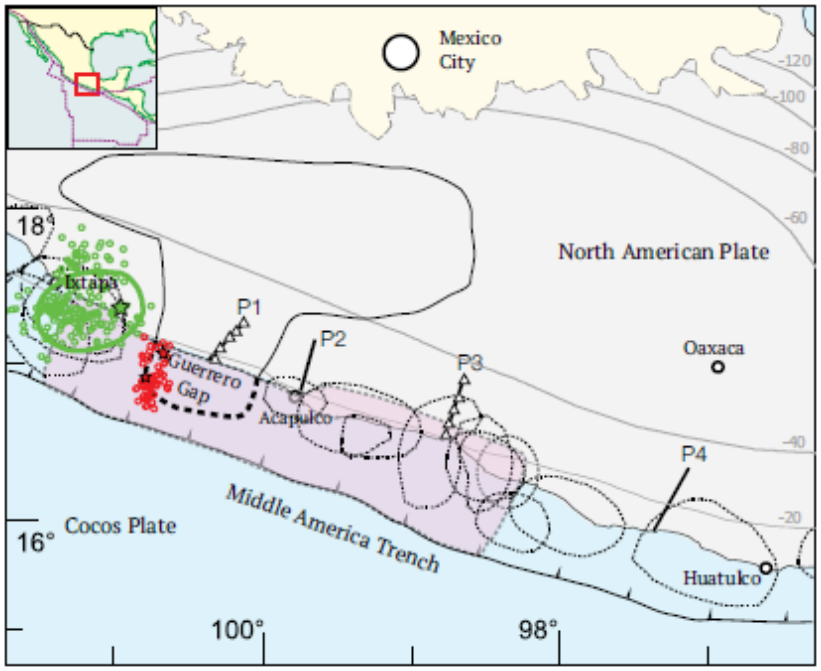

(a) Study area (red square, inset) in southern Mexico coast. Profiles P1-P4 are magnetotelluric profiles, with triangles showing sounding locations. Solid black line outlines repeating SSE region, with thick dashed line showing poorly constrained extent of SSEs [Radiguet *et al.*, 2012]. Thick green outline is area of 2014 M_w7.3 Papanoa, Mexico. Green star is epicenter of mainshock. Small green circles are aftershocks. Red stars are epicenters of the two largest aftershocks (M_w 6.5 and 6.1) with associated aftershocks as red circles. Dotted gray lines are contours of large historical mega-thrust earthquakes. Solid thin gray lines mark depth profile [Ferrari *et al.*, 2012]. Cream-colored region represents Trans-Mexican Volcanic Belt.

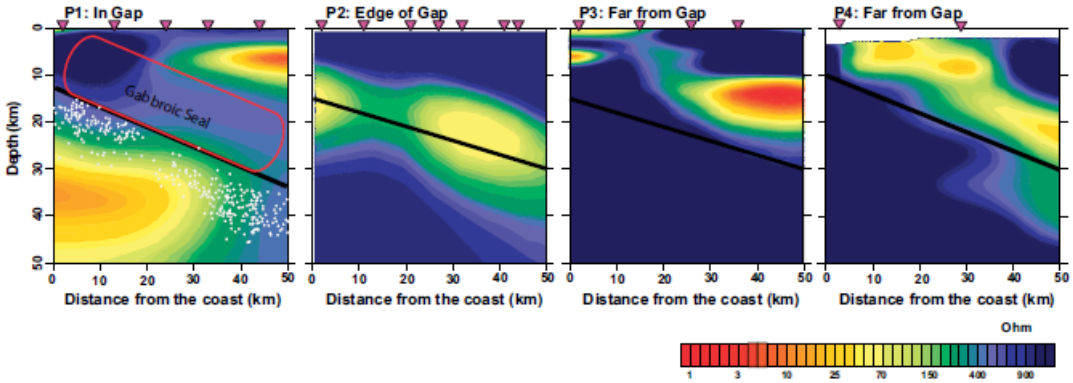

(b) Magnetotelluric (MT) profiles. Color scheme goes from resistive (blue) to conductive (red). Black line is a slab interface. In the gap (P1), the high-conductivity layer likely indicates free fluids within the oceanic crust, capped by an impermeable seal. Capped free fluids are likely over-pressurized, which lowers the normal stress allowing for the SSEs. [Husker *et al.*, 2017]

Figure 4-3: Modified from [Husker *et al.*, 2017]

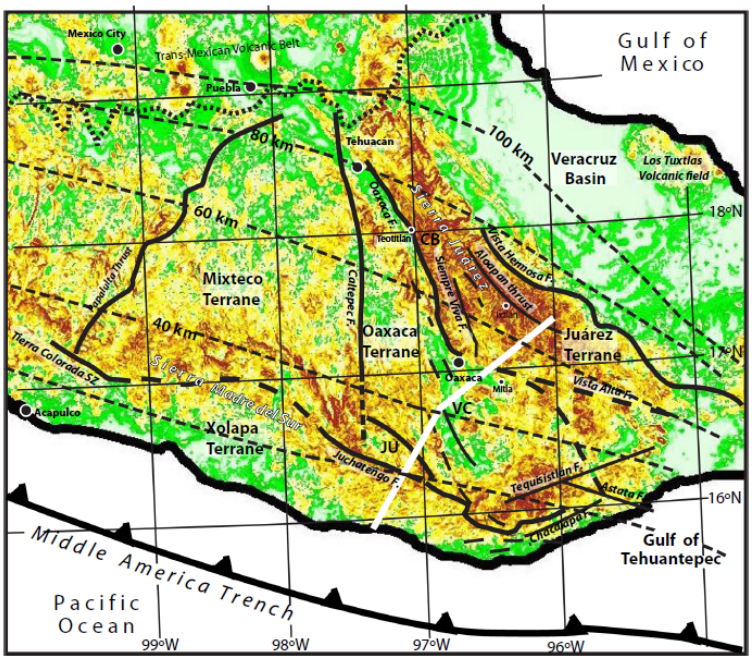

(a)

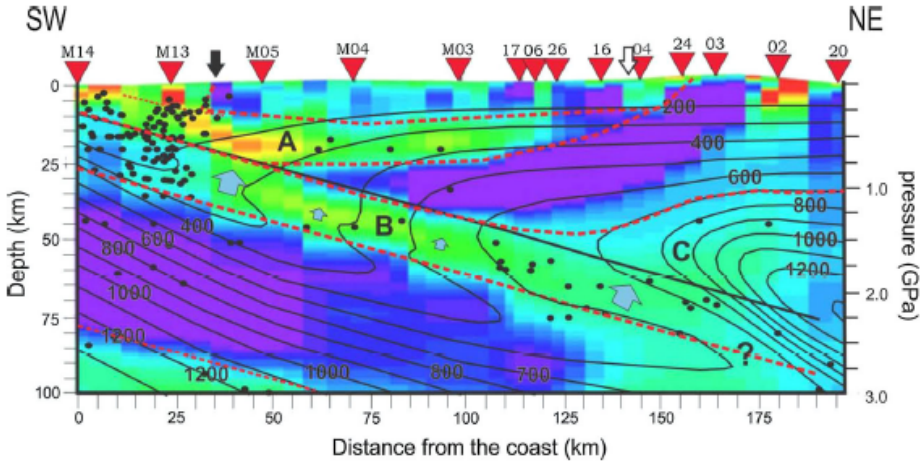

(b)

Figure 4-4: Magnetotelluric study in Oaxaca-Xolapa. a) Relative elevation image of southwestern Mexico showing main regional structures and terrane limits. Labeled dotted lines represent depth to the subducting interface from Pardo and Suárez [1995]. Continuous white line shows the trace of the interpreted magnetotelluric profile. VC Valles Centrales, JU Juchatengo terrane, CB Cuicateco Basin. b) Interpreted conductivity structure of the MT section. The red dashed lines separate anomalous conductivity regions. These conductive zones are associated to at least three geodynamic processes leveled with capitals letters. Arrows pointing downwards indicate the tectonostratigraphic limit of the Xolapa-Oaxaca terrain (black arrow) and the Oaxaca-Juarez terrane (white arrow) according to Campa and Coney [1983]. Blue arrows indicate zones of major dehydration within the oceanic conductive upper slab (B). MT stations are marked with inverted red triangles. (from Arzate-Flores *et al.* [2016])

Chapter 5

Conclusions

1. According to the analysis of slip partitioning in the forearc of the Mexican subduction zone using the method of McCaffrey [1992], the Xolapa sliver velocity with respect to the fixed NA plate is 10 ± 1 mm/year for local catalog and 5.6 ± 0.8 mm/year for Global CMT compilation. The difference between the results for two catalogs is explained by the inconsistency in local and teleseismic estimations of earthquake source parameters such as strike, dip and rake for the same events. The result from the Global CMT catalog is taken as the reference since it is in good agreement with the geologic and geodetic observations (5-6 mm/year in Guerrero). Despite the increase of convergence velocity and obliquity to the southeast, the slip rate on the LVC fault is decreasing contrary to what would be expected. Based on this observation, we assume a compressive deformation of the Xolapa sliver likely caused by the presence of a buttressing structure, such as subducting seamount chains in Oaxaca, at its leading edge (Fig. 3 in Kazachkina *et al.* [2019]). Detailed analysis of GPS time series and a refined fault trace mapping, especially in Oaxaca, will allow retrieving more information on the activity of forearc faults and associated seismic risk. [Kazachkina *et al.*, 2019]

2. Long-lasting GPS observations and geomorphology studies in the Guerrero-Oaxaca area of the Mexican subduction zone show that, despite the almost complete absence of historic and instrumentally recorded seismicity in the western LVC fault zone, this mainly left-

lateral shear zone is a complex and active system of numerous distributed strike-slip faults that accommodates strain partitioning produced by oblique subduction of the Cocos plate. As the result of the present study, we should admit that the La Venta-Chacalapa fault system is the principal active tectonic feature in Southern Mexico, which must be considered as a source of potential seismic hazard.

It is not known so far for how long time was the LVC fault zone active and what is a cumulative offset across the LVC fault zone in time. Existing GPS records only are not enough to constitute a previously unrecognized hazard in Southern Mexico related to the active LVC fault system. We need to obtain quantitative constraints on the age of the LVC faulting at least for the last few thousand years. Accurate trace and structure of the LVC was not yet explored except perhaps its western Guerrero segment [Gaidzik *et al.*, 2016]. The motion of the Xolapa sliver in Oaxaca remains rather hypothetic until more data would be available on new GPS stations installed inland from the LVC zone. Apart from the more precise location of the LVC fault and its coupling structure modeling, future investigations will also focus on a possible relationship between large subduction thrust slow slip events and displacements on the LVC fault zone.

The Xolapa sliver is obviously not a rigid block and should undergo different internal deformations, which depend on subduction rate, coupling and changes in the friction along the 650km length of the LVC. The leading edge of the LVC in the Guatemala basin is still undefined. It is apparently not related to the triple junction, but a contortion of the Xolapa sliver in the area of the Tehuantepec ridge is probably a key to make this problem clearer. [Kazachkina *et al.*, 2020]

3. Geodetic observations from GPS stations along the coast of Mexico and Oaxaca have shown that the behavior of the crustal left-lateral strike-slip LVC fault system is significantly affected by slow subduction zone transients. This research work has demonstrated the repeating pattern of accelerating-decelerating motion at the LVC fault that corresponds to subduction SSE occurences. During simple SSEs the deformation at the LVC

fault appears to be predominantly elastic. However, SSEs accompanied by a strong subduction earthquake, like 2014 M_w7.3 Papanoa or 2017 M_w7.2 Pinotepa earthquakes, cause an accumulation of sinistral deformation along the strike-slip fault.

Appendix A

Appendix A

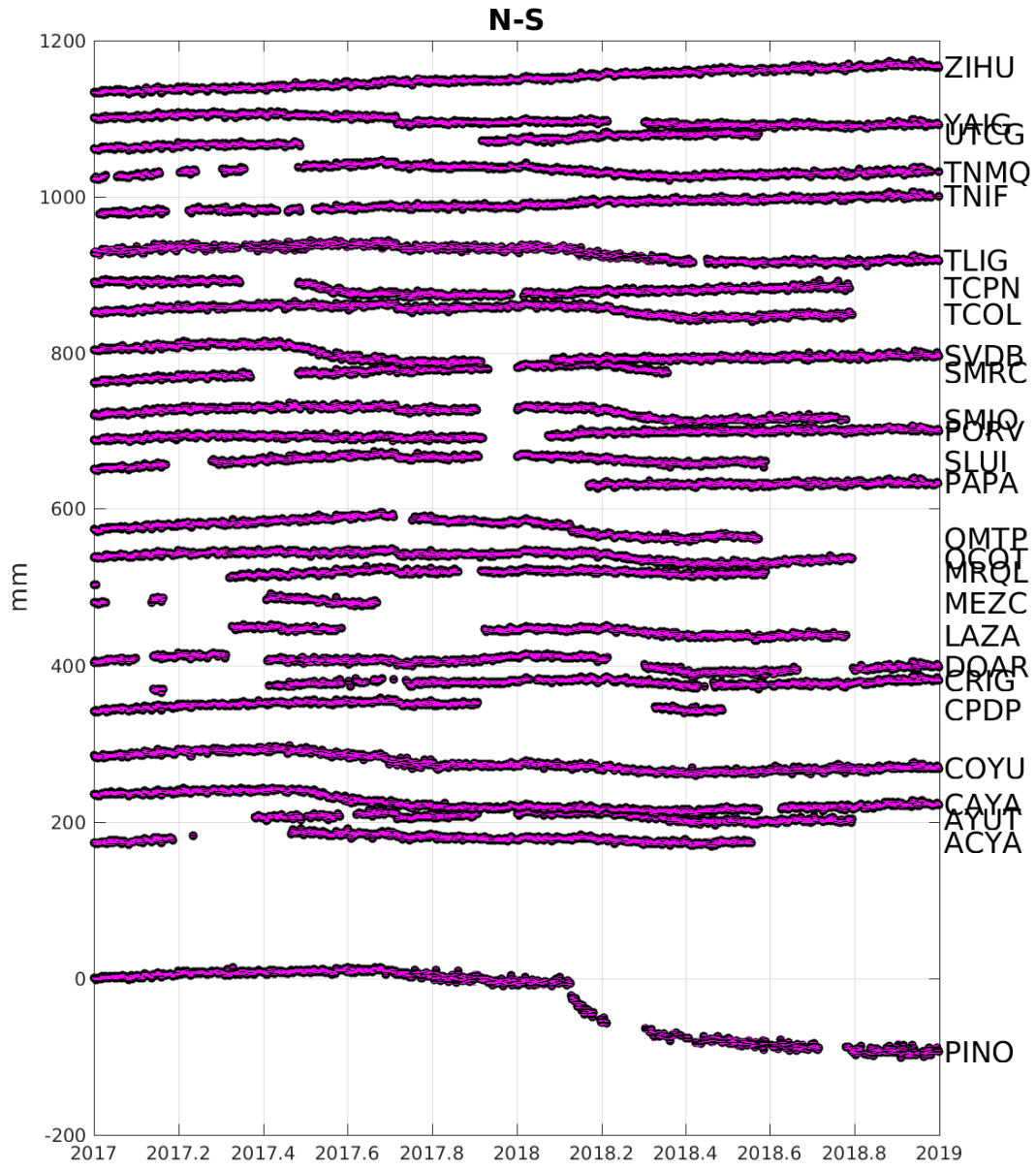

(a)

Figure A-1: Daily position time series at GPS stations in Guerrero used in the SSE inversion. (a) Northern components, (b) eastern components, (c) vertical components.

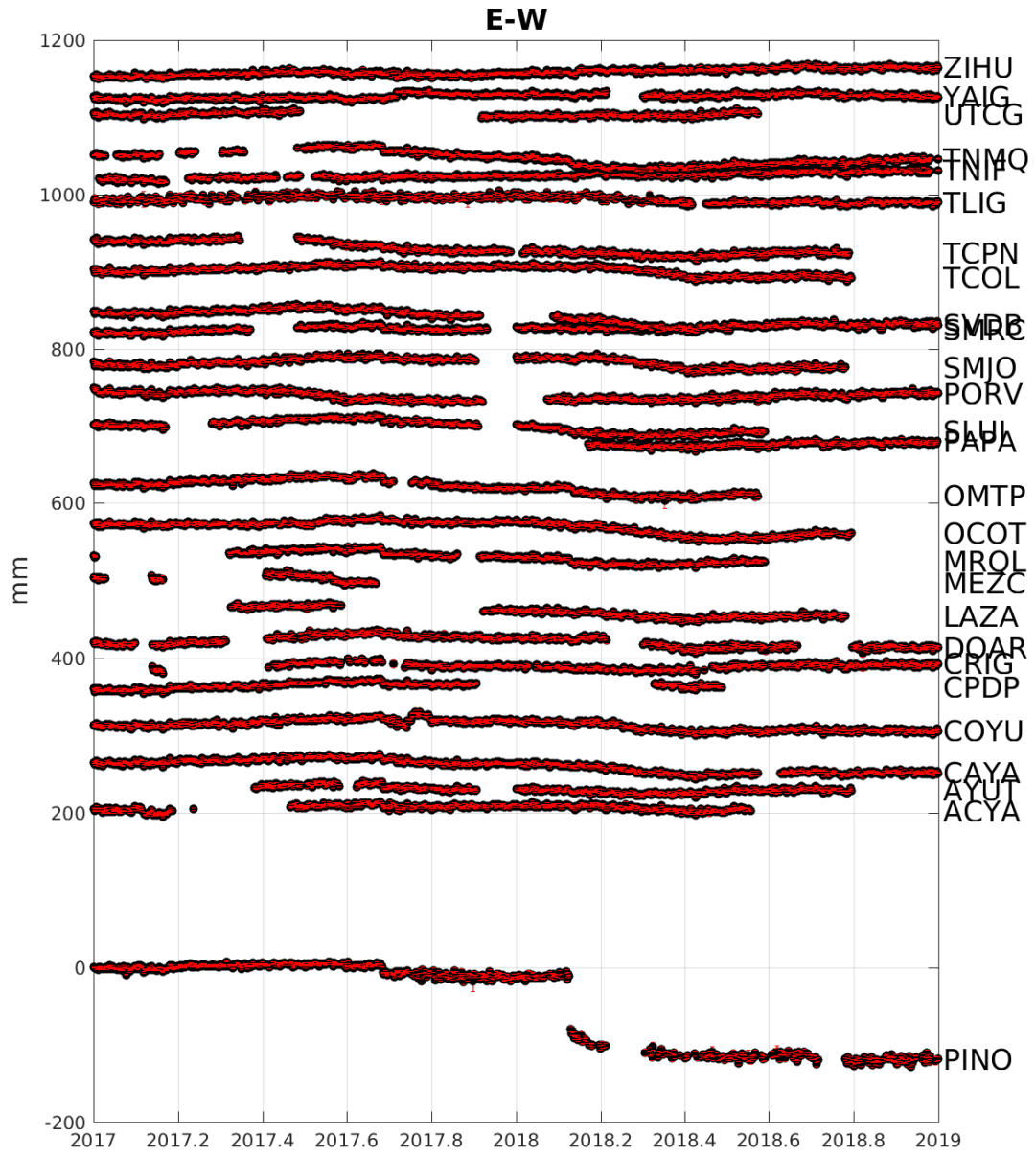

(b)

Figure A-1: Daily position time series at GPS stations in Guerrero used in the SSE inversion. (a) Northern components, (b) eastren components, (c) vertical components.

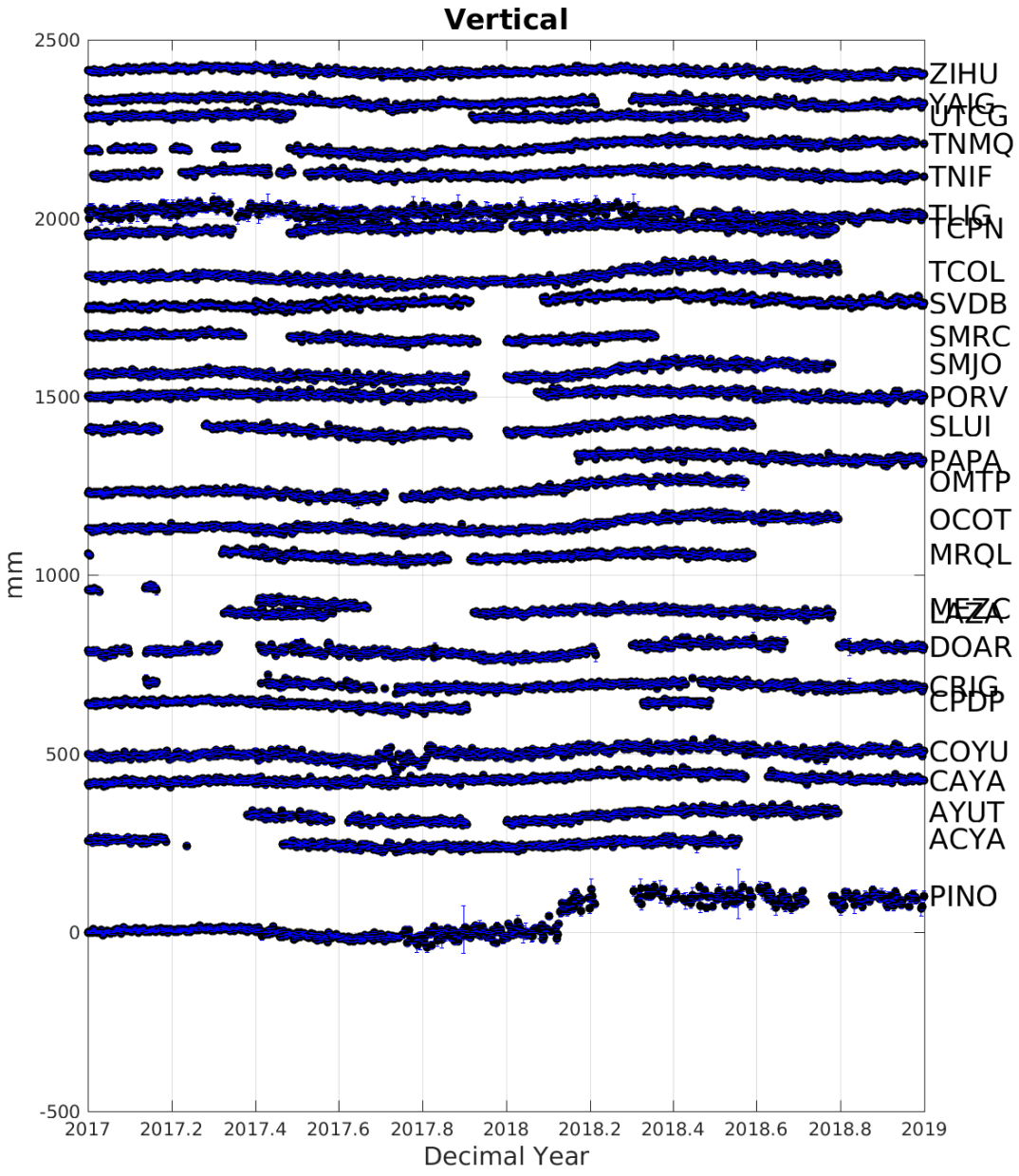

(c)

Figure A-1: Daily position time series at GPS stations in Guerrero used in the SSE inversion. (a) Northern components, (b) eastren components, (c) vertical components.

Appendix B

Appendix B

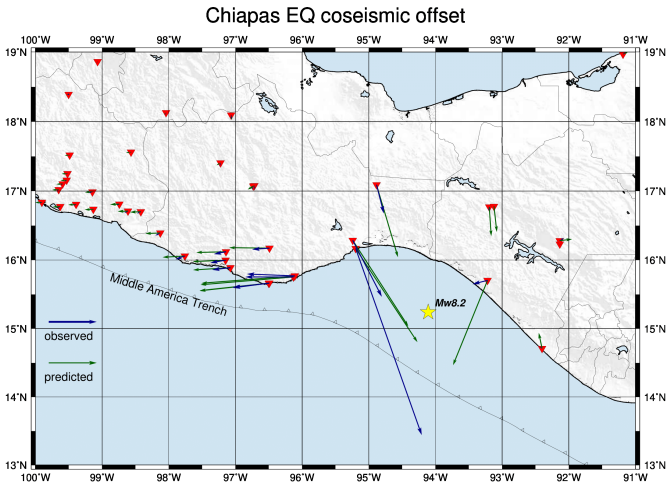

(a)

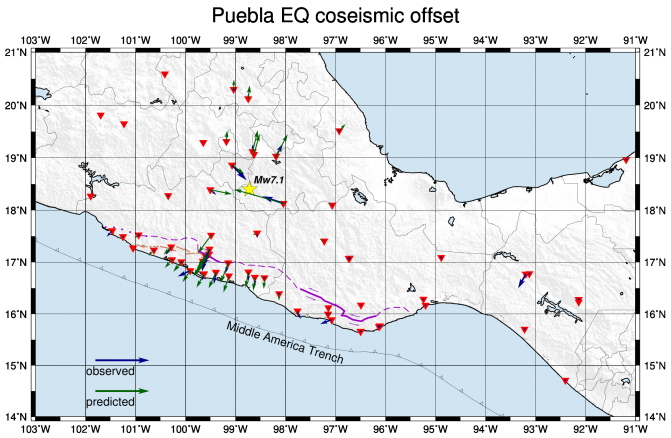

(b)

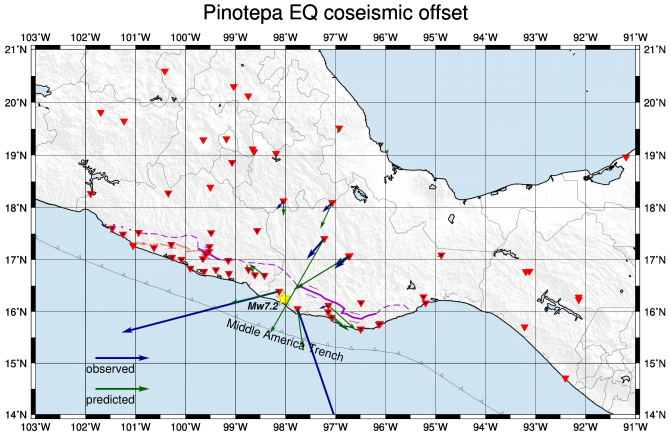

(c)

Figure B-1: Vectors of observed and predicted coseismic displacements for Chiapas, Puebla and Pinotepa events. Green arrows are modeled offsets; blue arrows –observed coseismic steps; yellow star –earthquake epicenters; red triangles –GPS stations used in the analysis.

Appendix C

Appendix C

Table C-1: Average interSSE velocities used to detrend GPS time series.

Station	**Longitude, E°**	**Latitude, N°**	Vel_E, **mm/yr**	Vel_N, **mm/yr**
ACYA	-99.90	16.84	11.446	19.886
ARIG	-100.34	18.28	4.580	11.351
AYUT	-99.15	16.99	7.824	22.177
CAYA	-100.27	17.05	11.506	15.756
COMI	-92.14	16.28	1.634	4.907
COYU	-100.08	17.01	11.160	18.653
CPDP	-99.63	16.78	11.075	18.534
CRIG	-99.13	16.74	12.337	23.400
DEMA	-99.04	20.30	0.654	1.886
DOAR	-99.65	17.02	10.762	18.120
HUAM	-96.13	15.75	10.964	16.760
HUAT	-96.11	15.77	11.444	15.470
ICEP	-98.19	19.03	4.392	4.047
ICHS	-93.19	16.77	1.348	2.504

Continued on next page

Table C-1 – continued from previous page

Station	**Longitude, E°**	**Latitude, N°**	Vel_E, **mm/yr**	Vel_N, **mm/yr**
IGUA	-99.50	18.39	6.806	11.893
IHGO	-98.74	20.12	3.299	0.602
LAZA	-99.49	17.52	8.648	13.415
MARO	-94.88	17.09	3.232	4.607
MRQL	-98.82	16.59	10.947	22.192
OAX2	-96.72	17.08	7.653	13.456
OAXA	-96.73	17.07	7.192	12.132
OCOT	-99.52	17.25	12.457	18.034
OMTP	-98.42	16.70	15.590	25.768
OXPE	-97.08	15.89	17.017	24.037
OXTH	-95.24	16.29	7.345	4.959
OXUM	-96.50	15.66	14.702	19.838
PAPA	-101.05	17.27	10.028	8.753
PEIG	-97.15	16.00	13.683	24.414
PINO	-98.13	16.39	9.167	15.569
POP1	-98.63	19.07	1.730	5.315
PORV	-100.94	17.53	9.252	9.624
PTCH	-92.40	14.71	4.970	6.971
PUAN	-96.49	15.67	12.759	22.187
SABY	-91.19	18.97	0.349	1.822
SLCR	-95.20	16.17	4.420	5.500
SLUI	-98.74	16.81	11.071	16.500
SMJO	-99.59	17.10	11.406	18.104
SMRC	-99.39	16.81	6.937	20.380
SSNX	-99.18	19.33	3.286	1.263

Continued on next page

Table C-1 – continued from previous page

Station	**Longitude, E°**	**Latitude, N°**	Vel_E, **mm/yr**	Vel_N, **mm/yr**
SVDB	-100.28	17.30	8.954	11.064
TCOL	-99.53	17.16	10.137	18.426
TCPN	-100.63	17.23	11.813	11.738
TGIG	-93.12	16.78	1.348	2.504
TLIG	-98.57	17.56	9.774	11.480
TNAL	-98.66	19.12	0.668	7.665
TNAT	-98.04	18.13	6.108	11.806
TNCY	-97.76	16.06	9.016	14.348
TNGF	-99.18	19.33	1.247	1.004
TNIF	-101.90	18.27	5.865	11.367
TNMO	-101.23	19.65	2.290	3.625
TNMQ	-98.61	16.71	16.933	16.834
TNNP	-97.14	16.12	10.803	23.271
TNNX	-97.22	17.41	5.642	11.459
TNPJ	-93.22	15.70	1.881	3.477
TNSJ	-96.49	16.17	12.755	18.181
TOIG	-97.06	18.10	4.510	2.652
TOL2	-99.64	19.29	3.389	4.612
UCOE	-101.69	19.81	1.887	4.495
UNIP	-99.18	19.31	1.239	5.242
UQRO	-100.41	20.59	2.988	0.401
UTCG	-101.25	17.49	16.215	9.673
UXAL	-96.92	19.52	2.581	1.191
YAIG	-99.07	18.86	3.151	5.315
ZIHU	-101.47	17.61	11.810	17.659

Appendix D

Appendix D

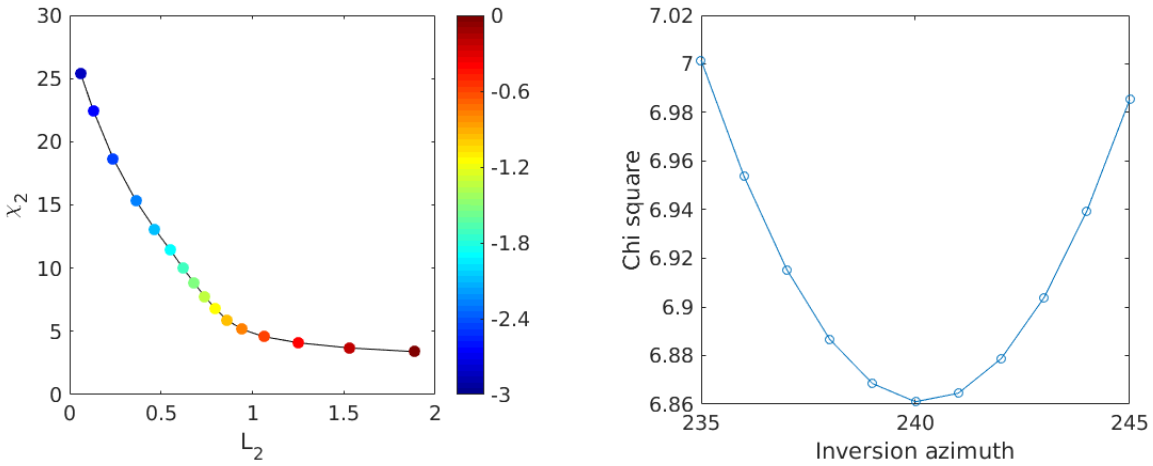

(a) (b)

Figure D-1: (a) Selection of the optimal values of smoothing parameters σ_m and λ. The optimal damping parameter σ_m is selected from the L-curve where the data misfit is plotted as a function of the regularized L2-norm solution. (b) Selection of the optimal tectonic angle θ using previously selected λ and σ_m.

Appendix E

Appendix E

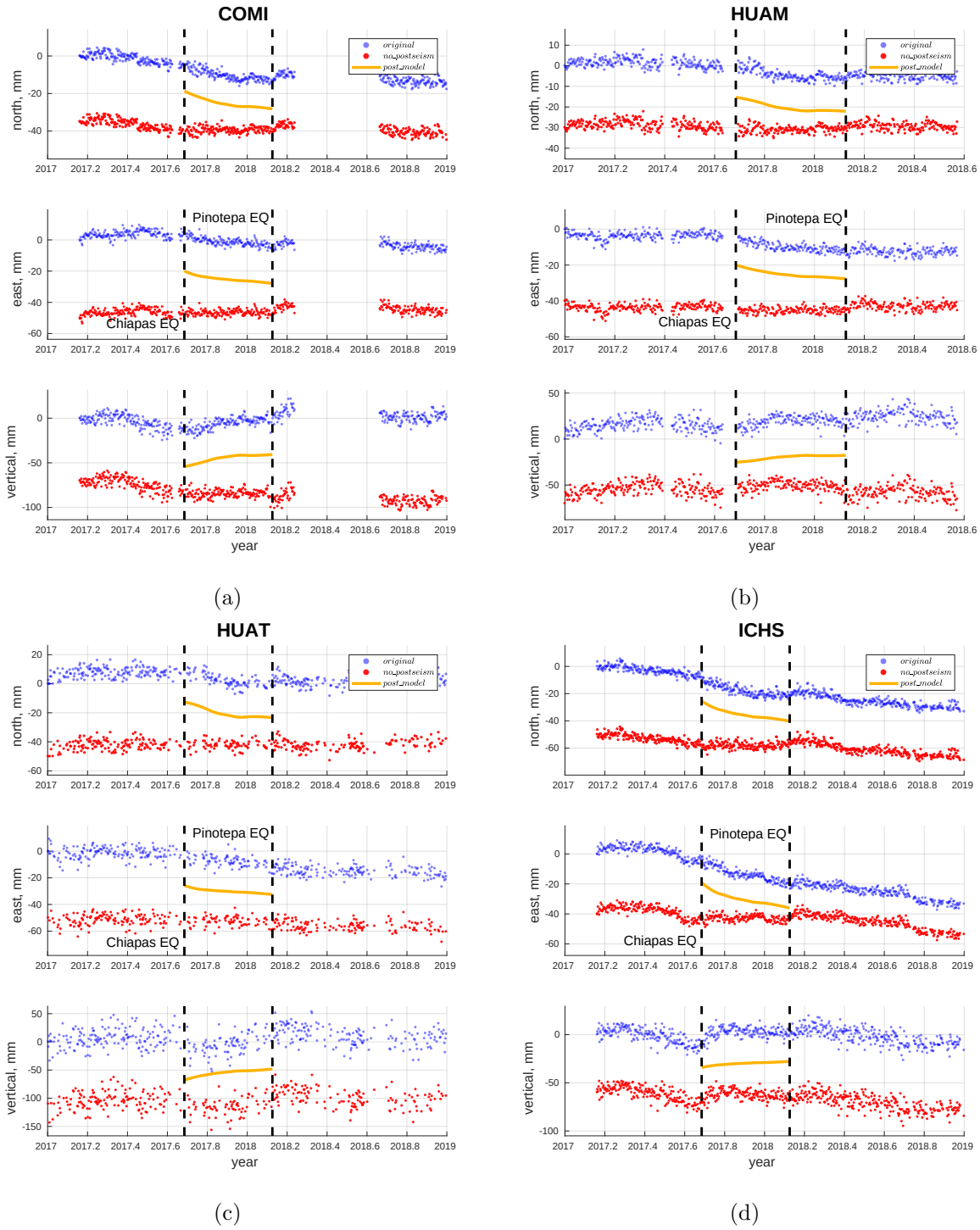

Figure E-1: Extracting postseismic afterslip due to M_w8.2 Chiapas and M_w7.2 Pinotepa earthquakes from GPS time series in preparation for inversion. Blue are original detrended time series without coseismic offsets. Yellow is the modeled postseismic signal for the Chiapas earthquake. Orange is the modeled postseismic signal for the Pinotepa earthquake. Red are time series used in the SSE inversion.

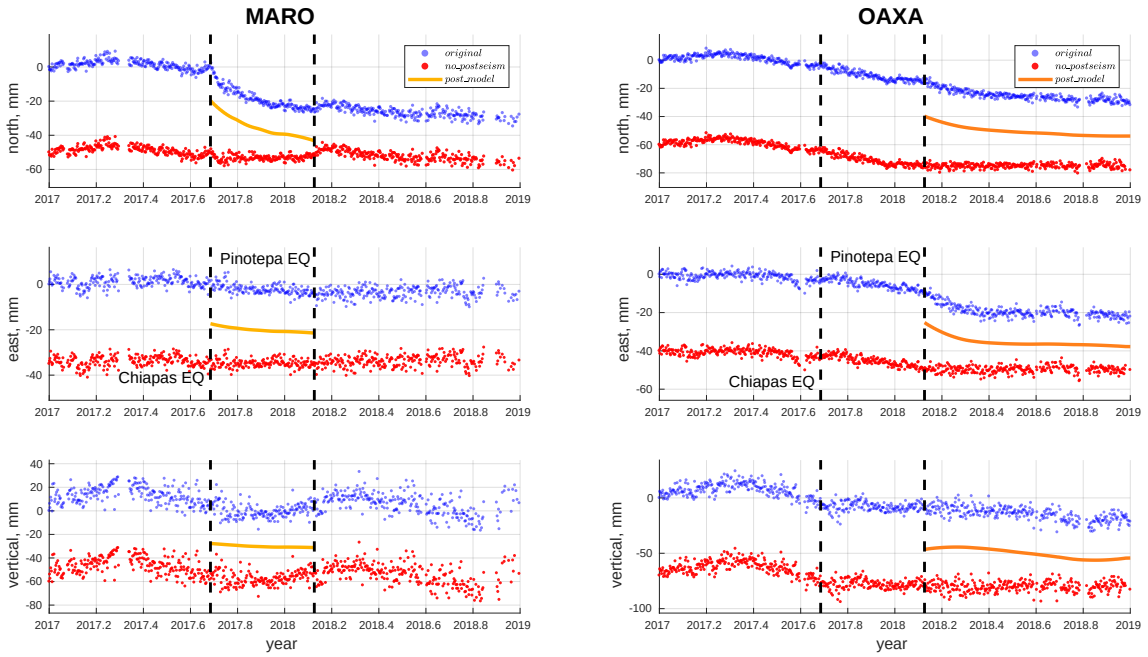

(e) (f)

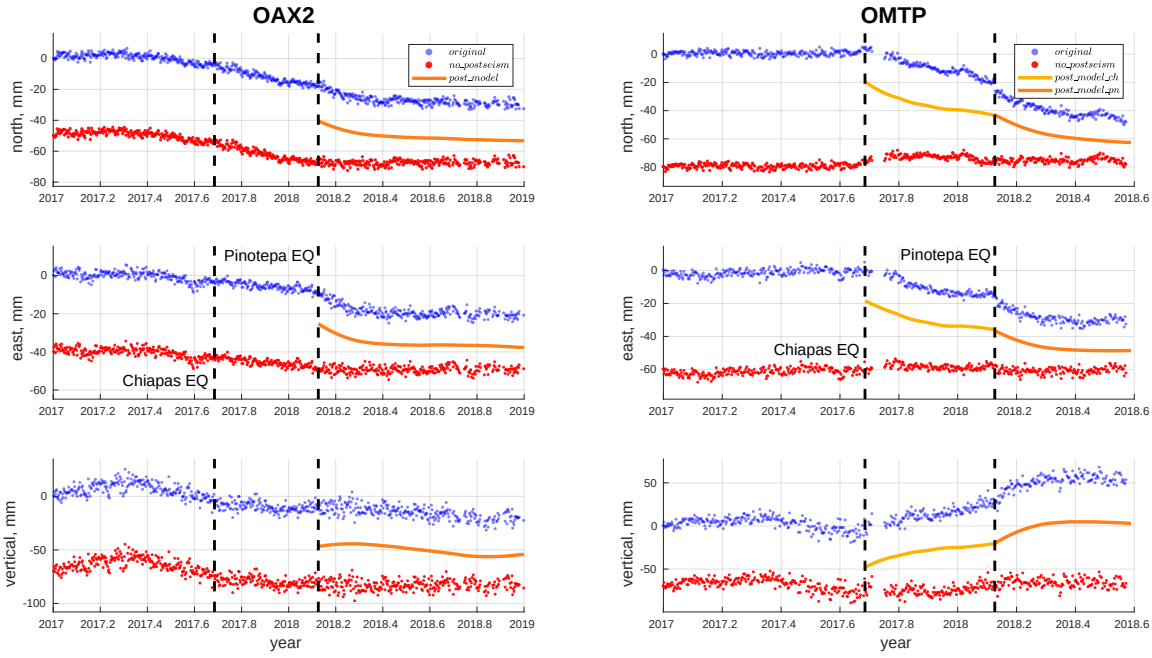

(g) (h)

Figure E-1: Extracting postseismic afterslip due to M_w8.2 Chiapas and M_w7.2 Pinotepa earthquakes from GPS time series in preparation for inversion. Blue are original detrended time series without coseismic offsets. Yellow is the modeled postseismic signal for the Chiapas earthquake. Orange is the modeled postseismic signal for the Pinotepa earthquake. Red are time series used in the SSE inversion.

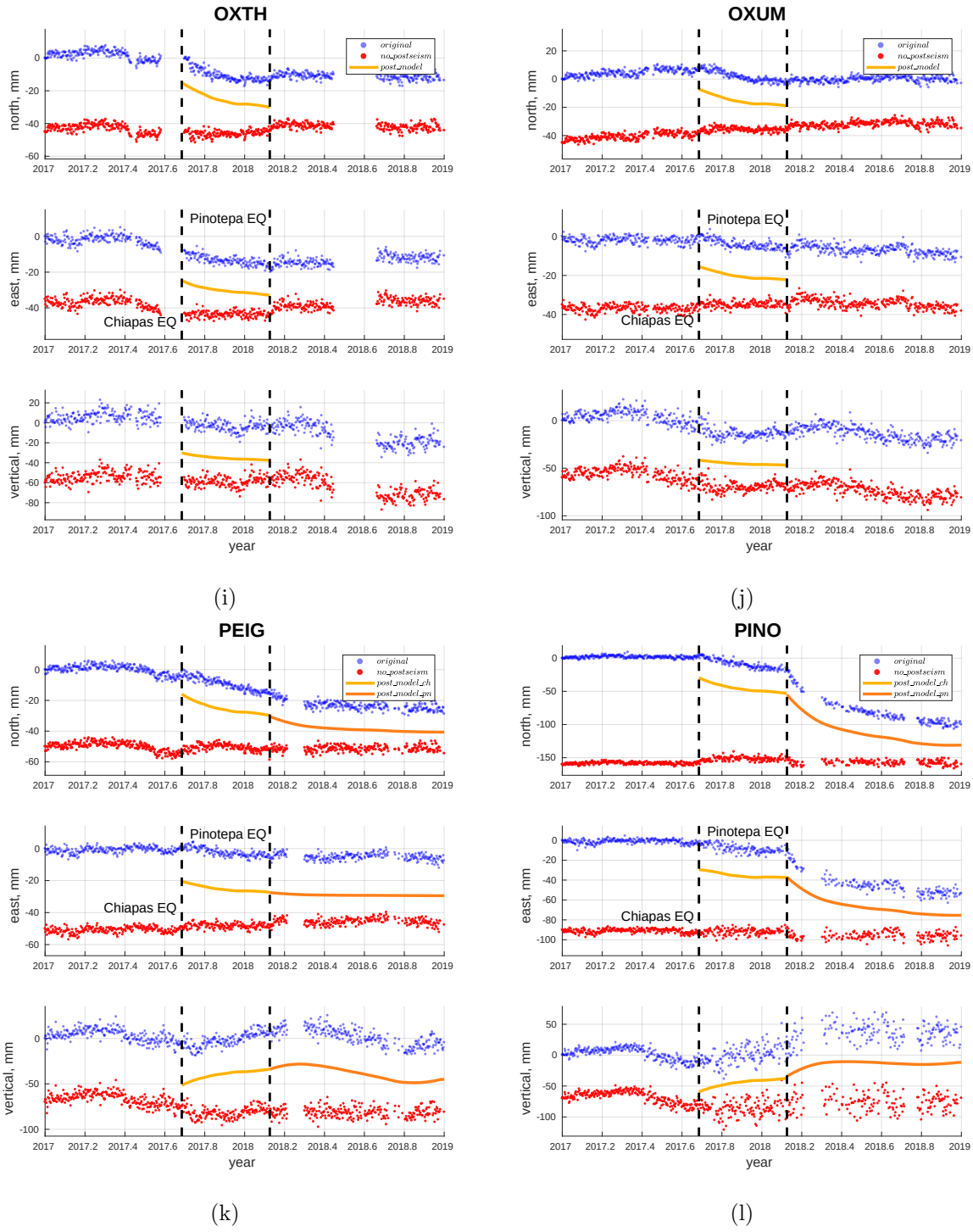

Figure E-1: Extracting postseismic afterslip due to M_w8.2 Chiapas and M_w7.2 Pinotepa earthquakes from GPS time series in preparation for inversion. Blue are original detrended time series without coseismic offsets. Yellow is the modeled postseismic signal for the Chiapas earthquake. Orange is the modeled postseismic signal for the Pinotepa earthquake. Red are time series used in the SSE inversion.

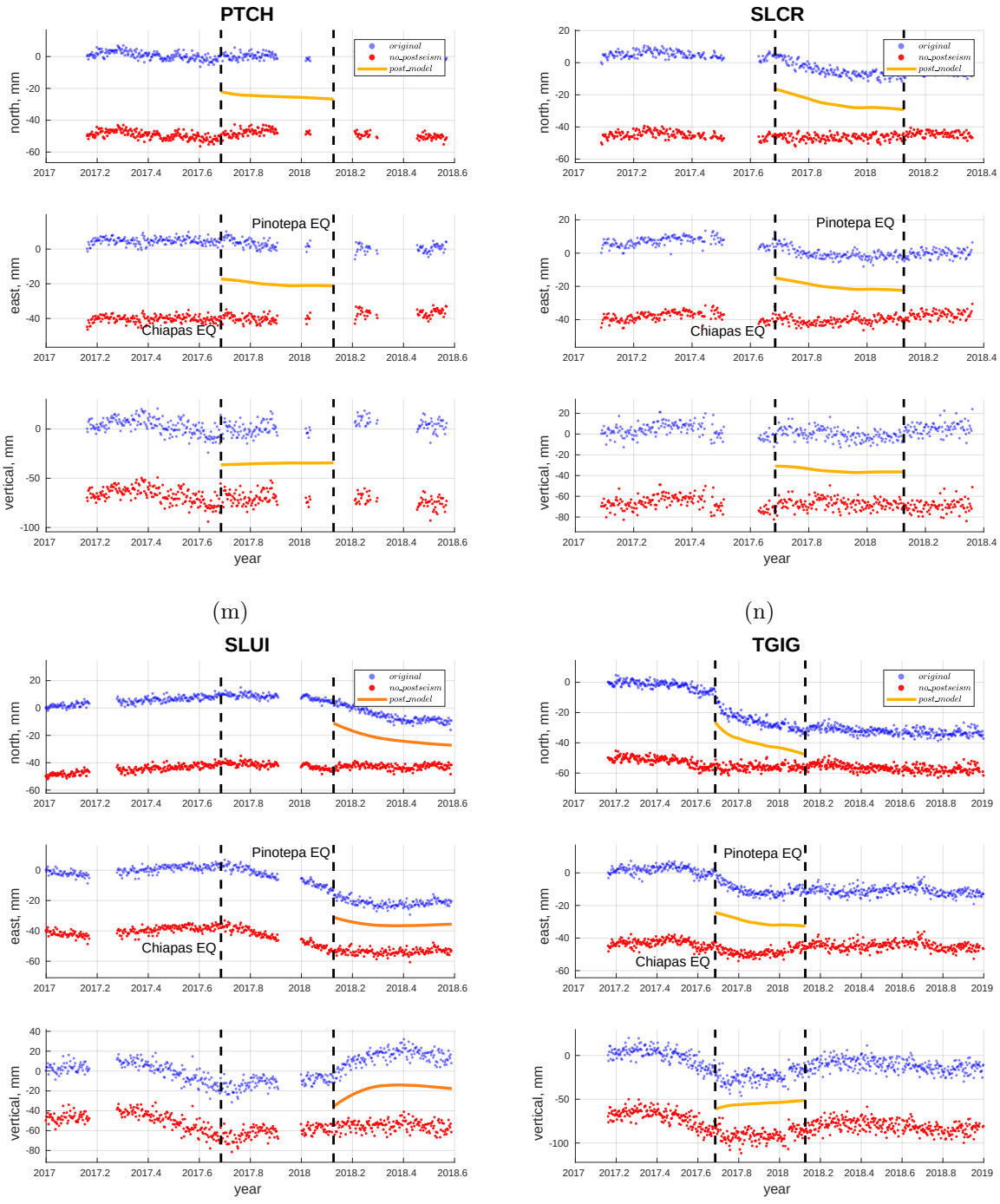

Figure E-1: Extracting postseismic afterslip due to M_w8.2 Chiapas and M_w7.2 Pinotepa earthquakes from GPS time series in preparation for inversion. Blue are original detrended time series without coseismic offsets. Yellow is the modeled postseismic signal for the Chiapas earthquake. Orange is the modeled postseismic signal for the Pinotepa earthquake. Red are time series used in the SSE inversion.

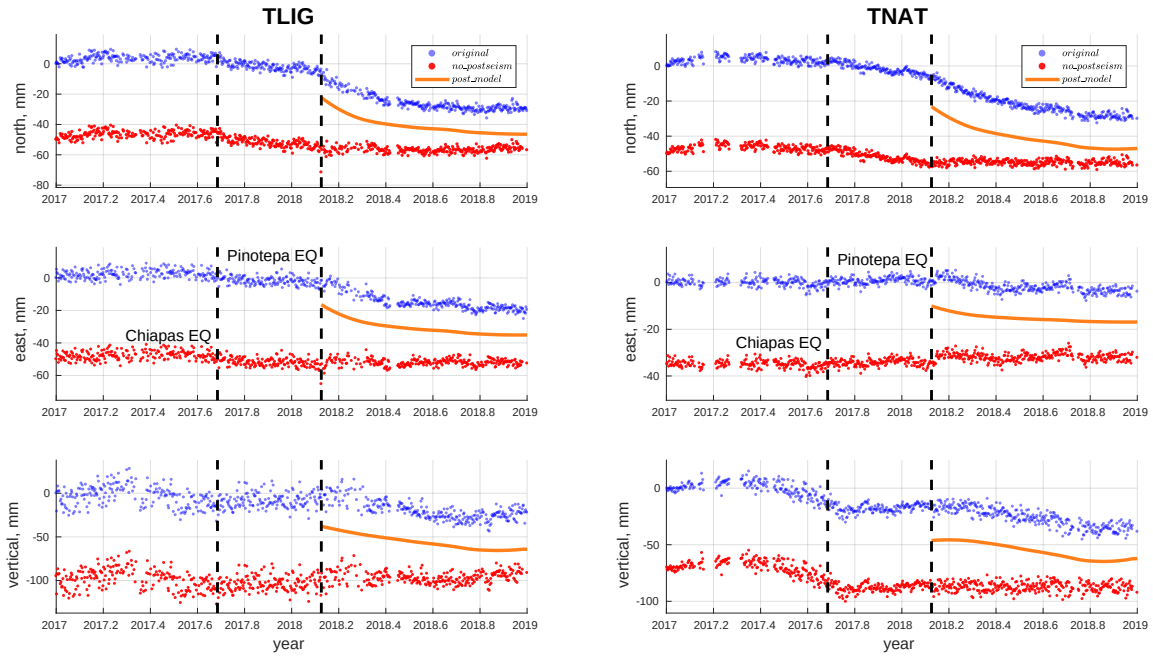

(q)

(r)

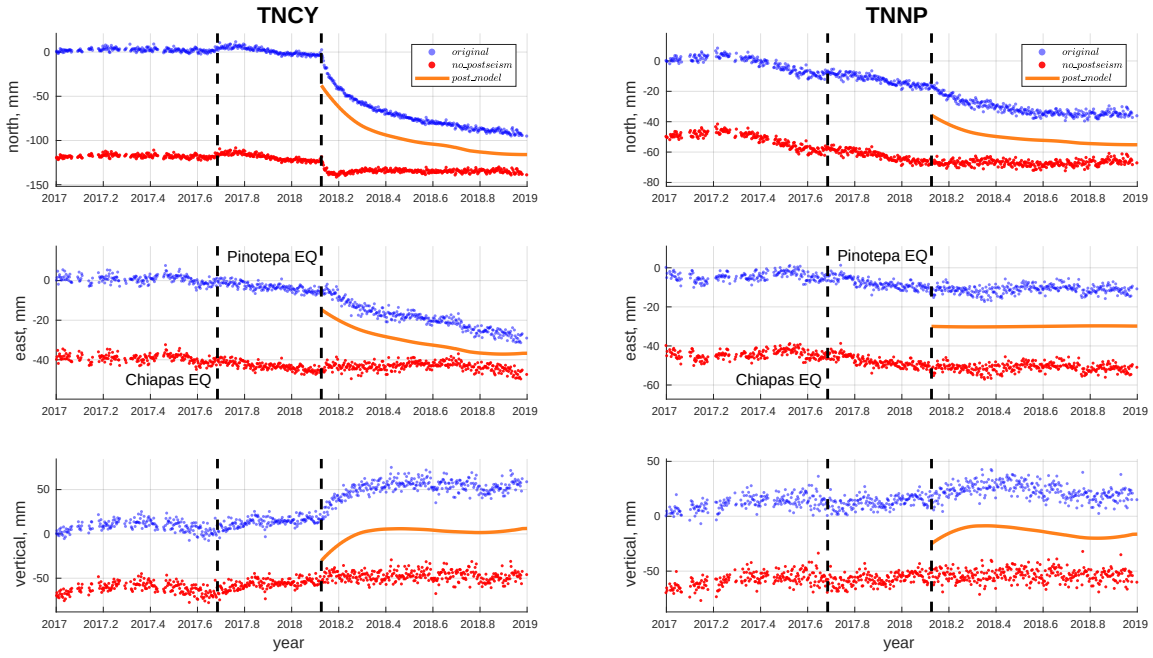

(s)

(t)

Figure E-1: Extracting postseismic afterslip due to M_w8.2 Chiapas and M_w7.2 Pinotepa earthquakes from GPS time series in preparation for inversion. Blue are original detrended time series without coseismic offsets. Yellow is the modeled postseismic signal for the Chiapas earthquake. Orange is the modeled postseismic signal for the Pinotepa earthquake. Red are time series used in the SSE inversion.

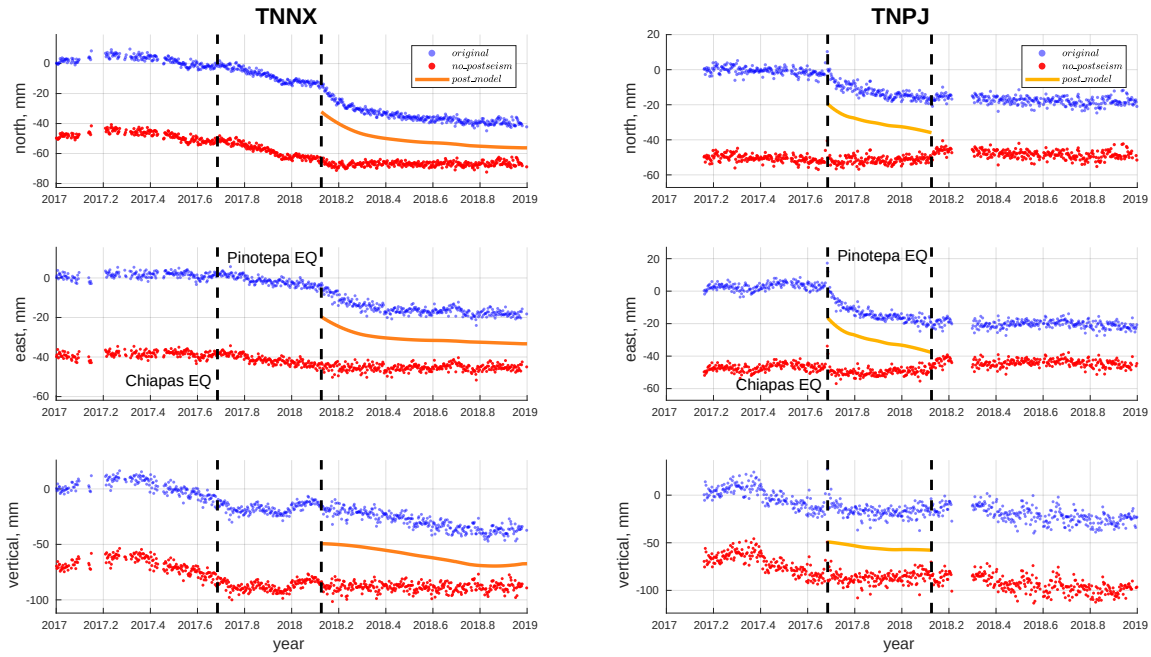

(u) (v)

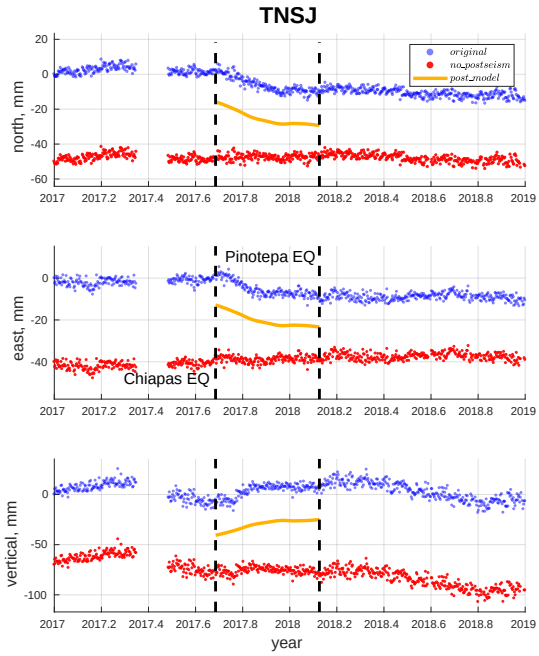

(w)

Figure E-1: Extracting postseismic afterslip due to M_w8.2 Chiapas and M_w7.2 Pinotepa earthquakes from GPS time series in preparation for inversion. Blue are original detrended time series without coseismic offsets. Yellow is the modeled postseismic signal for the Chiapas earthquake. Orange is the modeled postseismic signal for the Pinotepa earthquake. Red are time series used in the SSE inversion.

Appendix F

Appendix F

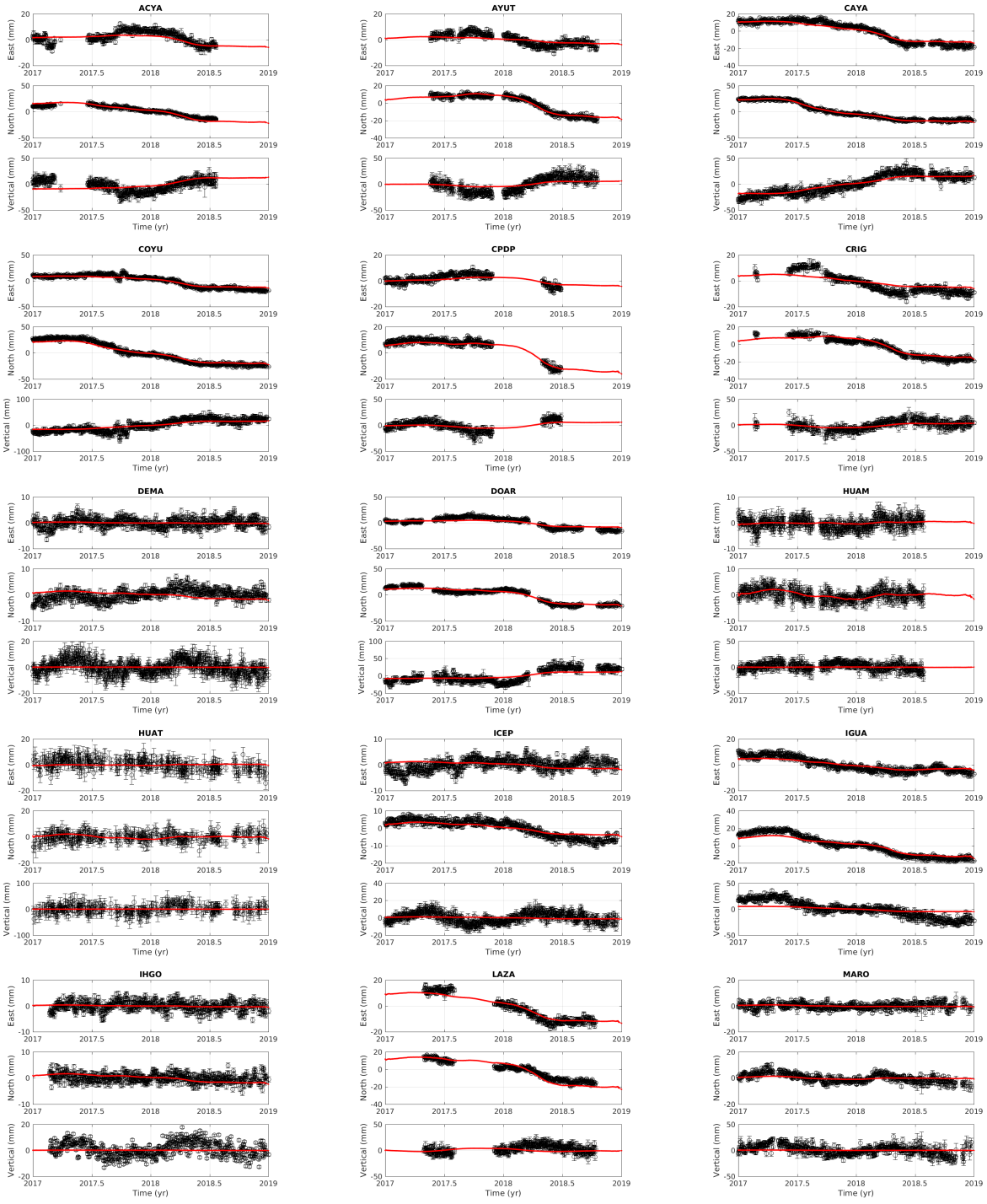

Figure F-1: Fit of model time series to data. Black circles are original detrended time series without coseismic offsets and postseismic signals. Red line is modeled time series obtained with ICA decomposition

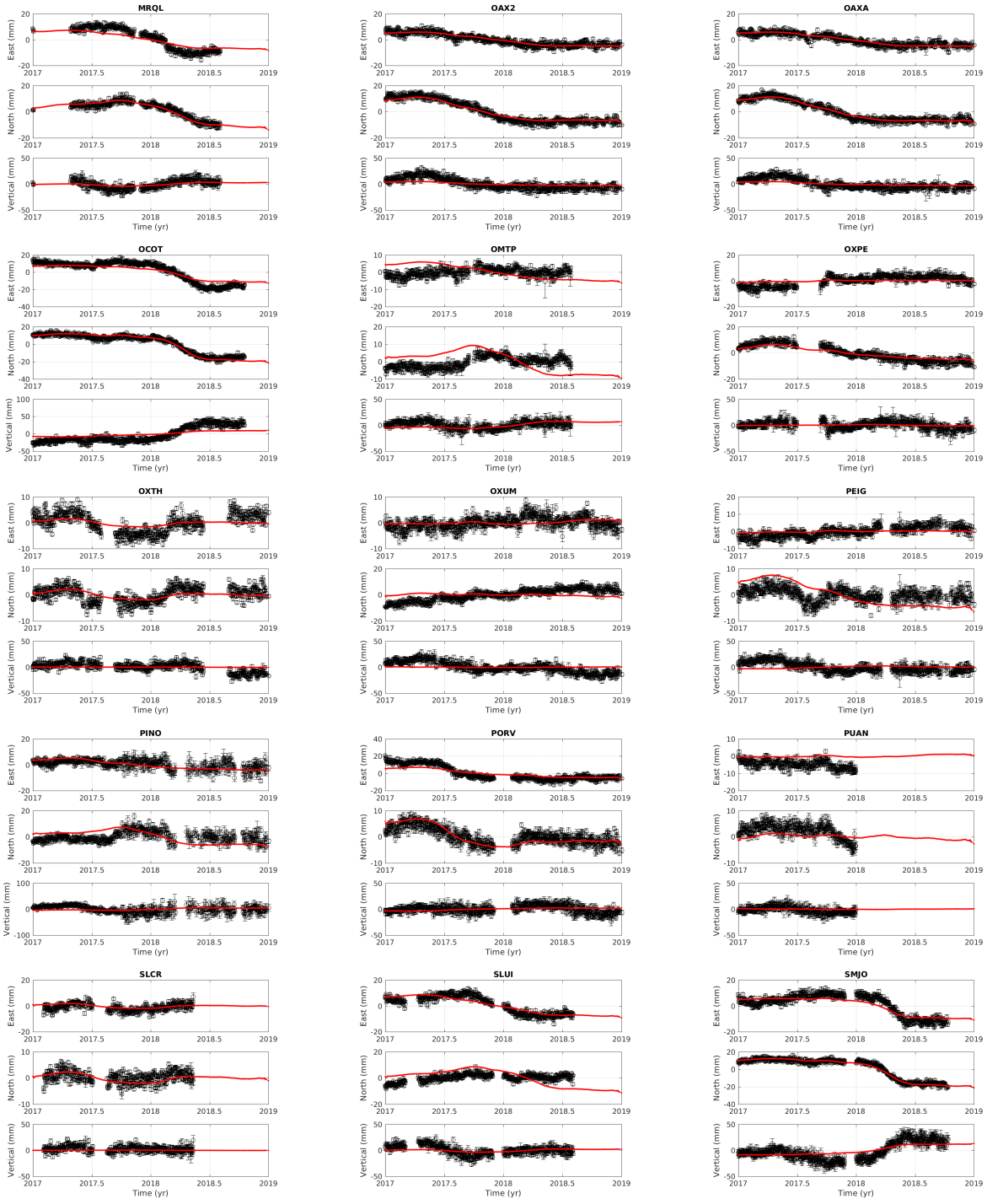

Figure F-1: Fit of model time series to data. Black circles are original detrended time series without coseismic offsets and postseismic signals. Red line is modeled time series obtained with ICA decomposition

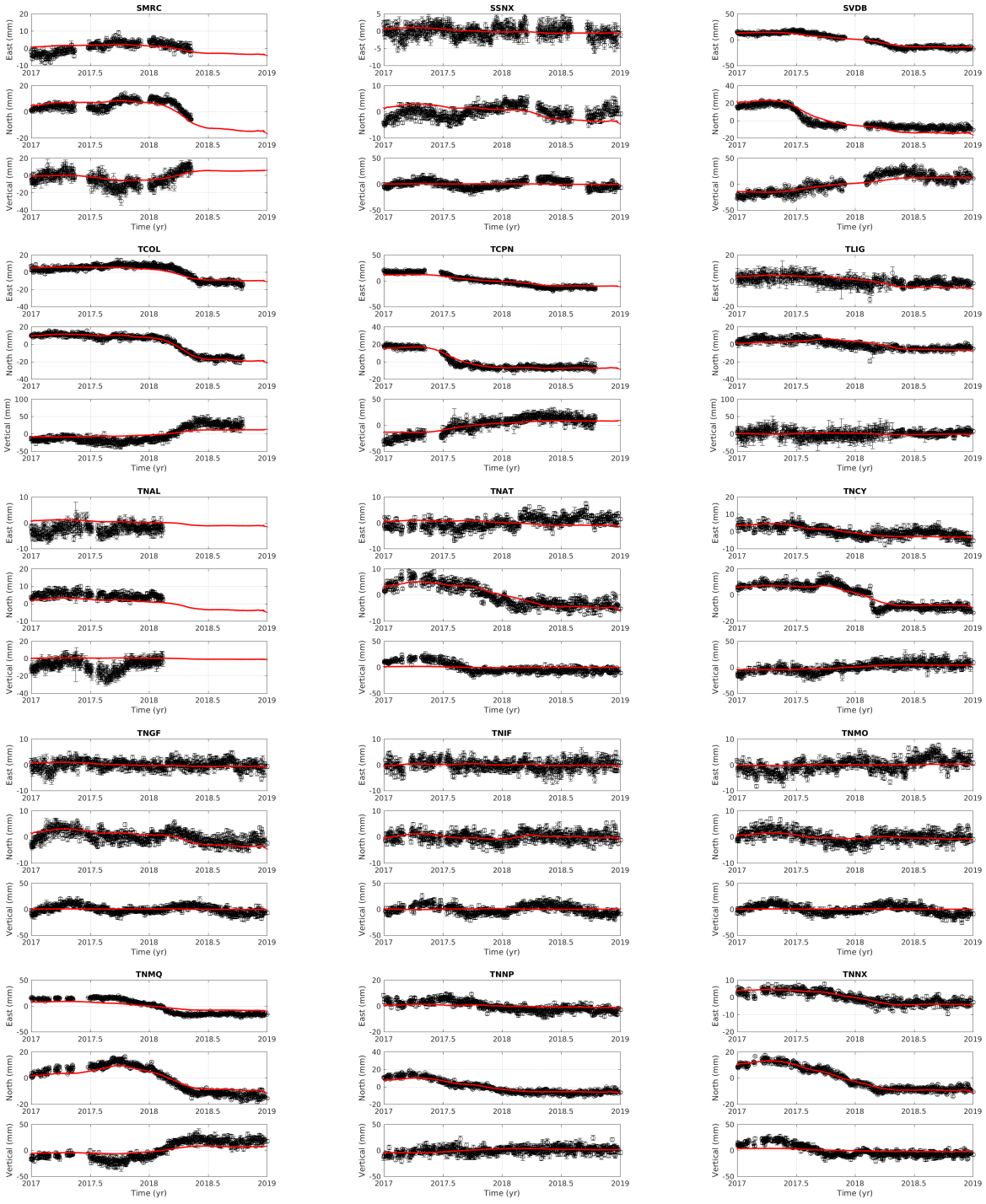

Figure F-1: Fit of model time series to data. Black circles are original detrended time series without coseismic offsets and postseismic signals. Red line is modeled time series obtained with ICA decomposition

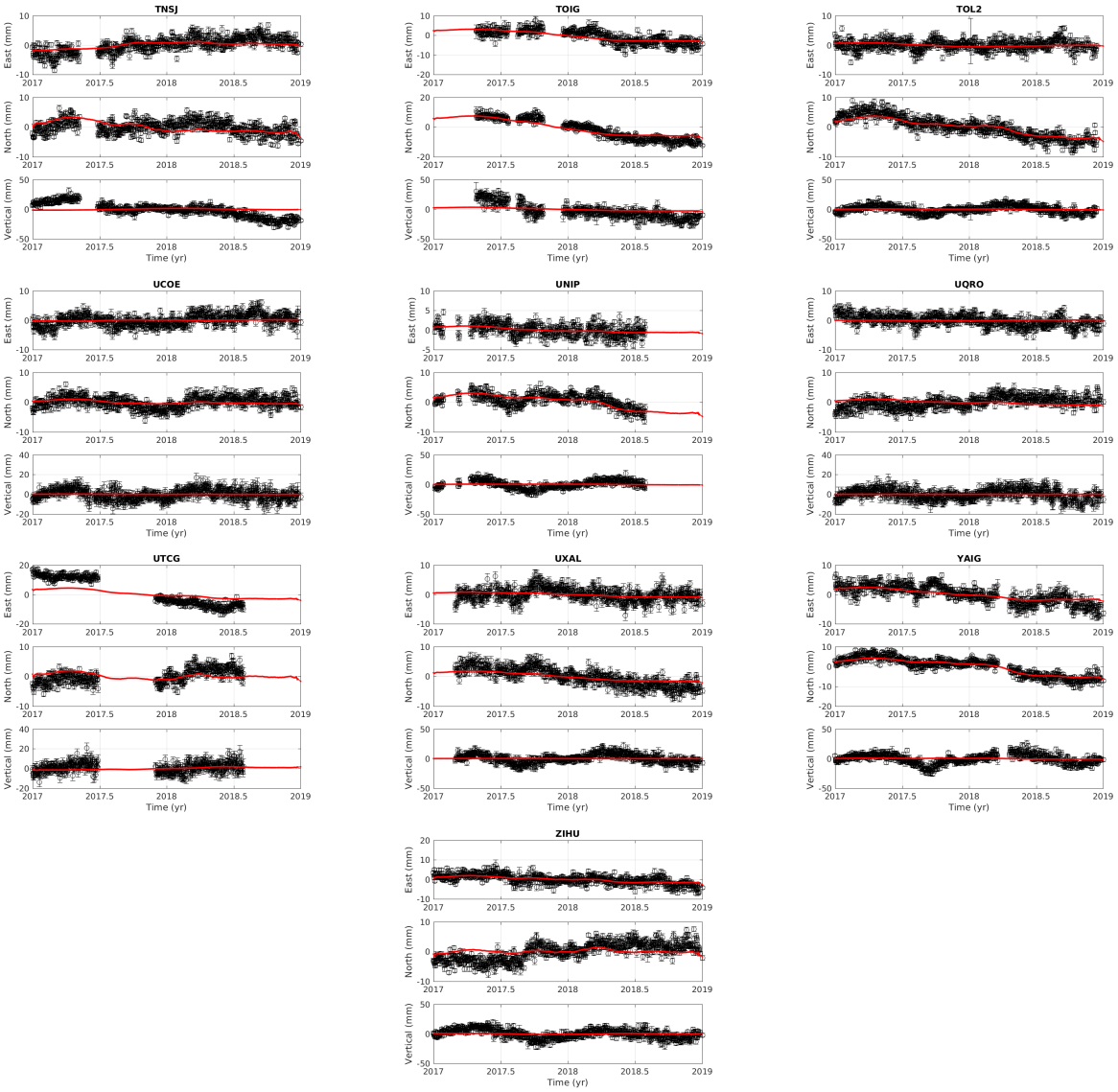

Figure F-1: Fit of model time series to data. Black circles are original detrended time series without coseismic offsets and postseismic signals. Red line is modeled time series obtained with ICA decomposition

Appendix G

Appendix G

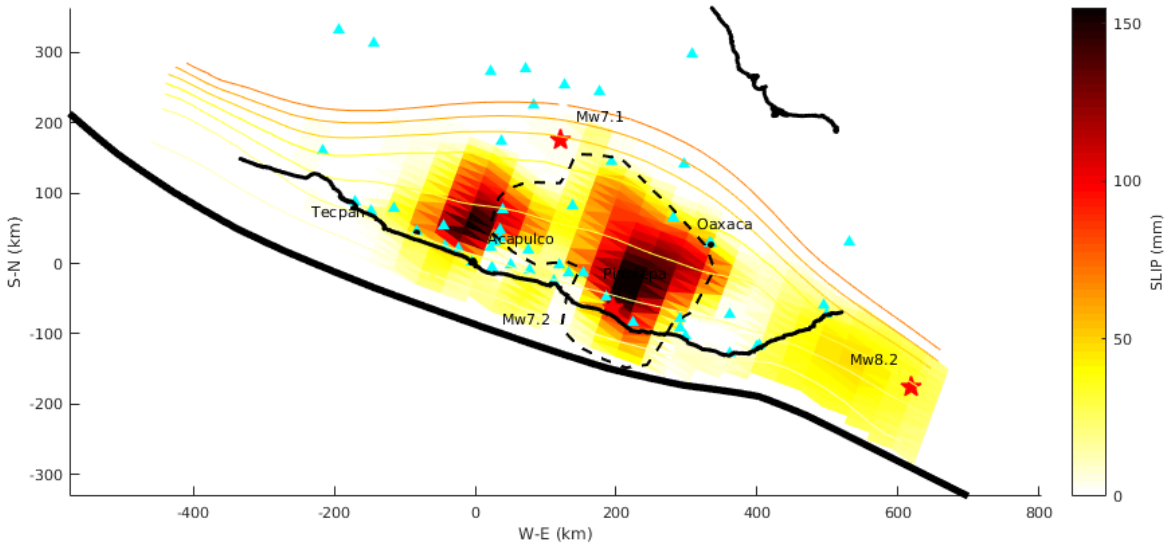

Figure G-1: Slip on the subduction fault interface obtained from the restored dataset (from the combination of the three tectonic signals - SSEs in Guerrero and Oaxaca and postseismic deformation after Chiapas and Pinotepa earthquakes).

Bibliography

Abaimov, S.G., Turcotte, D.L., and Rundle, J.B. Recurrence-time and frequency-slip statistics of slip events on the creeping section of the San Andreas fault in central California. *Geophys. J. Int.* **170**(3):https://doi.org/10.1111/j.1365-246X.2007.03479.x (2007)

Abba, I., Abidin, W.A., Masri, T., Hong Ping, K., Muhammad, M., and Voon Pai, B. Ionospheric Effects on GPS Signal in Low-Latitude Region: A Case Study Review of South East Asia and Africa. *Nigerian Journal of Technology* **34**:523 (2015)

Altamimi, Z., Rebischung, P., Métivier, L., and Collilieux, X. ITRF2014: A new release of the International Terrestrial Reference Frame modeling nonlinear station motions. *J. Geophys. Res. Solid Earth* **121**:doi:10.1002/2016JB013098 (2016)

Altamimi, Z., Métivier, L., Rebischung, P., Rouby, H., and Collilieux, X. ITRF2014 plate motion model. *Geophys. J. Int.* **209**(3):1906–1912 (2017)

Arzate-Flores, J., Molina-Garza, R., Corbo-Camargo, F., and Marquez-Ramirez, V. Low angle contact between the Oaxaca and Juarez Terranes deduced from magnetotelluric data. *Pageoph* **173**(4) (2016)

Audet, P. and Kim, Y. Teleseismic constraints on the geological environment of deep episodic slow earthquakes in subduction zone forearcs: A review. *Tectonophysics* **670**:1–15 (2016)

Aytun, A. Creep measurements in the Ismetpasa region of the North Anatolian Fault Zone. *Multidisciplinary Approach to Earthquake Prediction* págs. 279–292 (1982)

Beroza, G.C. and Ide, S. Slow Earthquakes and Nonvolcanic Tremor. *Annual Review of Earth and Planetary Sciences* **39**(1):https://doi.org/10.1146/annurev-earth-040809-152531 (2011)

Bird, P. and Kagan, Y.Y. Plate-Tectonic Analysis of Shallow Seismicity: Apparent Boundary Width, Beta, Corner Magnitude, Coupled Lithosphere Thickness, and Couplingin Seven Tectonic Settings. *BSSA* **94**(6):2380–2399 (2004)

Boettcher, M.S. and Jordan, T.H. Earthquake scaling relations for mid-ocean ridge transform faults. *J. Geophys. Res.* **109**(B04409):https://doi.org/10.1029/2004JB003110 (2004)

Brudzinski, M., Cabral-Cano, E., Correa-Mora, F., DeMets, C., and Márquez-Azúa, B. Slow slip transients along the Oaxaca subduction segment from 1993 to 2007. *Geophys. J. Int.* **171**(2):https://doi.org/10.1111/j.1365-246X.2007.03542.x (2007)

Bürgmann, R. The geophysics, geology and mechanics of slow fault slip. *Earth and Planetary Science Letters* **495**:112–134 (2018)

Bürgmann, R., Kogan, M.G., Levin, V.E., Scholz, C.H., King, R.W., and Steblov, G.M. Rapid aseismic moment release following the 5 December, 1997 Kronotsky, Kamchatka, earthquake. *Geophys. Res. Lett.* **28**:1331–1334 (2001)

Campa, M. and Coney, P. Tectonostratigraphic terranes and mineral resource distributions in Mexico. *Canadian Journal Earth Science* **20**:1,040–1,051 (1983)

Cavalié, O., Pathier, E., Radiguet, M., Vergnolle, M., Cotte, N., Walpersdorf, A., Kostoglodov, V., and Cotton, F. Slow slip event in the Mexican subduction zone: Evidence of shallower slip in the Guerrero seismic gap for the 2006 event revealed by the joint inversion of InSAR and GPS data. *Earth and Planetary Science Letters* **367**:https://doi.org/10.1016/j.epsl.2013.02.020 (2013)

Cerca, M., Ferrari, L., López-Martínez, M., Martiny, B., and Iriondo, A. Late Cretaceous shortening and early Tertiary shearing in the central Sierra Madre del Sur, south-

ern Mexico: Insights into the evolution of the Caribbean–North American plate interaction. *Tectonics* **26**(3) (2007)

Cervelli, P., Segall, P., Johnson, K., Lisowski, M., and Miklius, A. Sudden aseismic fault slip on the south flank of Kilauea Volcano. *Nature* **415**(6875):1014–1018 (2002)

Choudrey, R. *Variational methods for bayesian independent component analysis.* Tesis Doctoral, University of Oxford (2002)

Correa-Mora, F., DeMets, C., Cabral-Cano, E., Marquez-Azua, B., and Diaz-Molina, O. Interplate coupling and transient slip along the subduction interface beneath Oaxaca, Mexico. *Geophys. J. Int.* **175**(1):https://doi.org/10.1111/j.1365-246X.2008.03910.x (2008)

Correa-Mora, F., DeMets, C., Cabral-Cano, E., Diaz-Molina, O., and Marquez-Azua, B. Transient deformation in southern Mexico in 2006 and 2007: Evidence for distinct deep-slip patches beneath Guerrero and Oaxaca. *Geochemistry, Geophysics, Geosystems* **10**(2):https://doi.org/10.1029/2008GC002211 (2009)

Couch, R. and Woodcock, S. Gravity and structure of the continental margins of southwestern Mexico and northwestern Guatemala. *Journal of Geophysical Research: Solid Earth* **86**(B3):https://doi.org/10.1029/JB086iB03p01829 (1981)

DeMets, C., Gordon, R.G., Argus, D.F., and Stein, S. Current plate motions. *Geophys. J. Int.* **101**(2):https://doi.org/10.1111/j.1365-246X.1990.tb06579.x (1990)

Douglas, A., Beavan, J., Wallace, L., and Townend, J. Slow slip on the northern Hikurangi subduction interface, New Zealand. *Geophys. Res. Lett.* **32**(L16305):https://doi.org/10.1029/2005GL023607 (2005)

Dragert, H., Wang, K., and James, T.S. A silent slip event on the deeper Cascadia subduction interface. *Science* **292**(5521):1525–1528 (2001)

Ferrari, L., Orozco-Esquivel, T., Manea, V., and Manea, M. The dynamic history of the Trans-Mexican Volcanic Belt and the Mexico subduction zone. *Tectonophysics* **522**:122–149 (2012)

Fielding, E.J., Gonzalez-Ortega, J.A., Gombert, B., Duputel, Z., Liang, C., Jolivet, R., Bekaert, D., and Ampuero, J.P. The February 2018 Mw7.2 Pinotepa Earthquake in Mexico Ruptured Small Patch of the Oaxaca Megathrust. AGU (2018)

Freymueller, J.T., Hreinsdöttir, S., Zweck, S., and Haeussler, P. The 1998–2002 deep megathrust slip event, Alaska. *Eos Trans Amer. Geophys. Union* **83**(47) (2002)

Gaidzik, K., Ramírez-Herrera, M.T., and Kostoglodov, V. Active Crustal Faults in the Forearc Region, Guerrero Sector of the Mexican Subduction Zone. *Pure and Appl. Geophys.* **173**(10-11):https://doi.org/10.1007/s00024-015-1213-8 (2016)

Galehouse, J.S. Data from theodolite measurements of creep rates on San Francisco Bay Region faults, California: 1979–2001. *U.S. Geol. Surv. Open File Rep.* (2002)

Graham, S., DeMets, C., Cabral-Cano, E., Kostoglodov, V., B., R., Walpersdorf, A., Cotte, N., Lasserre, C., McCaffrey, R., and Salazar-Tlaczani, L. Slow slip history for the Mexico subduction zone: 2005 through 2011. *Pure Appl. Geophys.* https://doi.org/10.1007/s00024-015-1211-x (2015)

Graham, S.E., DeMets, C., Cabral-Cano, E., Kostoglodov, V., Walpersdorf, A., Cotte, N., Brudzinski, M., McCaffrey, R., and Salazar-Tlaczani, L. GPS constraints on the 2011–2012 Oaxaca slow slip event that preceded the 2012 March 20 Ometepec earthquake, southern Mexico. *Geophys. J. Int.* doi:10.1093/gji/ggu019 (2014a)

Gualandi, A., Serpelloni, E., and Belardinelli, M. Blind source separation problem in GPS time series. *J. Geod.* **90**:https://doi.org/10.1007/s00190-015-0875-4 (2016)

Guilhem, A. and Nadeau, R.M. Episodic tremor and deep slow-slip events in central California. *EPSL* **357-358**:1–10 (2012)

Guo, R., Zheng, Y., Xu, J., and Jiang, Z. Seismic and Aseismic Fault Slip Associated with the 2017 Mw 8.2 Chiapas, Mexico, Earthquake Sequence. *Seismological Research Letters* doi: 10.1785/0220180262 (2019)

Hayes, G.P., Moore, G.L., Portner, D.E., Hearne, M., Flamme, H., Furtney, M., and Smoczyk, G.M. Slab2, A comprehensive subduction zone geometry model. *Science* DOI: 10.1126/science.aat4723 (2018)

Heki, K., Miyazaki, S., and Tsuji, H. Silent fault slip following an interplate thrust earthquake at the Japan Trench. *Nature* **386**:595–598 (1997)

Hirose, H., Hirahara, K., Kimata, F., Fujii, N., and Miyazaki, S. A slow thrust slip event following the two 1996 Hyuganada earthquakes beneath the Bungo channel, southwest Japan. *Geophysical Research Letters* **26**(21):3237–3240 (1999)

Husker, A., Ferrari, L., Arango-Galván, C., Corbo-Camargo, F., and J.A., A.F. A geologic recipe for transient slip within the seismogenic zone: Insight from the Guerrero seismic gap, Mexico. *Geology* https://doi.org/10.1130/G39202.1 (2017)

Husker, A., Frank, W.B., Gonzalez, G., Avila, L., Kostoglodov, V., and Kazachkina, E. Characteristic tectonic tremor activity observed over multiple slow slip cycles in the Mexican subduction zone. *Journal of Geophysical Research: Solid Earth* **123**:https://doi.org/10.1029/2018JB016517 (2019)

Husker, A.L., Kostoglodov, V., Cruz-Atienza, V.M., Legrand, D., Shapiro, N.M., Payero, J.S., Campillo, M., and Huesca-Pérez, E. Temporal variations of non-volcanic tremor (NVT) locations in the Mexican subduction zone: Finding the NVT sweet spot. *Geochem. Geophys. Geosyst.* **13**(Q03011):doi:10.1029/2011GC003916 (2012)

Iglesias, A., Singh, S.K., Lowry, A.R., Santoyo, M., Kostoglodov, V., Larson, K.M., and Sánchez, I.F. The silent earthquake of 2002 in the Guerrero seismic gap, Mexico (Mw=7.6): Inversion of slip on the plate interface and some implications. *Geofísica Internacional* **43**:309–317 (2004)

Introduction to GNSS. *Introduction to GNSS*. 2ª edición. NovAtel Inc., 1120-68th Avenue N.E., Calgary, Alberta, Canada (2015)

Ito, Y., Hino, R., Kido, M., Fujimoto, H., Osada, Y., Inazu, D., Ohta, Y., Iinuma, T., Ohzono, M., Miura, S., Mishina, M., Suzuki, K., Tsuji, T., and Ashi, J. Episodic slow slip events in the Japan subduction zone before the 2011 Tohoku-Oki earthquake. *Tectonophysics* **600**:doi: 10.1016/j.tecto.2012.08.022 (2013)

Kato, T. *Slow Earthquake*, pág. 1374–1382. Springer Netherlands, Dordrecht (2011)

Kawasaki, I., Asai, Y., and Tamura, Y. Space-time distribution of interplate moment release including slow earthquakes and the seismo-geodetic coupling in the Sanriku-oki region along the Japan trench. *Tectonophysics* **330**:https://doi.org/10.1016/S0040-1951(00)00245-6 (2001)

Kazachkina, E., Kostoglodov, V., Husker, A., and Cotte, N. Activity of crustal faults and the Xolapa sliver motion in Guerrero–Oaxaca forearc of Mexico, from seismic data. *Earth, Planets and Space* **71**(104):https://doi.org/10.1186/s40623-019-1084-9 (2019)

Kazachkina, E., Kostoglodov, V., Cotte, N., Walpersdorf, A., Ramirez-Herrera, M.T., Gaidzik, K., Husker, A., and A., S.J. Active 650-km long fault system and Xolapa sliver in Southern Mexico. *Front. Earth Sci.* **8**(155):https://doi.org/10.3389/feart.2020.00155 (2020)

Kazachkina, E., Radiguet, M., Cotte, N., Jara, J., Kostoglodov, V., and Walpersdorf, A. Mexican 2017-2018 SSE sequence and its interaction with large earthquakes (in process)

Khoshmanesh, M. and Shirzaei, M. Multiscale Dynamics of Aseismic Slip on Central San Andreas Fault. *Geophysical Research Letters* **45**(5):https://doi.org/10.1002/2018GL077017 (2018)

Klein, E., Duputel, Z., Zigone, D., Vigny, C., Boy, J.P., Doubre, C., and Meneses, G. Deep transient slow slip detected by survey GPS in the region of Atacama, Chile. *Geophys. Res. Lett.* **45**:https://doi.org/10.1029/2018GL080613 (2018)

Kositsky, A.P. and Avouac, J.P. Inverting geodetic time series with a principal component analysis-based inversion method. *J. Geophys. Res.* **115**(B03401):https://doi.org/10.1029/2009JB006535 (2010)

Kostoglodov, V., Singh, S., Santiago, J., Franco, S., Larson, K., Lowry, A., and R., B. A large silent earthquake in the Guerrero seismic gap, Mexico. *Geophys. Res. Lett.* **30**(15):https://doi:10.1029/2003GL017219 (2003)

Kostoglodov, V., Shapiro, N., Larson, K., Payero, J., Husker, A., Santiago, L., Clayton, R., and Peyrat, S. Nonvolcanic tremors and their correlation with slow slip events in Mexico. *EGU2009-5638*, tomo 11. EGU General Assembly, Geophysical Research Abstracts (2009)

Larson, K., Lowry, A., Kostoglodov, V., Hutton, W., Sánchez, O., Hudnut, K., and Suárez, G. Crustal deformation measurements in Guerrero, Mexico. *J. Geophys. Res.* **109**(B04409):https://doi:10.1029/2003JB002843 (2004)

Larson, K., Kostoglodov, V., Miyazaki, S., and Santiago, J. The 2006 aseismic slow slip event in Guerrero, Mexico: New results from GPS. *Geophys. Res. Lett.* **34**(13):https://doi.org/10.1029/2007GL029912 (2007)

León-Loya, R., Perea, H., Lacan, P., Ortuño, M., and Zúñiga, R. Evaluating the coulomb static stress change and fault interaction in an extensional intra-volcanic arc: 1000 years of earthquake history in the Acambay Graben, Trans-Mexican Volcanic Belt. *Journal of South American Earth Sciences* **117** (2022)

Linde, A.T., Gladwin, M.T., Johnston, M.J.S., Gwyther, R.L., and Bilham, R.G. A slow earthquake sequence on the San Andreas fault. *Nature* **383**(6595):doi:10.1038/383065a0 (1996)

Lowry, A., Larson, K., Kostoglodov, V., and Bilham, R. Transient fault slip in Guerrero, southern Mexico. *Geophys. Res. Letters* **28**(19) (2001)

Mammerickx, J. and Klitgord, K. Northern East Pacific Rise: Evolution from 25 m.y. B.P. to the present. *Journal of Geophysical Research: Solid Earth* **87**(B8):https://doi.org/10.1029/JB087iB08p06751 (1982)

Manea, M., Manea, V., Kostoglodov, V., and Guzmán-Speziale, M. Elastic thickness of the oceanic lithosphere beneath Tehuantepec ridge. *Geofísica internacional* **44**(2):157–168 (2005a)

Manea, M., Manea, V., Ferrari, L., Kostoglodov, V., and Bandy, W. Tectonic evolution of the Tehuantepec Ridge. *Earth and Planetary Science Letters* **238**(1):64–77 (2005b)

Manea, V., Manea, M., Ferrari, L., Orozco-Esquivel, L., Valenzuela, R., Husker, A., and Kostoglodov, V. A review of the geodynamic evolution of flat slab subduction in Mexico, Peru, and Chile. *Tectonophysics* **695**:27–52 (2017)

McCaffrey, R. Oblique plate convergence, slip vectors, and forearc deformation. *J. Geophys. Res.* **97**(B6):https://doi.org/10.1029/92JB00483 (1992)

McCausland, W., Malone, S., and Johnson, D. Temporal and spatial occurrence of deep non-volcanic tremor: From Washington to northern California. *Geophys. Res. Lett.* **32**(L24311):https://doi.org/10.1029/2005GL024349 (2005)

Michel, S., Gualandi, A., and Avouac, J. Similar scaling laws for earthquakes and Cascadia slow-slip events. *Nature* **574**:https://doi.org/10.1038/s41586-019-1673-6 (2019)

Miller, M., Melbourne, T., Johnson, D., and Sumner, W. Periodic slow earthquakes from the Cascadia subduction zone. *Science* **295**(5564):DOI: 10.1126/science.1071193 (2002)

Obara, K. Nonvolcanic Deep Tremor Associated with Subduction in Southwest Japan. *Science* **296**(5573):DOI: 10.1126/science.1070378 (2002)

Obara, K. Characteristics and interactions between non-volcanic tremor and related slow earthquakes in the Nankai subduction zone, southwest Japan. *Journal of Geodynamics* **52**(3-4):https://doi.org/10.1016/j.jog.2011.04.002 (2011)

Ohta, Y., Kimata, F., and Sagiya, T. Reexamination of the interplate coupling in the Tokai region, central Japan, based on the GPS data in 1997-2002. *Geophys. Res. Lett.* **31**(L24604) (2004)

Okada, Y. Surface deformation due to shear and tensile faults in a half-space. *Bulletin of the Seismological Society of America* **75**(4):https://pubs.geoscienceworld.org/bssa/article-pdf/75/4/1135/2705188/BSSA0750041135.pdf (1985)

Ortega-Gutiérrez, F., Elías-Herrera, M., Morán-Zenteno, D., Solari, L., Luna-González, L., and Schaaf, P. A review of batholiths and other plutonic intrusions of Mexico. *Gondwana Research* **26**(3):834–868 (2014)

Ozawa, S., Murakami, M., and Tada, T. Time-dependent inversion study of the slow thrust event in the Nankai trough subduction zone, southwest Japan. *J. Geophys. Res.* **106**:787–802 (2001)

Ozawa, S., Murakami, M., Kaidzu, M., Tada, T., Sagiya, T., Y., H., Yarai, H., and Nishimura, T. Detection and monitoring of ongoing aseismic slip in the Tokai region, central Japan. *Science* **298**:1009–1012 (2002)

Pardo, M. and Suárez, G. Shape of the subducted Rivera and Cocos plates in southern Mexico: Seismic and tectonic implications. *Journal of Geophysical Research: Solid Earth* **100**(B7):https://doi.org/10.1029/95JB00919 (1995)

Payero, J., Kostoglodov, V., Shapiro, N., Mikumo, T., Iglesias, A., Pérez-Campos, X., and Clayton, R. Nonvolcanic tremor observed in the Mexican subduction zone. *Geophys. Res. Lett.* **35**(7):https://doi.org/10.1029/2007GL032877 (2008)

Perez Campos, X., Kim, Y., Husker, A., Davis, P.M., Clayton, R.W., Iglesias, A., Pacheco, J.F., Singh, S.K., Manea, V.C., and Gurnis, M. Horizontal subduction and truncation of the Cocos Plate beneath central Mexico. *Geophysical Research Letters* **35**(L18303):https://doi:10.1029/2008GL035127 (2008)

Peterson, C.L. and Christensen, D.H. Possible relationship between nonvolcanic tremor and the 1998-2001 slow slip event, south central Alaska. *JGR* **114**(B06302):doi:10.1029/2008JB006096 (2009)

Protti, M., González, V., Kato, T., Iinuma, T., Miyazaki, S., Obana, K., Kaneda, Y., La Femina, P., Dixon, T., and Schwartrz, S. A Creep Event on the Shallow Interface of the Nicoya Peninsula, Costa Rica Seismogenic Zone. *S41D-07*, tomo 2004. AGU, AGU Fall Meeting Abstracts (2004)

Radiguet, M., Cotton, F., Vergnolle, M., Campillo, M., Valette, B., Kostoglodov, V., and Cotte, N. Spatial and temporal evolution of a long term slow slip event: The 2006 Guerrero Slow Slip Event. *Geophys. J. Int.* **184**(2):https://doi.org/10.1111/j.1365-246X.2010.04866.x (2011)

Radiguet, M., Cotton, F., Vergnolle, M., M., C., Walpersdorf, A., Cotte, N., and Kostoglodov, V. Slow slip events and strain accumulation in the Guerrero gap, Mexico. *J. Geophys. Res.* **117**(4):https://doi.org/10.1029/2011JB008801 (2012)

Radiguet, M., Perfettini, H., Cotte, N., Gualandi, A., Valette, B., Kostoglodov, V., Lhomme, T., Walpersdorf, A., Cabral-Cano, E., and Campillo, M. Triggering of the 2014 Mw7.3 Papanoa earthquake by a slow slip event in Guerrero, Mexico. *Nature Geoscience* **9**:https://doi.org/10.1038/ngeo2817 (2016)

Rogers, G. and Dragert, H. Episodic Tremor and Slip on the Cascadia Subduction Zone: The Chatter of Silent Slip. *Science* **300**(5627):DOI: 10.1126/science.1084783 (2003)

Rousset, B., Jolivet, R., Simons, M., Lasserre, C., Riel, B., Milillo, P., Çakir, Z.,

and Renard, F. An aseismic slip transient on the North Anatolian Fault. *Geophys. Res. Lett.* **43**:https://doi.org/10.1002/2016GL068250 (2016)

Rousset, B., Bürgmann, R., and Campillo, M. Slow slip events in the roots of the San Andreas fault. *Sci. Adv.* **5**(2):DOI: 10.1126/sciadv.aav3274 (2019)

Ruiz, S., Metois, M., Fuenzalida, A., Ruiz, J., Leyton, F., Grandin, R., Vigny, C., Madariaga, R., and Campos, J. Intense foreshocks and a slow slip event preceded the 2014 Iquique Mw8.1 earthquake. *Science* **345**(6201):DOI: 10.1126/science.1256074 (2014)

Sagiya, T. Interplate coupling in the Kanto district, central Japan, and the Boso Peninsula silent earthquake in May 1996. *Pure Appl. Geophys.* **161**:https://doi:10.1007/s00024-004-2566-6 (2004)

Schwartz, S.Y. and Rokosky, J.M. Slow slip events and seismic tremor at circum-pacific subduction zones. *Rev. Geophys.* **45**(RG3004):doi:10.1029/2006RG000208 (2007)

Segall, P. and Bradley, A. Slow-slip evolves into megathrust earthquakes in 2D numerical simulations. *Geophysical Research Letters* **39**(L18308):doi:10.1029/2012gl052811 (2012)

Shmaliy, Y. *Continuous-Time Signals*. Springer, Dordrecht (2006)

Solari, L., Torres de León, R., Hernández-Pineda, G., Solé, J., Hernández-Treviño, T., and Solís-Pichardo, G. Tectonic significance of Cretaceous-Tertiary magmatic and structural evolution of the northern margin of the Xolapa Complex, Tierra Colorada area, southern Mexico. *Geological Society of America Bulletin* **119**(9/10):1,265–1,279 (2007)

Suárez, G., Monfret, T., Wittlinger, G., and David, C. Geometry of subduction and depth of the seismogenic zone in the Guerrero Gap, México. *Nature* **345** (1990)

Suter, M., Quintero, O., and Johnson, C.A. Active faults and state of stress in the central part of the Trans-Mexican Volcanic Belt, Mexico. The Venta de Bravo Fault. *Journal of Geophysical Research: Solid Earth* **97**(B8):11,983–11,993 (1992)

Tarantola, A. *Inverse problem theory and methods for model parameter estimation.* Society for Industrial and Applied Mathematics (SIAM), Philadelphia (2005)

Tolson, G. La falla Chacalapa en el sur de Oaxaca. *Boletín de la Sociedad Geológica Mexicana* **LVII**(1):111–122 (2005)

Tymofyeyeva, E., Fialko, Y., Jiang, J., Xu, X., Sandwell, D., Bilham, R., Rockwell, T.K., Blanton, C., Burkett, F., Gontz, A., and S., M. Slow Slip Event On the Southern San Andreas Fault Triggered by the 2017 Mw8.2 Chiapas (Mexico) Earthquake. *Journal of Geophysical Research: Solid Earth* **124**(9):https://doi.org/10.1029/2018JB016765 (2019)

Vergnolle, M., Walpersdorf, A., Kostoglodov, V., Tregoning, P., Santiago, J.A., Cotte, N., and Franco, S.I. Slow slip events in Mexico revised from the processing of 11 year GPS observations. *Journal of Geophysical Research: Solid Earth* **115**(B8):https://doi.org/10.1029/2009JB006852 (2010)

Vidale, J. and Houston, H. Slow Slip: A New Kind of Earthquake. *Physics Today* (2012)

Villegas-Lanza, J., Nocquet, J.M., Rolandone, F., Vallée, M., Tavera, H., Bondoux, F., Tran, T., Martin, X., and Chlieh, M. A mixed seismic-aseismic stress release episode in the Andean subduction zone. *Nature Geoscience* **9**:DOI:10.1038/NGEO262 (2015)

Wesson, R.L. Dynamics of fault creep. *Journal of Geophysical Research: Solid Earth* https://doi.org/10.1029/JB093iB08p08929 (1988)

Ye, L., Lay, T., Bai, Y., Cheung, K.F., and Kanamori, H. The 2017 Mw8.2 Chiapas, Mexico, earthquake: Energetic slab detachment. *Geophys. Res. Lett.* **44**:https://doi.org/10.1002/2017GL076085 (2017)

Yoshioka, S., Mikumo, M., Kostoglodov, V., Larson, K., Lowry, A., and Singh, S. Interplate coupling and a recent aseismic slow slip event in the Guerrero seismic gap of the Mexican subduction zone, as deduced from GPS data inversion

using a Bayesian information criterion. *Physics of the Earth and Planetary Interiors* **146**(3):https://doi.org/10.1016/j.pepi.2004.05.006 (2004)